

General Disclaimer

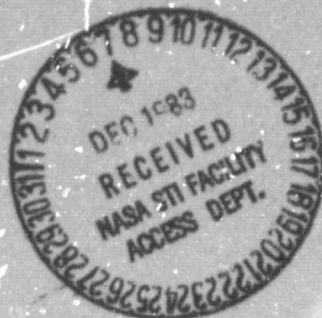
One or more of the Following Statements may affect this Document

- This document has been reproduced from the best copy furnished by the organizational source. It is being released in the interest of making available as much information as possible.
- This document may contain data, which exceeds the sheet parameters. It was furnished in this condition by the organizational source and is the best copy available.
- This document may contain tone-on-tone or color graphs, charts and/or pictures, which have been reproduced in black and white.
- This document is paginated as submitted by the original source.
- Portions of this document are not fully legible due to the historical nature of some of the material. However, it is the best reproduction available from the original submission.

DRA



National
Aeronautics and
Space
Administration



NASA CR-168243
GARRETT 21-4742-1

AEROTHERMAL MODELING PROGRAM PHASE I FINAL REPORT

by

R. Srinivasan, R. Reynolds, I. Ball,
R. Berry, K. Johnson, and H. Mongia

Garrett Turbine Engine Company
A Division of The Garrett Corporation

August 1983

Volume I

Prepared for

NATIONAL AERONAUTICS AND SPACE ADMINISTRATION
NASA-Lewis Research Center
Contract NAS3-23523

(NASA-CR-168243-Vol-1) AEROTHERMAL MODELING N84-12264
PROGRAM, PHASE I Final Report (Garrett
Turbine Engine Co.) 327 p HC A15/MF A01
CSCI 215 Unclas
G3/25 42524

1. Report No. CR-168243		2. Government Accession No.		3. Recipient's Catalog No.	
4. Title and Subtitle Aerothermal Modeling Program, Phase I Final Report				5. Report Date November 1983	
				6. Performing Organization Code	
7. Author(s) R. Srinivasan, R. Reynolds, I. Ball, R. Berry, K. Johnson, and H. Mongia				8. Performing Organization Report No. 21-4742	
9. Performing Organization Name and Address Garrett Turbine Engine Company 111 S. 34th Street, P.O. Box 5217 Phoenix, AZ. 80810				10. Work Unit No.	
				11. Contract or Grant No. NAS3-23523	
				13. Type of Report and Period Covered Final, Phase I	
12. Sponsoring Agency Name and Address NASA-Lewis Research Center				14. Sponsoring Agency Code	
15. Supplementary Notes Project Manager: Dr. J.D. Holdeman NASA-Lewis Research Center Cleveland, Ohio					
16. Abstract The main objective of the NASA Aerothermal Modeling Program, Phase I was to assess current submodels used in the Garrett combustor analytical models that have been successfully used in designing advanced technology combustors. Another objective of the study was to make specific recommendations for further improvement of model accuracy for combustor design purposes. Based upon an exhaustive literature survey, a number of test cases were selected to assess accuracy of submodels of turbulence, turbulence/chemistry interaction, spray combustion, and dilution jet mixing processes within a confined cross-stream. These test cases included simple flows and complex flows with and without swirl. Nonrecirculating and recirculating, and nonreactive and reactive flows were investigated. Based on this investigation and prior work at GTEC, it was concluded that the current models give qualitative trends for the recirculating secondary flows (as encountered in a gas turbine combustor primary zone), but the predictions are good for the dilution zone. Further work should include development of advanced numerical schemes and more accurate turbulence/chemistry interaction models. Benchmark quality data should be collected for flows of relevance to modern gas turbine combustors.					
17. Key Words (Suggested by Author(s)) Aerothermal Modeling Combustor Models Reacting Flows Gas Turbine Combustors			18. Distribution Statement		
19. Security Classif. (of this report) UNCLASSIFIED		20. Security Classif. (of this page) UNCLASSIFIED		21. No. of Pages 656	22. Price*

* For sale by the National Technical Information Service, Springfield, Virginia 22161

FOREWORD

Dr. S. Srivatsa was involved during the initial stages of this program. A number of other people have also helped in this investigation by supplying the detailed measurements and contributing significant discussions.

Special acknowledgement is given to the contributions made by the following:

Professor S. V. Patankar
Professor R. W. Bilger
Professor J. H. Whitelaw
Professor G. S. Samuelsen
Professor S. N. B. Murthy
Dr. C. J. Marek
Dr. W. M. Roquemore
Professor G. M. Faeth
Professor E. Logan

This report is printed in two volumes. Volume I contains Sections 1 through 6; Volume II contains Sections 7 through 10.

PRECEDING PAGE BLANK NOT FILMED

TABLE OF CONTENTS
VOLUME I

	<u>Page</u>
LIST OF ILLUSTRATIONS	vii
LIST OF TABLES	xxvii
SECTION I	
1.0 SUMMARY	1
SECTION II	
2.0 INTRODUCTION	3
2.1 Aerothermal Modeling Background	4
2.2 Garrett Empirical/Analytical Combustor Design Approach	6
SECTION III	
3.0 DESCRIPTION OF ANALYTICAL MODELS	13
3.1 The Analytical Models	13
3.2 Description of Turbulence and Scalar Transport	19
3.3 Gaseous Fuel Combustion Models	39
3.4 Spray Evaporation/Combustion Models	59
3.5 Soot Formation and Oxidation	70
3.6 Radiation Modeling	79
SECTION IV	
4.0 DESCRIPTION OF THE COMPUTATIONAL SCHEME	85
4.1 Description of the Numerical Method	85
4.2 Boundary Conditions	90
4.3 Convergence Criteria	92
SECTION V	
5.0 DATA BASE FOR BENCHMARK QUALITY TEST CASES	93
5.1 Data Base from Ideal Element Tests	93
5.2 Data Base from Garrett Gas Turbine Combustors	142
SECTION VI	
6.0 SIMPLE FLOWS	153
6.1 Flow Over a Flat Plate	153
6.2 Plane Couette Flow	165
6.3 Developing Flow in a Two-Dimensional Channel	175
6.4 Developing Pipe Flow	180
6.5 Fully Developed Pipe Flow	187
6.6 Two-Stream Mixing Layer	194
6.7 Mixing of Coaxial Jets in Ambient Air	201
6.8 Free Circular Jet	209
6.9 Flow Over a Heated Flat Plate	222
6.10 Plug Flow Reactor	237

TABLE OF CONTENTS (CONTD)

	<u>Page</u>
6.11 Laminar Diffusion Flame	240
6.12 Turbulent Premixed Flame in a Rectangular Duct	254
6.13 Free Methane Turbulent Jet Flame	288
VOLUME II	
7.0 COMPLEX NONSWIRLING FLOWS	303
7.1 Flow in a Curved Channel	303
7.2 Flow Over a Backward-Facing Plane Step	329
7.3 Flow Through a Sudden Pipe Expansion	360
7.4 Flow Over a Circular Ring	363
7.5 Flow Around a Wedge-Shaped Flameholder	366
7.6 Flow Around a Confined Disk	369
7.7 Confined Coaxial Jet Expansion	371
7.8 Nonreacting and Reacting Flow Behind a Step	384
7.9 Opposed Reacting Jet Flow	407
7.10 Axisymmetric Combustor with Coaxial Fuel and Air Jets	423
8.0 SWIRLING FLOWS	439
8.1 Free Swirling Jet in a Stagnant Medium	439
8.2 Nonreacting Swirling Combustor	465
8.3 Confined Swirler Flow	469
8.4 Swirl Combustor with Cooling Air	475
8.5 Swirling Flow in a Pipe Expansion	504
8.6 Confined Swirl-Driven Flow	528
8.7 Combusting Spray in Confined Swirling Flow	539
9.0 DILUTION JET MIXING VALIDATION	549
9.1 Effects of Finite-Difference Grid Distribution	549
9.2 Single-Sided Injection: Effects of Jet Size and Spacing	579
9.3 Single-Sided Injection: Effects of Jet Momentum Ratio and Cross-Stream Temperature Profile	585
9.4 Two-Side Jet Injection	595
10.0 CONCLUSIONS AND RECOMMENDATIONS	605
10.1 Conclusions	605
10.2 Recommendations	610
REFERENCES	611

LIST OF ILLUSTRATIONS

<u>Figure</u>	<u>Title</u>	<u>Page</u>
2.2-1	Combustor Models and Region of Application	7
2.2-2	Combustor Design Methodology	9
4.1-1	Typical Grid Spacing of the Swirling Flow Problem and Control Value around a Point P	89
5.2-1	Nonreacting Swirling Combustor Flow Validation	143
5.2-2	Cold Flow Can Combustor Mapping Setup and Test Conditions	144
5.2-3	Can Combustor for Reacting Flow Mapping	145
5.2-4	Natural Gas Nozzle and Airblast Nozzle Used for the Can Combustor Mapping	146
5.2-5	Axially Staged Burning Zones of the Piloted PM/PV Combustion System	148
5.2-6	Emission Sampling Probe Stations Inside the TFE731 Combustor	149
5.2-7	Schematic of Emissions Probe and Measurement Locations for Fuel/Air Rate Profiles in the UT76 Combustor	151
6.1-1	Watts and Brundrett ⁶⁷ Setup for Turbulent Flow over a Flat Plate	158
6.1-2	Turbulent Boundary Layer Mean Velocity Profiles with the Standard k- ϵ Model	159
6.1-3	Turbulent Boundary Layer Mean Velocity Profiles with the k- ϵ Model and Chien's Low Reynolds Number Correction (Low Reynolds Number (k- ϵ Model))	160
6.1-4	Turbulent Boundary Layer Mean Velocity Profiles with the Algebraic Stress Model (ASM)	161
6.1-5	Turbulent Boundary Layer Mean Velocity Profiles with ASM Modified by Low Reynolds Number Correction	162
6.1-6	Turbulent Kinetic Energy Profiles Predicted by the Four Turbulence Models	163

LIST OF ILLUSTRATIONS (CONTD)

<u>Figure</u>	<u>Title</u>	<u>Page</u>
6.1-7	Fluctuating Components of Axial, Radial and Transverse Velocities (u' , v' and w') Predicted by ASM, and ASM with Low Reynolds Number Correction	164
6.2-1	Geometry of Plane Couette Flow	168
6.2-2	Comparison Between $k-\epsilon$ Predictions and Measured Couette Flow Axial Velocity Profile (u_+ versus Y_+)	169
6.2-3	Comparison Between $k-\epsilon$ Model Predictions and Measured Shear Stress Profile (normalized by wall shear value)	169
6.2-4	Shear Stress Normalized by Turbulence Kinetic Energy (uv/K) Standard $k-\epsilon$ Model With $C_D = 0.09$	170
6.2-5	$k-\epsilon$ Model Predicted uv/k Profiles With $C_D = 0.144$	170
6.2-6	$k-\epsilon$ Model Predicted U_+ With $C_D = 0.144$	171
6.2-7	ASM Prediction and Measured u_+ Versus y_+ Profiles	171
6.2-8	ASM Prediction and Measured Normalized Shear Stress Profile	172
6.2-9	Shear Stress (uv) Normalized by Turbulence Kinetic Energy Predicted by ASM Versus Increased Data	172
6.2-10	Correlation Coefficient ($\overline{uv}/(\overline{uv}/u' \times v')$) Predicted by ASM Versus Measurements	173
6.2-11	ASM Predictions and Measured Axial Turbulence Intensity (u'/u^*)	173
6.2-12	ASM Predictions and Measured Radial Turbulence Intensity	174
6.2-13	ASM Predictions and Measured w'	174
6.3-1	Geometry of Developing Flow in a Two-Dimensional Duct	176
6.3-2	Predicted and Measured Distributions of Center-line Axial Velocity for Developing Flow in a Two-Dimensional Duct	177

LIST OF ILLUSTRATIONS (CONTD)

<u>Figure</u>	<u>Title</u>	<u>Page</u>
6.3-3	Predicted and Measured Mean Velocity Profiles at Different Axial Stations for Developing Channel Flow	178
6.3-4	Predicted and Measured Wall Shear Stress Distributions for Developing Flow in a Two-Dimensional Duct	179
6.4-1	Developing Pipe Flow Setup of Barbin and Jones ⁶⁸	182
6.4-2	Comparison Between k- ϵ Model Predictions and Profiles of Axial Velocity at Different Axial Stations in a Developing Pipe Flow (U_b = The Average Flow Velocity)	183
6.4-3	Comparison Between ASM Predictions and Measured Axial Velocity Profiles; $D = 20$ cm, $U_b = 33.17$ m/s	184
6.4-4	Comparison Between ASM Predictions and Measurements for Nondimensionalized Axial Turbulence Velocity Fluctuations	185
6.4-5	Comparison Between ASM Predictions and Measurements for Nondimensionalized Circumferential Turbulence Velocity Fluctuations	186
6.5-1	Geometry of the Pipe Flow	189
6.5-2	Low Reynolds k- ϵ Model Axial Velocity Profile	190
6.5-3	Low Reynolds k- ϵ Model Turbulence Kinetic Energy Profile	190
6.5-4	ASM With Low Reynolds Number Correction -- Axial Velocity Profile	191
6.5-5	ASM With Low Reynolds Number Correction -- Turbulence Kinetic Energy Profile	191
6.5-6	u'/u^* Profile	192
6.5-7	v'/u^* Profile	192
6.5-8	w'/u^* Profile	193
6.5-9	\overline{uv}/u_*^2 Profile	193

LIST OF ILLUSTRATIONS (CONTD)

<u>Figure</u>	<u>Title</u>	<u>Page</u>
6.6-1	Two-Stream Mixing-Layer Setup of Saiy and Peerless ⁶⁰	196
6.6-2	Mixing Layer Mean Axial Velocity and Turbulent Kinetic Energy (TKE) Profiles Predicted by the Standard k- ϵ Model	197
6.6-3	Mixing Layer Mean Axial Velocity Profiles Predicted by the Algebraic Stress Model (ASM)	198
6.6-4	Mixing Layer Fluctuating Velocity Components (u' , v' and w') Predicted by ASM	199
6.6-5	Mixing Layer Turbulent Kinetic Energy and Shear Stress Profiles Predicted by ASM	200
6.7-1	Coaxial-Jets Mixing Setup of Champagne et al ⁵⁹	203
6.7-2	Comparison Between k- ϵ Model Predictions and Measured Axial Velocity Profiles of Coaxial Jets in Ambient Air	204
6.7-3	Comparison Between ASM Predictions and Measured Axial Velocity Profiles of Coaxial Jets in Ambient Air	205
6.7-4	Predicted and Measured Profiles of RMS Axial Velocity (u') for Coaxial Jets in Ambient Air	206
6.7-5	Predicted and Measured Profiles of Fluctuating Radial Velocity Component (v')	207
6.7-6	Predicted and Measured Sheer Stress (\overline{uv}) Profiles for the Coaxial Jets in Ambient Air	208
6.8-1	Geometry of Single Free Jet Setup Studied by Wagnanski and Fiedler	212
6.8-2	Comparison Between k- ϵ Model Predictions and Measured Axial Velocity Profiles, Initial Jet Velocity = 51 m/s Initial Jet Diameter D = 26.4 mm	213
6.8-3	Modified k- ϵ Model Predictions with C_D and C_2 Constants Given by Equations (141) and (142)	214

LIST OF ILLUSTRATIONS (CONTD)

<u>Figure</u>	<u>Title</u>	<u>Page</u>
6.8-4	Modified k- ϵ Model (k- ϵ 1) Predictions with C_D as given by Equation 62	215
6.8-5	Modified k- ϵ Model (k- ϵ 2) Predictions with C_2 and C_D as Given by Equations 60 and 62	216
6.8-6	Comparison Between ASM Predictions and Measured Axial Velocity Profiles of a Free Jet	217
6.8-7	Comparison Between ASM Predictions and Measurements for Axial RMS Turbulence Velocity Fluctuations	218
6.8-8	Comparison Between ASM Predictions and Measurements for Radial RMS Turbulence Velocity Fluctuations	219
6.8-9	Comparison Between ASM Predictions and Measurements for Circumferential RMS Turbulence Velocity Fluctuations	220
6.8-10	Comparison Between ASM Predictions and Measurements for Turbulent Shear Stress	221
6.9-1	Geometry of Flow Over a Flat Plate with Step Change in Temperature	227
6.9-2	k- ϵ Model Predictions and Measured Mean Temperature Profile on a Flat Plate with Step Change in Temperature	228
6.9-3	k- ϵ Model Prediction, and Measured RMS Temperature Normalized by $(T_{w0} - T_{\infty})$	229
6.9-4	k- ϵ Model Predictions and Measured $(\sqrt{vT'})$ Normalized by $U (T_{w0} - T_{\infty})$	230
6.9-5	ASM Predictions of Mean Temperature Profile	231
6.9-6	ASM Predictions of RMS Temperature Profile	232
6.9-7	ASM Predictions of $(\sqrt{vT'})$	233
6.9-8	ASM Predictions of Mean Temperature Profiles	234

LIST OF ILLUSTRATIONS (CONTD)

<u>Figure</u>	<u>Title</u>	<u>Page</u>
6.9-9	ASTM Predictions of the RMS Temperature Profile	235
6.9-10	ASTM Predictions of $(\overline{vT'})$ Profiles	236
6.10-1	Princeton High Temperature Plug Flow Reactor	238
6.10-2	Comparison of 2-Step and 4-Step Kinetic Scheme With Lean Propane Premixed Flame Data from High Temperature Plug Flow Reactor	239
6.11-1	Schematic of Laminar Diffusion Flame Setup Used by Mitchell	242
6.11-2	Comparison Between Two-Step Model Predictions and Measurements for Axial Velocity and Temperature Profiles of the Mitchell's Laminar Diffusion Flame at 1.2 cm Above the Burner Plate	243
6.11-3	Two-Step Predictions and Measurements for CH ₄ , CO ₂ , H ₂ O and O ₂ Profiles, X = 1.2 cm	244
6.11-4	Two-Step Predictions and Measurements for N ₂ and CO Profiles, X = 1.2 cm	244
6.11-5	Comparison Between Two-Step Predictions and Measurements of Velocity and Temperature Profiles of the Mitchell's Laminar Diffusion Flame at X = 2.4 cm	245
6.11-6	Predicted and Measured Species Profiles at X = 2.4 cm (Two-Step)	245
6.11-7	Comparison Between Predicted and Measured Axial Velocity and Temperature Profiles and Mitchell's Laminar Diffusion Flame at X = 5.0 cm (Two-Step)	246
6.11-8	Predicted and Measured Species Profiles at X = 5.0 cm (Two Step)	246
6.11-9	4-Step Scheme, Axial Velocity Profiles	247
6.11-10	4-Step Scheme, Temperature Profiles	248
6.11-11	4-Step Scheme, Methane Profiles	249

LIST OF ILLUSTRATIONS (CONTD)

<u>Figure</u>	<u>Title</u>	<u>Page</u>
6.11-12	4-Step Scheme, CO ₂ Profiles	250
6.11-13	4-Step Scheme, CO Profiles	251
6.11-14	4-Step Scheme, O ₂ Profiles	252
6.11-15	4-Step Scheme, H ₂ O Profiles	253
6.12-1	Geometry of Turbulent Premixed Flame in a Rectangular Duct	259
6.12-2	Predicted Velocity Profiles With Design Criteria Rate Constants	260
6.12-3	Predicted Unburned Fuel Profiles With Design Criteria Rate Constants	261
6.12-4	Predicted CO Profiles With Design Criteria Rate Constants	262
6.12-5	Predicted Temperature Profiles With Design Criteria Rate Constants	263
6.12-6	Predicted O ₂ Mass Fraction With Design Criteria Rate Constants	264
6.12-7	Predicted CO ₂ Profiles With Design Criteria Rate Constants	265
6.12-8	Predicted H ₂ O Profiles With Design Criteria Rate Constants	266
6.12-9	Predicted Velocity Profiles With PM/PV Rate Constants	267
6.12-10	Predicted Unburned Fuel Profiles With PM/PV Rate Constants	268
6.12-11	Predicted CO ₂ Profiles With PM/PV Rate Constants	269
6.12-12	Predicted CO Profiles With PM/PV Rate Constants	270
6.12-13	Predicted Temperature Profiles With PM/PV Rate Constants	271
6.12-14	Predicted O ₂ Profiles With PM/PV Rate Constants	272

LIST OF ILLUSTRATIONS (CONTD)

<u>Figure</u>	<u>Title</u>	<u>Page</u>
6.12-15	Predicted H ₂ O Profiles With PM/PV Rate Constants	275
6.12-16	Predicted Velocity Profiles with the 4-Step Scheme	273
6.12-17	Predicted Unburned Fuel Profiles With the 4-Step Scheme	275
6.12-18	Predicted CO Profiles With the 4-Step Scheme	276
6.12-19	Predicted Temperature Profiles With the 4-Step Scheme	277
6.12-20	Predicted O ₂ Profiles With the 4-Step Scheme	278
6.12-21	Predicted CO ₂ Profiles With the 4-Step Scheme	279
6.12-22	Predicted H ₂ O Profiles With the 4-Step Scheme	280
6.12-23	4-Step Scheme With Modified Rate Constants for Fuel and Intermediate Fuel Reaction Steps (Modified 4-Step) Axial Velocity Profile	281
6.12-24	Modified 4-Step -- Unburned Fuel Profiles	282
6.12-25	Modified 4-Step CO Profiles	283
6.12-26	Modified 4-Step -- Temperature Profiles	284
6.12-27	Modified 4-Step -- O ₂ Profiles	285
6.12-28	Modified 4-Step -- CO ₂ Profiles	286
6.12-29	Modified 4-Step -- H ₂ O Profiles	287
6.13-1	Geometry of the Free Methane Turbulent Jet Flame Test Setup	293
6.13-2	Comparison Between Bilger Model Predictions With Measured Centerline Profiles of Temperature, CO, CO ₂ and O ₂ for Hassan and Lockwood Methane Jet Flame	294
6.13-3	Radial Profiles of Total Fuel (Bilger's Model)	295
6.13-4	Radial Profiles of Unburned Fuel Mass Fraction	296

LIST OF ILLUSTRATIONS (CONTD)

<u>Figure</u>	<u>Title</u>	<u>Page</u>
6.13-5	Radial Profiles of Temperature (Bilger's Model)	297
6.13-6	Radial Profiles of CO (Bilger's Model)	298
6.13-7	Radial Profiles of H ₂ (Bilger's Model)	299
6.13-8	Radial Profiles of O ₂ (Bilger's Model)	300
6.13-9	Radial Profiles of CO ₂ (Bilger's Model)	301
7.1-1	Configuration of the Curved Channel Test Setup	308
7.1-2	Comparison Between Predictions (k- ϵ Model) and Measurement Along the Inner (Convex) Wall	309
7.1-3	k- ϵ Model Velocity Profiles Along the Outer (Concave) Wall	310
7.1-4	k- ϵ Model With Streamline Curvature Correction -- Axial Velocity Profile Along the Inner (Convex) Wall	311
7.1-5	k- ϵ Model With Streamline Curvature Correction -- Axial Velocity Profile Along the Outer (Concave) Wall	312
7.1-6	ASM Prediction and Measured Axial Velocity Profiles Along the Inner (Convex) Wall	313
7.1-7	ASM Predictions and Measured Axial Velocity Profiles Along the Outer (Concave) Wall	314
7.1-8	ASM Predictions and Measured RMS Axial Velocity Profiles Along the Inner (Convex) Wall	315
7.1-9	ASM Predictions and Measured RMS Axial Velocity Profiles Along the Outer (Concave) Wall	316
7.1-10	ASM Predictions and Measured RMS Radial Velocity Profiles Along the Inner (Convex) Wall	317
7.1-11	ASM Predictions and Measured RMS Radial Velocity Profiles Along the Outer (Concave) Wall	318

LIST OF ILLUSTRATIONS (CONTD)

<u>Figure</u>	<u>Title</u>	<u>Page</u>
7.1-12	ASM Predictions and Measured Shear Stress (uv) Profiles Along the Inner (Convex) Wall	319
7.1-13	ASM Predictions and Measured Shear Stress (uv) Profiles Along the Outer (Concave) Wall	320
7.1-14	ASM With Streamline Curvature Correction -- Axial Velocity Profiles Along the Inner (Convex) Wall	321
7.1-15	ASM With Streamline Curvature Correction -- Axial Velocity Profiles Along the Outer (Concave) Wall	322
7.1-16	ASM With Streamline Curvature Correction -- RMS Axial Velocity Profiles Along the Inner (Convex) Wall	323
7.1-17	ASM With Streamline Curvature Correction -- RMS Axial Velocity Profiles Along the Outer (Concave) Wall	324
7.1-18	ASM With Streamline Curvature Correction -- RMS Radial-Velocity Profiles Along the Inner (Convex) Wall	325
7.1-19	AMS With Streamline Correction -- RMS Radial-Velocity Profiles Along the Outer (Concave) Wall	326
7.1-20	ASM With Streamline Curvature Correction -- uv Profiles Along the Inner (Convex) Wall	327
7.1-21	ASM With Streamline Curvature Correction -- uv Profiles Along the Outer (Concave) Wall	328
7.2-1	Geometry of the Backward Facing Plane Step Test Rig	336
7.2-2	Partial Grid Network for the Flow Behind the 3.81-cm Step	337
7.2-3	Standard k-ε Model -- Mean Axial Velocity Profiles for 3.81-cm Step	338
7.2-4	Predicted Streamline Plot With the Standard k-ε Model	339

LIST OF ILLUSTRATIONS (CONTD)

<u>Figure</u>	<u>Title</u>	<u>Page</u>
7.2-5	k- ϵ Model With Richardson Number Correction Axial Velocity Profiles for the 3.81-cm Step	340
7.2-6	Predicted Streamline Plot With Richardson Number Correction	341
7.2-7	ASM With Richardson Number Correction -- Axial Velocity Profiles for the 3.81-cm Step	342
7.2-8	ASM With Richardson Number Correction -- Turbulence Kinetic Energy Profiles for the 3.81-cm Step	343
7.2-9	AMS With Richardson Number Correction -- RMS Axial Velocity Profiles (u^2/U_{Ref}^2) for the 3.81-cm Step	345
7.2-10	ASM With Richardson Number Correction -- RMS Radial Velocity (v^2/U_{Ref}^2) for the 3.81-cm Step	345
7.2-11	ASM With Richardson Number Correction -- Shear Stress (\overline{uv}/U_{Ref}^2) Distribution	346
7.2-12	Comparison Between Standard k- ϵ Model Pre- dictions and Measured Streamwise Velocity Components for 2.54-cm Step Height	347
7.2-13	k- ϵ Model With Richardson Number Correction - Axial Velocity Profile for the 2.54-cm Step	348
7.2-14	ASM with Richardson Number Correction - Axial Velocity Profile	349
7.2-15	ASM with Richardson Number Correction - Turbulence Kinetic Energy Profile	350
7.2-16	Axial Velocity Fluctuations ($\overline{u^2}/U_{Ref}^2$)	351
7.2-17	Normal Velocity Fluctuations ($\overline{v^2}/U_{Ref}^2$)	352
7.2-18	Shear Stress (\overline{uv}/u_{Ref}^2) Profiles for the 2.54-cm Step	353

LIST OF ILLUSTRATIONS (CONTD)

<u>Figure</u>	<u>Title</u>	<u>Page</u>
7.2-19	Comparison Between the Standard k- ϵ Model Predictions and Measured Streamwise Velocity Components for the 5.08 cm Step	354
7.2-20	k- ϵ Model with Richardson Number Correction - Axial Velocity Profile	355
7.2-21	ASM with Richardson Number Correction - Axial Velocity Profile	356
7.2-22	ASM with Richardson Number Correction - Axial Velocity Fluctuations (u^2/U_{Ref}^2)	357
7.2-23	Shear Stress (\overline{uv}/U_{Ref}^2) Distribution	358
7.2-24	Comparison Between Predicted and Measured Wall Static Pressure Distribution	359
7.3-1	Sudden Pipe-Expansion Setup of Moon and Rudinger ⁸⁹	361
7.3-2	Comparison Between the Standard k- ϵ Prediction and Measured Axial Velocity Profiles in a Tube With Sudden Expansion	362
7.4-1	Schematic of Logan's Setup for Studying Flow Over a Ring in a Pipe	364
7.4-2	Comparison Between Predicted and Measured Axial Velocity and Turbulent Kinetic Energy for Logan's H-Ring	365
7.5-1	Wedge-Shaped Flameholder Setup	367
7.5-2	Comparison Between Measured and Predicted Streamline Plots Around a Wedge-Shaped Flameholder	367
7.6-1	APL Combustion Tunnel Setup	370
7.6-2	Comparison Between Measured and Predicted Centerline Velocity Profile Behind a Confined Disk	370
7.7-1	Geometry of Confined Coaxial Jet Expansion Setup	374

LIST OF ILLUSTRATIONS (CONTD)

<u>Figure</u>	<u>Title</u>	<u>Page</u>
7.7-2	Finite Difference Grid Network for Confined Coaxial Jet Expansion	375
7.7-3	Standard k- ϵ Model - Axial Velocity Profiles	376
7.7-4	Standard k- ϵ Model - Turbulence Kinetic Energy Profiles	377
7.7-5	k- ϵ Model with Richardson Number Correction - Mean Axial Velocity Profiles	378
7.7-6	k- ϵ Model with Richardson Number Correction - Turbulence Kinetic Energy Profiles	379
7.7-7	ASM with Richardson Number Correction - Mean Axial Velocity Profiles	380
7.7-8	ASM with Richardson Number Correction - Fluctuating Axial Velocity Profiles	381
7.7-9	ASM with Richardson Number Correction - Fluctuating Radial Velocity Profiles	382
7.7-10	ASM with Richardson Number Correction - Shear Stress Profiles	383
7.8-1	Schematic of the Test Rig for Nonreacting and Reacting Flow Behind a Step	389
7.8-2	Comparison Between the k- ϵ Model Prediction and Measured Streamwise Velocity Components for Nonreacting Flow Behind a Step	390
7.8-3	ASM with Richardson Number Correction - Nonreacting Mean Axial Velocity Profile	391
7.8-4	ASM with Richardson Number Correction - Nonreacting Axial Turbulence Intensity Profiles	392
7.8-5	k- ϵ Model with 2-Step Reaction Scheme - Mean Axial Velocity Profiles	393
7.8-6	2-Step Reaction Scheme - Mean Temperature Profiles	394
7.8-7	Four-Step Reaction Scheme-Mean Axial Velocity Profiles	395

LIST OF ILLUSTRATIONS (CONTD)

<u>Figure</u>	<u>Title</u>	<u>Page</u>
7.8-8	Four-Step Reaction Scheme - Mean Temperature Profiles	396
7.8-9	Measured Wall Temperature Distribution Behind the Step	397
7.8-10	Two-Step Reaction Scheme with Measured Wall Temperature Distribution - Mean Axial Velocity Profiles	398
7.8-11	Two-Step Reaction Scheme With Measured Wall Temperature Distribution - Mean Temperature Profiles	399
7.8-12	Two-Step Reaction Scheme With Measured Wall Temperature Distribution - CO and CO ₂ Profiles	400
7.8-13	Four-Step Reaction Scheme With Measured T _w Distribution - Mean Axial Velocity Profiles	401
7.8-14	Four-Step Reaction Scheme With Measured T _w Distribution - Mean Temperature Profiles	402
7.8-15	Four-Step Reaction Scheme With Measured T _w Distribution - CO and CO ₂ Profiles	403
7.8-16	Four-Step Reaction Scheme With Modified Rate Constants - Mean Axial Velocity Profiles	404
7.8-17	Four-Step Reaction Scheme With Modified Rate Constants - Mean Temperature Profiles	405
7.8-18	Four-Step Scheme With Modified Rate Constants - CO and CO ₂ Profiles	406
7.9-1	Geometry of the Opposed Jet Combustion Setup	410
7.9-2	2-Step Kinetic Scheme - Mean Temperature Profile	411
7.9-3	2-Step Scheme - Unburned Fuel Profiles	412
7.9-4	2-Step Scheme - CO ₂ Profiles	413
7.9-5	2-Step Scheme - CO Profiles	414

LIST OF ILLUSTRATIONS (CONTD)

<u>Figure</u>	<u>Title</u>	<u>Page</u>
7.9-6	2-Step Scheme - H ₂ O Profiles	415
7.9-7	2-Step Scheme - O ₂ Profiles	416
7.9-8	4-Step Reaction Scheme with Original Rate Constants - Temperature Profiles	417
7.9-9	4-Step Scheme - Unburned Fuel Profiles	418
7.9-10	4-Step Scheme - CO ₂ Profiles	419
7.9-11	4-Step Scheme - CO Profiles	420
7.9-12	4-Step Scheme - H ₂ O Profiles	421
7.9-13	4-Step Scheme - O ₂ Profiles	422
7.10-1	Geometry of Axisymmetric Combustor With Coaxial Fuel and Air Jets	426
7.10-2	2-Step Scheme - Total Fuel Profiles	427
7.10-3	2-Step Scheme - Unburned Fuel Profiles	428
7.10-4	2-Step Scheme - CO and Temperature Profiles	429
7.10-5	4-Step Scheme - Total Fuel Profiles	430
7.10-6	4-Step Scheme - Unburned Fuel Profiles	431
7.10-7	4-Step Scheme - CO ₂ Profiles	432
7.10-8	4-Step Scheme - CO and Temperature Profiles	434
7.10-9	4-Step Scheme - O ₂ Profiles	435
7.10-10	4-Step Scheme - H ₂ O Profiles	436
7.10-11	4-Step Scheme - H ₂ Profiles	438
8.1-1	Test Setup for Swirling Air Injected Into Stagnant Air	446
8.1-2	Standard k-ε Model - Mean Axial Velocity Profiles	447
8.1-3	Standard k-ε Model - Mean Tangential Velocity Profile	448

LIST OF ILLUSTRATIONS (CONTD)

<u>Figure</u>	<u>Title</u>	<u>Page</u>
8.1-4	Standard k- ϵ Model with 0.7 Prandtl Number - Mean Axial Velocity Profiles	449
8.1-5	Standard k- ϵ Model with 0.7 Prandtl Number - Mean Tangential Velocity Profiles	450
8.1-6	k- ϵ 1 Turbulence Model - Mean Axial Velocity Profiles	451
8.1-7	k- ϵ 1 Turbulence Model - Mean Tangential Velocity Profiles	452
8.1-8	k- ϵ 1 Model with 0.7 Prandtl Number - Mean Axial Velocity Profiles	453
8.1-9	k- ϵ 1 Model with 0.7 Prandtl Number - Mean Tangential Velocity Profiles	454
8.1-10	k- ϵ 1 Model with Richardson Number Correction - Mean Axial Velocity Profiles	455
8.1-11	k- ϵ 1 Model with Richardson Number Correction - Mean Tangential Velocity Profiles	456
8.1-12	ASM - Mean Axial Velocity Profiles	457
8.1-13	ASM - Mean Tangential Velocity Profiles	458
8.1-14	ASM - u' Profiles	459
8.1-15	ASM - v' Profiles	460
8.1-16	ASM - w' Profiles	461
8.1-17	ASM - Shear Stress (uv) Profiles	462
8.1-18	ASM - (vw) Profiles	463
8.1-19	ASM - (uw) Profiles	464
8.2-1	Nonreacting Swirling Combustor Flow Validation	466
8.2-2	Comparison Between Measured Axial Velocity and k- ϵ Turbulence Model	467
8.2-3	Comparison Between Measured Angular Velocity and Predictions of k- ϵ Turbulence Model	468

LIST OF ILLUSTRATIONS (CONTD)

<u>Figure</u>	<u>Title</u>	<u>Page</u>
8.3-1	Configuration of the Swirling Flow Investigation at Garrett	472
8.3-2	Comparison Between Predicted and Measured Axial Velocity Profiles Behind a Confined Disk	473
8.3-3	Comparison Between Predicted and Measured Axial Velocity Profiles in Confined Recirculating Swirling Flows	474
8.4-1	Brum and Samuelson Setup for Swirl Combustor with Cooling Air	480
8.4-2	Comparison Between Measured and Predicted Centerline Axial Velocity	481
8.4-3	Comparison Between Measured and Calculated Axial Velocity Profiles	482
8.4-4	Comparison Between Measured and Calculated Swirl Velocity Profiles	484
8.4-5	Turbulence Kinetic Energy Profiles	486
8.4-6	Measured Streamline Plot	488
8.4-7	Calculated Streamline Plot	489
8.4-8	Second Set of Calculations - Centerline Axial Velocity Development	490
8.4-9	Second Set of Calculations - Axial Velocity Profiles	491
8.4-10	Second Set of Calculations - Swirl Velocity Profile	493
8.4-11	Second Set of Calculation - Turbulence Kinetic Energy Profiles	495
8.4-12	Third Set of Calculations - Centerline Axial Velocity Development	497
8.4-13	Third Set of Calculations - Axial Velocity Profiles	498

LIST OF ILLUSTRATIONS (CONTD)

<u>Figure</u>	<u>Title</u>	<u>Page</u>
8.4-14	Third Set of Calculations - Swirl Velocity Profiles	500
8.4-15	Third Set of Calculations - Turbulence Kinetic Energy Profiles	502
8.5-1	Test Setup of Swirling Flow in a Pipe Expansion	511
8.5-2	k- ϵ Model for Nonswirling Flow - Axial Velocity Profiles	512
8.5-3	k- ϵ Model with Richardson Number Correction - Axial Velocity Profiles in Nonswirling Flow Field	513
8.5-4	ASM - Axial Velocity Profiles (Nonswirling)	514
8.5-5	Nonswirling u' , v' and \overline{uv} Profiles	515
8.5-6	Comparison Between k- ϵ Model Prediction and Chaturvedi Data of Mean Axial Velocity	516
8.5-7	Chaturvedi Mean Axial Velocity Data and k- ϵ Model with Richardson Number Correction	517
8.5-8	ASM Prediction and Chaturvedi Data - Mean and Fluctuating Axial Velocity Profiles	518
8.5-9	ASM Predictions and Chaturvedi Data - \overline{uv} and \overline{v} Profiles	519
8.5-10	Standard k- ϵ Model - Mean Axial and Tangential Velocity Profiles	520
8.5-11	k- ϵ Model with Richardson Number Correction - Mean Axial and Tangential Velocity Profiles	521
8.5-12	ASM - Mean Axial and Tangential Velocity Profiles	522
8.5-13	ASM - u' , v' and \overline{uv} Profiles	523
8.5-14	ASM - w' , \overline{uw} and \overline{vw} Profiles	524
8.5-15	Reynolds Stress Shear Component (uv)	525
8.5-16	Reynolds Stress Shear Component (uw)	526

LIST OF ILLUSTRATIONS (CONTD)

<u>Figure</u>	<u>Title</u>	<u>Page</u>
8.5-17	Reynolds Stress Shear Component (vw)	527
8.6-1	Confined Swirl-Driven Flow Setup of Altgeld, Jones and Wilhelmi	531
8.6-2	Comparison Between k- ϵ Model Prediction and Measured Axial Velocity Profile in Configuration I	532
8.6-3	Configuration I - Tangential Velocity Profiles	534
8.6-4	Configuration II (Exit Baffle) - Axial Velocity Profiles	535
8.6-5	Configuration II (Exit Baffle) Tangential (Swirl) Velocity Profiles	537
8.7-1	Combusting Spray in Confined Swirling Flow (El Banhawy and Whitelaw Test Setup)	542
8.7-2	El Banhawy and Whitelaw Test Case Grid System (51 x 27)	543
8.7-3	Temperature Contours	544
8.7-4	Contour Maps of CO Volume Concentration (%)	545
8.7-5	Contour Maps of CO ₂ Volume Concentration (%)	546
8.7-6	Contour Maps of O ₂ Volume Concentration (%)	547
9.1-1	Multiple Jet Mixing Coordinate System and Important Nomenclature	556
9.1-2	Finite Difference Grid Network for Fine Grid (45x26x17) Computations	557
9.1-3	Comparison Between Data and Predictions for Test No. 1, Straight Duct, TM = Const	559
9.1-4	Finite Difference Grid Network for Coarse Grid (27x26x8) Computations	561
9.1-5	Comparison Between Data and Predictions for Test No. 1, Straight Duct, 4-Node Jet	563

LIST OF ILLUSTRATIONS (CONTD)

<u>Figure</u>	<u>Title</u>	<u>Page</u>
9.1-6	Predicted Centerplane Temperature Contours with the Fine and Coarse Grid Systems	565
9.1-7	Comparison Between Data and Predictions for Test No. 6, Test Section I, TMAIN = Const	567
9.1-8	Comparison Between Data and Predictions for Test No. 6, Straight Duct, 4-Node Jet	569
9.1-9	Predicted Centerplane Temperature Contours with the Fine and Coarse Grid Systems	571
9.1-10	Finite Difference Grid Network for Fine Grid (35x33x17) Computations	572
9.1-11	Comparison Between Data and Predictions for Test No. 50, Test Section I, TM = Const	573
9.1-12	Finite Difference Grid Network for the Finer Grid (32x29x21) Computations	575
9.1-13	Comparison Between Data and Predictions for Test No. 50, Test Section I, TM = Const	577
9.2-1	Comparison Between Data and Predictions for Test No. 02, Test Section I, TM = Const	581
9.2-2	Comparison Between Data and Predictions for Test No. 4, Test Section I, One Sided	583
9.3-1	Comparison Between Data and Predictions for Test No. 2, Test Section I, TM = Const	589
9.3-2	Measured Mainstream Inlet Profiles	591
9.3-3	Comparison Between Data and Predictions for Test No. 13, Test Section I, Top Cold TM	593
9.4-1	Schematic of the Test Setup and Typical Orifice Configurations for Two-Sided Jet Injection	599
9.4-2	Comparison Between Data and Predictions for Test No. 2, Test Section I, Opposed (INL)	601
9.4-3	Comparison Between Data and Predictions for Test No. 28, Test Section I, Opposed (STG)	603

LIST OF TABLES

<u>Table</u>	<u>Title</u>	<u>Page</u>
1	Computer Models and Physical Submodels (Modules)	14
2	Source Terms for Chemical Species	42
3	Simple Flows	96
4	Streamline Curvature Effects	101
5	Recirculating Flows	103
6	Swirling Flows	109
7	Scalar Transport	114
8	Laminar Premixed Flames	119
9	Laminar Diffusion Flames	120
10	Turbulent Premixed Flames	121
11	Turbulent Diffusion Flames	122
12	Spray Evaporation and Combustion	132
13	Soot Data	138
14	Two-Step Rate Constants for Garrett/AVLABS and Premixed/Prevaporizing Reaction	254
15	Rate Constants for 4-Step Kinetic Scheme	257
16	Grid Note Distribution	330
17	Ring Configurations Investigated by Logan, et al	363

SECTION I

1.0 SUMMARY

The main objective of the NASA-sponsored Aerothermal Modeling Program, Phase I was to assess current aerothermal submodels used in the Garrett Turbine Engine Company (GTEC) analytical combustor models.

A number of "benchmark" quality test cases were selected after an extensive literature survey. The selected test cases, both nonreacting and reacting flows, were broadly divided into the following categories:

- o Simple flows
- o Complex nonswirling flows
- o Swirling flows
- o Dilution jet mixing in confined crossflows.

These test cases were used to assess the following submodels separately and jointly for various combustion processes:

- o $k-\epsilon$ model of turbulence and algebraic stress model, with and without various corrections including low Reynolds number and Richardson number corrections
- o Scalar transport models
- o Multistep kinetic schemes
- o Turbulence/chemistry interaction
- o Spray combustion.

The following general conclusions were derived from Phase I work.

- o An accurate numerical scheme should be developed to minimize numerical diffusion in the computations of recirculating flows
- o Benchmark quality data should be generated under well-defined environments for validating the various submodels used in gas turbine combustion analysis.
- o Although current aerothermal models make reasonable predictions, intensive model development and validation effort should continue for the following submodels:
 - Algebraic stress model
 - Algebraic scalar transport model
 - Two-step and four-step schemes
 - Probability density function approach for a two-step scheme
 - Double-reaction zone model.

SECTION II

2.0 INTRODUCTION

The objectives of the NASA Aerothermal Modeling Program are to assess the current state-of-the-art and identify the deficiencies in current aerothermal models for gas turbine combustors. The program involves the following tasks:

- Task 1.1 - Model Definition
- Task 1.2 - Data Base Generation
- Task 1.3 - Benchmark Test Case Definition
- Task 2.1 - Model Execution
- Task 2.2 - Model Assessment
- Task 2.3 - Program Plan for Model Improvement.

Paragraph 2.1 gives a brief background of aerothermal modeling followed by a description of the Garrett empirical/analytical combustor design approach in Paragraph 2.2. This design approach is based on the use of a number of interrelated multidimensional analytical models that contain appropriate submodels (modules) of turbulence, chemistry, spray combustion/evaporation, soot, and high pressure radiation. These modules are described in Section 3.0. A description of the numerical schemes employed are provided in Section 4.0, and a survey of relevant literature is presented in Section 5.0.

The model assessment results are presented in four different sections:

- o Section 6.0 - Results for simple flows, with and without combustion
- o Section 7.0 - Results for complex nonswirling flows

- o Section 8.0 - Evaluation of the models for swirling flows
- o Section 9.0 - Three-dimensional (3-D) dilution jet-mixing validation results

Section 10.0 presents the conclusions and the recommendations for model improvements.

2.1 Aerothermal Modeling Background

Substantial increases in gas turbine performance have been achieved in recent years due largely to the use of advanced technologies in components and material, in addition to operation at higher cycle pressures and temperatures. To meet the trend toward higher pressure ratio gas turbines with increased turbine inlet temperatures, increased research and development efforts have been directed toward the combustion system. These efforts have contributed largely toward gaining a better understanding of the overall combustion process and have led to the development of an advanced combustor design methodology based on a combination of empirical and analytical techniques. The challenging demands placed upon the combustion system due to increased performance and life requirements, as well as the need to reduce combustor design and development cost, have provided the primary motivation for using multi-dimensional combustion analysis procedures. The advanced combustion analysis forms the basis for the design and development procedures of advanced technology combustors at Garrett Turbine Engine Company. ¹⁻¹⁰

To provide greater confidence in the design of high-performance, durable combustors for advanced aircraft turbine engines, a thorough understanding and accurate characterization of the various physical phenomena involved is required. Over the years, Garrett has been actively involved in the assessment, validation, and

updating of combustor aerothermal models in the areas of multidimensional flow effects, effects of turbulence scale and intensity, combustion kinetics, fuel spray and flow field interactions, soot formation, and high-pressure flame radiation characteristics. Garrett has continued to assess every submodel within each model against fundamental data from ideal element tests.¹⁰⁻¹⁴ Concurrently, model accuracy has been indirectly assessed by comparing predictions with measurements on a number of production and advanced combustors.¹⁻⁹ Through an integrated effort of assessing both the models and the submodels, it has been possible to continually improve the accuracy and reliability of the empirical/analytical design procedure described in the following paragraph.

2.2 Garrett Empirical/Analytical Combustor Design Approach

Past approaches to the design and development of gas turbine combustion systems have largely involved the application of fundamental knowledge of turbulent reacting flows on an empirical basis, followed by component testing to achieve optimum performance objectives. A number of semiempirical relationships have been developed through the years to provide guidelines for the initial design of a new combustion system and to predict attainable performance on the basis of experience curves. Such an approach has been quite successful in the design and development of combustor configurations that are derived from proven concepts.

The development of an empirical data base for combustors is evolutionary. Its limitations, regarding the development of advanced combustion systems with requirements outside of experience bounds, became apparent to Garrett in the early 1970's. The inadequacy of the empirical approach in solving combustion development problems relating to gaseous and particulate emissions; carbon formation; and, more recently, liner and nozzle structural durability for high-temperature-rise applications required complementing this approach with advanced analytical methods.

Garrett has developed a number of analytical models that form the basis for the design and development of advanced technology combustors. The internal flow field of modern gas turbine combustors is a highly complex 3-D phenomenon involving regions of reverse-flow. In addition, the various combustor regions require varying degrees of field resolution to predict accurately the convective and radiative fluxes. A modular approach, therefore, has been developed at Garrett allowing use of different computer models, as depicted in Figure 2.2-1.

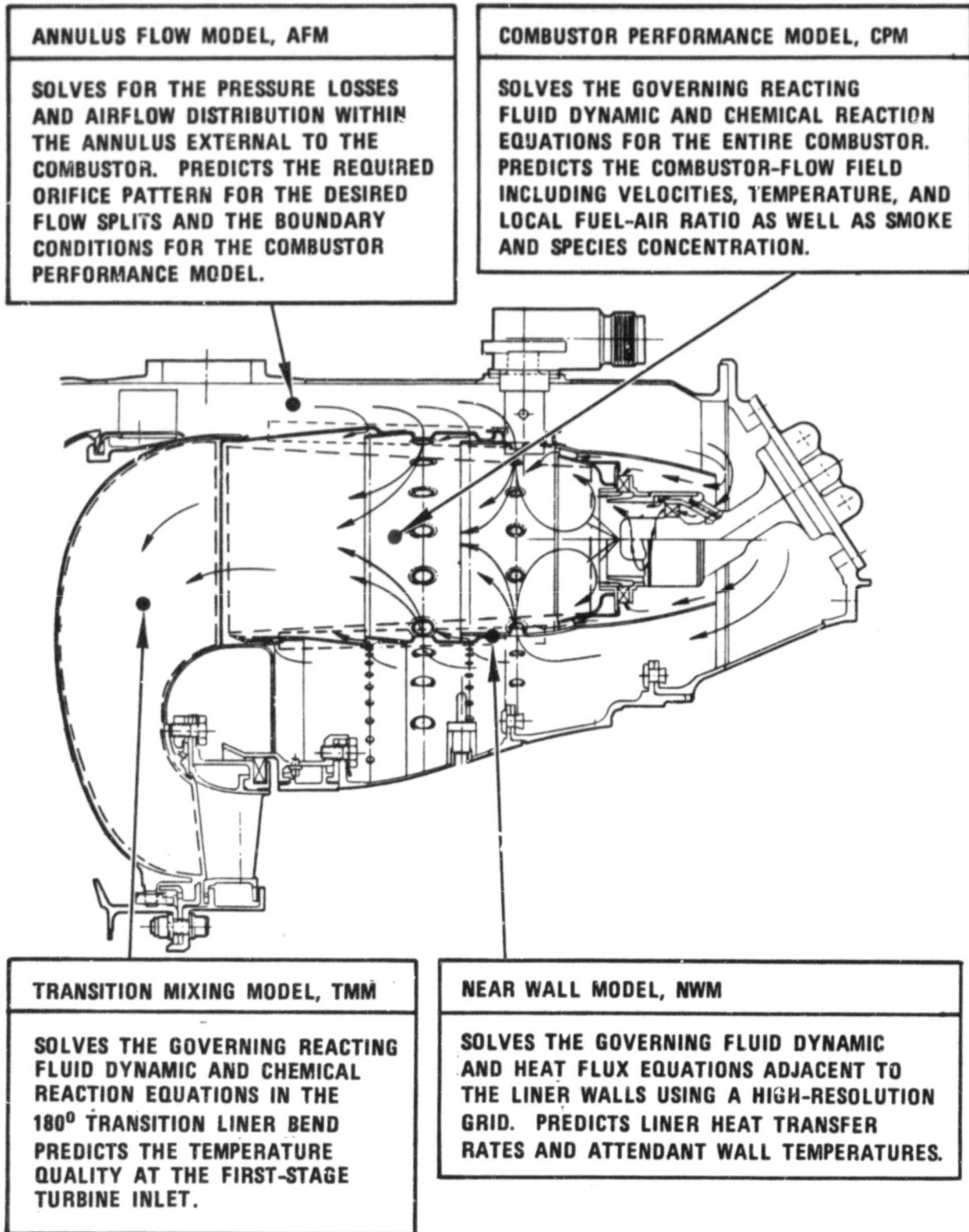


Figure 2.2-1 Combustor Models and Region of Application.

An annulus flow model is used to calculate pressure losses and airflow distribution within the annulus external to the combustor liner. This model calculates boundary conditions, such as flow distribution around the liner, jet velocity, and efflux angles, which are required as inputs for the combustor internal flow models.

Two-dimensional (2-D) and 3-D combustor performance models are used to predict internal profiles of dependent variables including velocity, species, and temperature by solving fully coupled transport equations for turbulent, recirculating, spray-combusting flow fields. Up to 20,000 finite-difference grid nodes are numerically solved in these programs to ensure a relatively "grid-independent" solution for the main flow field. However, for the region close to the film-cooled wall, a better field resolution is required to accurately predict the convective fluxes and the wall temperatures. This is done by using near-wall models.

The reverse-flow annular combustors generally employ transition liners where the main flow direction changes from axial to radial for radial-inflow turbines or a full 180-degree bend for axial flow turbines. The flow field has only small pockets of reverse-flow regions. Computationally more efficient 2-D and/or 3-D transition mixing models are used for calculating the mixing rate of the cold dilution jets in the transition liner. These models calculate the turbine stator inlet profiles of temperature, velocity, and turbulence intensity, which are needed for assessing turbine hardware life. The various analytical models are used in the overall combustor design to arrive at a final combustor design in a timely and cost-effective manner.

The empirical/analytical combustor design approach is shown in Figure 2.2-2. The engine requirements and design define the combustor inlet conditions and limiting envelope constraints. Using

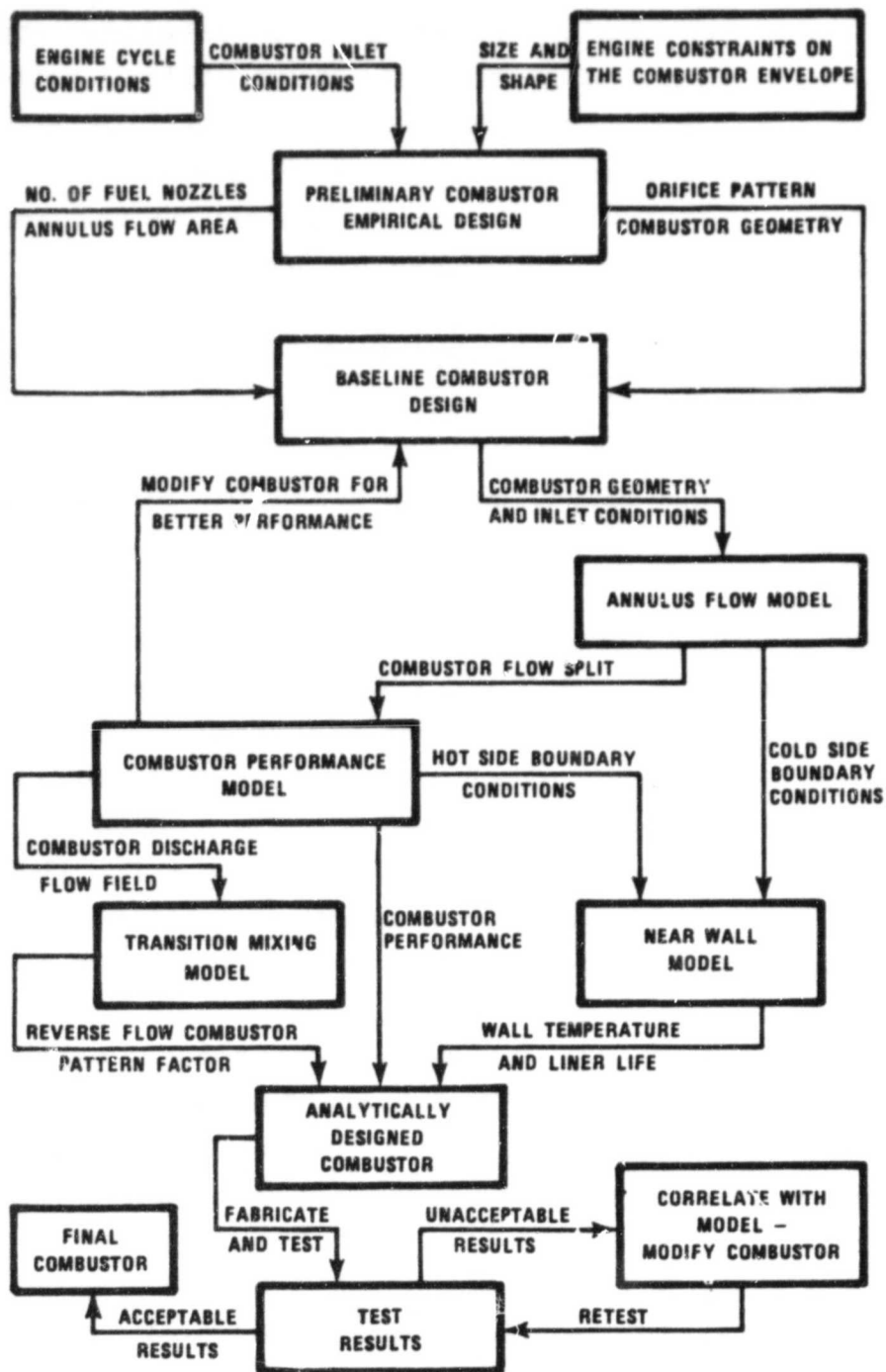


Figure 2.2-2. Combustor Design Methodology.

existing empirical design relations, a baseline combustor is defined and includes the appropriate flow splits, number of fuel nozzles, and orifice locations. The annulus flow model is then used to determine the orifice sizes to obtain the desired overall pressure drop, and flow splits needed to define the boundary conditions for the combustor performance model.

The combustor performance model is run at various power conditions to evaluate combustor internal flow characteristics. If the design requires changes, the baseline combustor is altered, the annulus flow model is rerun, and the combustor performance model is again used to evaluate the new design.

The combustor liner wall convective and radiative fluxes and attendant temperature levels and gradients are calculated with the near-wall model. The hot-side boundary conditions are defined by the combustor performance model. The cold-side boundary conditions are defined by the annulus flow model. The combustor performance model is also used to define initial conditions for the transition mixing model, which is used to calculate the mixing in the transition liner and the resulting burner exit temperature quality.

The results from the combustor performance model, near-wall model, and transition mixing model are factored into the analytically designed combustor. If the design is lacking, iterations are performed using the various models to arrive at an acceptable final configuration.

The configuration is then fabricated and tested. If the result is unacceptable, the test data is compared with the analytical predictions and the appropriate subcomponent is modified, reanalyzed, and retested to verify that the modifications corrected the problems. This procedure is repeated until all the combustor design goals are achieved. Experience shows that this design

approach minimizes the number of changes required on actual hardware to achieve the design objectives.

SECTION III

3.0 Description of Analytical Models

Detailed descriptions of the combustor analytical models are provided in Paragraph 3.1. Each analytical model contains several submodels, which are described separately in Paragraphs 3.2 through 3.6.

3.1 The Analytical Models

The Garrett modular analytical approach uses the following four models for analyzing gas turbine combustor flow field.

- o Annulus Flow Model (AFM)
- o Combustor Performance Model (CPM), 2-D and 3-D
- o Transition Mixing Model (TMM), 2-D and 3-D
- o Near-Wall Model (NWM)

These models use submodels of turbulence, kinetics, radiation, and spray combustion/evaporation and dispersion as summarized in Table 1.

3.1.1 Annulus Flow Model

The first task in analyzing any combustion system is to predict the annulus flow external to the combustor. For this, the AFM is used. The combustor annulus is divided into a number of sections with the section boundaries defined by orifice rows in the liner or points of significant area change. In each section, the AFM solves the one-dimensional (1-D) equations for axial and tangential velocity. Mass is extracted from the annulus flow at each orifice row. The extracted mass is governed by the liner orifice

TABLE 1. COMPUTER MODELS AND PHYSICAL SUBMODELS (MODULES).

MODEL	DIMEN- SIONS	NUMERICAL TYPE	SUBMODELS (MODULES)				INPUTS INFO TO:	OBTAINS INFO FROM:
			TURBU- LENCE	KINETICS	RADIA- TION	SPRAY		
ANNULUS FLOW (AFM)	1	-	-	-	-	-	CPM	-
COMBUSTOR PERFORMANCE (CPM)	2/3	ELLIPTIC; ORTHOGONAL/ NONORTHOGONAL	K-ε	2-STEP/ 4-STEP	4-FLUX/ 6 FLUX	LAGRANGIAN AND/OR EULERIAN	TMM NWM	AFM
TRANSITION MIXING (TMM)	2/3	PARABOLIC/ ELLIPTIC; NONORTHOGONAL	K-ε	2-STEP	NONE/ 6 FLUX	NONE	-	CPM
NEAR WALL (NWM)	1/ 2/ 3	PARABOLIC/ ELLIPTIC	K-ε	2-STEP	2-FLUX	NONE	-	CPM

geometry and semi-analytical correlations for discharge coefficient. Pressure loss, both frictional and dump types, and heat transfer are included in the calculations. Iteration on combustor liner pressure drop continues until the total orifice flow rate achieves the desired value. The AFM predicts the static pressure distribution around the combustor, the liner pressure drop, orifice flow splits, and injection angles and velocities. These values are required as boundary conditions for the internal combustor flow programs (CPM, TMM, and NWM).

3.1.2 Combustor Performance Model

The CPM has two versions: 2-D and 3-D.

2-D Combustor Performance Model

If the internal flow field of the combustor is predominantly 2-D plane flow or axisymmetric flow, a 2-D CPM is used to calculate combustor internal flow field. The 2-D CPM is a generalized finite-difference program that solves the conservative form of the the governing fluid dynamic and chemical reaction equations, using the numerical scheme of Patankar-Spalding.¹⁵ The following variables are solved:

- o Axial, radial, and tangential velocity
- o Turbulent kinetic energy and dissipation
- o Total fuel, unburned fuel, and other chemical species including carbon monoxide
- o Pressure
- o Stagnation enthalpy

- o Radiation
- o Liquid particle droplet size, velocity, and evaporation rate

Cylindrical or rectangular coordinates are used along with the capability of specifying any arbitrary shape for the liner wall or any arbitrary internal object such as a fuel nozzle shroud. Using the flow rates and velocities, etc., from the AFM, cooling slots, primary and dilution orifices, swirlers, and liquid or gaseous fuel nozzles are all modeled simultaneously. This gives the overall combustor flow field and the species and temperature distributions. Bulk flow properties determined include recirculation zone size and shape, primary and dilution jet penetration, and combustion efficiency.

3-D Combustor Performance Model

In many situations, the combustor geometry is not 2-D. In these cases, 3-D CPM must be used. The 3-D CPM is based on the USARTL 3-D Model¹² and can be considered an extension of the 2-D CPM to three dimensions. Both models use the same numerical scheme and the coordinate system. Like the 2-D CPM, the 3-D CPM solves for similar variables and requires boundary condition input from the AFM. Arbitrary complex boundaries and nozzle shrouds can be simulated. The 3-D CPM can analyze such 3-D flow situations as single (or multiple) swirlers in an annular combustor, tangential fuel nozzles, and discrete primary and dilution jets.

3.1.3 Transition Mixing Model

The TMM has two versions: 2-D and 3-D.

2-D Transition Mixing Models

Though the 2-D CPM and 3-D CPM can analyze arbitrary shapes, they are limited to cylindrical or Cartesian coordinates. They cannot economically calculate the flow in the transition liner used in reverse-flow annular combustion systems. For relatively long combustors where the flow entering the transition liner is predominantly 2-D, the 2-D transition mixing model (2-D TMM) is used. This model is based on the GENMIX program of Patankar and Spalding¹⁶. Modifications have been added that allow the program to negotiate 180-degree bends with the source terms added to account for the induced radial pressure gradients. Since it is a parabolic numerical scheme, this model is limited to transition liners in which the radii of curvature are large. Otherwise the pressure effects would have to propagate upstream. As in the other Garrett models, the two-equation $k-\epsilon$ turbulence model is used along with the 2-step reaction mechanism. For initial profiles, the 2-D TMM uses the exit profiles as predicted by either the 2-D CPM or 3-D CPM. It then generates the exit profiles from the transition liner to which the turbine stator is exposed.

3-D Transition Mixing Models

With current trends toward shorter turbo-propulsion combustors and more compact transition liners, a significant amount of dilution jet mixing and spreading takes place within the transition liner. Attendant 3-D flow characteristics result from this mixing and spreading. Moreover, due to tight-bend radii of the transition liner, upstream (elliptic) effects caused by streamline curvature cannot be ignored.

A 3-D elliptic transition mixing model has therefore been developed that includes radiation and kinetic effects on the transition liner. This program is similar to the 3-D CPM, but has been structured to afford more than 2000 L finite-difference

nodes, where L is the number of nodes along the predominant flow direction. Theoretically, there is no limit on L ; however, due to computer time consideration, L is generally kept less than 50. The 3-D TMM can be adopted to analyze turbopropulsion combustors with much more complex geometries that cannot be adequately discretized by a cylindrical or Cartesian coordinate system.

3.1.4 Near-Wall Models

To accurately predict hot-side convective and radiative fluxes to the liner wall, a 2-D parabolic film cooling analytical model was developed during the Army Combustor Design Criteria Program. Subsequently, an improved 2-D NWM has been developed to allow a more accurate assessment of the effects of the following on liner cooling effectiveness:

- o Slot geometry
- o Primary/dilution jets
- o Flow in the lateral directions
- o Radiation from the bulk flow field and the opposite wall
- o Spray combustion adjacent to the wall.

The 2-D NWM can be used interactively with the combustor performance models to more accurately predict near-wall flow field. The 2-D NWM uses the same modules as the CPM.

To further improve near-wall calculations, 2-D elliptic and 3-D parabolic NWM have also been developed at Garrett.

3.2 Description of Turbulence and Scalar Transport

The internal flow field in gas turbine combustors is highly turbulent and recirculating. Efficient design of combustion systems requires a detailed understanding of the physico-chemical processes of such systems. A prerequisite for this understanding is an ability to analyze the nonreacting turbulent recirculating flows.

The fluid dynamics of turbulent flows are governed by the time-dependent Navier-Stokes equations. Solutions of these equations are extremely difficult and require prohibitively large computational time. Furthermore, subgrid models are required to describe the transport phenomena in addition to the Navier-Stokes equations. A common alternative is to use time-averaged Navier-Stokes equations. This system of equations contains unknown higher order correlations resulting in a greater number of unknowns than the number of available equations. Turbulence models of the higher order correlations based on phenomenological assumptions are needed to close this system of equations. The degree of success of a turbulence model depends on the nature and accuracy of the phenomenological assumptions.

The simplest of the turbulence models are the mixing-length models. In these models, the characteristic length scales of turbulence are often prescribed to close the system of equations. These models have been successful in treating simple flows like boundary layers and pipe flows, but have been unsuccessful in analyzing recirculating flows.

The next higher order turbulence models are the one-equation models. These models solve one differential equation for determining the distribution of the turbulent kinetic energy or equivalent characteristic property of turbulence. The characteristic

length scale is defined in a manner similar to mixing-length models. Consequently, the one-equation models have also been unsuccessful in predicting turbulent recirculating flows.

The two-equation models are more complex than the mixing length models. These models use two differential equations for computing characteristic velocity and length scales. Among the two-equation models, the $k-\epsilon$ model has been the most successful so far. The $k-\epsilon$ model is used in the Garrett combustor analytical models and is described in Paragraph 3.2.1. In regions adjacent to walls, the viscous effects play a prominent role. To provide an accurate prediction of the flow in these regions, a low Reynolds number version of the $k-\epsilon$ model is used in the Garrett near-wall models. This model is described in Paragraph 3.2.2.

Even though the $k-\epsilon$ model has been the most successful in predicting recirculating flows, the predictions for flows with streamline curvatures have been only qualitatively correct. Flow fields involving streamline curvatures have been known to have increased turbulence diffusion rates due to enhanced turbulence production. This increased turbulence production is not adequately accounted for in the $k-\epsilon$ model. One way to include this extra production of turbulence is to modify the constants in the $k-\epsilon$ model in proportion to the Richardson number, which is a measure of the extra strain rate produced by the streamline curvature. These corrections are described in Paragraph 3.2.3.

The Richardson number corrections are applicable for flows with moderate streamline curvature effects. For flows with strong curvature effects, a solution of the Reynolds stress equations is necessary. Solution of the complete Reynolds stress components results in increased computational time. An attractive alternative is the use of an algebraic Reynolds stress model. In this model,

the terms in the Reynolds stress transport equations are approximated to yield algebraic expressions in terms of the turbulence kinetic energy and length scale. The degree of approximations employed would determine the accuracy of predictions. The algebraic Reynolds stress model is described in Paragraph 3.2.4.

In complex combustor flow fields, the approximations used in developing the algebraic Reynolds stress model are not valid. For such flow fields, the Reynolds stress components must be obtained from the solution of differential transport equations for the appropriate Reynolds stress component. A description of these equations used by Garrett are provided in Paragraph 3.2.4.

Another important submodel for combustor internal flows is the scalar transport model. The accuracy of the combustor performance predictions depends upon the accuracy of predicting the transport of scalar properties such as concentration of reactants, etc. The most commonly used scalar transport model is the gradient diffusion model. The gradient diffusion model does not adequately account for counter-gradient transport, which has been known to exist in most combustor internal flow fields. An algebraic scalar transport model (ASTM) has been developed at Garrett, which can predict counter-gradient scalar transport. This model is described in Paragraph 3.2.2.

3.2.1 Governing Equations for the k- ϵ Model

The time-averaged transport equations for turbulence kinetic energy (k) and its dissipation rate (ϵ) can be written in the following generalized variable form:

ORIGINAL PAGE IS
OF POOR QUALITY

$$\begin{aligned} & \frac{1}{r} \left\{ \frac{\partial}{\partial x} (\rho r U \phi) + \frac{\partial}{\partial r} (\rho r V \phi) + \frac{\partial}{\partial \theta} (\rho W \phi) \right. \\ & - \frac{\partial}{\partial x} (r \Gamma_{\text{eff}, \phi} \frac{\partial \phi}{\partial x}) - \frac{\partial}{\partial r} (r \Gamma_{\text{eff}, \phi} \frac{\partial \phi}{\partial r}) \\ & \left. - \frac{1}{r} \frac{\partial}{\partial \theta} (\Gamma_{\text{eff}, \phi} \frac{1}{r} \frac{\partial \phi}{\partial \theta}) \right\} = S_{\phi} \end{aligned} \quad (1)$$

Here ρ , $\Gamma_{\text{eff}, \phi}$ and S_{ϕ} denote the fluid density, the local effective exchange coefficient of variable ϕ , and sources/sinks. The source terms for the dependent variables are

o Turbulence kinetic energy, $k = \frac{1}{2} (\overline{u^2} + \overline{v^2} + \overline{w^2})$

$$S_k = G_k - \rho \epsilon \quad (2)$$

where

$$\begin{aligned} G_k = \mu_t \left[2 \left\{ \left(\frac{\partial U}{\partial x} \right)^2 + \left(\frac{\partial V}{\partial r} \right)^2 + \left(\frac{1}{r} \frac{\partial W}{\partial \theta} + \frac{V}{r} \right)^2 \right. \right. \\ \left. \left. + \left(\frac{\partial W}{\partial x} + \frac{1}{r} \frac{\partial U}{\partial \theta} \right)^2 + \left(\frac{\partial U}{\partial r} + \frac{\partial V}{\partial x} \right)^2 \right. \right. \\ \left. \left. + \left(\frac{\partial W}{\partial r} + \frac{1}{r} \frac{\partial V}{\partial \theta} - \frac{W}{r} \right)^2 \right] \end{aligned} \quad (3)$$

o Dissipation rate,

$$S_{\epsilon} = (C_1 G_k - C_2 \rho \epsilon) \frac{\epsilon}{k} \quad (4)$$

The effective viscosity is obtained from the relation

$$\mu_{\text{eff}} = \mu + \mu_t$$

where μ and μ_t are the molecular and turbulent viscosities, respectively. μ_t is related to k and ϵ via

$$\mu_t = C_D \rho k^2 / \epsilon \quad (5)$$

The exchange coefficients are defined as

$$\Gamma_{\text{eff}, \phi} = \mu_{\text{eff}} / \sigma_{\text{eff}, \phi}$$

Recommended values for the constants in the above equations are

$$\begin{aligned} C_D &= 0.09 \\ C_1 &= 1.44 \\ C_2 &= 1.92 \\ \sigma_{\text{eff}, k} &= 0.9 \end{aligned}$$

$\sigma_{\text{eff}, \epsilon}$ is calculated from

$$\sigma_{\text{eff}, \epsilon} = \frac{\kappa^2}{(C_2 - C_1) C_D^{1/2}} \quad (6)$$

where the κ is the von Karman constant taken to be 0.41.

The near-wall region is given a special treatment in the program. Since the expression for Γ_{eff} is accurate for turbulent flows only, a means is provided for the inclusion of the correct shear stresses and other fluxes at the wall. Therefore, the nodes next to the wall are assigned the following values as per an empirical wall law:

$$\begin{aligned}
y^+ \leq 11.5 & \quad \Gamma_{\phi, \text{wall}} = \frac{\mu}{\sigma \phi} \\
y^+ > 11.5 & \quad \Gamma_{\phi, \text{wall}} = \frac{\mu}{\sigma \phi} \frac{y^+}{\frac{1}{\kappa} \ln(9y^+) + P_\phi}
\end{aligned} \tag{7}$$

$$\begin{aligned}
y^+ &= \rho k^{1/2} C_D^{1/4} \frac{\delta}{\mu} \\
P_\phi &= 9.0 \left(\frac{\sigma}{\sigma_{\text{eff}}} - 1 \right) \left(\frac{\sigma}{\sigma_{\text{eff}}} \right)^{-1/4}
\end{aligned} \tag{8}$$

where δ is the normal distance of the wall from the first interior adjacent node and σ is the laminar Schmidt number.

The kinetic energy of turbulence has small diffusion near the wall; hence, Γ_{wall} for k is set equal to zero. Instead of computing Γ_{wall} for ϵ , it is calculated for the near-wall node by assuming a linear variation of the length scale giving the following expression:

$$\epsilon = C_D^{3/4} k^{3/2} / (\kappa \delta) \tag{9}$$

3.2.2 Near-Wall Low Reynolds Number Correction

In the near-wall region, the wall function approach, described in the previous paragraph does not properly describe the behavior of turbulence kinetic energy and its dissipation rate. A systematic Taylor Series expansion technique has been developed by Chien,¹⁷ which correctly describes the turbulent shear stresses, kinetic energy, and its dissipation rate in the region near a wall. To maintain the consistency of the behavior of k and ϵ near the

ORIGINAL PAGE IS
OF POOR QUALITY.

wall, additional terms had to be added to the k and ϵ equations and the turbulent effective diffusion rates were modified. The corrected equations of Chien near the wall are as follows:

Turbulence kinetic energy; k

$$\begin{aligned} \frac{\partial}{\partial x} (\rho U k) + \frac{1}{r} \frac{\partial}{\partial r} (r \rho V k) &= \frac{\partial}{\partial x} \left(\Gamma_{\text{eff},k} \frac{\partial k}{\partial x} \right) \\ &+ \frac{1}{r} \frac{\partial}{\partial r} \left[r \Gamma_{\text{eff},k} \frac{\partial k}{\partial r} \right] + S_k + D \end{aligned} \quad (10)$$

where, D is the extra source term, given by

$$D = -2\mu \frac{k}{y^2} \quad (11)$$

$$\Gamma_{\text{eff},k} = (\mu + \mu_t f_\mu) / \sigma_{\text{eff},k} \quad (12)$$

$$f_\mu = 1.0 - \exp(-0.0115 y^+) \quad (13)$$

S_k is the source term described in equation (2)

Dissipation Rate, ϵ

$$\begin{aligned} \frac{\partial}{\partial x} (\rho U \epsilon) + \frac{1}{r} \frac{\partial}{\partial r} (r \rho V \epsilon) &= \frac{\partial}{\partial x} \left[\Gamma_{\text{eff},\epsilon} \frac{\partial \epsilon}{\partial x} \right] \\ &+ \frac{1}{r} \frac{\partial}{\partial r} \left[r \Gamma_{\text{eff},\epsilon} \frac{\partial \epsilon}{\partial r} \right] + S_\epsilon + E \end{aligned} \quad (14)$$

where, E is the additional source term for dissipation, defined as

$$E = -2\mu \exp(-0.5 y+) \frac{\epsilon}{y^2} \quad (15)$$

and

$$S_\epsilon = (C_1 G_k - C_2 f_2 \rho \epsilon) \frac{\epsilon}{k} \quad (16)$$

with

$$f_2 = 1.0 - 0.22 \exp(-R_T/6)^2 \quad (17)$$

$$R_T = \frac{\rho k^2}{\mu \epsilon}$$

In the modified k and ϵ equations, it is possible to apply the boundary conditions at the wall, with $k = 0$ and $\epsilon = 0$ at $y = 0$. This approach gives consistent results near the wall.

3.2.3 Richardson Numbers Correction to k - ϵ Model

The standard k - ϵ model presented in Paragraph 3.2.1 describes the turbulence characteristics at any point in the flow field by a single velocity and length scale. These scales are obtained from an assumed isotropic turbulence structure. This model is adequate for simple flow fields. When significant streamline curvatures are introduced into the flow field, such as strong recirculation zones or swirl, the k - ϵ model does not adequately account for the enhanced turbulence diffusion caused by the extra strain rates associated with streamline curvature. For analyzing such flow fields, the k - ϵ model should be modified.

A measure of the extra strain rate due to the streamline curvature is given by the Richardson number, Ri . The extra strain rate imposed on the flow field would tend to increase both the velocity and the length scales of turbulence. One way to account for the changes in the characteristic scales is to modify the turbulence

ORIGINAL PAGE 19
OF POOR QUALITY

constants depending upon the Richardson number. For 2-D recirculating flows, the Richardson number can be defined as

$$Ri_c = \frac{k^2}{\epsilon^2} \frac{V_R}{R^2} \frac{\partial}{\partial R} (RV_R) \quad (18)$$

where, V_R and R are the resultant velocity and the radius of curvature respectively. They are defined as

$$V_R = \sqrt{U^2 + v^2} \quad (19)$$

$$\frac{1}{R} = \frac{UV \left(\frac{\partial V}{\partial y} - \frac{\partial U}{\partial x} \right) + U^2 \frac{\partial V}{\partial x} - v^2 \frac{\partial U}{\partial y}}{V_R^3} \quad (20)$$

For swirling flows, the corresponding Richardson number is defined by

$$Ri_{V_\theta} = \frac{\left(\frac{V_\theta}{r} \right) \frac{\partial}{\partial r} (r V_\theta)}{\left(\frac{\partial U}{\partial r} \right)^2 + \left(r \frac{\partial}{\partial r} \left[\frac{V_\theta}{r} \right] \right)^2} \quad (21)$$

In the $k-\epsilon$ model, the governing equation for k is an exact equation and no empirical modeling is involved in it. However, the ϵ equation is a modeled equation containing two empirical constants. The adopted approach is to modify the constant C_2 in the equation by the following expression

$$C_2 = 1.92 \exp(-\alpha_{V\theta} Ri_{V\theta} - \alpha_c Ri_c). \quad (22)$$

Here $\alpha_{V\theta}$ and α_c are empirical constants, whose values are of the order of 0.2.

3.2.4 Algebraic Reynolds Stress Model

Turbulent flow fields occurring in combustors are generally nonisotropic in character. The turbulent diffusion rates in different directions are different depending upon the strain-rate tensor. Descriptions of such flow fields necessitate knowledge of the complete Reynolds stress components. Solution of the complete Reynolds stress components is expensive and complex. An alternative to this approach is the algebraic Reynolds stress model.

The algebraic Reynolds stress model is obtained by approximating some of the higher order terms in the Reynolds stress equation based upon phenomenological simplifications. The approximations result in algebraic expressions for the Reynolds stress components with added empirical constants.

The exact transport equation for Reynolds stress $\overline{u_i u_j}$ at high Reynolds numbers in an incompressible flow can be written in the form

ORIGINAL PAGE IS
OF POOR QUALITY.

$$\begin{aligned}
 \underbrace{\frac{D}{Dt} (\overline{u_i u_j})}_{\text{Convection}} &= \underbrace{-\frac{\partial}{\partial x_k} (\overline{u_k u_i u_j}) - \frac{1}{\rho} \left(\frac{\partial \overline{u_j p'}}{\partial x_i} + \frac{\partial \overline{u_i p'}}{\partial x_j} \right)}_{\text{Diffusion}} - \underbrace{2 \frac{\mu}{\rho} \left(\frac{\partial \overline{u_i}}{\partial x_k} - \frac{\partial \overline{u_j}}{\partial x_k} \right)}_{\epsilon_{ij} = \text{Viscous Destruction}} \\
 &- \underbrace{\left(\frac{\overline{u_i u_k}}{u_i u_k} \frac{\partial U_j}{\partial x_k} + \frac{\overline{u_j u_k}}{u_j u_k} \frac{\partial U_i}{\partial x_k} \right)}_{P_{ij} = \text{Production}} + \underbrace{\frac{p'}{\rho} \left(\frac{\partial \overline{u_i}}{\partial x_j} + \frac{\partial \overline{u_j}}{\partial x_i} \right)}_{\pi_{ij} = \text{Pressure-Strain}} \quad (23)
 \end{aligned}$$

At high Reynolds numbers, the viscous dissipation ϵ_{ij} is essentially due to the small scale turbulent motions and hence tends to isotropize $\overline{u_i u_j}$. The pressure-strain term has been modeled by Rodi¹⁸ in the form

$$\pi_{ij} = \pi_{ij,1} + \pi_{ij,2} \quad (24)$$

$\pi_{ij,1}$ represents the contributions to pressure strain arising from fluctuating velocities only, and $\pi_{ij,2}$ accounts for the interactions between fluctuating velocities and mean strain. These terms are modeled as follows:

$$\pi_{ij,1} = -C_1' \frac{\epsilon}{k} [\overline{u_i u_j} - \frac{2}{3} \delta_{ij} k] \quad (25)$$

$$\pi_{ij,2} = -\alpha \left(P_{ij} - \frac{2}{3} P \delta_{ij} \right) - \beta \left(D_{ij} - \frac{2}{3} P \delta_{ij} \right) - \gamma k \left(\frac{\partial U_i}{\partial x_j} + \frac{\partial U_j}{\partial x_i} \right) \quad (26)$$

where:

ORIGINAL PAGE IS
OF POOR QUALITY

$$C'_1 = 1.5, \alpha = \frac{8 + C'_2}{11}, \beta = \frac{8 C'_2 - 2}{11}$$

$$\gamma = \frac{30 C'_2 - 2}{55}, \text{ and } C'_2 = 0.5$$

$$P_{ij} = - \left(\overline{u_i u_k} \frac{\partial U_i}{\partial x_k} + \overline{u_j u_k} \frac{\partial U_i}{\partial x_k} \right) \quad (27)$$

$$D_{ij} = - \left(\overline{u_i u_k} \frac{\partial U_k}{\partial x_j} + \overline{u_j u_k} \frac{\partial U_k}{\partial x_i} \right) \quad (28)$$

Rodi has proposed that the convection and diffusion of $\overline{u_i u_j}$ can be scaled by

$$\begin{aligned} \frac{D}{D_t} \overline{(u_i u_j)} - \text{Diff} \overline{(u_i u_j)} &= \frac{\overline{u_i u_j}}{k} \left\{ \frac{Dk}{D_t} - \text{Diff}(k) \right\} \\ &= \frac{\overline{u_i u_j}}{k} (P - \epsilon) \end{aligned} \quad (29)$$

With this simplification, the above equation reduces to the form

$$\overline{u^2} = \frac{\frac{2}{3} \epsilon (C'_1 - 1) + \frac{2}{3} P (\alpha + \beta) + 2 (1 - \alpha) P}{C'_1 \frac{\epsilon}{k} + C_{u'} \frac{P - \epsilon}{k}} \quad (30)$$

$$\overline{v^2} = \frac{\frac{2}{3} \epsilon (C'_1 - 1) + \frac{2}{3} P (\alpha + \beta) - 2 P \beta}{C'_1 \frac{\epsilon}{k} + C'_v \frac{P - \epsilon}{k}} \quad (31)$$

$$\overline{w^2} = (2k - \overline{u^2} - \overline{v^2}) \quad (32)$$

$$-\overline{uv} = \left[\frac{(1 - \alpha) \frac{\overline{v^2}}{k} + \gamma - \beta \frac{\overline{u^2}}{k}}{C'_1} \right] \frac{k^2}{\epsilon} \frac{\partial U}{\partial r} \quad (33)$$

$$-\overline{vw} = \left\{ (1 - \alpha) \left(\overline{v^2} \frac{\partial V_\theta}{\partial r} - \overline{w^2} \frac{V_\theta}{r} + \overline{uv} \frac{\partial V_\theta}{\partial x} \right) + \gamma k \frac{\partial V_\theta}{\partial r} \right. \\ \left. + \beta \left(\overline{v^2} \frac{V_\theta}{r} - \overline{w^2} \frac{\partial V_\theta}{\partial r} - \overline{uw} \frac{\partial U}{\partial r} \right) \right\} / C'_1 \frac{\epsilon}{k} \quad (34)$$

$$-\overline{uw} = \left\{ (1 - \alpha) \left(\overline{u^2} \frac{\partial V_\theta}{\partial x} + \overline{uv} \frac{\partial V_\theta}{\partial r} \right) - \beta \left(\overline{w^2} \frac{\partial V_\theta}{\partial x} - \overline{uv} \frac{V_\theta}{r} \right) \right. \\ \left. - \gamma k \frac{\partial V_\theta}{\partial x} \right\} / C'_1 \frac{\epsilon}{k} \quad (35)$$

From Equation (33):

$$C_D = \left[(1 - \alpha) \frac{\overline{v^2}}{k} + \gamma - \beta \frac{\overline{u^2}}{k} \right] / C'_1 \quad (36)$$

The ASM provides a mechanism by which anisotropic turbulence structure can be predicted without substantial increase in computational effort. The empirical constants in the ASM have not been fully established. They have to be determined by comparing the predictions with the data base.

3.2.5 Reynolds Stress Transport Model

Although the algebraic Reynolds stress model provides a means of computing the anisotropic structure of turbulence, its accuracy in complex turbulent flows is not expected to be good. In the algebraic Reynolds stress model, the closure of the system of equations for Reynolds stresses was achieved by using a scaling law through which the higher order correlations were expressed as functions of lower order correlations. In complex internal combustor flows, the validity of the scaling laws is questionable. In such cases, the only recourse available is to use the Reynolds stress transport model, where the Reynolds stress components are determined by solving modeled differential transport equations for each stress component. The closure of these transport equations was achieved by modeling the higher order correlation terms in a manner analogous to the methods used in the k-ε model.

The governing equations for the Reynolds stress components can be written in generalized form as follows:

$$\begin{aligned} \frac{1}{r} \left\{ \frac{\partial}{\partial x} (\rho r U \phi) + \frac{\partial}{\partial r} (\rho r V \phi) + \frac{\partial}{\partial \theta} (\rho W \phi) \right. \\ \left. - \frac{\partial}{\partial x} (r \Gamma_{\text{eff}, \phi} \frac{\partial \phi}{\partial x}) - \frac{\partial}{\partial r} (r \Gamma_{\text{eff}, \phi} \frac{\partial \phi}{\partial r}) \right. \\ \left. - \frac{1}{r} \frac{\partial}{\partial \theta} (\Gamma_{\text{eff}, \phi} \frac{1}{r} \frac{\partial \phi}{\partial \theta}) \right\} = S_{\phi} \end{aligned} \quad (37)$$

Here ρ , $\Gamma_{\text{eff}, \phi}$ and S_{ϕ} represent the fluid density, local effective exchange coefficient, and the source term for the dependent variable, ϕ . The source terms are

- c Axial turbulence normal stress, $\overline{u^2}$

ORIGINAL PAGE IS
OF POOR QUALITY

$$\begin{aligned}
 S_{\overline{u^2}} &= \frac{2}{3} \rho \epsilon (C'_1 - 1) + \frac{2}{3} G_k (\alpha + \beta) - 2(1 - \alpha) \rho \overline{uv} \frac{\partial U}{\partial r} \\
 &+ 2 \rho \beta \left[\overline{uv} \frac{\partial V}{\partial x} + \overline{uw} \frac{\partial V_\theta}{\partial x} \right] - 2 \gamma \rho k \frac{\partial U}{\partial x} \\
 &- 2 \rho \overline{u^2} \frac{\partial U}{\partial x} (1 - \alpha - \beta) - C'_1 \rho \frac{\epsilon}{k} \overline{u^2}
 \end{aligned} \tag{38}$$

o Radial Turbulence normal stress, $\overline{v^2}$

$$\begin{aligned}
 S_{\overline{v^2}} &= \frac{2}{3} \rho \epsilon (C'_1 - 1) + \frac{2}{3} G_k (\alpha + \beta) - 2 \gamma \rho k \frac{\partial V}{\partial r} \\
 &- 2 \rho (1 - \alpha) \left[\overline{uv} \frac{\partial V}{\partial x} - \overline{vw} \frac{V_\theta}{r} \right] \\
 &+ 2 \rho \beta \left[\overline{uv} \frac{\partial U}{\partial r} - \overline{vw} \frac{\partial V_\theta}{\partial r} \right] \\
 &- C'_1 \frac{\epsilon}{k} \rho \overline{v^2} - 2(1 - \alpha - \beta) \rho \overline{v^2} \frac{\partial V}{\partial r}
 \end{aligned} \tag{39}$$

o Turbulence Shear Stress, \overline{uv}

$$\begin{aligned}
 S_{\overline{uv}} &= -\rho (1 - \alpha) \left[\overline{v^2} \frac{\partial U}{\partial r} - \overline{uw} \frac{V_\theta}{r} + \overline{u^2} \frac{\partial V}{\partial x} \right] \\
 &+ \rho \beta \left[\overline{v^2} \frac{\partial V}{\partial x} + \overline{vw} \frac{\partial V_\theta}{\partial x} + \overline{uw} \frac{\partial V_\theta}{\partial r} + \overline{u^2} \frac{\partial U}{\partial r} \right] \\
 &- \gamma \rho k \left(\frac{\partial U}{\partial r} + \frac{\partial V}{\partial x} \right) + \rho \overline{uv} \frac{V}{r} (1 - \alpha - \beta) - C'_1 \frac{\rho \epsilon}{k} \overline{uv}
 \end{aligned} \tag{40}$$

o Turbulence Shear Stress, \overline{vw}

$$\begin{aligned}
 S \overline{vw} = & -\rho(1-\alpha) \left[\overline{v^2} \frac{\partial V_\theta}{\partial r} - \overline{w^2} \frac{V_\theta}{r} + \overline{uv} \frac{\partial V_\theta}{\partial x} + \overline{uw} \frac{\partial V}{\partial x} \right] \\
 & + \rho\beta \left[\overline{w^2} \frac{\partial V_\theta}{\partial r} + \overline{uw} \frac{\partial U}{\partial r} - \overline{v^2} \frac{V_\theta}{r} \right] - \rho\gamma k \frac{\partial V_\theta}{\partial r} \\
 & + \rho \overline{vw} \frac{\partial U}{\partial x} (1-\alpha-\beta) - C_1' \frac{\rho\epsilon}{k} \overline{vw}
 \end{aligned} \tag{41}$$

o Turbulence shear stress, \overline{uw}

$$\begin{aligned}
 S \overline{uw} = & -\rho(1-\alpha) \left[\overline{vw} \frac{\partial U}{\partial r} + \overline{u^2} \frac{\partial V_\theta}{\partial x} + \overline{uv} \frac{\partial V_\theta}{\partial r} \right] \\
 & + \rho\beta \left[\overline{vw} \frac{\partial V}{\partial x} + \overline{w^2} \frac{\partial V_\theta}{\partial x} - \overline{uv} \frac{V_\theta}{r} \right] \\
 & - \rho\gamma k \frac{\partial V_\theta}{\partial x} - C_1' \frac{\rho\epsilon}{k} \overline{uw} + \rho \overline{uw} (1-\alpha-\beta) \frac{\partial V}{\partial r}
 \end{aligned} \tag{42}$$

Here, C_1' , α , β , and γ are empirical constants, whose values are defined in Equation 26.

Solutions obtained from these equations are used in the momentum equations instead of using the gradient diffusion assumptions. In the new-wall region, boundary conditions for the dependent Reynolds stress components are applied by assuming the convection and diffusion terms to be small, in accordance with the wall function approach. The Reynolds stress component $\overline{w^2}$ is computed from the relation

$$\overline{w^2} = 2k - \overline{u^2} - \overline{v^2}$$

3.2.6 Scalar Transport Model

The turbulent transport of Scalar properties in a flow is quite different from the transport of momenta. The most common method of describing turbulent scalar transport is the gradient transport law through the use of Prandtl/Schmidt numbers. This approach is adopted in the standard k- ϵ model. In the gradient transport model, the turbulent transport parameters of interest are defined by the following.

$$\overline{\rho u \theta'} = - \Gamma_{\text{eff}, \theta} \frac{\partial \bar{\theta}}{\partial x} \quad (43)$$

$$\overline{\rho v \theta'} = - \Gamma_{\text{eff}, \theta} \frac{\partial \bar{\theta}}{\partial r} \quad (44)$$

$$\overline{\rho \theta'^2} = \frac{2}{\alpha_\theta} \frac{k}{\epsilon} \Gamma_{\text{eff}, \theta} \left[\left(\frac{\partial \bar{\theta}}{\partial x} \right)^2 + \left(\frac{\partial \bar{\theta}}{\partial r} \right)^2 \right] \quad (45)$$

where

$$\Gamma_{\text{eff}, \theta} = \mu_{\text{eff}} / \sigma_\theta$$

Here, σ_θ is the Prandtl/Schmidt number for the scalar, θ and α_θ is an empirical constant. Recommended values for these are, $\sigma_\theta = 0.9$ and $\alpha_\theta = 0.8$

The gradient diffusion model does not predict any counter-gradient diffusive transport. However, in many flows, regions of counter-gradient diffusive transport have been known to exist. For such flows, the scalar transport terms must be obtained from appropriate transport equations.

3.2.7 Algebraic Scalar Transport Model

The governing equations for scalar transport are coupled non-linear differential equations, which are quite time consuming to solve. However, by using scaling laws analogous to the method used in developing the ASM, it is possible to obtain algebraic expressions for the scalar transport correlations. These expressions could still account for the counter-gradient scalar transport. The detailed steps used in deriving the algebraic scalar transport terms are described in this paragraph.

Transport Equations for $u_j \theta'$:

$$\underbrace{\text{Div}(\rho \vec{v} \overline{u_j \theta'})}_{\text{Convection}} - \underbrace{\text{Diff}(\rho \overline{u_j \theta'})}_{\text{Diffusion}} = \underbrace{\rho P_{j\theta}}_{\text{Production}} - \underbrace{\rho \epsilon_{j\theta}}_{\text{Dissipation}} + \underbrace{\rho \psi_{j\theta}}_{\text{Redistribution}} \quad (46)$$

$$P_{j\theta} = - \overline{u_i u_j} \frac{\partial \bar{\theta}}{\partial x_i} - \overline{u_i \theta'} \frac{\partial U_j}{\partial x_i} \quad (47)$$

$$\epsilon_{j\theta} = \mu_{\text{eff}} \left(\overline{\frac{\partial u_j}{\partial x_i} \frac{\partial \theta'}{\partial x_i}} \right) \quad (48)$$

$$\psi_{j\theta} = - C_{1\theta} \frac{\epsilon}{k} \overline{u_j \theta'} + c_{2\theta} \overline{u_i \theta'} \frac{\partial U_j}{\partial x_i} \quad (49)$$

Assumption:

$$\text{Div}(\rho \vec{v} \overline{u_j \theta'}) - \text{Diff}(\rho \overline{u_j \theta'}) = a_1 \frac{\overline{u_j \theta'}}{k} (P - \epsilon) + a_2 \frac{\overline{u_j \theta'}}{\theta'^2} (P_\theta - \epsilon_\theta) \quad (50)$$

ORIGINAL PAGE IS
OF POOR QUALITY

where:

$$P_{\theta} = - 2 \overline{u_j \theta'} \frac{\partial \bar{\theta}}{\partial x_j} \quad (51)$$

$$\epsilon_{\theta} = \alpha_{\theta} \frac{\epsilon}{k} \overline{\theta'^2} \quad (52)$$

a_1 and a_2 are empirical constants to be determined.

The transport equation for scalar fluctuations, $\overline{\theta'^2}$, is

$$\underbrace{\text{div } (\rho \vec{v} \overline{\theta'^2})}_{\text{Convection}} - \underbrace{\text{Diff } (\rho \overline{\theta'^2})}_{\text{Diffusion}} = \underbrace{\rho P_{\theta}}_{\text{Production}} - \underbrace{\rho \epsilon_{\theta}}_{\text{Dissipation}} \quad (53)$$

where,

$$P_{\theta} = - 2 \overline{u_j \theta'} \frac{\partial \bar{\theta}}{\partial x_j} = - 2 \overline{u \theta'} \frac{\partial \bar{\theta}}{\partial x} - 2 \overline{v \theta'} \frac{\partial \bar{\theta}}{\partial r} \quad (54)$$

and

$$\epsilon_{\theta} = \alpha_{\theta} \frac{\epsilon}{k} \overline{\theta'^2} \quad (55)$$

For minimizing computational effort, the following assumption is made in a form consistent with the model for velocity fluctuations.

Assume:

$$\text{div} (\rho \overline{v \theta'^2}) - \text{Diff} (\rho \overline{\theta'^2}) \approx C_\theta \frac{\overline{\rho \theta'^2}}{k} (P - \epsilon) \quad (56)$$

Using Equations (53) and (56)

$$\rho P_\theta - \rho \epsilon_\theta = C_\theta \frac{\overline{\rho \theta'^2}}{k} (P - \epsilon) \quad (57)$$

With these simplifications, the correlations for scalar quantities reduce to the form:

$$-\overline{v \theta'} = \left[\overline{uv} \frac{\partial \bar{\theta}}{\partial x} + \overline{v^2} \frac{\partial \bar{\theta}}{\partial r} \right] / \left[c_{1\theta} \frac{\epsilon}{k} + \alpha_1 \left(\frac{P - \epsilon}{k} \right) \right] \quad (58)$$

$$-\overline{u \theta'} = \left[\overline{u^2} \frac{\partial \bar{\theta}}{\partial x} + \overline{uv} \frac{\partial \bar{\theta}}{\partial r} + \overline{v \theta'} \frac{\partial U}{\partial r} (1 - c_{2\theta}) \right] / \left[\alpha_1 \left(\frac{P - \epsilon}{k} \right) + c_{1\theta} \frac{\epsilon}{k} + (1 - c_{2\theta}) \frac{\partial U}{\partial x} \right] \quad (59)$$

$$\overline{\theta'^2} = -2 \left[\overline{u \theta'} \frac{\partial \bar{\theta}}{\partial x} + \overline{v \theta'} \frac{\partial \bar{\theta}}{\partial r} \right] / \left[c_\theta \left(\frac{P - \epsilon}{k} \right) + \alpha_\theta \frac{\epsilon}{k} \right] \quad (60)$$

The assumptions used in the derivation of the algebraic stress model are applicable for the flows that are close to local equilibrium. However, this model does not neglect any of the terms in the transport equation, and only a scaling law has been employed.

The algebraic relations shown above express the turbulent scalar transport as a function of both mean scalar gradients and mean velocity gradients and hence can predict counter-gradient scalar transport.

3.3 Gaseous Fuel Combustion Models

Successful modeling of combustors depends upon a correct description and coupling of the fluid mechanics, turbulence, heat transfer, and chemical processes involved. The rates of turbulent exchange of various species and the rates of chemical change need to be modeled. In turn, this modeling will determine the details of quantities such as energy input to the gas stream, flow patterns, temperatures, and species concentrations. Turbulence models have been developed to a reasonably satisfactory stage. The state of development of chemical models is not nearly so satisfactory and is discussed in Paragraph 3.3.1.

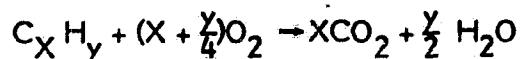
The turbulence/chemistry interaction model currently used by Garrett is a modified version of the eddy-breakup model; work is in progress on the development of a perturbation analysis technique. These models are described in Paragraph 3.3.2.

3.3.1 Hydrocarbon Reaction Mechanisms

A successful modeling of combustion systems depends on an adequate description of the reaction mechanism. For hydrocarbon oxidation, a large number of species participating simultaneously in numerous elementary kinetic steps is required to specify the reaction mechanism. These differential equations are "stiff" and require special time-consuming integration methods. For a complex 3-D problem, the computing costs would be prohibitive. Besides the large number of species equations to be solved, the elementary steps and their rate constants are not well known except for the simplest of hydrocarbons (e.g., CH_4). To avoid this problem, the gas turbine combustion modeling effort has frequently been simplified by using a global approach that reduces chemistry to the specification of an overall global oxidation scheme. This can predict quantities of interest: fuel consumption and heat release rates.

One Step Scheme

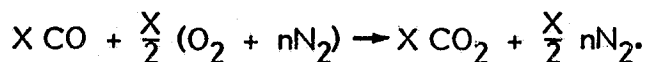
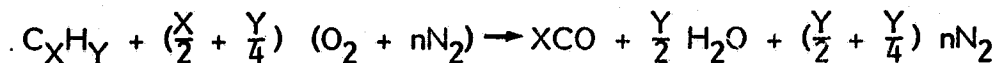
The simplest global mechanism is the one-step scheme:



The advantage of this mechanism is its simplicity; it involves the solution of the conservation equations for unburned fuel and the mixture fraction. The heat release and the concentrations of the other species are then obtained from linear functions of the amount of fuel consumed. This mechanism, however, fails to predict the important characteristics of hydrocarbon oxidation, i.e., the formation of intermediates and CO, which influence the process considerably. As a result, this mechanism is inadequate for obtaining quantitative predictions.

Two-Step Scheme

A slightly more complex scheme is the two-step mechanism:



This scheme involves the solution of one additional equation: that for the concentration of CO. Although the two-step scheme has been widely used by Garrett, it is deficient in that the formation of intermediates is ignored. The derivation of the pertinent equations is given below.

For the first reaction,

$$\begin{aligned}
 r_1 &= (\text{mass of } O_2) / (\text{mass of fuel}), \\
 r_2 &= (\text{mass of CO}) / (\text{mass of fuel}), \\
 r_3 &= (\text{mass of } H_2O) / (\text{mass of fuel}); \tag{61}
 \end{aligned}$$

in the second reaction:

$$\begin{aligned}
 r_4 &= (\text{mass of } O_2) / (\text{mass of CO}), \\
 r_5 &= (\text{mass of } CO_2) / (\text{mass of CO}). \tag{62}
 \end{aligned}$$

The values of these ratios can be calculated in a straight-forward manner:

$$\begin{aligned}
 r_1 &= \left(\frac{X}{2} + \frac{Y}{4}\right) W_{O_2} / W_{fu} \\
 r_2 &= X W_{CO} / W_{fu} \\
 r_3 &= (Y/2) W_{H_2O} / W_{fu} \\
 r_4 &= (1/2) W_{O_2} / W_{CO} \\
 r_5 &= W_{CO_2} / W_{CO} \tag{63}
 \end{aligned}$$

Here the W's are the molecular weights of the chemical species.

The mass fractions of all chemical species obey the general differential equation with S_ϕ as defined in Table 2. Further, the diffusion coefficient Γ_ϕ can be taken to be the same for all species, especially when the flow is turbulent. The value of Γ_ϕ is then μ_t / σ_t , where σ_t is the turbulent Prandtl (or Schmidt) number. The source terms for various species are related via the ratios defined in Equations (61) and (62). As a result, the mass fractions of the species can be added in certain proportions to yield

zero source terms. This is shown in Table 2. Here S_{fu} denotes the source for fuel due to the first reaction, while S_{CO} stands for the rate of production of CO in the second reaction.

TABLE 2. SOURCE TERMS FOR CHEMICAL SPECIES.

ϕ	S
M_{fu}	S_{fu}
m_{CO}	$S_{CO} - r_2 S_{fu}$
m_{OX}	$r_1 S_{fu} + r_4 S_{CO}$
M_{CO_2}	$- r_5 S_{CO}$
M_{H_2O}	$- r_3 S_{fu}$
$\phi_A \equiv m_{OX} - (r_1 + r_2 + r_4) m_{fu} - r_4 m_{CO}$	0
$\phi_B \equiv m_{CO_2} + r_5 m_{CO} + r_2 r_5 m_{fu}$	0
$\phi_C \equiv m_{H_2O} + r_3 m_{fu}$	0

The last three entries in Table 2 show that, because their source term is zero, a single solution for them would suffice provided their boundary conditions are the same. This condition can be ensured by normalizing the ϕ 's with reference to their values in the air and fuel streams. Thus a single variable f with a zero source term and with values 0 and 1 in the air and fuel streams

respectively can be regarded as providing the solutions for ϕ_A , ϕ_B and ϕ_C via the following relationships:

$$f = \frac{\phi_A - \phi_{A, \text{air}}}{\phi_{A, \text{fuel}} - \phi_{A, \text{air}}} = \frac{\phi_B - \phi_{B, \text{air}}}{\phi_{B, \text{fuel}} - \phi_{B, \text{air}}} = \frac{\phi_C - \phi_{C, \text{air}}}{\phi_{C, \text{fuel}} - \phi_{C, \text{air}}} \quad (64)$$

Further, let:

$$\left. \begin{aligned} (m_{fu})_{\text{fuel}} &= 1 \\ \text{and} \\ (m_{OX})_{\text{air}} &= R \\ (m_{N_2})_{\text{air}} &= 1-R \end{aligned} \right\} \quad (65)$$

Combining Equations (64), (65), and the definitions of ϕ_A , ϕ_B , ϕ_C , we have:

$$m_{OX} = R(1-f) + r_4 m_{CO} + (r_1 + r_2 r_4) (m_{fu} - f) \quad (66)$$

$$m_{CO_2} = r_2 r_5 (f - m_{fu}) - r_5 m_{CO} \quad (67)$$

$$m_{H_2O} = r_3 (f - m_{fu}) \quad (68)$$

Incidentally, f can be considered as the mass fraction of "total fuel" that would prevail if the fuel did not react at all.

The reaction rates S_{fu} and S_{CO} are given by the following relations:

$$S_{fu} = - (\text{The smaller of } S_1 \text{ and } S_2),$$

where

$$S_1 = F_1 \rho^{1.5} m_{fu}^{0.5} m_{OX} \exp(-E_1/RT),$$
$$S_2 = C_{R,1} \rho m_{fu} \epsilon/k. \quad (69)$$

Here, $C_{R,1}$ is the eddy breakup constant for first reaction. Recommended value for $C_{R,1}$ is 3.0

$$S_{CO} = - (\text{The smaller of } S_3 \text{ and } S_4),$$

where

$$S_3 = F_2 \rho^2 m_{CO} m_{OX} \exp(-E_2/RT),$$
$$S_4 = C_{R,2} \rho m_{CO} \epsilon/k. \quad (70)$$

$C_{R,2}$ is the eddy breakup constant for the second reaction, recommended value for $C_{R,2}$ is 4.0

The constants in the above expressions are given the following values:¹

$$F_1 = 3.3 \times 10^{14}, \quad E_1/R = 27000., \quad C_{R,1} = 3,$$

$$F_2 = 6.0 \times 10^8, \quad E_2/R = 12500., \quad C_{R,2} = 4,$$

all in S.I. Units.

To summarize, the quantities m_{fu} , m_{CO} , and f are used as the dependent variables of the differential equations. The source terms for m_{fu} and m_{CO} are calculated from Equation (69) and (70), while the source for f is zero. The values of m_{OX} , m_{CO_2} , and m_{H_2O} are then obtained from Equations (66), (67), and (68). Lastly, m_{N_2} is calculated from the fact that all mass fractions should add up to unity.

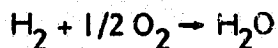
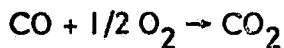
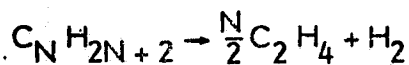
Four-Step Scheme

The oxidation of hydrocarbon fuel can be described by the following steps:

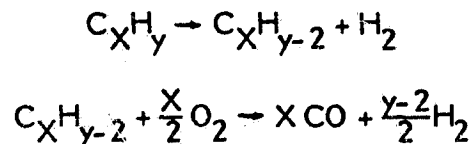
- (a) Transformation of the hydrocarbon fuel into intermediate hydrocarbons and hydrogen with little release of energy
- (b) Oxidation of intermediates to CO and H₂
- (c) Oxidation of CO to CO₂
- (d) Oxidation of H₂ to H₂O.

Steps (b) through (d) are exothermic and are responsible for the release of energy and associated temperature rise. A reaction scheme, which is designed to correctly model the oxidation process, must include a description of these steps.

The simplest mechanism that accounts for the essential features of the hydrocarbon oxidation is the following four-step scheme proposed by Hautman, et al.¹⁹



which is valid only for aliphatic hydrocarbons (of the type $C_N H_{2N+2}$). To accommodate a general hydrocarbon $C_X H_Y$, the first two steps have been modified:



This scheme involves the solution of two transport equations for the concentrations of $C_X H_{Y-2}$ and H_2 , in addition to the transport operations for unburned fuel, CO, and "total fuel" as outlined in the two-step scheme.

3.3.2 Turbulence/Chemistry Interaction

In this section, a review of turbulent combustion models is provided. This is followed by a description of the models under investigation at Garrett. Finally, a summary of turbulence/chemistry interaction modeling is provided.

Review of Turbulent Combustion Models

An adequate treatment of turbulence/chemistry interactions is essential for a reliable combustion model. Since the kinetic equations are nonlinear in temperature and concentrations, large errors can be caused by incorrect time-averaging of the various terms with attendant effects on heat release rates, time-averaged gas temperatures, and convective and radiative fluxes to the liner walls.

The Problem - It has long been realized that the practice of writing chemical kinetic equations in terms of time-averaged local variables such as

$$\bar{W}_i = \bar{Y}_i \bar{Y}_j A \exp \{-\theta/T\} \quad (71)$$

is unsound in turbulent mixing flows with relatively fast kinetics. Here W_i is the chemical reaction rate for species i of mole fraction Y_i ; Y_j is the mole fraction of another species; A is the pre-exponential factor in the Arrhenius expression for the chemical kinetic rate; θ is the activation temperature; and T is the absolute temperature, the overbar indicating time averaging. Equation (71) neglects the correlations between fluctuations in the various quantities, e.g., $\overline{Y'_i Y'_j}$, $\overline{Y'_i T'}$ and the contributions from these terms can change the computed reaction rate by an order of magnitude or more. Attempts to compute the various correlations directly, as has been done by Donaldson²⁰ and Borghi,²¹ have proved successful only in flows where the fluctuations are low and the heat release is not large.

The Fast-Chemistry Approach - A more satisfactory approach in non-premixed combustion systems is based on the assumption that the chemistry is fast. The chemical reaction rates are then entirely mixing controlled and are a function of the turbulence rather than the chemical kinetics. Two versions of this approach are in current use.

In the first version, equations for conserved scalars such as the element mass fractions or the mixture fraction are solved, instead of solving directly for the individual combustion product species. Molecular species concentrations and temperature are then determined from the computed moments of the conserved scalar, usually by assuming some probability density function for the conserved scalar. The fast chemistry assumption implies an instantaneous relationship between molecular species or temperature and the conserved scalar. Chemical reaction rates can be found, if needed, by differentiation. Such an approach has been used by some investigators, e.g., Lockwood.²² The problem is that the extension to include the treatment of any type of reaction mechanism, even a single-step one, entails complications.

In the second version, molecular equations are solved and the chemical reaction rate is modeled directly in terms of turbulence quantities. The Spalding eddy breakup (EBU) model²³ is the prime example of this approach, in which single or multi-step reaction mechanisms can be handled, when suitable modifications to the model are made. This has been done by Garrett, which has developed a modified version of this model.

Both of these approaches give qualitatively satisfactory results for the main species concentrations and temperature. The problem, however, is that chemical kinetics is no longer involved.

The Inclusion of Chemical Kinetics - Although the majority of fuel oxidation in gas turbine combustion systems is essentially mixing controlled under most operating conditions, the chemical kinetic effects must be included to predict hydrocarbon emissions, flame stabilization or blowout, CO emissions, soot formation and burnout, and NO formation. The problems of satisfactorily including the chemical kinetics into the chemical reaction rate have proved to be formidable.

As a first step towards inclusion of the kinetics, the EBU model has been modified at Garrett to compute the reaction rate R from the minimum of the EBU rate and the well-stirred reactor global reaction rates. Garrett has used 2-step and, recently, 4-step kinetic schemes. The procedure is illustrated here with a single-step reaction scheme.

$$R = \min [R_{\text{EBU}}, R_{\text{WS}}] \quad (72)$$

$$R_{\text{EBU}} = C_R \rho \phi \epsilon / k \quad (73)$$

$$R_{\text{WS}} = A \rho^{1.5} M_{\text{ox}} M_{\text{fu}}^{0.5} \exp(-E/RT) \quad (74)$$

$$\phi = \min [M_{\text{fu}}, M_{\text{ox}}/i] \quad (75)$$

where:

R_{EBU} = the eddy-breakup rate of chemical reaction;

R_{WS} = the well-stirred rate of chemical reaction;

C_{R} = empirical constant;

A = Arrhenius pre-exponential factor;

ρ = density;

M_{Ox} = mass fraction of oxidant

M_{fu} = mass fraction of fuel

E/R = activation temperature;

T = absolute temperature;

k = turbulence kinetic energy

ϵ = dissipation rate of k

i = mass of oxidant per unit mass of fuel.

This model, which was used in the computer codes developed by Garrett for the US Army,¹² has been found suitable for qualitative correlations. A further extension of the model at Garrett solves a transport equation for the fluctuation, $g (= \phi^2)$, of the fuel concentration rather than obtaining ϕ from Equation (75). This additional equation results in better agreement between the predictions and experimental data for typical combustor geometries. It is still not suitable for accurate quantitative predictions and for problems such as kinetic effects on temperature or satisfactory

estimates of free-radical concentrations. These quantities are required for accurate prediction of CO, since CO consumption often occurs via the reaction $\text{CO} + \text{OH} = \text{CO}_2 + \text{H}$.

Achievement of a satisfactory approach to the modeling of the chemical reactions has led to several rather novel approaches to the problem. Many of these methods, such as Spalding's ESCIMO model,²⁴ Chorin's Vortex Dynamics, large eddy simulation techniques, and joint PDF approaches,²⁵ involve at least an order of magnitude increase in the size and complexity of the computation and as yet are not completely formulated. One approach, based on a perturbation analysis for reaction kinetics, does not involve such an increase in size and complexity, and has been formulated by Bilger.²⁶ This method, as described in the next paragraph, has been adapted by Garrett.

The Perturbation Analysis for Reaction Kinetics

In this approach, a turbulent diffusion flame model has been developed.²⁷ It uses a double reaction zone model and perturbation analysis for finite rate kinetics for hydrocarbon combustion. A system of eight parabolic transport equations is solved. The system consists of the usual k - ϵ model equation in Favre averaged form for continuity, momentum, mean mixture fraction, specific turbulent kinetic energy, and turbulent kinetic energy dissipation rate, with additional scalar transport equations for mixture mole number perturbation, unburned fuel mass fraction perturbation, and mixture fraction variance. The thermodynamic state (and composition) of the flow field is contained in an equilibrium model of the hydrocarbon-air mixture in terms of mean mixture fraction. The progress of the chemical reactions (and thereby the molecular kinetic rates) is contained in perturbations or constraints on the equilibrium in terms of mole number and unburned fuel mass fraction. The unburned

fuel mass fraction and the intermediate are specified as functions of mixture mass fraction, ξ . For the fuel,

$$Y_{13} = Y^{\circ}_{13} + y \quad (76)$$

where

$$Y^{\circ}_{13} = 0 \quad 0 \leq \xi < \xi_{ig}$$

and

$$Y^{\circ}_{13} = \frac{(\xi - \xi_{ig})}{1 - \xi_{ig}} \quad \xi_{ig} < \xi \leq 1$$

where

y is the perturbation in fuel mass fraction

Y°_{13} is the "fast chemistry" (i.e., zero perturbation) fuel mass fraction

Y_{13} is the fuel mass fraction

ξ_{ig} is the mixture fraction where a "reaction sheet" consumption or pyrolysis of fuel occurs under fast chemistry conditions similar to the classical Burke-Schumann formulation. ξ_{ig} here is taken as 0.073.

For the intermediate hydrocarbon, its mass fraction is given by,

$$Y_{12} = 0 \quad 0 \leq \xi \leq \xi_s \quad (77)$$

$$Y_{12} = \frac{e\Gamma}{1 - \xi_s} (\xi - \xi_s) \quad \xi_s < \xi \leq \xi_{ig} \quad (78)$$

$$Y_{12} = \frac{e\Gamma(\xi_{ig} - \xi_s)}{(1 - \xi_s)(1 - \xi_{ig})} (1 - \xi) \quad \xi_{ig} < \xi \leq 1 \quad (79)$$

where

Γ is the mass fraction of fuel in the inlet fuel stream

Y_{12} is the intermediate hydrocarbon mass fraction

e is the fraction of fuel by mass that is converted to intermediate at ξ_{ig} for fast chemistry conditions. e is taken as 0.2

and ξ_s is the stoichiometric mixture fraction

Hence, the double reaction zone at ξ_s and ξ_{ig} .

Thirteen species are considered in the reactions. H , H_2 , H_2O , O , OH , O_2 , HO_2 , N_2 , Ar , CO , and CO_2 are calculated from partial or constrained equilibrium, and the fuel and intermediate are specified as in Equations 76-79. The perturbation in mole number space is a result of the rate of three-body recombination reactions,



The progress of these reactions toward equilibrium is measured by mole number, N

$$N = \sum_{i=1}^n \frac{Y_i}{W_i} \quad \frac{\text{Mole}}{\text{Kg}} \quad (80)$$

where

Y_i is the mass fraction of species i

and

W_i is the molecular weight of species i

The perturbation in mole number is defined as

$$n = N - N^0 \quad (81)$$

Where N° is the number of moles at full equilibrium. Then, for various perturbations in mole number space for a given mixture mass fraction, the time rate of change of N can be calculated from reactions R1-R4 using here the kinetic data of Jensen and Jones.²⁸

Perturbation Equations

From the species balance transport equation,

$$\frac{\partial Y_i}{\partial t} + \rho U_k \frac{\partial Y_i}{\partial x_k} - \frac{\partial}{\partial x_k} \left(\rho D \frac{\partial Y_i}{\partial x_k} \right) = 0 \quad (82)$$

where the molecular diffusivity is assumed to be the same for all species, and using Equations 80 and 81 gives,

$$\frac{\partial n}{\partial t} + \rho U_k \frac{\partial n}{\partial x_k} + \frac{\partial}{\partial x_k} \left(\rho D \frac{\partial n}{\partial x_k} \right) = \rho D \left(\frac{\partial \xi}{\partial x_k} \right)^2 \frac{d^2 N^\circ}{d\xi^2} + w_n \quad (83)$$

w_n is the source term for mole number

A similar equation can be written for the fuel mass fraction perturbation.

$$\frac{\partial y}{\partial t} + \rho U_k \frac{\partial y}{\partial x_k} - \frac{\partial}{\partial x_k} \left(\rho D \frac{\partial y}{\partial x_k} \right) = \rho D \left(\frac{\partial \xi}{\partial x_k} \right)^2 \frac{d^2 Y_{13}^\circ}{d\xi^2} + w_y \quad (84)$$

w_y is the source term for mass fraction

where the dependence of y on N° is neglected.

Then using density weighting (Favre averaging), the equations for turbulent flow become,

$$\bar{\rho} \tilde{u}_k \frac{\partial \tilde{n}}{\partial x_k} + \frac{\partial}{\partial x_k} (\bar{\rho} u''n'') = \rho D \left(\frac{\partial \xi}{\partial x_k} \right)^2 \frac{d^2 N^0}{d\xi^2} + \bar{w}_n \quad (85)$$

$$\bar{\rho} \tilde{u}_k \frac{\partial \tilde{y}}{\partial x_k} + \frac{\partial}{\partial x_k} (\bar{\rho} u''y'') = \rho D \left(\frac{\partial \xi}{\partial x_k} \right)^2 \frac{d^2 Y^0}{d\xi^2} + \bar{w}_y \quad (86)$$

Using gradient modeling of the turbulent fluxes and k-ε modeling of the scalar dissipation X

where

$$X = 2 D \left(\frac{\partial \xi''}{\partial x_k} \right)^2 \quad (87)$$

the Favre averaged scalar dissipation rate is

$$\chi = C_{g_2} \xi''^2 (\epsilon/k) \quad (88)$$

where C_{g_2} is a model constant with value of 1.79. Then,

$$\bar{\rho} \tilde{u}_k \frac{\partial \tilde{n}}{\partial x_k} - \frac{\partial}{\partial x_k} \left[\frac{\mu_{eff}}{\sigma_n} \frac{\partial \tilde{n}}{\partial x_k} \right] = 1/2 \bar{\rho} C_{g_2} \xi''^2 (\epsilon/k) \Delta_{N,s} \tilde{p}(\xi_s) + \bar{w}_n \quad (89)$$

$$\bar{\rho} \tilde{u}_k \frac{\partial \tilde{y}}{\partial x_k} - \frac{\partial}{\partial x_k} \left[\frac{\mu_{eff}}{\sigma_y} \frac{\partial \tilde{y}}{\partial x_k} \right] = 1/2 \bar{\rho} C_{g_2} \xi''^2 (\epsilon/k) \Delta_y \tilde{p}(\xi_{ig}) + \bar{w}_y \quad (90)$$

ORIGINAL PAGE IS
OF POOR QUALITY

The parameters $\Delta_{N,S}$ and Δ_Y represent the net change in $dN^\circ/d\xi$ and $dY^\circ_{13}/d\xi$ across the reaction zones at ξ_s and ξ_{ig} , respectively, and $p(\xi)$ is the Favre probability density of ξ . In deriving these equations, the usual high Reynolds number assumptions have been made and the scalar dissipation is assumed not to be correlated with the mixture fraction.

Finally, the mixture fraction perturbation,

$$\xi'' = \xi - \tilde{\xi}$$

gives the transport equation for the variance of the mixture fraction

$$\overline{\rho} \tilde{u}_k \frac{\partial \xi''^2}{\partial x_k} - \frac{\partial}{\partial x_k} \left(\frac{\mu_{eff}}{\sigma_{\xi''^2}} \frac{\partial \xi''^2}{\partial x_k} \right) = C_{g1} \mu_{eff} \left(\frac{\partial \xi''^2}{\partial x_k} \right)^2 - C_{g2} \overline{\rho} \epsilon \frac{\xi''^2}{r} \quad (91)$$

The main features of measured probability density functions are the strong spike associated with the free stream and the continuous distribution generated by turbulence. By splitting the two, a clipped Gaussian intermittent formula is used to represent the Favre averaged probability density at a particular value, ξ_a

$$\tilde{p}(\xi_a) = \frac{\gamma}{\sqrt{2\pi} (\xi''^2)_t}^{1/2} \exp \left\{ -1/2 \frac{(\tilde{\xi}_t - \xi_a)^2}{(\xi''^2)_t} \right\} \quad (92)$$

where $\tilde{\xi}_t = \tilde{\xi}/\tilde{\gamma}$

$$\tilde{\gamma} = 1 \quad \text{for } \xi''^2 < 0.25 \tilde{\xi}^2$$

$$\tilde{\gamma} = \frac{1.25}{\xi''^2 / \tilde{\xi}^2 + 1} \quad \text{for } \xi''^2 \geq 0.25 \tilde{\xi}^2$$

and

$$(\tilde{\xi}''^2) = \tilde{\gamma} \left[(\tilde{\xi}''^2)_t + (\tilde{\xi}_t - \tilde{\xi})^2 \right] + (1 - \tilde{\gamma}) \tilde{\xi}^2$$

(93)

Also from simple fits to the partial equilibrium calculations, the mean density as a function of the mole number and fuel mass function perturbations is

$$\bar{\rho} = \left[v^\circ(\tilde{\xi}) \right]^{-1} + \tilde{\gamma} (0.022 \tilde{n} + 1.38 \tilde{\gamma})$$

(94)

where $v^\circ(\tilde{\xi})$ is the Favre average specific volume for zero perturbations.

Lastly, the kinetic dependent source terms \bar{w}_n and \bar{w}_y are given by,

$$\bar{w}_n = \bar{\rho} \iiint q(\xi, n, \gamma) w_n(\xi, n, \gamma) (1/\rho) \tilde{p}(\xi, n, \gamma) d\xi dn d\gamma$$

(95)

and

$$\bar{w}_y = - \bar{\rho} \iiint S_y^*(\xi, n, \gamma) \tilde{p}(\xi, n, \gamma) d\gamma dn d\xi$$

(96)

where

$$w_n/\rho = - 9000 n^2 \frac{\text{moles}}{\text{kg sec}}$$

from consideration of the partial equilibrium calculations and $q(\xi, n, \gamma)$ is a quenching function to allow for breakdown of the constrained equilibrium represented as follows:

$$\begin{aligned}
q(\xi, n, \gamma) = B^*(\xi) &= 0 && \text{for } \tilde{\xi} < 0.01 \\
&= 50(\tilde{\xi} - 0.01) && 0.01 \leq \tilde{\xi} \leq 0.03 \\
&= 1 && \tilde{\xi} > 0.03
\end{aligned}$$

Simplification of the joint P.D.F. yields

$$\bar{w}_n = -\rho B^* 9000 \tilde{n}^2$$

The fuel source term w_y is evaluated based on the kinetic rate of Duterque²⁹ over the range of expected values of ξ , n , and γ and again the joint P.D.F. is avoided, as

$$\bar{w}_y = -\frac{1}{\rho} \int_0^1 S_y^*(\xi, \tilde{n}, \tilde{\gamma}) \tilde{P}(\xi) d\xi$$

where

(97)

$$S_y^* = \frac{w_y}{\rho} = 8.53 \cdot 10^{14} \left(\frac{X_{O_2} \gamma}{T} \right) \exp\left(\frac{-23500}{T} \right) \text{ sec}^{-1}$$

where X_{O_2} oxygen mole fraction and temperature, T , are taken from the partial equilibrium calculations for Methane.

The above three differential equations are combined with the other five Favre averaged equations, as mentioned above, written in cylindrical coordinates and transformed using the stream function

$$\partial \psi = \rho \tilde{u} r \partial r$$

and put in finite difference form using a Crank-Nicholson central difference scheme. The nonlinear coefficient terms and source terms were evaluated as the mean of the upstream value and the first estimate of the downstream value.

Then, for any "output" position in the flame, the effect of perturbations on species mole fractions and temperature is calculated from the local P.D.F.,

$$\tilde{X}_i = \int_0^1 x_i(\xi, \tilde{n}, \tilde{y}) \tilde{P}(\xi) d\xi \quad (98)$$

$$\tilde{T} = \int_0^1 T(\xi, \tilde{n}, \tilde{y}) \tilde{P}(\xi) d\xi \quad (99)$$

again, where joint probabilities have been avoided.

3.4 Spray Evaporation/Combustion Models

Since the influence of the liquid fuel spray on combustor performance is quite pronounced, an accurate spray model is essential for any combustor modeling effort. The modeling of liquid fuel sprays is discussed in this section.

The spray model currently used by Garrett is based on a Lagrangian discrete-droplet approach allowing for droplet slip but no turbulent dispersion. Eulerian (continuous formulations) versions allowing for dispersion, with or without droplet slip, have also been developed by Garrett. Both approaches offer advantages in certain circumstances.

3.4.1 A Review of Spray Models

A number of spray evaporation/combustion models have been developed and used with varying degrees of success. Several review papers are available in the literature;^{30,31} an excellent recent review paper is by Faeth.³² Faeth has divided the spray model work into two major categories:

- o Locally homogeneous flow (LHF) models
- o Separated flow (SF) models

In LHF models, the gas and liquid phases are assumed to be in dynamic and thermodynamic equilibrium at all times, with no droplet slip. Consequently, the use of LHF models should be limited to finer droplet sprays. Although the LHF predictions tend to approach measurements as the droplet size reduces, the agreement is relatively poor, even for the sprays that have an SMD of around 30 microns.³² Compared to the SF models, the LHF models are easy to use because they require minimum information concerning fuel injector characteristics, fewer empirical constants, and shorter computation time. The LHF models give useful qualitative descriptions of the spray development, the rate of which is generally over-estimated.

In SF models, finite interphase transport processes of mass, momentum, and heat are taken into account; and these models are therefore of more interest in gas turbine combustor modeling. The SF models can be broadly divided into the following two major categories:

- o Discrete Droplet Models (DDM) - Lagrangian
- o Continuous Formulation Models (CFM) - Eulerian

Both categories contain features that make their application to practical combustors desirable. In DDM, the fuel droplets are assumed to exist sufficiently removed from each other that droplet-to-droplet interaction can be neglected. This assumption is quite reasonable for regions in the combustor other than very close to the fuel nozzle spray origin. Thus, the analytical modeling of a single droplet can be applied to the gas turbine spray that greatly simplifies the formulation. The nozzle spray is divided into a number of size groups usually determined experimentally,³³ with one droplet representing the behavior of all the droplets in its group. A DDM is constructed for each size group. Given an initial velocity and temperature as determined from the injector characteristics, the droplet trajectory is calculated through the flow domain

as governed by drag and other forces, until the droplet evaporates or exits the calculation grid. At each point along the flight path as evaporation occurs, modifications are made to the momentum, enthalpy, and species equations that govern the gas phase flow.

The second major category of SF models is CFM. These models solve turbulent transport equations for the motion of the droplets and the turbulent diffusion of droplets is included. An underlying assumption is that all the droplets and the gas phase have the same velocity. The computational effort required for CFM is greatly increased because a complete equation (similar to the momentum, species, etc., equations) must be solved for each droplet group. Computer storage must also be allocated for the extra variables. A major disadvantage of this approach is that errors are generated in the vicinity of the fuel nozzle. Since the difference in the liquid and gas phase velocities is very significant in this region, a better resolution of grid spacing is needed than can be managed.

3.4.2 Garrett's Spray Models

The main requirement of a spray model is accurate predictive capability within a reasonable amount of computational effort, especially for 3-D flows of practical interest. To achieve accuracy, various physical processes must be incorporated into the model in a realistic manner. Thus, relative velocity differences between the gaseous and liquid phases (droplet slip), resulting in interphase momentum transfer, must be considered. Also, the evaporation of droplets during heat-up time (interphase heat and mass transfer) is important in order to predict ignition processes. Finally, turbulent diffusion of droplets is important but is generally ignored in most of the spray models. Stochastic models to consider turbulent diffusion, as reported by Gosman³⁵ are computationally expensive when applied to real combustors.

On the computational aspect of spray modeling, it should be realized that a different degree of resolution is required in the near-injector and far-injector regions.

Consideration of these factors has led to the development of the Garrett spray models, the features of which are described below.

Evaporation during heat-up time is considered in the Garrett model and the computation of heat-up and evaporation rates includes realistic properties of jet aviation fuels. The spray model is applicable to both dense and sparse sprays and is coupled into either the 2-step or the 4-step global hydrocarbon oxidation scheme; it is available in both 2-D and 3-D combustor performance programs.

Velocity differences (slip) between the droplets and the gas phase are modeled, and so is turbulent diffusion of the droplets. For computational purposes, the droplet size distribution is discretized, and differential equations in a Eulerian framework are solved for the velocity components and concentration of droplets in each size group (typically five size groups are considered). To obtain good resolution in the near injector region, Lagrangian equations of motion for the droplets are solved in this region. Each class of droplets is tracked through the flow field in the vicinity of the injector and the interphase transports of mass, momentum, and energy are used to couple this solution to the Eulerian equations. The model thus combines the desirable features of the DDM and CFM approaches.

Lagrangian Model

The Lagrangian model was initially pursued since the formulation allows the tracking of small fuel droplets that are significantly smaller than typical grid dimensions and since the computational requirements for 3-D flows are quite small. In addition, the assumption of sparse sprays and no droplet-droplet interaction is quite reasonable for most regions in a gas turbine combustor.

The generalized governing equation for fuel mass fraction is

$$\text{div}(\rho \vec{V} m_{fu}) - \Gamma_{fu,eff} \text{grad} m_{fu} = \dot{m}_e''' - R_{fu} \quad (100)$$

where R_{fu} is the destruction rate of fuel and \dot{m}_e''' is the rate of vapor production from the fuel droplets. The vapor production rate or evaporation rate is determined from the burning rate constant k_o , which relates the change in the square of the droplet diameter (D) with time.

$$k_o = \frac{d(-D^2)}{dt} = \frac{8\lambda_1}{\rho_f C_{p1}} \ln(1+B) \quad (101)$$

where:

- λ_1 = Thermal conductivity of vapor
- C_{p1} = Weighted average specific heat of vapor and air
- B = Mass transfer number
- ρ_f = Fuel density

From the burning rate constant, the fraction of fuel evaporated from a group of droplets (ΔF_i) can be determined from the time integral;

$$\Delta F_i = \frac{1.5}{\rho_f D_{i_0}^3} \int \rho_f D_i k_i dt \quad (102)$$

where D_{i_0} is the initial droplet diameter and the i subscript denotes parameters of the i th droplet group.

The total evaporation rate is then given by

$$\dot{m}_e''' = \frac{\dot{m}_{fu}}{N\Delta V} \sum_{i=1}^N \Delta F_i \quad (103)$$

where: \dot{m}_{fu} = The total fuel flow rate
N = Number of droplet groups
 ΔV = Volume of grid cell through which droplet is passing

The calculation of \dot{m}_e''' given above is based on the model of Williams,³⁰ which uses the temperature difference between the droplet and ambient as the driving force. An alternate approach is that of Priem and Heidmann,³⁶ who use the partial pressure of the fuel vapor as the driving force. The advantage of the Priem and Heidmann technique is its applicability to low temperature situations such as altitude ignition, unlike the Williams model.

The expression for evaporation rate for the Priem and Heidmann model is

$$\dot{m}_e''' = \pi D^2 K P_{vap} \alpha \quad (104)$$

where:

K = Function of vapor diffusivity and droplet Reynolds number

P_{vap} = Vapor pressure of fuel at droplet surface

$$\alpha = \frac{P_{\infty}}{P_{\text{vap}}} \ln \left[\frac{P_{\infty}}{P_{\infty} - P_{\text{vap}}} \right]$$

P_{∞} = Ambient pressure

Eulerian Model

The salient features of the model are (a) velocity differences (slip) between the droplets and gas phase are allowed; and (b) turbulent diffusion of the droplets is included. For computational purposes, the droplets are considered to be present in a certain number (typically 5 to 10) of discrete size ranges. Differential equations in an Eulerian framework are solved for the velocity components and concentrations of the droplets in each size group. Interphase transport of mass and energy (due to droplet evaporation and combustion) and momentum (due to drag between gas and liquid phases) are taken into account. Turbulent diffusion of drops is treated as if the droplets were present as a gaseous constituent. The approach used here is to assume the diffusion to be governed by a Fickian type law with an appropriate turbulent Schmidt number, assumed to be uniform over the flow field; but this is easily extended by specifying the turbulent Schmidt number as a function of local flow characteristics. The model is applicable to both dense and sparse sprays insofar as the volume occupied by the droplets is included in the governing equations.

The partial differential equations governing the droplet motion and concentration of each size group are all written in one general form as

$$\frac{\partial}{\partial t} (R\rho\phi) + \text{div} \left\{ R(\vec{\rho}u\phi - \frac{\mu}{\sigma_{\phi}} \text{grad} \phi) \right\} = S_{\phi} \quad (105)$$

where: R = Volume fraction of the droplet size considered
 ρ = Density of the droplets
 ϕ = Velocity component or concentration of droplet size considered
 \vec{U} = Velocity vector of droplet size considered
 μ = Turbulent viscosity
 σ_ϕ = Effective Schmidt number
 S_ϕ = Source of ϕ .

The term S_ϕ contains the pressure gradient, surface friction, and interphase drag if ϕ is a velocity component; interphase mass transfer (evaporation rate) if ϕ is droplet concentration; and interphase heat transfer (heat-up) if ϕ is the enthalpy.

A drawback of the Eulerian model is that it cannot give adequate resolution in the near injector region. An excessively fine finite-difference grid would be required to obtain adequate resolution. The Lagrangian method is capable of providing this resolution in the near injector region. Garrett has therefore coupled two methods in order to utilize the advantages of each. The method is described next.

Lagrangian/Eulerian Model

The concept of this model is analogous to the near-wall treatment described in Paragraph 3.2 and it can be called the near-nozzle spray treatment. The interaction between the Lagrangian and Eulerian solution is through the boundary conditions and the source terms.

To obtain good resolution in the near-injector region, a special treatment is used in this region. The gas properties evaluated by the Eulerian solution are used to solve a set of Lagrangian equations of motion for the droplets again allowing for

interphase mass, momentum, and energy transfer. Each class of droplets is tracked through the flow field in the vicinity of the injector and the interphase mass, momentum, and energy transport that appear as source terms in the gas phase equations are thus evaluated. These terms are obtained by summing overall droplet size groups for each elementary control volume. The Eulerian equations are then solved again including the interphase transport items. The procedure is repeated until it converges to the desired degree of accuracy.

Physical Processes

The physical processes involved in spray modeling are interphase momentum transfer (drag forces), interphase heat transfer (droplet heat-up) and interphase mass transfer (droplet evaporation), and turbulent dispersion of droplets. A brief description is provided in the following paragraphs.

Drag Forces - To calculate the drag forces on the droplet, the drag coefficient, C_D , must be determined. Several expressions are available and Garrett has adopted the suggestion of Briffa³⁷ who measured water droplet velocity decay using a shadowgraph technique. Other forces, such as buoyancy or gravity, acting on the droplet, are quite small in comparison to drag and are usually neglected.

Droplet Heat-Up and Evaporation - Calculation procedures for the rate of phase change of droplets fall into two basic categories: two-stage and transient heat-up models. In two-stage models, as discussed by Williams,³⁰ the droplet is assumed to heat up to the boiling temperature with no evaporation occurring. Once obtained, the evaporation rate is governed by expression for the burning rate constant, defined as the time rate of change of the square of the

droplet diameter. Expressions can be used that account for the existence of an envelope or wake-type flame. The driving force is the temperature difference between the droplet and the surrounding gas phase.

Transient heat-up models such as that of Priem and Heidmann,³⁶ use the difference in fuel vapor concentrations between the droplet surface and its surroundings as the driving force. The temperature of the drop is determined from the consideration of heat transfer to the drop and the fuel latent heat of vaporization.

Though it offers the advantage of ease of computation, the two-stage models best represent droplets in the high-temperature zones of the combustor, where droplet heat-up time is quite short and local fuel concentration is low.

Droplets exist for a significant period of time in the relatively cool, fuel-rich zone near the nozzle. The transient models better represent such droplets. The transient models are more complex from a computation standpoint, but they reflect the varying boiling temperature through the droplet life history and are superior in predicting the evaporation in low-temperature environments (during an altitude start, for example).

To evaluate the evaporation rates, fuel properties such as specific heat and distillation curves are required. For typical aviation fuels, these properties are usually available in the literature or can be estimated from basic characteristics such as specific gravity.³⁸

Turbulent Diffusion of Droplets - In most of the spray models, turbulent dispersion of droplets is ignored or introduced in an oversimplified manner. Some recent studies have adopted a stochastic approach to model this feature. Recently, Gosman, et al.,³⁵ have

presented a stochastic discrete droplet method. In this method, a statistically significant number of random droplet samples is tracked in a Lagrangian framework and the ensemble-averaged behavior is assumed to represent the turbulent dispersion of droplets. This procedure is likely to be computationally expensive for real combustors where a large number of samples is required to obtain statistical averages.

The Garrett Eulerian model includes turbulent diffusion. The model of diffusion of droplets is assumed to be the same as that of the gaseous phase; the extent of diffusion is controlled through the specification of the turbulent Schmidt number for droplet diffusion.

3.5 Soot Formation and Oxidation

In this paragraph, soot formation and oxidation in combustion chambers are discussed. A general background on soot emissions is provided first. Quasi-global expressions for soot formation and oxidation are described. A description of the influence of turbulence on soot formation and oxidation is included. The current approach adopted by Garrett is described next. This approach considers the influence of turbulent fluctuations on soot formation and oxidation rates.

3.5.1 Background

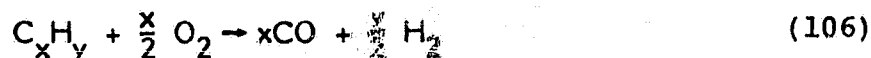
The particulate emission of primary concern in the combustion of hydrocarbon fuels is soot, which is evident in the form of exhaust smoke. The emission of smoke from gas turbine engines is responsible for the following problems of concern in this program:

- o Higher liner temperatures due to increased radiative heat transfer
- o Impingement of carbon on metal surfaces, resulting in erosion and reduced equipment lifetimes
- o Distortion of fuel spray distribution due to carbon deposits, leading to hot spots.

Recently, attention is being directed toward the combustion of alternate fuels derived from coal liquids and shale oil. Since the use of these fuels results in significant increases in smoke production, a better understanding of the physical and chemical processes governing soot production is needed.

The processes governing the formation and subsequent oxidation of soot are of a particularly complex nature and, as such, quantitative models of soot production have yet to be developed. Soot is not an equilibrium product of combustion and, therefore, its formation is influenced as much by the physical processes of atomization, evaporation, and fuel/air mixing as by reaction kinetics. Soot is generally produced anywhere within the combustor where fuel/air mixing is inadequate, resulting in oxygen-deficient, high-temperature zones.

For the pressures and temperatures normally prevalent in gas turbine combustors, equilibrium calculations indicate that solid carbon appears when there is insufficient oxygen to oxidize the hydrocarbon to CO and H₂ according to the relation:



That is, the carbon-oxygen mass ratio for incipient soot formation is 12:16, or alternatively, the atomic C-O ratio is unity. However, since soot formation is essentially a nonequilibrium phenomenon, experimentally, soot is observed at C-O ratios (a) much less than unity at low temperatures (<2000°K); and (b) greater than unity at higher temperatures.³⁹

Smoke levels are primarily dependent on

- o Air/fuel mixing
- o Temperature
- o Equivalence ratio
- o Residence time of air/fuel mixture
- o Pressure
- o Fuel composition.

These factors influence both the formation and subsequent oxidation of soot and are dependent on engine operating conditions, details of the combustor internal flow field, fuel droplet characteristics, etc.

3.5.2 Quasi-Global Models of Soot Formation and Oxidation

Since the elementary steps in the formation and oxidation of soot are not totally understood, Garrett uses quasi-global models that characterize soot production occurring via a few overall steps. Such models have been successful in predicting soot production.⁴⁰

The quasi-global models do not predict the size of soot particles. With the current state-of-the-art, it is not possible to predict the size of formation of the soot particles in any practical flow situation. Therefore, it is assumed that particles are produced at a known size in any analysis. It may also be assumed that particles are produced in accordance with a specified size distribution (e.g., Gaussian).

Tesner, et al.,⁴¹ proposed a soot production model that grouped the complex processes of pyrolysis, nuclei formation, and soot formation into three rate-limited subglobal steps:

Pyrolysis:

$$n_o = a_o C_{fu} \exp(-E/RT) \text{ (part./in}^3\text{.s)} \quad (107)$$

Nuclei Formation:

$$R_{n,f} = n_o + (f-g)n - g_o Nn \text{ (part./m}^3\text{.s)} \quad (108)$$

Soot Formation:

$$R_{s,f} = m_p (a - bN)n \text{ (kg/m}^3\text{.s)} \quad (109)$$

where a_0 , E , g , g_0 , a , and b are constants for given fuel; n_0 is the rate of spontaneous formation of nuclei; n is the nucleus concentration; N is the concentration of soot particles; and m_p is the mass of a soot particle.

Khan and Greeves⁴² proposed a single-step global expression as a function of the partial pressure of unburned hydrocarbons (P_{HC}), the unburned equivalence ratio (ϕ_u), and the temperature (T):

$$\frac{dC_s}{dt} = 0.468 P_{HC} \phi_u^3 \exp(-40,000/RT) \text{ gm/cm}^3 \text{ s.} \quad (110)$$

In both the above models, soot oxidation rates are not considered.

Edelman, et al,⁴⁰ consider both soot formation (R_f) and soot oxidation (R_{ox}) and express the net soot formation rate as

$$\frac{dC_s}{dt} = R_f - A_t R_{ox} \quad (111)$$

where A_t equals total surface area available for oxidation. The formation step is expressed by a modified Arrhenius type of relation:

$$R_f = AT^\alpha C_{HC}^a C_{O_2}^b \exp(-E/RT) \text{ gm/cm}^3 \text{ s.} \quad (112)$$

where C_{O_2} , C_{HC} equal the concentration of unburned oxygen and hydrocarbon (gm/cm^3), and where A , α , a , b , E are model constants.

For the oxidation step, Edelman, et al.,⁴⁰ adopt the semi-empirical formula of Nagle and Strickland-Constable⁴³ for pyrolytic graphite oxidation; this formula is nonlinear and non-Arrhenius in P_{O_2} and T :

$$A_t R_{ox} = 12 \left[\left(\frac{K_A P_{O_2}}{1 + K_Z P_{O_2}} \right) \psi + K_B P_{O_2} (1 - \psi) \right] A_t \text{ gm/s} \quad (113)$$

where:

$$\psi = [1 + K_T / (K_B P_{O_2})]^{-1} \quad (114)$$

$$K_A = 20 \exp(-30,000/RT) \quad (115)$$

$$K_B = 4.46 \times 10^{-3} \exp(-15,200/RT) \quad (116)$$

$$K_T = 1.51 \times 10^5 \exp(-97,000/RT) \quad (117)$$

$$K_Z = 21.3 \exp(4100/RT) \quad (118)$$

Shock-tube measurements⁴⁴ of soot oxidation rates qualitatively confirm the features of the above formula. With these expressions for soot formation and oxidation and assuming a single soot particle size of 250\AA , Edelman, et al.,⁴⁰ obtained close agreement of the predicted soot concentration (mg/l) with the experimental data in a jet-stirred reactor. Thus, these expressions assume perfect mixing. In a gas-turbine combustor, however, regions of unmixed species will exist, and turbulence will also influence the soot production rates. As such, modifications to these expressions are required before they can be used for a general 3-D turbulent flow.

3.5.3 Influence of Turbulence on Soot Formation and Oxidation

Magnussen, et al.,^{45,46} have proposed a model that accounts for the influence of turbulent fluctuations on soot production rates. In turbulent flows, chemical reaction occurs when reactants at a sufficiently high temperature are mixed at the molecular level. The molecular mixing process is analogous to the dissipation (ϵ) of turbulent kinetic energy k and is associated with the smallest scales of turbulence. Dissipation is concentrated in highly strained regions of the fluid occupied by fine structures with characteristic dimensions of the same magnitude as the Kolmogorov microscale. The reactants are molecularly mixed in these fine structures, where reaction occurs. Magnussen, et al., proposed the following expressions for the mass fraction contained in the fine structures:

$$\gamma^* = 9.7 \cdot (R_t)^{-3/4} \quad (119)$$

where R_t is the turbulence Reynolds number, and the rate of transfer of mass per unit mass between the fine structures and the surrounding fluid is

$$\dot{m} = 23.6 \cdot (R_t)^{-1/4} \frac{\epsilon}{k} \quad (120)$$

The rate of reaction is proportional to $\dot{m} \chi$ where χ is the fraction of small-structure eddies that are sufficiently heated to react. It is assumed that χ is proportional to the ratio of local reacted fuel concentration and total fuel concentration. Thus, the rate of reaction is

$$R_{fu} = 23.6 (R_t)^{-1/4} \frac{\epsilon}{k} \chi C_{\min} \text{ (kg/m}^3\text{.s)} \quad (121)$$

where

$$X = \frac{C_{pr}/(1+i)}{C_{pr}/(1+i) + C_{fu}} \quad (122)$$

C_{pr} = Product concentration
 C_{fu} = Fuel concentration

C_{min} is the smaller of C_{fu} and (CO_2/i) and i is the stoichiometric oxygen requirement. The temperature T^* of the reacting fine structures is T above the local time-mean temperature T :

$$T^* = T + \Delta T = T + \frac{\Delta H_R C_{min}}{\rho C_p} \quad (123)$$

where:

H_R = the heat of reaction
 C_p = the specific heat.

and the surrounding temperature T^o is

$$T^o = T - \Delta T \left(\frac{\gamma^* X}{1 - \gamma^* X} \right) \quad (124)$$

Using Equations (107) and (109), the mean rates of nuclei and soot formation are then expressed as

$$R_{n,f} = n_{o,T^*} \cdot \gamma^* \cdot X \cdot \rho/\rho^* + n_{o,T^o} (1 - \gamma^* X) \cdot \rho/\rho^o + (f-g) n$$

$$- g_o n^* N^* \gamma^* X \rho/\rho^* - g_o n^o N^o (1 - \gamma^* X) \rho/\rho^o \quad (125)$$

and

$$R_{s,f} = m_p (a - b N^*) n^* \gamma^* X \rho/\rho^* + m_p \cdot (a - b \cdot N^o) \cdot n^o (1 - \gamma^* X) \cdot \rho/\rho^o \quad (126)$$

Finally, the mean rates of nuclei and soot oxidation are expressed as:

$$R_{n,c} = R_{fu} n/C_{fu} \text{ (part/m}^3\text{.s)} \quad (127)$$

$$R_{s,c} = R_{fu} C_s/C_{fu} \text{ (kg/m}^3\text{.s)} \quad (128)$$

Magnussen, et al., used this model to compute the soot concentrations in a turbulent C_2H_2 diffusion flame. By adjusting the particle diameter [entered as m_p , the particle mass in Equation (109)], and the constant a_0 in Equation (107), good agreement with experimental measurements was obtained.

3.5.4 The Garrett Soot-Emission Model

The model adopted by Garrett for computing soot emissions under NASA Contract NAS3-22542 is described in the following paragraphs.

The computation of soot emissions involves the solution of two additional transport equations for the concentrations of nuclei and soot. To complete the equation specifications, the source terms and the Schmidt numbers for these two variables are as follows:

The source term for nuclei concentration is expressed as

$$R_{n,f} - R_{n,c}$$

where $R_{n,f}$ is given by the smaller of the two values from Equations (108) and (125), $R_{n,c}$ is given by Equation (127). Thus, these expressions amount to the use of the turbulent reaction rates, subject to the limitation that they cannot be greater than the rates under well-stirred reactor conditions.

The source term in the soot concentration Equation (111) is similarly expressed as:

$$R_{S,f} - R_{S,c}$$

where $R_{S,f}$ is given by the smaller of the two values from Equations (112) and (126); $R_{S,c}$ is given by the smaller of the two values from Equations (113) and (128).

The turbulent Schmidt numbers σ_s and σ_n for soot and nuclei concentrations are assumed the same as for gaseous fuel (i.e., 0.9).

This model has been incorporated into the Garrett 3-D combustor performance program. Preliminary computations indicate its ability to make qualitative predictions.

3.6 Radiation Modeling

An adequate treatment of radiative heat transfer from combustion products is essential for the prediction of gas-turbine liner temperatures and heat-transfer rates. For this purpose, Garrett is at present using the six-flux radiation model based on the Schuster-Hamaker⁴⁷ approximation. The influence of soot, CO₂, and H₂O on the radiation properties (absorptivities and emissivities) is included in these equations.

3.6.1 The Flux Methods

In the flux methods, the angular distribution of radiation intensities is replaced by a number of discrete intensity vectors in different directions, thus reducing the complexity of the integro-differential equation of radiation heat transfer. The energy transfer in each direction is represented by a closed first-order ordinary differential equation obtained by integrating the radiation transfer equation over a solid angle. This method was originated for the 1-D case as the two-flux method, wherein only two directions are considered. Considerable errors exist in the two-flux solution in the case of essentially 1-D heat transfer between parallel plates; a situation for which the method is supposedly best-suited. This suggests that the two-flux method is not sufficiently accurate to permit its application to the prediction of radiant transfer in practical systems.

Spalding⁴⁸ extended the 1-D formulation to two and three dimensions by formulating the four- and six-flux models. Extensions of the two-flux model to multi-flux and nongrey emitting absorbing media are also discussed by Siddall.⁴⁹ The four-flux model applied to an axisymmetric combustor underestimated wall radiation fluxes, although temperature predictions were reasonable.⁵⁰

The reasons for the inaccuracies in these flux methods are (a) the radiant flux is divided into too few directions (2, 4, or 6 being small for many applications or (b) the fluxes in the different directions are unrealistically independent of each other. Another limitation of the flux models is that their extension to general curvilinear coordinates for handling complex geometries is rather cumbersome.

3.6.1.1 The Six-Flux Model Used at Garrett

A six-flux radiation model based on the Schuster-Hamaker approximation⁴⁷ is used currently at Garrett. It should be noted that, as pointed out by Siddall⁴⁹, other flux model approximations such as Milne-Eddington and Schuster-Schwarzschild can be represented by the same form of flux equations with constants being different.

The differential equations describing the variations of the fluxes along six directions can be reduced to the following three second-order ordinary differential equations:

$$\frac{d}{dx} \left(\frac{1}{a+s} \frac{dR^X}{dx} \right) = a(R^X - E) + \frac{s}{3} (2R^X - R^r - R^Z) \quad (129a)$$

$$\frac{1}{r} \frac{d}{dr} \left(\frac{r}{a+s+\frac{1}{r}} \frac{dR^r}{dr} \right) = a(R^r - E) + \frac{s}{3} (2R^r - R^X - R^Z) \quad (129b)$$

$$\frac{1}{r} \frac{d}{d\theta} \left(\frac{1}{a+s} \frac{dR^Z}{r d\theta} \right) = a(R^Z - E) + \frac{s}{3} (2R^Z - R^X - R^r) \quad (129c)$$

Where the composite-fluxes R^x , R^r and R^z are defined as

$$R^x = \frac{1}{2} (I_{x+} + I_{x-})$$

$$R^r = \frac{1}{2} (I_{r+} + I_{r-})$$

$$R^z = \frac{1}{2} (I_{\theta+} + I_{\theta-})$$

where I_{x+} , I_{r+} and $I_{\theta+}$ are the fluxes along the positive directions of axial, radial, and circumferential directions, respectively; I_{x-} , I_{r-} , and $I_{\theta-}$ are the corresponding fluxes along the negative directions.

a = absorption coefficient, defined as radiation absorbed per unit length

s = scattering coefficient, defined as radiation scattered per unit length

E = black body emissive power = σT^4

σ = the Stefan-Boltzman constant.

3.6.2 Discrete Transfer Method

Lockwood and Shah⁵¹ have presented a method called the discrete transfer method. This method is based on the solution of representatively directed beams of radiation within the combustor, as in the Monte Carlo method. However, in this method the directions of the rays are specified in advance and they are solved for only between two boundary walls contrary to the Monte Carlo method where the ray directions are specified at random and the rays are tracked to extinction. Lockwood and Shah have shown that this

method closely reproduces the analytical solution for radiation between parallel plates (1-D case), radiation in a square enclosure (2-D), and in a cubic enclosure (3-D). The conventional two-, four-, and six-flux models for these cases show larger errors. This new method is economical, geometrically adaptable, provides ease of application, and has the possibility of obtaining any degree of precision (through the specification of number of rays). The method is designed to be coupled to fluid flow solutions. GTEC has used this method in its 2-D combustor program.

3.6.3 Radiation Properties

The contributors to radiation fluxes in gas turbine combustors are: soot, CO_2 , H_2O (vapor), inorganic particles, etc. Only the influence of soot, CO_2 , and H_2O (vapor) is discussed here. Although CO and unburned C_xH_y contribute to emission and attenuation of radiation within flames, these contributions are localized and of secondary importance for computing radiative fluxes. The contributions of NO_x and SO_2 can be neglected because of their low concentrations.

The radiation properties of the principal radiating species including soot, CO_2 , and H_2O are significantly nongrey. Consequently, the calculation of the radiation properties is a time-consuming task. However, detailed spectral calculations are unnecessary since approximate calculations (by means of curve fits) are more convenient and provide good accuracy.⁵² Garrett has employed the approximate curve-fit procedure for the calculation of radiation properties under NASA Contract NAS3-22542.¹⁴

The absorptivity (α) of the gas-soot mixture includes the soot absorptivity, the absorptivity due to the absorption bands of CO_2 , and H_2O and corrections for the overlapping of bands.

Using the spectral data,⁵³ the gas absorptivity is calculated by taking a summation over the absorption bands of CO₂ and H₂O. In the approximate calculation method adopted by Garrett, a simpler approach is used. The gas absorptivity, α_g is written as⁵⁴

$$\alpha_g \epsilon_g (T/T_s)^{(0.6-0.2\zeta)}$$

where $\zeta = P_w / (P_w + P_c)$

ϵ_g = gas emissivity at a temperature T and path length LT_s/T

P_c, P_w = partial pressure of CO₂ and H₂O

$$\epsilon_g = \epsilon_c + \epsilon_w - \Delta\epsilon_{cw}$$

where

ϵ_c, ϵ_w = emissivities of CO₂ and H₂O

$\Delta\epsilon_{cw}$ = overlap correction factor.

ϵ_g can be computed using a temperature adjusted version of Leckner's⁵⁵ approximate overlap correction $\Delta\epsilon_{cw}$, and approximating ϵ_c and ϵ_w by curve fits of P_c, P_w, T and path length to spectral calculations. In the range of interest in gas-turbine combustors, such calculations agree to within 5 percent of the spectral calculations and the experimental results. The absorptivity (α) of the gas-soot mixture is given by

$$\alpha = \alpha_s + \alpha_g - \alpha_s \alpha_g$$

With α_g obtained above, it remains to determine α_s , the soot absorptivity. This is obtained by the method of Felske and Tien.⁵⁶ This method assumes that the complex refractive index of soot is independent of wavelength and that the soot particle diameter is small compared to the wavelength of radiation, so that scattering is negligible. The spectrally integrated absorptivity can then be written in a closed-form expression to determine α_s .

By using the radiative property calculations of the type described above, Sarofim⁵⁷ indicated that radiation calculations can be made with fair confidence, and that the major source of uncertainty in such calculations is soot concentration, rather than gas-radiation properties.

SECTION IV

4.0 DESCRIPTION OF THE COMPUTATIONAL SCHEME

The governing differential equations described in Section 3.0 are nonlinear and coupled partial differential equations. In most practical situations, it is not possible to obtain analytical solutions to these equations and numerical methods have to be used. A description of the numerical scheme used in the CPM is provided in Paragraph 4.1. The treatment of the boundary conditions is given in Paragraph 4.2, and the criteria for convergence and the method for assessing grid independence are outlined in Paragraph 4.2.

4.1 Description of the Numerical Method

The numerical method used in the CPM's are based upon the finite difference technique of Patankar,⁵⁸ which used the Semi-Implicit Method for Pressure Linked Equation (SIMPLE) algorithm. The features of this computational procedure include the following:

- o Solution of a sufficiently general single form of differential equations
- o Provision for use with different physical models
- o Use of pressure and velocities as the main hydrodynamic variables
- o Use of the pressure-correction technique
- o Use of nonuniformly spaced grids
- o Use of staggered storage locations

- o Derivation of finite-difference equations by integrating the differential equations over finite control volumes
- o Line-by-line solution of the difference equations

The finite-difference equations are derived for a box-shaped flow domain. Over the region of interest, a number of grid planes parallel to the two coordinates are placed. For each grid node, the finite-difference equations are set up for each of the flow variables to be solved. Since the governing equations for axial- and radial-velocities (Equation 1) contain pressure gradient terms, these two variables are solved along planes staggered with respect to the main grid planes described above.

A typical grid node spacing for a general flow problem is shown in Figure 4.1-1. Finite-difference equations for a node are obtained by integrating the differential equations over a control volume enclosing a grid node. For evaluating the convection and diffusion fluxes through a control volume face, a linear variation (in the direction normal to the face) of the flow properties is assumed. For other purposes, a stepwise variation with discontinuities at control-volume boundaries is assumed. Net rate of flow of ϕ into the control volume around a node P (Figure 4.1-1) by convection and diffusion in the x-direction is

$$\begin{aligned}
 & [T_{X-} + (1 - f_{X-}) L_{X-}] \phi_{X-} + [T_{X+} - f_{X+} L_{X+}] \phi_{X+} \\
 & - [T_{X-} - f_{X-} L_{X-} + T_{X+} + (1 - f_{X+}) L_{X+}] \phi_P
 \end{aligned}
 \tag{130}$$

where

$$T_X = \Gamma_{\text{eff},\phi} A_X / \delta X$$

$$L_X = \dot{m}_X''/\delta X$$

$$A_X = 0.5(r_+ + r_-)\Delta Y$$

Defining $\iiint S_\phi dV = S_u + S_p \phi_p$, the one-dimensional transport equation for the variable becomes

$$\begin{aligned} & [T_{X-} + (1 - f_{X-})L_{X-} + T_{X+} - f_{X+}L_{X+} - S_p] \phi_p \\ & = [T_{X-} + (1 - f_{X-})L_{X-}] \phi_{X-} + [T_{X+} - f_{X+}L_{X+}] \phi_{X+} + S_u \end{aligned}$$

(131)

The linear-profile assumption becomes unacceptable when $f_{X+} L_{X+}$ is large compared with T_{X+} because with weighting factor $(T_{X+} - f_{X+} L_{X+})$ then becomes negative, implying an unrealistic physical process through which raising the value of ϕ_{X+} could lower the value of ϕ_p . Therefore, it is assumed that if the convective flow rates (L) are large compared to the diffusion coefficients (T), the diffusion across the control-volume face is zero and the value of convected is equal to the value at the node on the upwind side of the face. With this assumption, the coefficient $T_{X+} - f_{X+} L_{X+}$ is replaced by $T_{X+}^* - F_{X+} L_{X+}$ where

$$T_{X+}^* = [T_{X+}, -(1 - f_{X+})L_{X+}, f_{X+}L_{X+}]$$

Here $[a_1, a_2, a_3]$ stands for the largest of the three quantities $a_1, a_2,$ and a_3 .

Using a similar procedure for the fluxes in the radial direction, the final finite-difference equation is reduced to

$$A_p \phi_p = A_{X+} \phi_{X+} + A_{X-} \phi_{X-} + A_{Y+} \phi_{Y+} + A_{Y-} \phi_{Y-} + S_u$$

(132)

The solution of the above equation is obtained by line-by-line relaxation using an efficient tri-diagonal matrix algorithm. By this method, a traverse along one direction, for example, the X-direction, is made with old values for the y-direction nodes. Using this solution as the best estimate, the y-direction is then traversed. The solution method adopted is based on the SIMPLE algorithm of Patankar and Spalding as described in Reference 15.

ORIGINAL PAGE IS
OF POOR QUALITY

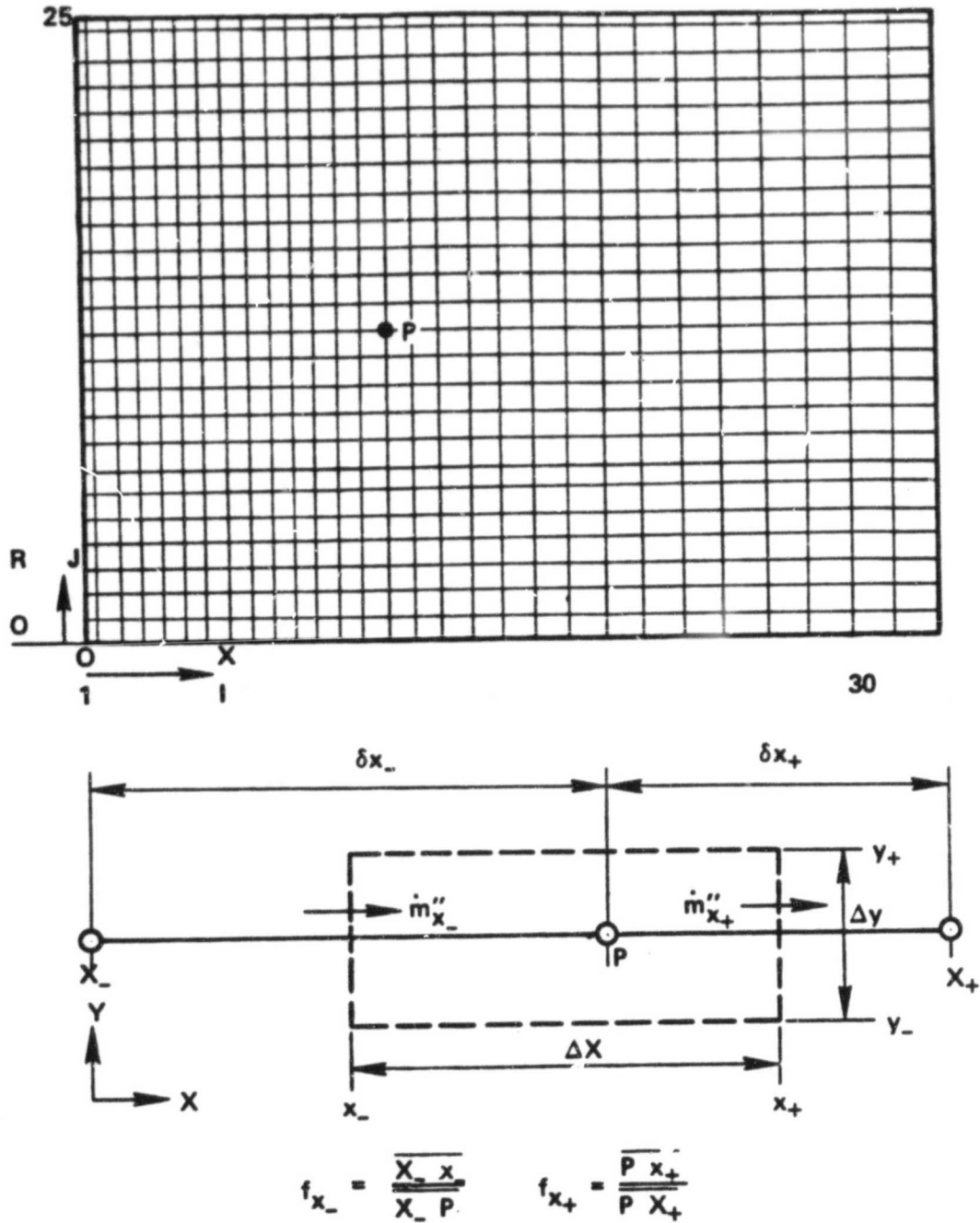


Figure 4.1-1. Typical Grid Spacing of the Swirling Flow Problem and Control Value around a Point P.

4.2 Boundary Conditions

The boundary conditions are enforced by appropriately modifying the finite-difference coefficients at the first interior point adjacent to the boundary. For the inlet boundaries, the velocity components, density, and turbulence profiles are either experimentally known or estimated. At the inlet boundary, if pressure is specified, the pressure correction is set to zero. When the normal velocities at the boundary point are specified, the coefficients in the pressure correction are modified in such a way that the mass fluxes through the control volume satisfy the overall continuity equation.

For boundaries of the second kind, where gradients and not the values of the variables are specified, the program uses one of the following two approaches. In the first approach, the boundary value is guessed and continually updated to satisfy the given gradient condition. The second approach breaks the link through the boundary to all adjoining external control volumes by first arranging for the finite-difference coefficient connecting the boundary node to an internal node to be zero, and then inserting the correct flux at the boundary as a source of diffusion and/or convection for that internal node.

At the symmetry plane, the convection and diffusion fluxes in the radial direction are zero. Therefore, the finite-difference coefficients containing these fluxes are set to zero at the axis of symmetry. For the exit plane, information about some of the variables is not available. However, since it is the process occurring in the calculation domain that decides values of the variables that the outgoing fluid will carry, there is no need for information at such boundaries. These boundaries are simply treated by neglecting the diffusion at the exit boundary.

Boundary conditions at the near-wall nodes are treated in the manner outlined in Section 3.0 (Equations 7 through 9).

The input parameters depend upon the nature of flow problem computed. In many of the test cases, initial profiles of turbulence kinetic energy (k) and length scales (L) are not available. For these cases, uniform profiles of k and L are prescribed at the inlet and the default values used are

$$k = 0.003 U_{av}^2$$

$$L = 0.02 R_{max}$$

where, U_{av} is the average inlet velocity, and R_{max} is the maximum cross-stream dimension of the flow geometry. If information about turbulence intensity levels is available at the inlet, appropriate uniform k values are used at the inlet.

4.3 Convergence Criteria

The solution is accepted as the converged solution when the total mass source error is less than about 0.1 percent of the total mass flow rate. For all the test cases, the computations were carried out further to ensure that the profiles of the dependent variables did not appreciably change. For all the test cases considered in this program, when the solution converged to the acceptable limit of 0.001 on the total mass source error, the maximum mass source error in the computational domain was less than 0.0002. The number of iterations required to reach the acceptable convergence level varied from problem to problem. In most of the recirculating flows, a minimum of 350 iterations were needed to reach the convergence criterion.

During the computations, the values of each dependent variable are monitored to ensure that the maximum change in the value of each dependent variable is a small fraction of the reference value. When this condition is satisfied, and if the total mass source error is less than 0.1 percent, plots of all the variables of interest are obtained. Computations are then continued for another 50 iterations and plots are obtained again. If these plots are identical to within graphical accuracy, the solutions are accepted as converged solutions.

The numerical solution obtained for any given flow problem depends upon the grid density and grid distributions. The solutions are accepted as grid independent if the predicted results are essentially invariant when the grid density or the grid distributions are changed. This type of test was performed for many of the test cases, but these test results will be presented only for a few of them. For the other cases, the predictions presented in this report are essentially grid independent. The details about the grid distributions for each test case will be provided along with the discussion of the results.

SECTION V

5.0 DATA BASE FOR BENCHMARK QUALITY TEST CASES

To assess and critique the current models and generate a program plan to improve their accuracy and usefulness as a combustor design tool, the assessment of the models was conducted in the following two interrelated steps:

- o Assess and critique the physical submodels involving the fundamental processes of combustion, individually, with data from ideal element tests under well-defined conditions. The physical submodels considered here are turbulence modeling, gaseous fuel combustion, spray evaporation and combustion, soot formation and oxidation, and radiation modeling.

- o Assess and critique the model predictions against the data from advanced gas turbine combustors.

Accordingly, the data base is arranged in two sections: Paragraph 5.1 includes a description of the data base from ideal element tests and Paragraph 5.2 contains a description of the data from a number of gas turbine combustors.

5.1 Data Base from Ideal Element Tests

A literature survey of recently published work (generally 1970 or later) was conducted to compile a data base necessary for a benchmark quality test case. Published literature related to the following submodels was reviewed:

- o Turbulence Modeling
- o Gaseous Fuel Combustion
- o Spray Evaporation and Combustion
- o Soot Formation and Oxidation

In the following paragraphs, a data base from ideal element tests is provided. The ideal tests range from simple entrance flows in pipes and 2-D channels to more complex flows like the flow fields behind steps, blockages, and swirling recirculating flows. These tests are intended to encompass the range of complexities involved in combustor internal flows. Simple entrance flows are included in the validation efforts to ensure that the analytical models can be used to predict simple flows without any modification to the model. The data base selected has fairly detailed measurements, including turbulence parameter measurements, with estimations on errors.

5.1.1 Turbulence Modeling

In this paragraph, a data base for assessing turbulence models is provided. The assessment procedure for the $k-\epsilon$ turbulence models will consist of comparing the predicted time-mean velocity components with the corresponding measurements. For the algebraic and full Reynolds stress models, the predictions of the turbulence intensities and cross correlations will also be compared with the measurements. Some cases involving scalar transport are also considered, and these involve predictions of the concentration of a trace gas (inert) or temperature under heated but inert conditions.

The references reported in the following tables provide information about the available measurements reported in the literature.

These references were selected based upon the extent and accuracy of the data and the nature of the geometry of test conditions. The references selected are presented in the form of increasing order of complexity of the flow field in the form:

- o Simple Flows (Boundary Layers, Jets, Mixing Layers, etc.) (2-D Parabolic) - Table 3
- o Streamline Curvature Effects (Curved Ducts, Curved Boundary Layers, etc.) (2-D Parabolic) - Table 4
- o Recirculating Flows (Nonswirling) (Both Unconfined and Confined) (2-D Elliptic) - Table 5
- o Swirling Flows (With and Without Recirculation) (2-D Elliptic/2-D Parabolic) - Table 6
- o Scalar Transport - Table 7.

From the references provided in these tables, benchmark test cases were selected, as described in Sections 6.0, 7.0 and 8.0. These cases were used to evaluate the turbulence and kinetic model predictions.

TABLE 3. SIMPLE FLOWS.

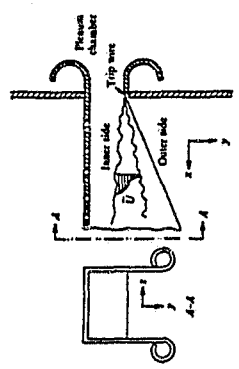
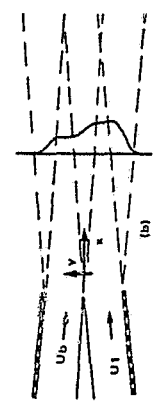
CASE	GEOMETRY AND MEASUREMENT TECHNIQUES	NUMBER OF TEST CASES	NUMBER OF MEASUREMENT LOCATIONS							REMARKS
			MEAN VELOCITY		TURBULENCE PROFILES				INITIAL CONDITIONS	
			U	V or W	u'^2	v'^2	w'^2	uv'		
CHAMPAGNE F.H. PAO, Y.H. WYGMANSKI L.J. (1976) REF. 59	 <p>2-D MIXING REGION</p> <p>HOT WIRE ANEMOMETERS (2-D PARABOLIC)</p>	1	3		3	1				PROBABILITY DENSITY FUNCTIONS OF u', v', w' . FLOW FIELD IS UNCONFINED.
SAIV M. AND PEERLESS S.J. (1978) REF. 60 SECTION 6.6	 <p>TWO STREAM MIXING LAYER</p> <p>HOT WIRE & PITOT TUBE (2-D PARABOLIC)</p>	2	5		3	3	3	3	3	$q^2 = \frac{1}{2}(u'^2 + v'^2 + w'^2)$ UNCONFINED FLOW.
BIRNGEN S. (1975) REF. 61										

TABLE 3. SIMPLE FLOWS (CONTD).

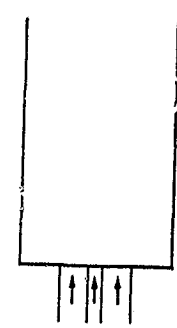
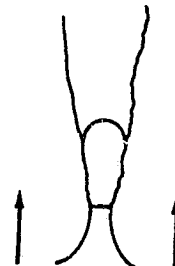
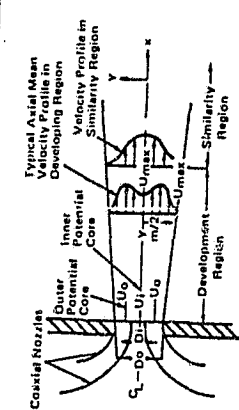
CASE	AUTHOR (YEAR)	GEOMETRY AND MEASUREMENT TECHNIQUES	NUMBER OF TEST CASES	NUMBER OF MEASUREMENT LOCATIONS							REMARKS
				MEAN VELOCITY		TURBULENCE PROFILES				INITIAL CONDI- TIONS	
				U	V OF W	$\overline{u'^2}$	$\overline{v'^2}$	$\overline{w'^2}$	$\overline{u'v'}$		
HABIB, M.A. AND WHITELAW, J.H. (1979) REF. 62	 <p>CONFINED COAXIAL JET</p> <p>DISA SINGLE HOT WIRE PROBES (2-D ELLIPTIC)</p>	2	4	4	4	4	4	4	4	FULLY DEV PIPE	FLOW FIELD HAS RECIRCULATION REGIONS
SMITH, D.J. AND HUGHES (1977) REF. 63	 <p>JET INTO COFLOWING FREE STREAM</p> <p>HOT WIRE (2-D PARABOLIC)</p>	3	5	5	5	5	5	5	5		FLOW IS UNCONFINED
CHAMPAGNE F.H. & WYGNANSKI I.J. (1970) REF. 64 SECTION 6.7	 <p>Typical Axial Mean Velocity Profile in Developing Region</p> <p>Velocity Profile in Similarity Region</p> <p>Development Region</p> <p>Similarity Region</p> <p>Outer Potential Core</p> <p>Insect Core</p> <p>Potential Core</p> <p>Hot Wire</p> <p>Development Region</p> <p>Similarity Region</p> <p>Hot Wire (2-D PARABOLIC)</p>	3	8	8	8	8	8	8	8	WELL DEFINED	ORIGINAL PAGE IS OF POOR QUALITY

TABLE 3. SIMPLE FLOWS (CONTD).

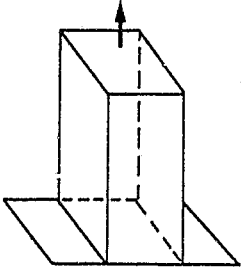
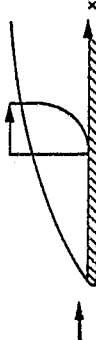
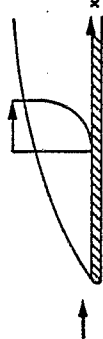
CASE	AUTHOR (YEAR)	GEOMETRY AND MEASUREMENT TECHNIQUES	NUMBER OF TEST CASES	NUMBER OF MEASUREMENT LOCATIONS						REMARKS		
				MEAN VELOCITY		TURBULENCE PROFILES					INITIAL CONDITIONS	
				\bar{u}	\bar{v} or \bar{w}	\bar{u}^2	\bar{v}^2	\bar{w}^2	$\overline{u'v'}$	OTHERS		
	EMERY, A.F. AND GESSNER, F.B. (1976) REF. 65 SECTION 6.3	DEVELOPING DUCT FLOW  (2-D PARABOLIC)	2	7						MIXING LENGTH		
	WIEGHARDT, K. AND TILLMANN, W. (1944) REF. 66	 MEASUREMENTS USING A RAKE OF PRESSURE PROBES. (2-D PARABOLIC)	1	23						CLASSIFIER PLOTS	TURBULENCE INTENSITY .25%	
	WATTS, K.C. AND BRUNDRETT, E. (1979) REF. 67 SECTION 6.1	 HOT WIRE (2-D PARABOLIC)	36	8								
									8			DATA INCLUDE COMPUTED VALUES OF BOUNDARY LAYER INTEGRAL PARAMETERS CASE #612 OF STANFORD CONFERENCE
												DATA INCLUDES 1 CASE WITH NO SUCTION. ALL OTHER CASES HAVE SUCTION

TABLE 3. SIMPLE FLOWS (CONTD).

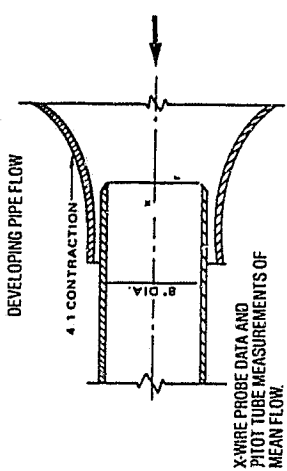
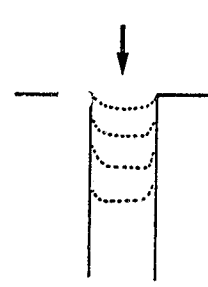
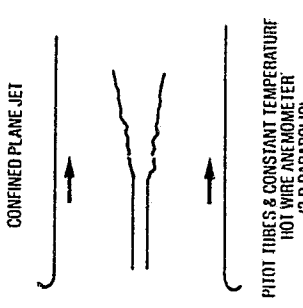
CASE	GEOMETRY AND MEASUREMENT TECHNIQUES	NUMBER OF TEST CASES	NUMBER OF MEASUREMENT LOCATIONS							REMARKS	
			MEAN VELOCITY		TURBULENCE PROFILES						INITIAL CONDITIONS
AUTHOR (YEAR)			\bar{u}	\bar{v} or \bar{w}	\bar{u}^2	\bar{v}^2	\bar{w}^2	$\overline{u'v'}$	$\overline{u'w'}$		
BARBIN, A.R. & JONES, J.B. (1963) REF. 23 SECTION 6.4	 <p>DEVELOPING PIPE FLOW 4:1 CONTRACTION X-WIRE PROBE DATA AND PITOT TUBE MEASUREMENTS OF MEAN FLOW. (2-D PARABOLIC)</p>	1	5		5		5			UNIFORM VELOCITY	
LAWS, E.M., LIM, E.H., LIVESY, J.L. (1979) REF. 59	 <p>DEVELOPING PIPE FLOW (2-D PARABOLIC)</p>	3	29	29	29	29	29	29		WELL DEFINED	PRESENTED FOR EVALUATION OF THE TURBULENCE MODELS
EVERITT, K.W. AND ROBINS, A.C. (1976) REF. 70	 <p>CONFINED PLANE JET PILOT TUBES & CONSTANT TEMPERATURE HOT WIRE ANEMOMETER (2-D PARABOLIC)</p>	2	1		1	1	1	1	1	FULLY DEV	JET ISSUES INTO MOVING STREAM

TABLE 3. SIMPLE FLOWS (CONTD).

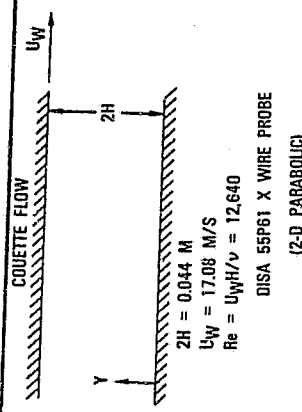
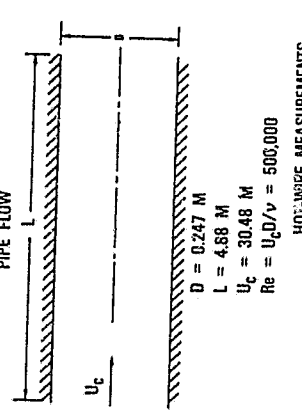
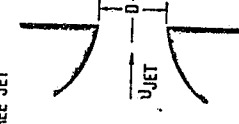
CASE	AUTHOR (YEAR)	GEOMETRY AND MEASUREMENT TECHNIQUES	NUMBER OF TEST CASES	NUMBER OF MEASUREMENT LOCATIONS										REMARKS
				MEAN VELOCITY		TURBULENCE PROFILES					INITIAL CONDITIONS			
				U	V	U ²	V ²	W ²	U'V'	OTHEREES				
EL TELBÁNY, M.M-M AND REYNOLDS, A.J. (1982) REF. 208 SECTION 6.2	 <p>COUETTE FLOW</p> <p>$2H = 0.044 \text{ M}$ $U_w = 17.08 \text{ M/S}$ $Re = U_w H / \nu = 12,640$ DISA 55P61 X WIRE PROBE (2-D PARABOLIC)</p>	4	1	1	1	1	1	1	1	1	1	FULLY DEV FLOW		
LAUFER, J. (1953) REF. 209 SECTION 6.5	 <p>FULLY DEVELOPED PIPE FLOW</p> <p>$D = 0.247 \text{ M}$ $L = 4.88 \text{ M}$ $U_c = 30.48 \text{ M}$ $Re = U_c D / \nu = 500,000$ HOT-WIRE MEASUREMENTS (2-D PARABOLIC)</p>	2	1	1	1	1	1	1	1	1	1	PLUG FLOW INLET CONDITIONS	PRE-SURE SKEWNESS, FLATNESS, ENERGY SPECTRA	
WYGNAŃSKI, L. AND FIEDLER, H. (1969) REF. 210 SECTION 6.8	 <p>ASYMMETRIC FREE JET</p> <p>DISA HOT-WIRE ANEMOMETER (2-D PARABOLIC)</p> <p>$D = 0.0284 \text{ M}$ $U_{JET} = 51 \text{ M/S}$ $T_{JET} = 300^\circ \text{ K}$</p>	1	5	4	3	3	3	3	3	3	3	TRIPLE CORRELATIONS, SKEWNESS, FLATNESS, INTERMITTENCY AND INTEGRAL SCALES	WELL DEFINED AT X/D = 40	

TABLE 4. STREAMLINE CURVATURE EFFECTS.

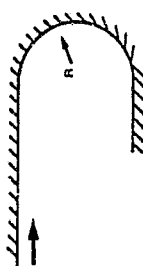
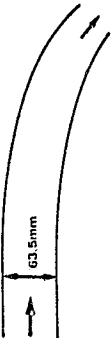

CASE	AUTHOR (YEAR)	GEOMETRY AND MEASUREMENT TECHNIQUES	NUMBER OF TEST CASES	NUMBER OF MEASUREMENT LOCATIONS						REMARKS		
				MEAN VELOCITY		TURBULENCE PROFILES					INITIAL CONDITIONS	
				U	V	W	U ²	V ²	W ²	U'V'	OTHERS	
	A PRABHU AND B.N.S. RAU (1981) REF. 71	 <p>HOT WIRE PROBE MEASUREMENTS IN THE BOUNDARY LAYER IN THE BOUNDARY LAYER $Re/\delta = 1480 - 5990$; $\delta =$ MOMENTUM THICKNESS (2-D PARABOLIC)</p>	3	6			6			6		NO SIMILARITY LAW APPLICABLE. FLOW IS PARABOLIC. STREAMLINE CURVATURE EFFECT IS LARGE - MOSTLY DUE TO THE INFLUENCE OF TAYLOR-GORTLER VORTICITY.
	I.A. HUNT AND P.N. JOURLIT (1979) REF. 72	 <p>$Re = 30,000, 60,000 \& 130,000$ HOT WIRE PROBE MEASUREMENTS (2-D PARABOLIC)</p>	3	7	7	7	7	7	7	7	SPECTRAL DATA	POSSIBLE 3-DIMENSIONALITY OF FLOW FIELD DUE TO SMALL DUCT HEIGHT.
	J.R. SCHULTZ (1976) REF. 73	 <p>PRESSURE PROBE AND TRACER GAS CONCENTRATION (C) MAPPING. $C_1 = CRAYA - CURTET NUMBER$ $C_1 = 1 + (M_2/M_1) \cdot (M_2^2/M_1^2 + 1/2)^{1/2}$ (2-D ELLIPTIC)</p>	C_1 0.127 0.15 0.208	7 6								FLOW IS RECIRCULATING. $U_2 \sim 0.02 - 0.075 U_1$

TABLE 4. STREAMLINE CURVATURE EFFECTS (CONTD).

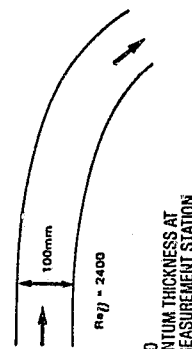
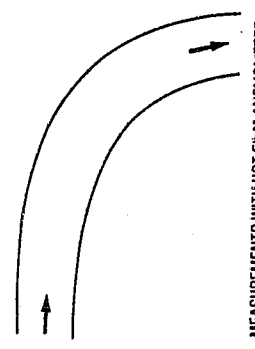
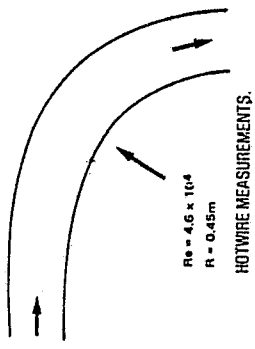
CASE	AUTHOR (YEAR)	GEOMETRY AND MEASUREMENT TECHNIQUES	NUMBER OF TEST CASES	NUMBER OF MEASUREMENT LOCATIONS						REMARKS		
				MEAN VELOCITY		TURBULENCE PROFILES					INITIAL CONDITIONS	
				U	V	W	U ²	V ²	W ²	UV	OTHERS	
	B.G. SHIVAPRASAD AND B.R. RAMAPRIYAN (1970) REF. 74 SECTION 7.1	 <p>100mm $Re(D) = 2400$ $D =$ MOMENTUM THICKNESS AT THE FIRST MEASUREMENT STATION. MEASUREMENTS USING X-WIRE. (2-D PARABOLIC)</p>	1	6	6	6	6	6	6	6	PRODUCTION OF K	NO OBSERVABLE 3-DIMENSIONALITY. GOOD ESTIMATES OF ERROR BANDS, AND ρ_{EFF} .
	A.H. JEANS AND J.P. JOHNSTON (1982) REF. 75	 <p>MEASUREMENTS WITH HOT FILM ANEMOMETER. (2-D PARABOLIC)</p>	1	4			4					CLAUSER PLOTS AND FLOW VISUALIZATION DATA AVAILABLE.
	J. GILLIS AND J.P. JOHNSTON (1980) REF. 76	 <p>$Re = 4.6 \times 10^4$ $R = 0.45m$ HOTWIRE MEASUREMENTS. (2-D PARABOLIC)</p>	1	11			12	12	12	12		CLAUSER PLOTS AVAILABLE. STRONG CURVATURE EFFECTS WITH RECOVERY. AT $x = 0.1$

TABLE 5. RECIRCULATING FLOWS.

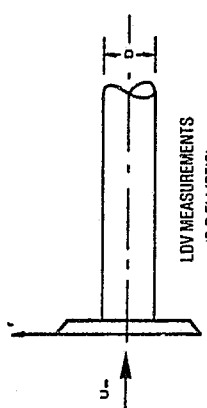
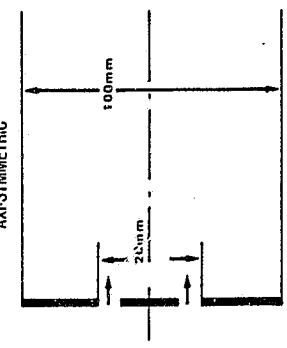
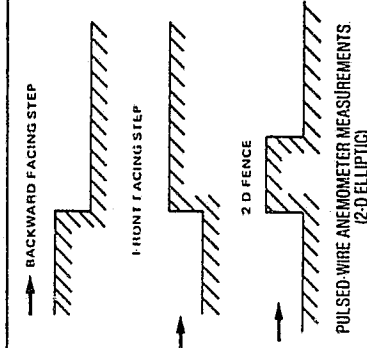
CASE	GEOMETRY AND MEASUREMENT TECHNIQUES	NUMBER OF TEST CASES	NUMBER OF MEASUREMENT LOCATIONS					REMARKS	
			MEAN VELOCITY		TURBULENCE PROFILES				INITIAL CONDITIONS
			U	V or W	u'^2	w'^2	uv'		
R. SMYTH (1979) REF. 77	 LDV MEASUREMENTS (2-D ELLIPTIC)	1	16	(V) 16	16	16		ALL THE DATA AT X/D = -.05	PROFILES ARE GIVEN AT X D = -0.333, -0.167, -0.083, 0, 0.2, 0.4, 0.6, 0.8, 1.0, 1.2, 1.4, 1.6, 1.8, 2.0 and 2.2. UNCERTAINTY ESTIMATES PROVIDED. UNCONFINED FLOW.
D.F.G. DURAO AND J.H. WHELAN (1978) REF. 78	 AXI-SYMMETRIC LDA MEASUREMENTS (2-D ELLIPTIC)	4 CASES WITH $Re_{Dh} =$ 3500 - 28,300	7	7	6	6	6	5	TURBULENCE IS ANISOTROPIC. GRADIENT DIFFUSION DOES NOT APPEAR TO BE ACCURATE, SINCE LOCATION OF ZERO SHEAR STRESS DOES NOT COINCIDE WITH LOCATION OF ZERO VELOCITY GRADIENT.
W.D. MOSS AND S. BAKER (1980) REF. 79	 PULSED-WIRE ANEMOMETER MEASUREMENTS (2-D ELLIPTIC)	1 1 1	9 19 28		11 16 25				FLOW IS UNCONFINED, NOT AS DETAILED AS THE STANDARD DATA, BUT MORE CONFIGURATIONS ARE STUDIED.

TABLE 5. RECIRCULATING FLOWS (CONTD).

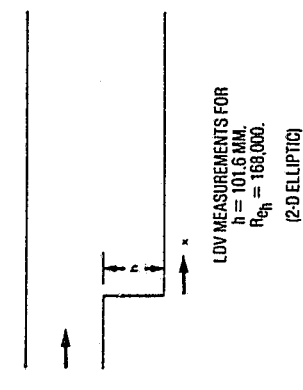
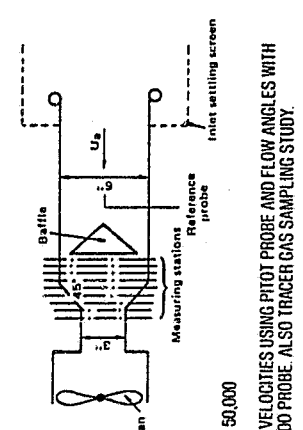
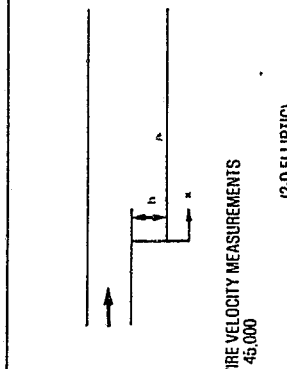
CASE	GEOMETRY AND MEASUREMENT TECHNIQUES	NUMBER OF TEST CASES	NUMBER OF MEASUREMENT LOCATIONS						REMARKS		
			MEAN VELOCITY		TURBULENCE PROFILES					INITIAL CONDITIONS	
AUTHOR (YEAR)			U	V	W	U ²	V ²	W ²	U'V'	OTHERS	
R. BREMMER, H.D. THOMPSON AND WH. STEVENSON (1980) REF. 80	 <p>LDV MEASUREMENTS FOR $h = 101.6 \text{ MM.}$ $Re_h = 168,000.$ (2-D ELLIPTIC)</p>	1	5	3	5	5	5	5			UNCERTAINTY ABOUT FLOW STEADINESS AND THREE DIMENSIONALITY. THE AMOUNT OF DATA IS LIMITED COMPARED TO STANFORD WORK.
W.H. SCHOFIELD AND T.S. KEEBLE (1974) REF. 81	 <p>$Re_D = 50,000$ MEAN VELOCITIES USING PITOT PROBE AND FLOW ANGLES WITH RICARDO PROBE. ALSO TRACER GAS SAMPLING STUDY. (2-D ELLIPTIC)</p>	1	9							c	SIMILARITY PROFILES FOR \bar{u} AND TRACER GAS CONCENTRATIONS
J. KIM, S.J. KLINE AND J.P. JOHNSTON (1978) REF. 82 SECTION 7.2	 <p>HOT WIRE VELOCITY MEASUREMENTS $Re_h = 45,000$ (2-D ELLIPTIC)</p>	1	13								DOCUMENTATION IN REATTACHED LAYER IS GOOD. PRESSURE DISTRIBUTION ON UPPER AND LOWER WALLS AVAILABLE.

TABLE 5. RECIRCULATING FLOWS (CONTD).

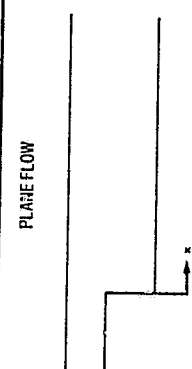
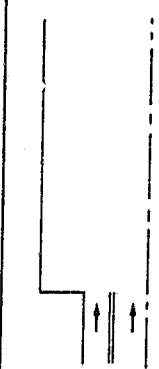
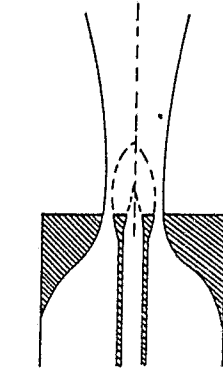
CASE	AUTHOR (YEAR)	GEOMETRY AND MEASUREMENT TECHNIQUES	NUMBER OF TEST CASES	NUMBER OF MEASUREMENT LOCATIONS							REMARKS			
				MEAN VELOCITY		TURBULENCE PROFILES				INITIAL CONDI- TIONS				
				U	V	W	u'^2	v'^2	w'^2	uv'	OTHERS			
J.K. EATON AND J.P. JOHNSTON (1980) REF. 83 SECTION 7.2		<p>PLANE FLOW</p>  <p>PULSED WIRE ANEMOMETER (2-D ELLIPTIC)</p> <p>(l) IS THE MOMENTUM THICKNESS</p>	$Re_{\theta} =$ 240 510 850	9			9					WELL-DEFINED	CONTINUATION OF EFFORT BY KIM, ET. AL.	
F.K. OWEN (1976) REF. 84		 <p>$Re_{\theta} = 150,000$</p> <p>LDV MEASUREMENTS, COAXIAL JETS (2-D ELLIPTIC)</p>	1	5	3		1	1		1			DATA IS VERY LIMITED.	
N.A. CHIGIER AND J.M. BEER (1964) REF. 85		 <p>VELOCITY MEASUREMENTS USING PITOT TUBES (2-D ELLIPTIC)</p>		5									\bar{u} AT $x=0$ P ψ	STREAMLINE AND ISOBAR CONTOURS ARE AVAILABLE. FLOW IS UNCONFINED. ψ IS THE STREAM FUNCTION.

TABLE 5. RECIRCULATING FLOWS (CONTD).

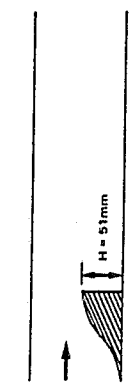
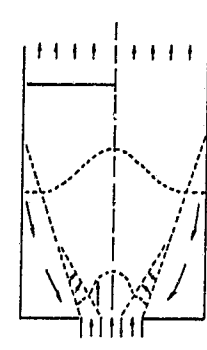
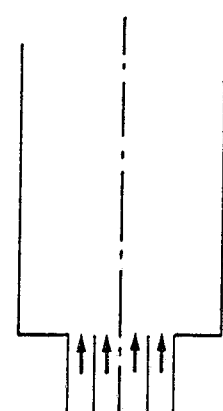
CASE	GEOMETRY AND MEASUREMENT TECHNIQUES	NUMBER OF TEST CASES	NUMBER OF MEASUREMENT LOCATIONS						REMARKS					
			MEAN VELOCITY		TURBULENCE PROFILES					INITIAL CONDI- TIONS				
AUTHOR (YEAR)			U	V	W	U ²	V ²	W ²	U'V'	U'W'	V'W'	OTHERS		
R.W. PITZ (1981) REF. 86 SECTION 7.8	 LDV MEASUREMENTS WITH AND WITHOUT CHEMICAL REACTION (2-D ELLIPTIC)	$Re_{ch} =$ $1.5 \times 10^4 =$ $2.2 \times 10^4 =$ $3.7 \times 10^4 =$	8 8 8	4		8 8 8	4					SKEW-NESS AND FLAT-NESS	U_0 U' δ'	SIZE AND MASS OF RECIRCULATION ZONE: GOOD ESTIMATES OF BIASING ERRORS. δ' = DISPLACEMENT THICKNESS
K. GURUZ AND C. ILICALLY (1981) REF. 87	 HOT WIRE MEASUREMENTS. (C_p = CRAVA-CURTET NUMBER) (2-D ELLIPTIC)	$C_p =$ 0.06 0.08 0.23	7			5	5		6					MEASURED PROFILES SHOW NO RECIRCULATION. DATA MAY BE QUESTIONABLE.
B.V. JOHNSON AND J.C. BENNETT (1981) REF. 88 SECTION 7.7	 LDV/LIF MEASUREMENTS. (2-D ELLIPTIC)	2 CASES WITH $Re =$ 15,900 AND 47,500	7			7	7	7	7			$\frac{U'}{U}$ $\frac{V'}{V}$ $\frac{W'}{W}$		WORKING FLUID IS WATER. P.D.F. SKEWNESS & FLATNESS ARE AVAILABLE.

TABLE 5. RECIRCULATING FLOWS (CONTD).

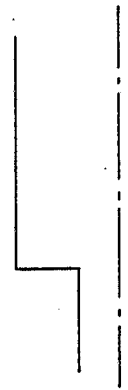
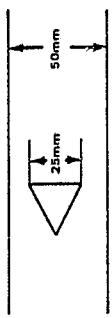
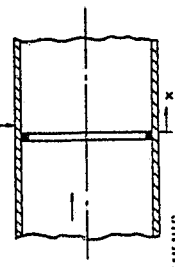
CASE	AUTHOR (YEAR)	GEOMETRY AND MEASUREMENT TECHNIQUES	NUMBER OF TEST CASES	NUMBER OF MEASUREMENT LOCATIONS						REMARKS		
				MEAN VELOCITY		TURBULENCE PROFILES					INITIAL CONDI- TIONS	
				U	V	U ²	V ²	W ²	U'V'			OTHERS
	I. F. MOON AND G. RUDINGER (1977) REF. 89 SECTION 7.3	 Re = 280,000 LDV MEASUREMENTS. (2-D ELLIPTIC)	1	6							ONLY MEAN VELOCITY PROFILES ARE REPORTED.	
	S. FUJII, M. GOMI AND K. EGUCHI (1978) REF. 90 SECTION 7.5	 LDV MEASUREMENTS AND TRACER GAS CONCENTRATION SAMPLING. (2-D ELLIPTIC)	1	9		K 4	4		ϵ & μT SKEW- NESS & FLAT- NESS OF PROBABI- LITY FUNC- TIONS	\bar{u}^2 \bar{v}^2	$\bar{u}, \bar{v}, \bar{w}, k, \epsilon$ & μT WITH BLOWING AT 4 AXIAL PLANES. SIMILARITY PROFILES FOR MEAN VELOCITY FIELD	
	P. PHATAPHRUK AND E. LOGAN (1979) REF. 91 SECTION 7.4	 HOT WIRE MEASUREMENTS Re = 50,000 (2-D ELLIPTIC)	RING CONFIGS. 9	5						5	INITIAL PROFILE WITHOUT THE RING.	$\bar{u}, \bar{v}, \bar{w}$ PROFILES AVAILABLE FOR ONE OF THE CONFIGURATIONS SOME UNCERTAINTY ABOUT ACCURACY OF DATA/OR STEADINESS OF FLOW.

TABLE 5. RECIRCULATING FLOWS (CONTD).

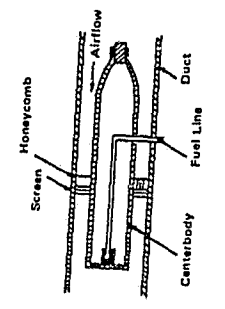
CASE	AUTHOR (YEAR)	GEOMETRY AND MEASUREMENT TECHNIQUES	NUMBER OF TEST CASES	NUMBER OF MEASUREMENT LOCATIONS						REMARKS								
				MEAN VELOCITY		TURBULENCE PROFILES					INITIAL CONDITIONS							
				U	V	U^2	V^2	W^2	OTHERS									
	M. ROQUEMORE et al. (1981) REF. 92 SECTION 7.6	 <p>LDV MEASUREMENTS BEHIND AN AXI-SYMMETRIC BODY WITH AND WITHOUT INJECTION OF INERT GAS. (2-D ELLIPTIC)</p>	4 MASS FLOW RATES.	10						10						INITIAL PROFILES ARE WELL DEFINED. AT X=-1mm		
																		ORIGINAL PAGE IS OF POOR QUALITY

TABLE 6. SWIRLING FLOWS.

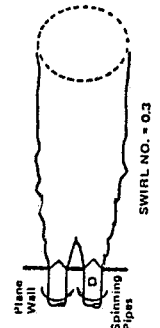
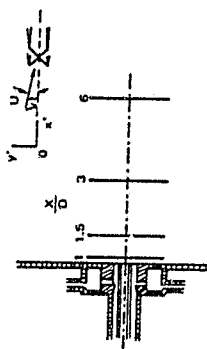
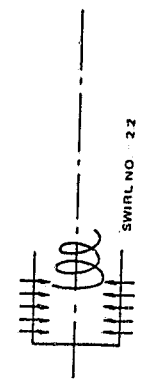
CASE	AUTHOR (YEAR)	GEOMETRY AND MEASUREMENT TECHNIQUES	NUMBER OF TEST CASES	NUMBER OF MEASUREMENT LOCATIONS							INITIAL CONDI- TIONS	REMARKS
				MEAN VELOCITY		TURBULENCE PROFILES						
				U	V or W	$\overline{u'^2}$	$\overline{v'^2}$	$\overline{w'^2}$	$\overline{uv'}$	OTHERS		
B.D. PRATTE AND J.F. KEEFER (1972) REF. 93	 <p>SWIRL INDUCED BY ROTATING PIPES SWIRL NO. = 0.3</p> <p>MEASUREMENTS WITH HOT WIRE ANEMOMETER (2-D PARABOLIC)</p>	1	6	3	3	3	3	3	3	3	UN-CONFIRMED FLOW DATA FOR U AT X/D = 1, 6, 12, 20, 30, & 44 W PROFILES AT X/D = 6, 12, & 20 V ² AT X/D = 6, 12, & 20 NO RECIRCULATION	
M. M. RIBIERO AND J. W. WHITELAW (1980) REF. 94	 <p>SWIRL NO. = 0.26</p> <p>Arrangement of coaxial jet measurement station.</p> <p>HOT WIRE MEASUREMENTS (2-D PARABOLIC)</p>	1	4	4	4	4	4	4	4	4	UN-CONFIRMED FLOW NO RECIRCULATION	
N. SYRED, J.M. BEER AND N.A. CHIGER (1971) REF. 95	 <p>TANGENTIAL PORTS</p> <p>HOT WIRE MEASUREMENTS (2-D ELLIPTIC)</p> <p>SWIRL NO. = 2.2</p>	1	7	7	7	7	7	7	7	7	DATA PRESENTED IN ISOPLETH CONTOUR PLOTS. FLOW FILED IS UN-CONFIRMED WITH RECIRCULATION. SWIRL NUMBER IS VERY HIGH.	

TABLE 6. SWIRLING FLOWS (CONTD).

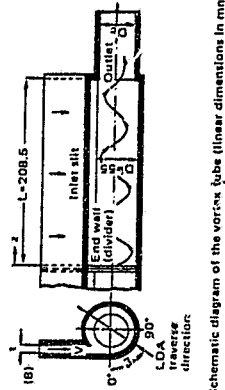
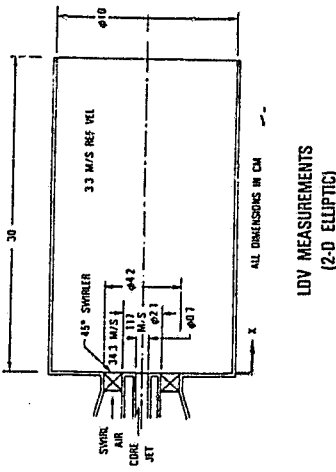
CASE	GEOMETRY AND MEASUREMENT TECHNIQUES	NUMBER OF TEST CASES	NUMBER OF MEASUREMENT LOCATIONS						REMARKS
			MEAN VELOCITY		TURBULENCE PROFILES			INITIAL CONDITIONS	
			U	V or W	$\overline{u'^2}$	$\overline{v'^2}$	$\overline{w'^2}$		
M.P. ESCUDIER, J. BORNSTEIN AND N. ZEHNDER (1980) REF. 99	 <p>L.D.A. 30° Inlet slit End wall divider Outlet</p> <p>Schematic diagram of the vortex tube (linear dimensions in mm).</p>	2	9	10	9	10	10		ANOTHER TEST CASE WITH BAFFLE AT THE EXIT OF THE TEST SECTION. INLET VELOCITIES ARE SMALL IN MAGNITUDE
ALTGED, H. JONES, W.P. AND WILHELM, J. (1983) REF. 218 SECTION 8.6	 <p>CONFIRMED SWIRL-ORBITER FLOW</p> <p>45° SWIRLER 34.3 M/S 3.3 M/S REF. VEL 1.7 M/S 10 7 ALL DIMENSIONS IN CM</p> <p>LDV MEASUREMENTS (2-D ELLIPTIC)</p>								

TABLE 6. SWIRLING FLOWS (CONTD).

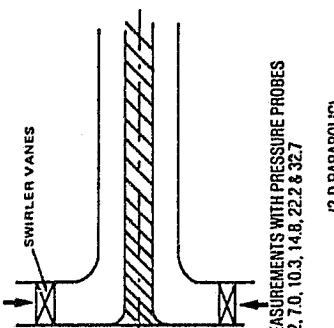
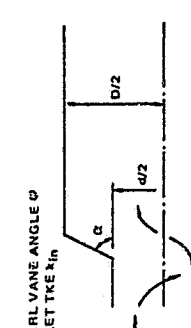
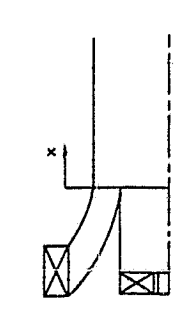
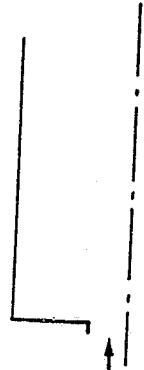
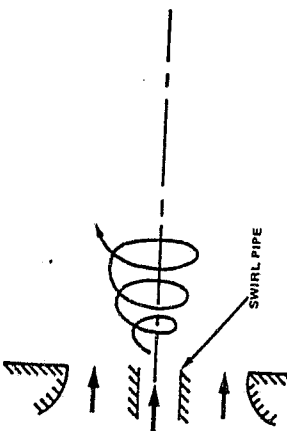
CASE	GEOMETRY AND MEASUREMENT TECHNIQUES	NUMBER OF TEST CASES	NUMBER OF MEASUREMENT LOCATIONS							REMARKS
			MEAN VELOCITY		TURBULENCE PROFILES				INITIAL CONDITIONS	
			U	V	U ²	V ²	W ²	U'V'		
C.J. SCOTT AND D.R. HASK (1973) REF. 97	 <p>SWIRLER VANES</p> <p>VELOCITY MEASUREMENTS WITH PRESSURE PROBES AT $X=1.7, 4.2, 7.0, 10.3, 14.8, 22.2$ & 32.7 (2-D PARABOLIC)</p>	VANE ANGLE OF 45°	7							<p>CONFINED FLOW, NO RECIRCULATION U, W AND PRESSURE DISTRIBUTIONS, ANNULUS FLOW</p>
D.L. RHODE AND D.G. LILLEY AND D.K. McLAUGHLIN (1982) REF. 98	 <p>SWIRL VANE ANGLE α INLET TUBE r_{in}</p> <p>MEASUREMENTS USING 5 HOLE PRESSURE PROBE. ALSO FLOW VISUALIZATION WITH TUFTS AND SMOKE WIRE. (2-D ELLIPTIC)</p>	6 CASES WITH $\alpha=45^\circ$ AND $\alpha=90^\circ$ $\phi=0^\circ, 45^\circ$ AND 70°	5						<p>$Re_D = 7.8 \times 10^4 - 1.05 \times 10^6$ DATA AVAILABLE AT $X/D=0.5, 1, 1.5, 2$ & 2.5 \bar{U} & \bar{W} AT $X=0$ FOR $\alpha=90^\circ$</p>	
B.T. VU AND F.C. GOULDIN (1980) REF. 99	 <p>MEAN VELOCITIES WITH DIRECTIONAL PITOT PROBE. TURBULENCE DATA WITH HOT-WIRE ANEMOMETERS. (2-D ELLIPTIC)</p>	2 (CO-SWIRL COUNTER-SWIRL)	5 7						<p>OVERALL m. SWIRL NO.</p> <p>MEAN VEL. PROFILES AVAILABLE AT $X/R_0 = 0.1, 0.21, 1.05, 2.1, 3.15, 4.2$ AND 8.92</p>	

TABLE 6. SWIRLING FLOWS (CONTD).

CASE	AUTHOR (YEAR)	GEOMETRY AND MEASUREMENT TECHNIQUES	NUMBER OF TEST CASES	NUMBER OF MEASUREMENT LOCATIONS										REMARKS
				MEAN VELOCITY		TURBULENCE PROFILES					INITIAL CONDITIONS			
				U	V or W	U ²	V ²	W ²	U'V'	U'W'		V'W'	OTHERS	
	S. I. JANUHA, D.K. McLAUGHLIN, T.W. JACKSON AND D.G. LILLEY (1982) REF. 100	 <p>MEASUREMENTS WITH HOT-WIRE ANEMOMETER. (2-D ELLIPTIC)</p>	SWIRL ANGLE 0° 30°	6 3	6 3	6 3	6 3	6 3	6 3	6 3	6 3	U'W' V'W'	GEOMETRY SAME AS RHODE & LILLEY. TURBULENCE DATA ON SWIRLING FLOW AVAILABLE ONLY AT X/D = 0.5, 1.0 & 1.5. COMPARISON OF DATA WITH RHODE & LILLEY'S DATA SHOW SOME DIFFERENCES IN W	
	A.P. MORSE (1980) REF. 101	 <p>MEASUREMENTS WITH HOT WIRE ANEMOMETER (2-D PARABOLIC)</p>	4 S=0.25 S=0.36	7 4	7 4	7 4	7 4	7 4	7 4	7 4	7 4	U'W' (VW) 5 4	AT X/D=0.5 S=SWIRL NO. DATA AVAILABLE WITH AND WITHOUT COAXIAL OUTER FLOW DATA ALSO AVAILABLE WITHOUT SWIRL. FLOW FIELD IS UNCONFINED.	

ORIGINAL PAGE 16
OF POOR QUALITY

TABLE 6. SWIRLING FLOWS (CONTD).



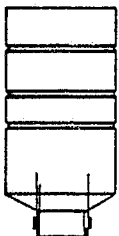
CASE	AUTHOR (YEAR)	GEOMETRY AND MEASUREMENT TECHNIQUES	NUMBER OF TEST CASES	NUMBER OF MEASUREMENT LOCATIONS						REMARKS	
				MEAN VELOCITY		TURBULENCE PROFILES					INITIAL CONDITIONS
				U	V or W	u'^2	v'^2	w'^2	$u'v'$	OTHERS	
	M.L. MATHUR AND N.R.L. MACCALLUM (1967) REF. 102	 3-D PRESSURE PROBE SURVEY (2-D ELLIPTIC)	6	4	2					WALL STATIC PRESS.	ACCURACY OF DATA IS UNCERTAIN. PROBE INTERFERENCE EFFECTS ARE UNKNOWN. SWIRLER VALVE ANGLES OF 15°, 30°, 45°, 60°, 70° AND 75°.
	GTEC (1981) REF. 103 SECTION 8.3	 LOV MEASUREMENTS (2-D ELLIPTIC)	4	5	\bar{w} 5	5		5			SOME UNCERTAINTIES ABOUT STEADINESS, 3-DIMENSIONALITY AND ACCURACY IN SOME REGIONS. SWIRLER VALVE ANGLES OF 0°, 30°, 60° AND 60° WITH A RING.
	GTEC (1981) REF. 104 SECTION 8.2	 3 HALF PRESSURE PROBE MEASUREMENTS (2-D ELLIPTIC)	1	5	5						MEASUREMENTS IN A CAN COMBUSTOR. NO TURBULENCE DATA.

TABLE 7. SCALAR TRANSPORT.

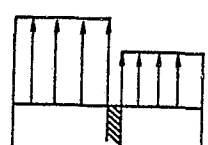
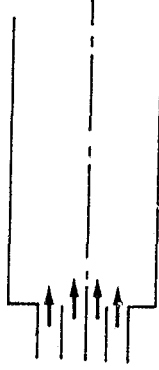
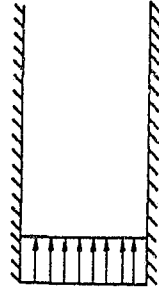
CASE	GEOMETRY AND MEASUREMENT TECHNIQUES	NUMBER OF TEST CASES	NUMBER OF MEASUREMENT LOCATIONS							REMARKS
			MEAN VELOCITY		TURBULENCE PROFILES				INITIAL CONDITIONS	
AUTHOR (YEAR)			V	W	V ²	W ²	V ² + W ²	OTHERS		
J.F. KEFFER, G.J. OLSON AND J.G. KAWALL (1977) REF. 105	 (2-D PARABOLIC)	1							2 1 4	DATA IS VERY LIMITED.
B.V. JOHNSON AND J.C. BENNETT (1981) REF. 88	 LDV AND LIF MEASUREMENTS. (2-D ELLIPTIC)	2 CASES WITH Re: 15,900 AND 47,500	7	7	7	7	7	7	(C) 7 (C) 7 (C) 7 AT $\chi = 0.25'$	EXTENSIVE DATA FLOW IS RECIRCULATING. C = AVG. CONCENTRATION OF FLUORESCENT DYE. FLUID MEDIUM - WATER
M. HISHIDA AND Y. NAGANA (1978) REF. 106	 Re = 40,000 PIPE-WIRE MEASUREMENTS FOR FULLY DEVELOPED PIPE FLOW (2-D PARABOLIC)	1							(T) 1	DATA AVAILABLE IS VERY LIMITED.

TABLE 7. SCALAR TRANSPORT (CONT'D).

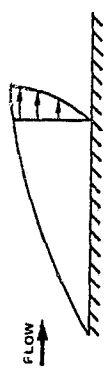
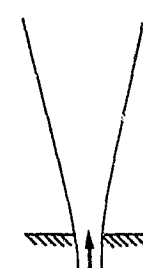
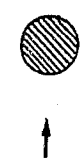

CASE	AUTHOR (YEAR)	GEOMETRY AND MEASUREMENT TECHNIQUES	NUMBER OF TEST CASES	NUMBER OF MEASUREMENT LOCATIONS							REMARKS		
				MEAN VELOCITY		TURBULENCE PROFILES				INITIAL CONDI- TIONS			
				U	V	W ²	W ³	W ⁴	OTHERS				
D.S. JOHNSON (1959) REF. 107		FULLY DEVELOPED TURBULENT BOUNDARY LAYER MAPPING WITH X WIRE ANEMOMETER AND FINE WIRE THERMOCOUPLE AT X = 47". (2-D PARABOLIC)	1	1	1	1	1	1	1	1	1	1	TRIPLE CORRELATIONS SUCH AS $\overline{UV^2}$, $\overline{VW^2}$, $\overline{U^3}$, $\overline{V^3}$ ARE ALSO AVAILABLE θ = TEMPERATURE
R. CHEVREY AND N.K. TUTU (1977) REF. 108		HOT WIRE AND FINE-WIRE THERMOCOUPLE MEASUREMENTS. CONVENTIONAL AND CONDITIONAL SAMPLING DATA AT X/D = 15. (2-D PARABOLIC)	1	1	1	1	1	1	1	1	1	1	DATA AVAILABLE ONLY IN THE SELF-SIMILAR REGION.
G. FARRIS (1977) REF. 109		FAR WAKE OF A CYLINDER. FOUR-WIRE PROBE MEASUREMENTS. AT X/D = 400.	1	1	1	1	1	1	1	1	1	1	DATA LIMITED TO FAR WAKE PAST RECIRCULATION ZONE

TABLE 7. SCALAR TRANSPORT (CONTD).

CASE	GEOMETRY AND MEASUREMENT TECHNIQUES	NUMBER OF TEST CASES	NUMBER OF MEASUREMENT LOCATIONS							REMARKS
			MEAN VELOCITY		TURBULENCE PROFILES				INITIAL CONDITIONS	
			U	V W	U ²	V ²	W ²	U'V'		
G. CHARNAV, J.P. SCHON, E. ALCARAZ AND J. MATHIEU (1977) REF. 110 SECTION 6.9	 <p>HOT-WIRE ANEMOMETER MEASUREMENTS AT X = 70, 80, 90, 105 & 140 CM. (2-D PARABOLIC)</p>	1	5	5	5	5	5	5	U'^2 V'^2 W'^2 $U'V'$ $U'W'$ $V'W'$	INTERMITTENCY OF TEMPERATURE FIELD FOR INTERNAL AND EXTERNAL LAYERS ARE AVAILABLE.

ORIGINAL PAGE IS
OF POOR QUALITY

5.1.2 Gaseous Fuel Combustion

In this paragraph, a data base for assessing gaseous fuel combustion models is provided. The assessment procedure consists of comparing the predictions of time-mean velocity components, temperature, concentrations of species (unburned fuel, CO, CO₂, H₂, H₂O, O₂, N₂) against the experimentally measured values of these quantities. These quantities were selected because they are of interest in gas turbine combustors. Reliable measurements of these quantities are available, and they are a good indication of the predictive capability of the gaseous combustion model consisting of the turbulence/chemistry interactions and the hydrocarbon reaction mechanisms. The assessment will be done for different flow types: turbulent/laminar, premixed/diffusion, one/two/three-dimensional flow, parabolic/elliptic, swirling/nonswirling.

In accordance with the assessment procedure, the data base is categorized into four sections:

- o Laminar Premixed Flames - Table 8
- o Laminar Diffusion Flames - Table 9
- o Turbulent Premixed Flames - Table 10
- o Turbulent Diffusion Flames - Table 11.

In each of these tables, the data is arranged in order of increasing complexity, starting from 1-D parabolic to 3-D swirling elliptic flows.

During the search for compiling the data base, several publications were encountered wherein the boundary conditions or other information required for modeling were not clearly or completely stated. Such cases (e.g., References 111-123) have not been included here. Measurements of quantities not related to the assessment procedure given above have also been excluded. The data base is concerned with the measurements of quantities listed above for steady gaseous hydrocarbon flames.

TABLE 8. LAMINAR PREMIXED FLAMES.

AUTHOR (YEAR)	FLOW DESCRIPTION	FLOW TYPE	FUEL	NUMBER OF CASES	QUANTITIES MEASURED AND MEASUREMENT TECHNIQUE			MEASUREMENT LOCATIONS			REMARKS
					TEMPERATURE	COMPOSITION	OTHER	TEMPERATURE	COMPOSITION	OTHER	
CHANG AND TIEMAN (1982) REF. 124	1-D FLAT PREMIXED FLAME	1-D PARABOLIC	CH ₄ -AIR AND CH ₄ -O ₂	3 EQUIVALENT RATIOS		CO, CO ₂ , O ₂ , H ₂ O, C ₂ H ₄ , QUARTZ MICRO-PROBE AND MASS SPECTROMETER			ALONG FLAME AXIS		DATA USEFUL FOR VALIDATING 2 AND 4 STEP HYDROCARBON OXIDATION MECHANISMS AND ESTABLISHING VALUES OF RATE CONSTANTS
COOK AND SIMMONS (1982) REF. 125	1-D FLAT PREMIXED FLAME	1-D PARABOLIC	C ₃ H ₈ -O ₂ DILUTED WITH Ar	TWO EQUIVALENT RATIO	THERMO-COUPLE	C ₃ H ₈ , CO, CO ₂ , QUARTZ MICRO-PROBE AND MASS SPECTROMETER			ALONG FLAME AXIS		DATA USEFUL FOR VALIDATING 2 AND 4 STEP HYDROCARBON OXIDATION MECHANISMS AND ESTABLISHING VALUES OF RATE CONSTANTS
BECHTEL ET AL (1981) REF. 126	1-D PREMIXED FLAME	1-D PARABOLIC	CH ₄ -AIR AND C ₃ H ₈ -AIR	RICH, LEAN, STOICH, CH ₄ AND STOICH. C ₃ H ₈	N ₂ RAMAN SPECTRUM	O ₂ , CO, H ₂ , CO ₂ , H ₂ O, OH, C ₂ H ₄ , LASER RAMAN SCATTERING			ALONG FLAME AXIS		DATA USEFUL FOR VALIDATING 2 AND 4 STEP HYDROCARBON OXIDATION MECHANISMS AND ESTABLISHING VALUES OF RATE CONSTANTS
HAUTMAN ET AL REF. 19 SECTION 6.10	PLUG FLOW REACTOR	1-D PARABOLIC	C ₃ H ₈ -AIR	RICH, LEAN AND STOICH.	THERMO-COUPLE	C ₃ H ₈ , CO, CO ₂ , H ₂ , C ₂ H ₄ WATER-COOLED STAINLESS STEEL SAMPLING PROBE AND GAS CHROMATOGRAPHY			ALONG FLAME AXIS		THIS DATA WAS USED TO COMPARE 2 AND 4 STEP HYDROCARBON OXIDATION MECHANISMS IN REF. 153

TABLE 9. LAMINAR DIFFUSION FLAMES.

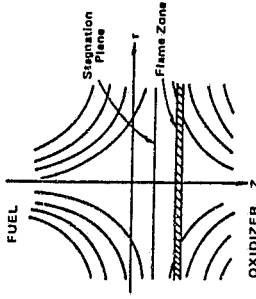
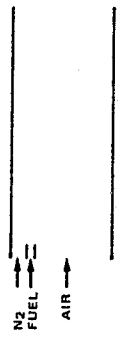
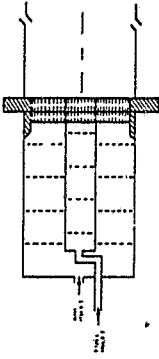
AUTHOR (YEAR)	FLOW DESCRIPTION	FLOW TYPE	FUEL	NUMBER OF CASES	QUANTITIES MEASURED AND MEASUREMENT TECHNIQUE			MEASUREMENT LOCATIONS			REMARKS
					TEMPERATURE	COMPOSITION	OTHER	TEMPERATURE	COMPOSITION	OTHER	
HAHN, WENDT AND TYSON (1981) REF. 127	OPPOSED JET DIFFUSION FLAME: FUEL O ₂ AND N ₂ MIXED AND FED TO TWO OPPOSING BURNERS CONTAINED IN A RECTANGULAR COMBUSTION CHAMBER. 	2-D ELLIPTIC	MIXED CO - AIR	ONE	TEMPERATURE THERMO-COUPLE	COMPOSITION CO, CO ₂ , O ₂ , H ₂ O, UNCOOLED QUARTZ PROBE AND GAS CHROMATOGRAPHY	OTHER	ALONG FLAME AXIS	ALONG FLAME AXIS	OTHER	LIMITED AMOUNT OF DATA.
KAWAMURA ET AL. (1980) REF. 128	RECTANGULAR COMBUSTION CHAMBER WITH FUEL FED THRU A RECTANGULAR NOZZLE SURROUNDED BY AIR. 	2-D ELLIPTIC	CH ₄ -AIR	2 CASES FOR DIFFERENT AIR VELOCITIES	TEMPERATURE THERMO-COUPLE	COMPOSITION CH ₄ , CO ₂ , H ₂ O, O ₂ , N ₂ , CO - SAMPLING PROBE AND FISHER-HAMILTON GAS PARTICULATORS.	STREAM-LINES, VELOCITY, PARTICLE TRACKING TECHNIQUE	CONTOUR PLOTS	CONTOUR PLOTS OF STREAM-LINES	OTHER	CONCENTRATION MEASUREMENTS ABSENT, DIRECT ASSESSMENT OF CHEMISTRY MODEL NOT POSSIBLE.
MITCHELL ET AL. (1980) REF. 129 SECTION 6.11	CONCENTRIC FUEL AND AIR JETS CONTAINED IN A VERTICAL CYLINDRICAL COMBUSTOR. 	2-D ELLIPTIC	CH ₄ -AIR	ONE	TEMPERATURE THERMO-COUPLE	COMPOSITION CH ₄ , CO ₂ , H ₂ O, O ₂ , N ₂ , CO - SAMPLING PROBE AND FISHER-HAMILTON GAS PARTICULATORS.	AXIAL VELOCITY - LDV	RADIAL PROFILES AT 3 AXIAL LOCATIONS	RADIAL PROFILES AT 3 AXIAL LOCATIONS	RADIAL PROFILES OF AXIAL VELOCITY AT 3 AXIAL LOCATIONS	INFLUENCE OF BUOYANCY IS IMPORTANT RADIATION AND CONDUCTION CORRECTIONS TO TEMPERATURE MEASUREMENTS MADE. GARRETT HAS COMPUTED THIS CASE WITH 2 STEP HYDROCARBON OXIDATION SCHEME AND AGREEMENT WITH DATA IS FAIRLY GOOD COMPUTATIONS WITH 4-STEP SCHEME NEED TO BE DONE

TABLE 1.1. TURBULENT PREMIXED FLAMES.

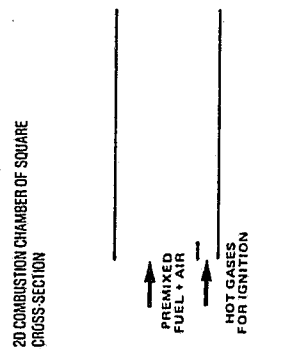
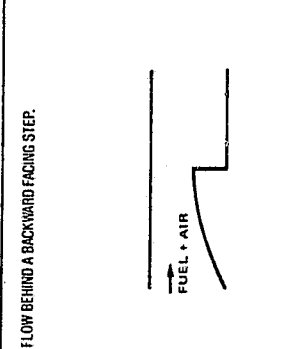
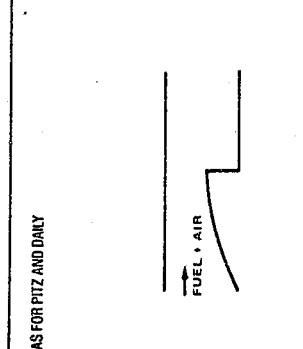
AUTHOR (YEAR)	FLOW DESCRIPTION	FLOW TYPE	FUEL	NUMBER OF CASES	QUANTITIES MEASURED AND MEASUREMENT TECHNIQUE			MEASUREMENT LOCATIONS			REMARKS
					TEMPERATURE	COMPOSITION	OTHER	TEMPERATURE	COMPOSITION	OTHER	
MOREAU AND LABBE (1978) REF. 130	2D COMBUSTION CHAMBER OF SQUARE CROSS SECTION 	2-D ELLIPTIC	CH ₄ -AIR	ONE			VELOCITY AND TURBULENCE INTENSITY - LDV.			RADIAL PROFILES OF VELOCITY AND TURBULENCE INTENSITY AT 7 AXIAL LOCATIONS.	LIMITED AMOUNT OF DATA AND THEREFORE LIMITED UTILITY
PIZ AND DAILY (1981) REF. 131	FLOW BEHIND A BACKWARD FACING STEP. 	2-D ELLIPTIC	C ₃ H ₈ -AIR	COLD AND HOT FLOW, WITH THREE REYNOLDS NUMBERS FOR EACH			VELOCITY COMPONENTS AND TURBULENCE INTENSITY - LDV.			CROSS-STREAM PROFILES OF VELOCITY AT 8 AXIAL LOCATIONS.	INLET VELOCITY AND TURBULENCE INTENSITY PROFILES MEASURED. PROVIDES ACCURATE BOUNDARY CONDITION INPUT
GANJI AND SAWYER (1979) REF. 132 SECTION 7.8	AS FOR PIZ AND DAILY 	2-D ELLIPTIC	C ₃ H ₈ -AIR	COLD AND HOT FLOWS	THERMO-COUPLE	CO, CO ₂ SAMPLING PROBE-NON- DISPERSIVE INFRARED ANALYZER. City FLAME IONISATION DETECTOR				CROSS-STREAM PROFILES AT 4 AXIAL LOCATIONS CROSS-STREAM PROFILES AT 4 AXIAL LOCATIONS	SAME SETUP AS PIZ AND DAILY TOGETHER A DETAILED SET OF DATA IS AVAILABLE

TABLE 11. TURBULENT DIFFUSION FLAMES.

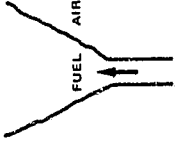
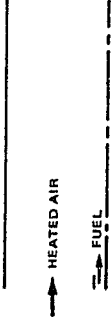
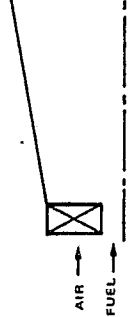
AUTHOR (¹ - ⁴ AR)	FLOW DESCRIPTION	FLOW TYPE	FUEL	NUMBER OF CASES	QUANTITIES MEASURED AND MEASUREMENT TECHNIQUE			MEASUREMENT LOCATIONS			REMARKS
					TEMPERATURE	COMPOSITION	OTHER	TEMPERATURE	COMPOSITION	OTHER	
HASSAN, LOCKWOOD AND MONEEB (1990) REF. 133 SECTION 6.13	VERTICAL FREE-JET CH ₄ FLAME IN AIR. 	2-D PARABOLIC	CH ₄ - AIR	FOUR DIFFERENT RE NO. AND FIVE VARYING AMOUNTS OF N ₂ ADDED TO FUEL STREAM.	THERMO- COUPLE	CO, CO ₂ , O ₂ , QUARTZ MICROPROBE, CO, CO ₂ - INFRARED GAS ANALYZERS, O ₂ - PARA- MAGNETIC ANALYZER.	OTHER	AXIAL DISTRIBU- TION ALONG CENTERLINE RADIAL DISTRIBU- TION AT 4 AXIAL LOCATIONS	AXIAL DISTRIBU- TION ALONG CENTERLINE RADIAL DISTRIBU- TION AT 4 AXIAL LOCATIONS	OTHER	DISCUSSION ON ACCURACY OF MEASUREMENTS PROVIDED. VALIDATION FOR DIFFERENT FLOW CONDITIONS POSSIBLE
TAKENO AND KOTAWA (1975) REF. 134	ENCLOSED JET FLAME IN A COFLOWING HIGH TEMPERATURE AIR STREAM 	2-D PARABOLIC	CITY GAS-AIR H ₂ + CO + CH ₄ + OTHER (C ₂ H ₆)	ONE	THERMO- COUPLE		TOTAL PRESSURE - PILOT TUBE	RADIAL PROFILES AT 8 AXIAL LOCATIONS.		TOTAL PRESSURE -RADIAL PROFILES AT 6 AXIAL LOCATIONS	RADIAL PROFILES OF AXIAL VELOCITY AND TEMPERATURE MEASURED AT INLET - PROVIDES ACCURATE BOUNDARY CONDITION INPUT.
PAUVA REF. 135	CENTRAL FUEL JET SURROUNDED BY AIR THROUGH ANNULAR SWIRLER IN A CONICAL COMBUSTOR 	2-D PARABOLIC	CH ₄ - AIR	ONE	THERMO- COUPLE	N ₂ , O ₂ , CH ₄ , SAMPLING PROBE AND GAS CHROMATO- GRAPHY	AXIAL VELOCITY - FIVE HOLE PILOT PROBE	RADIAL PROFILES AT 4 AXIAL LOCATIONS	RADIAL PROFILES AT 4 AXIAL LOCATIONS	AXIAL VELOCITY - RADIAL PROFILES AT 4 AXIAL LOCATIONS	DATA PROVIDES FOR VALIDATION UNDER CONFIRMED PARABOLIC FLOW CONDITIONS.

TABLE 11. TURBULENT DIFFUSION FLAMES (CONTD).

ORIGINAL PAGE IS
OF POOR QUALITY

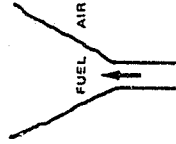
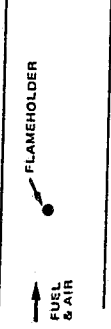
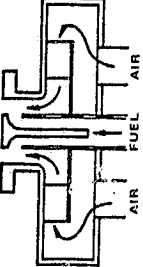
AUTHOR (YEAR)	FLOW DESCRIPTION	FLOW TYPE	FUEL	NUMBER OF CASES	QUANTITIES MEASURED AND MEASUREMENT TECHNIQUE				MEASUREMENT LOCATIONS			REMARKS
					TEMPERATURE	COMPOSITION	OTHER	TEMPERATURE	COMPOSITION	OTHER		
YOU AND FAITH (1982) REF. 136	BUOYANT AXISYMMETRIC FLAME RISING VERTICALLY IN STILL AIR 	2-D PARABOLIC	CH ₄ -AIR	2 WITH DIFFERENT FUEL FLOW RATES	THERMO-COUPLE	CH ₄ , H ₂ , CO ₂ , CO, H ₂ O, O ₂ , H ₂ ISOKINETIC SAMPLING AND GAS CHROMATOGRAPHY	AXIAL VELOCITY - LDV RADIATIVE HEAT FLUX PIANOMETER	RADIAL PROFILES AT 3 AXIAL LOCATIONS	RADIAL PROFILES AT 3 AXIAL LOCATIONS	AXIAL VELOCITY - RADIAL PROFILES AT 3 AXIAL LOCATIONS AXIAL VARIATION OF RADIATION FLUX	EFFECTS OF LOW REYNOLDS NUMBER INFLUENCE OF BUOYANCY ON TURBULENCE, AND SOOTING EFFECTS POSE SOME PROBLEMS IN MODELING. SOME UNCERTAINTY IN ESTIMATING INITIAL CONDITIONS, SO CALCULATION CAN BE STARTED FROM FIRST MEASURED LOCATION.	
SHIPMAN AND WORKERS (1963 AND 1967) REF. 137 REF. 138 SECTION 6.12	CONFINED FLAME STABILIZED ON A CYLINDRICAL FLAME HOLDER IN A RECTANGULAR DUCT 	2-D PARABOLIC	C ₃ H ₈ -AIR	5 WITH DIFFERENT INLET VELOCITIES		C ₃ H ₈ , CO, CO ₂ , O ₂ , H ₂ , N ₂ SAMPLING PROBE AND GAS CHROMATOGRAPHY	AXIAL VELOCITY PILOT TUBE	TRANSVERSE PROFILE AT 7 AXIAL LOCATIONS.	AXIAL VELOCITY TRANSVERSE PROFILE AT 7 AXIAL LOCATIONS			
HELLAT, LENZ, AND GUNTHER (REF. 139)	ENCLOSED JET FLAME 	2-D PARABOLIC SWIRLING AND NON-SWIRLING	CH ₄ -AIR	ONE NON-SWIRLING AND THREE SWIRLING WITH VARYING SWIRL NUMBER.	THERMO-COUPLE		T ₁ , AXIAL VELOCITY	RADIAL PROFILES AT 2-4 AXIAL LOCATIONS	T ₁ , AXIAL VELOCITY - RADIAL PROFILES AT 2-4 AXIAL LOCATIONS	ABSENCE OF COMPOSITION MEASUREMENTS PRECLUDES DIRECT VALIDATION OF CHEMISTRY MODEL		

TABLE 11. TURBULENT DIFFUSION FLAMES (CONTD).




AUTHOR (YEAR)	FLOW DESCRIPTION	FLOW TYPE	FUEL	NUMBER OF CASES	QUANTITIES MEASURED AND MEASUREMENT TECHNIQUE			MEASUREMENT LOCATIONS			REMARKS
					TEMPERATURE	COMPOSITION	OTHER	TEMPERATURE	COMPOSITION	OTHER	
LEWIS AND SMOOT (1981) REF. 140 REF. 141 SECTION 7.10	ASYMMETRIC COMBUSTOR WITH COAXIAL FUEL AND AIR JETS 	2-D ELLIPTIC	CH ₄ - AIR	28 TESTS	TEMPERATURE THERMO- COUPLE	COMPOSITION O ₂ , N ₂ , H ₂ , CH ₄ , CO, CO ₂ , H ₂ O, QUENCHED & WATER- COOLED PROBES, GAS CHROMATO- GRAPHY	OTHER	TEMPERATURE RADIAL PROFILES AT 8 AXIAL LOCATIONS	COMPOSITION RADIAL PROFILES AT 8 AXIAL LOCATIONS	OTHER	DISCUSSION ON THE ACCURACY OF MEASURE- MENTS PROVIDED COMPUTATIONS WITH a c MODEL REPORTED; REASONABLE AGREEMENT WITH DATA
CHANG AND TIERMAN (1982) REF. 124	RAMJET DUMP COMBUSTOR 	2-D ELLIPTIC	CH ₄ - AIR	COLD AND HOT FLOW		O ₂ , CO, CO ₂ , H ₂ O, CH ₄ , QUARTZ MICROPROBE, MASS SPECTRO- METER FOR COLD FLOW INERT AR.			RADIAL PROFILES AT 7 AXIAL LOCATIONS		DISCUSSION ON THE ACCURACY OF MEASUREMENTS PROVIDED
LIGHTMAN ET AL. (1980) REF. 142	APL RESEARCH COMBUSTOR: DUCTED BLUFF BODY COMBUSTOR CONSISTING OF COAXIAL FUEL AND AIR JETS 	2-D ELLIPTIC	C ₃ H ₈ - AIR CO ₂ - AIR FOR COLD FLOW	COLD AND HOT FLOW FOR 4 DIFFERENT CO ₂ AND C ₃ H ₈ FLOW RATES			AXIAL VELOCITY, TURBU- LENCE INTENSITY - LDV		RADIAL PROFILES AT 7 AXIAL LOCATIONS	AXIAL VELOCITY, TURBU- LENCE INTENSITY - AXIAL PROFILES ALONG CENTERLINE AND OFF- CENTERLINE	DISCUSSION ON THE ACCURACY OF MEASURE- MENTS PROVIDED ABSENCE OF TEMPERATURE AND COMPOSITION MEASURE- MENTS PRECLUDES DIRECT VALIDATION OF COMBUSTION MODEL

TABLE 11. TURBULENT DIFFUSION FLAMES (CONTD).

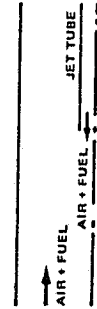
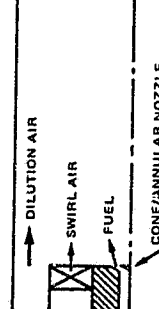

AUTHOR (YEAR)	FLOW DESCRIPTION	FLOW TYPE	FUEL	NUMBER OF CASES	QUANTITIES MEASURED AND MEASUREMENT TECHNIQUE				MEASUREMENT LOCATIONS			REMARKS
					TEMPERATURE	COMPOSITION	OTHER	TEMPERATURE	COMPOSITION	OTHER		
PECK AND SAMUELSEN (1977) REF. 143	OPPOSED JET COMBUSTOR 	2-D ELLIPTIC	CH ₄ -AIR	COLD AND HOT FLOW	TEMPERATURE THERMO-COUPLE	COMPOSITION C ₂ H ₄ , CO EXHAUST GAS ANALYSIS SYSTEM.	OTHER	TEMPERATURE RADIAL PROFILE AT EXHAUST	COMPOSITION RADIAL PROFILE AT EXHAUST	OTHER	MEASUREMENTS ONLY AT EXHAUST PLANE - INCOMPLETE FOR DETAILED VALIDATION	
BRUM AND SAMUELSEN (1982) REF. 144 SECTION 8.4	DILUTE SWIRL COMBUSTOR 	2-D ELLIPTIC	C ₂ H ₆ -AIR AND C ₂ H ₁₈ -AIR	COLD AND HOT FLOW			AXIAL VELOCITY = LDV			AXIAL VELOCITY - RADIAL PROFILES AT 4 AXIAL LOCATIONS, ALSO AXIAL PROFILE OF AXIAL VELOCITY ALONG CENTERLINE	TEMPERATURE AND COMPOSITION MEASUREMENTS NOT AVAILABLE - DIRECT VALIDATION OF COMBUSTION MODEL NOT POSSIBLE	
EL-MAHALLAWY, LOCKWOOD AND SPALDING REF. 145	CYLINDRICAL FURNACE, AXIALLY FIRED BY COAXIAL FUEL AND AIR JETS. 	2-D ELLIPTIC SWIRLING AND NON-SWIRLING	CH ₄ -AIR (TOWN GAS)	ONE NON-SWIRLING AND FOUR DIFFERENT SWIRL NUMBERS.			FLAME LENGTH		CENTOUR PLOTS	FLAME LENGTH AT 4 SWIRL NUMBERS	RADIATION EFFECTS SAID TO BE SMALL - LIMITED AMOUNT OF DATA - LIMITED UTILITY	

TABLE 11. TURBULENT DIFFUSION FLAMES (CONTD).


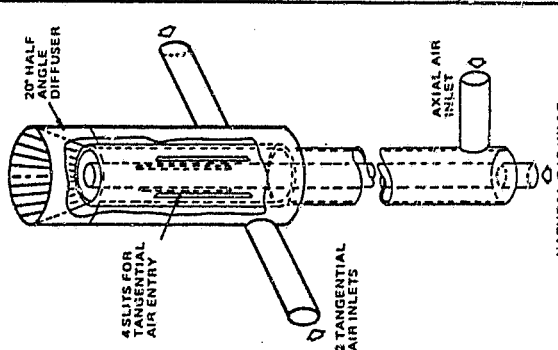
AUTHOR (...AR)	FLOW DESCRIPTION	FLOW TYPE	FUEL	NUMBER OF CASES	QUANTITIES MEASURED AND MEASUREMENT TECHNIQUE			MEASUREMENT LOCATIONS			REMARKS
					TEMPERATURE	COMPOSITION	OTHER	TEMPERATURE	COMPOSITION	OTHER	
SCHIEFER AND SAWYER (1976) REF. 146 SECTION 7.9	OPPOSED REACTING JET COMBUSTOR. PREMIXED C_2H_2/AIR STREAM STABILIZED BY A COUNTERFLOWING JET OF THE SAME REACTANTS 	2-D ELLIPTIC	C_2H_2/AIR	3 WITH DIFFERENT INLET TEMPERATURE AND EQUIVALENCE RATIO.	TEMPERATURE THERMOCOUPLE	$H_2O, O_2, N_2, CO_2, CO, H_2$ UNCOOLED QUARTZ PROBE AND MASS SPECTRO-METER CO-MONOSPHERIC INFRARED ANALYZER.	OTHER	AXIAL PROFILES AT 2 RADIAL LOCATIONS. RADIAL PROFILES AT 3 AXIAL LOCATIONS	AXIAL PROFILES AT 2 RADIAL LOCATIONS. RADIAL PROFILES AT 3 AXIAL LOCATIONS	OTHER	DISCUSSIONS ON THE ACCURACY OF MEASUREMENTS PROVIDED CONSIDERABLE AMOUNT OF DATA FOR DETAILED VALIDATION OF COMBUSTION MODEL
CHIEBER AND DVORAK (1975) REF. 147	CYLINDRICAL COMBUSTOR WITH NATURAL GAS THRU A CENTRAL PIPE AND AIR INTRODUCED THRU FOUR TANGENTIAL SLOTS AND THRU AN AXIAL INLET PIPE. 	2-D ELLIPTIC SWIRLING	NATURAL GAS/AIR	COLD AND HOT FLOW			OTHER	AXIAL PROFILES AT 2 RADIAL LOCATIONS. RADIAL PROFILES AT 3 AXIAL LOCATIONS	AXIAL PROFILES AT 2 RADIAL LOCATIONS. RADIAL PROFILES AT 3 AXIAL LOCATIONS	OTHER	TEMPERATURE AND COMPOSITION MEASUREMENTS NOT AVAILABLE - DIRECT ASSESSMENT OF COMBUSTION MODEL NOT POSSIBLE

TABLE 11. TURBULENT DIFFUSION FLAMES (CONTD).

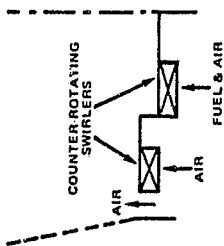
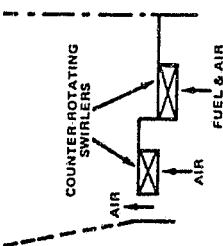
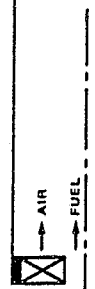
AUTHOR (YEAR)	FLOW DESCRIPTION	FLOW TYPE	FUEL	NUMBER OF CASES	QUANTITIES MEASURED AND MEASUREMENT TECHNIQUE			MEASUREMENT LOCATIONS			REMARKS
					TEMPERATURE	COMPOSITION	OTHER	TEMPERATURE	COMPOSITION	OTHER	
THOMPSON, CHIGIER AND UNGUT (1977). REF. 148	NASA CONTRA SWIRL CAN: TWO COUNTER-ROTATING ANNULAR AIR AND AIR + FUEL STREAMS IN UNCONFINED STAGNANT AIR. 	2-D ELLIPTIC SWIRLING	C ₃ H ₈ -AIR	3 FLAMES WITH DIFFERENT FUEL/AIR RATIOS	TEMPERATURE THERMOCOUPLE	COMPOSITION CO ₂ , O ₂ , CO, H ₂ , QUARTZ MICROPROBE AND GAS ANALYSIS CHROMATOGRAPHY	OTHER AXIAL VELOCITY - LDV	TEMPERATURE RADIAL PROFILES AT 7 AXIAL LOCATIONS	COMPOSITION RADIAL PROFILES AT 7 AXIAL LOCATIONS	OTHER RADIAL PROFILES OF AXIAL VELOCITY AT 2 AXIAL LOCATIONS.	DATA PROVIDED FOR ASSESSMENT OF COMBUSTION MODEL UNDER SWIRLING FLOW CONDITIONS
THOMPSON, CHIGIER AND VENTURA (1978). REF. 149	NASA CONTRA SWIRL CAN: TWO COUNTER-ROTATING ANNULAR AIR AND AIR + FUEL STREAMS IN UNCONFINED STAGNANT AIR. 	2-D ELLIPTIC SWIRLING	C ₃ H ₈ -AIR	4 DIFFERENT FUEL/AIR RATIO PERATURES	TEMPERATURE THERMOCOUPLE	COMPOSITION CO ₂ , H ₂ , O ₂ , CO, QUARTZ MICROPROBE AND GAS ANALYSIS CHROMATOGRAPHY		CONTOUR PLOT OF WHOLE TEMPERATURE FIELD.	RADIAL PROFILE AT EXIT PLANE AND ONE MORE PLANE. AXIAL PROFILE ALONG CENTERLINE.		EFFECT OF PREHEATING STUDIED. TOGETHER WITH THOMPSON, CHIGIER AND UNGUT, THIS PROVIDES A DETAILED DATA SET
OWEN (1976). REF. 150	CONFINED TURBULENT DIFFUSION FLAME BURNER. CENTRAL FUEL JET AND A COAXIAL ANNULAR AIR STREAM. 	2-D ELLIPTIC SWIRLING AND NON-SWIRLING	NATURAL GAS AIR	TWO - DIFFERENT AMOUNTS OF SWIRL.			AXIAL AND TANGENTIAL VELOCITY COMPONENTS - LDV			RADIAL PROFILES OF AXIAL AND TANGENTIAL VELOCITIES AT 3 AXIAL LOCATIONS.	USED TO STUDY SWIRL EFFECTS UNDER VARYING CONDITIONS. COMPOSITION AND TEMPERATURE MEASUREMENTS NOT AVAILABLE. DIRECT ASSESSMENT OF COMBUSTION MODEL NOT POSSIBLE

TABLE 11. TURBULENT DIFFUSION FLAMES (CONTD).

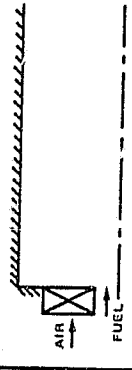
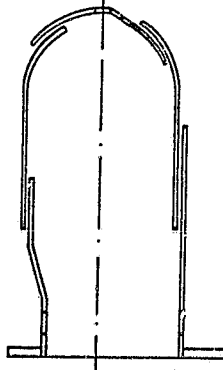
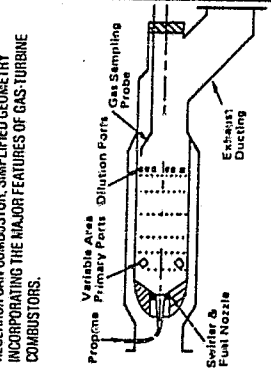
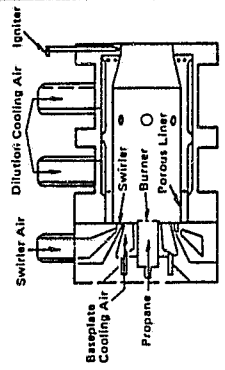
AUTHOR (YEAR)	FLOW DESCRIPTION	FLOW TYPE	FUEL	NUMBER OF CASES	QUANTITIES MEASURED AND MEASUREMENT TECHNIQUE			MEASUREMENT LOCATIONS			REMARKS
					TEMPERATURE	COMPOSITION	OTHER	TEMPERATURE	COMPOSITION	OTHER	
CLAYPOLE AND STROD (1981) REF. 151	COAXIAL FUEL AND AIR SWIRLING JETS 	2-D ELLIPTIC SWIRLING	CH ₄ -AIR	COLD AND HOT FLOW, 2 FLOW EACH	THERMO-COUPLE	CH ₄ , CO	AXIAL AND TANGENTIAL VELOCITY COMPONENTS - LDV. STREAMLINE PATTERN	CONTOUR PLOT OF AXIAL AND TANGENTIAL VELOCITIES OVER COM- PLETE FIELD.	CONTOUR PLOT OF COM- PLETE FIELD	DATA PROVIDES FOR MODEL ASSESSMENT UNDER SWIRLING FLOW CONDITIONS.	
TORAL (1980), TORAL AND WHITELAW (1982) REF. 152 REF. 153	SECTOR OF AN ANNULAR COMBUSTOR. 	3-D ELLIPTIC	NATURAL GAS-AIR	COLD AND HOT FLOW, 2 FLOW CONDITIONS EACH	THERMO-COUPLE	COLD FLOW: H ₂ SEEDING HOT FLOW: C ₂ H ₄ , CO, CO ₂ , O ₂ WATER COOLED PROBE FLAME IONIZATION DETECTOR, INFRARED AND PARA- MAGNETIC ANALYZERS	COLD FLOW: U.V. W AT 3 CROSS- STREAM PLANES. HOT FLOW: U.V. AT 2 AXIAL AND 3 AXIAL PLANES.	COLD FLOW: U.V. W AT 3 AXIAL AND 3 CROSS- STREAM PLANES. HOT FLOW: U.V. AT 2 AXIAL AND 3 AXIAL PLANES.	DISCUSSION ON THE ACCURACY OF MEASUREMENTS PROVIDED. DATA PROVIDES FOR MODEL ASSESSMENT UNDER CONDITIONS CLOSE TO THOSE IN GAS-TURBINE COMBUSTORS		
HOYCE SHEPPARD AND YAMBA (1981) REF. 154	RESEARCH CAN COMBUSTOR, SIMPLIFIED GEOMETRY INCORPORATING THE MAJOR FEATURES OF GAS-TURBINE COMBUSTORS. 	3-D ELLIPTIC	C ₃ H ₈ -AIR	ONE	THERMO-COUPLE	CO, C ₃ H ₈ , H ₂ EQUIVALENCE RATIO, SAMPLING PROBE AND GAS ANALYSIS	UP-STREAM OF PRIMARY ZONE, 3 INTERMEDIATE PLANKS AND JUST UP-STREAM OF DILUTION JETS	AS FOR TEMPERATURE	FLOW SPLITS THROUGH PRIMARY JETS NOT GIVEN, CAN BE CALCULATED BY ANNULUS LOSS MODEL. DATA PROVIDES FOR MODEL ASSESSMENT UNDER CONDITIONS CLOSE TO THOSE IN GAS-TURBINE COMBUSTORS		

TABLE 11. TURBULENT DIFFUSION FLAMES (CONTD).

AUTHOR (YEAR)	FLOW DESCRIPTION	FLOW TYPE	FUEL	NUMBER OF CASES	QUANTITIES MEASURED AND MEASUREMENT TECHNIQUE			MEASUREMENT LOCATIONS			REMARKS
					TEMPERATURE	COMPOSITION	OTHER	TEMPERATURE	COMPOSITION	OTHER	
JONES ET AL (1977) REF. 155	<p>SMALL SCALE RESEARCH CAN COMBUSTOR.</p> 	3-D ELLIPTIC	C ₃ H ₈ -AIR	ONE	THERMO-COUPLE	O ₂ , N ₂ , CO, CO ₂ , WATER-COOLED PROBE GAS CHROMATOGRAPHY, C ₂ H ₄ FLAME IONISATION DETECTOR.	VELOCITY: 7 HOLE PITOT PROBE	RADIAL PROFILES AT 7 AXIAL LOCATIONS.	RADIAL PROFILES AT 7 AXIAL LOCATIONS.	RADIAL PROFILES OF AXIAL VELOCITY AT 7 AXIAL LOCATIONS.	DISCUSSION ON ACCURACY OF MEASUREMENTS PROVIDED. ALL DIMENSIONS AND FLOW SPLITS NOT GIVEN. DISCREPANCY SOME APPROXIMATIONS NECESSARY FOR MODELING.

5.1.3 Spray Evaporation and Combustion

In this paragraph, a data base for assessing spray evaporation and combustion models is provided. The assessment procedure will consist of comparing the predicted spray trajectory, droplet concentrations, velocities and size distribution, temperature, and concentrations of species (unburnt fuel, CO, CO₂, H₂, H₂O, O₂, N₂) against the experimentally measured values of these quantities. The available data on spray evaporation and combustion is listed in Table 12. The predictions of these quantities is an indication of the accuracy of the various features of the spray model:

- o The prediction of spray trajectory, droplet concentrations, velocities, and size distribution under non-burning and nonevaporating conditions reflects on the accuracy of the spray dynamics model, which includes the modeling of the drag forces between the spray and the gas phase.
- o The prediction of the droplet concentrations and size distributions along with the mixture fraction under non-burning (but evaporating) conditions serves to test the droplet heat-up and evaporation models.
- o Finally, the prediction of droplet concentration and size distribution along with gas temperature and composition serves to test the validity of the spray combustion model.

Thus by assessing the predictions of the quantities listed above, all features of spray evaporation and combustion involving interphase momentum (spray dynamics, drag), heat (droplet heat-up) and mass (droplet evaporation and combustion) transfer are tested individually and jointly.

The data base is arranged in order of increasing flow complexity. Sources in which all boundary and initial conditions required for modeling were not completely or clearly stated have not been included in the data base (e.g. References 156-170). It should be noted that complex two-phase slip models as used at Garrett require detailed information specifying the initial conditions at the fuel injector; initial drop size distribution, initial velocity distribution, etc. This information is generally not available and therefore has to be estimated from the available injector characteristics.

TABLE 12. SPRAY EVAPORATION AND COMBUSTION.

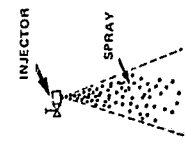
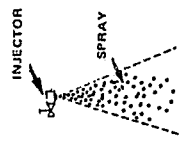
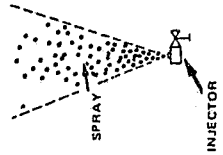
AUTHOR (YEAR)	FLOW DESCRIPTION	FLOW TYPE	FUEL	NUMBER OF CASES	QUANTITIES MEASURED AND MEASUREMENT TECHNIQUE				MEASUREMENT LOCATIONS				REMARKS	
					SPRAY FEATURES	TEMPERATURE	COMPOSITION	OTHER	SPRAY FEATURES	TEMPERATURE	COMPOSITION	OTHER		
YULE ET AL (1982) REF. 171	TURBULENT KEROSENE SPRAY INJECTED INTO A COFLOWING AIR STREAM THROUGH A TWIN FLUID ATOMIZER. 	2-D PARABOLIC	KEROSENE	FOUR: TWO WITH SPRAY (HOT & COLD) TWO W/O SPRAY (HOT & COLD) HOT = EVAPORATING COLD = NON-EVAPORATING	DROPLET VOLUME FRACTION; DROPLET SIZE; DROPLET VELOCITY; USING LASER DOPPLER VELOCITY TOMOGRAPHY				GAS VELOCITY; LASER DOPPLER VELOCITY TOMOGRAPHY				SPRAY FEATURES: DROPLET CONCENTRATION - RADIAL PROFILES AT 5 AXIAL LOCATIONS; DROPLET SIZE AND VELOCITY - RADIAL PROFILES AT 6 AXIAL LOCATIONS.	SPRAY EVAPORATION: SINCE MEASUREMENTS WITH AND W/O SPRAY UNDER HOT AND COLD CONDITIONS ARE AVAILABLE, A SYSTEMATIC STEPWISE TESTING OF THE MODEL IS POSSIBLE.
SHEARER AND FAETH (1979) REF. 172	JET ISSUING VERTICALLY DOWNWARD INTO STAGNANT AIR. 	2-D PARABOLIC	FREON-11	THREE: 1) ISO-THERMAL AIR JET 2) ISO-THERMAL DENSE GAS JET 3) EVAPORATING SPRAY JET	DROP SIZE DISTRIBUTION AND LIQUID MASS FLOW - SLIDE IMPACTOGRAPHY	THERMO-COUPLE	MIXTURE FRACTION - ISO-KINETIC SAMPLING AND GAS CHROMATOGRAPHY	GAS VELOCITY AND TURBULENCE INTENSITY - LDV					TEMPERATURE MEASUREMENTS QUALITATIVE SINCE DROP IMPROVEMENT EFFECTS IGNORED. LOCALLY HOMOGENEOUS FLOW PREDICTIONS OVER-ESTIMATE RATE OF FLOW DEVELOPMENT BY 20-40%. SYSTEMATIC STEPWISE VALIDATION POSSIBLE WITH THE THREE CASES.	
MAO, SZEKELY AND FAETH (1980) REF. 173	JET ISSUING VERTICALLY UPWARD INTO STAGNANT AIR, AIR ATOMIZED SPRAY. 	2-D PARABOLIC	CASEOUS LIQUID: PROPANE; PENTANE	ONE WITH EACH FUEL	THERMO-COUPLE	CO, C ₂ H ₄ , O ₂ , CO ₂ - H ₂ , H ₂ O - ISOKINETIC SAMPLING AND GAS CHROMATOGRAPHY	GAS VELOCITY AND TURBULENCE INTENSITY - LDV						LOCALLY HOMOGENEOUS FLOW PREDICTIONS OVER-ESTIMATE RATE OF FLOW DEVELOPMENT BY ~30%. GOOD AGREEMENT OF PREDICTIONS WITH DATA FOR PROPANE FLAME WITH K-C-G MODEL. THERMO-COUPLE SHIELDED FOR DROP IMPINGEMENT. BUOYANCY IMPORTANT THIS TOGETHER WITH SHEARER AND FAETH (1979) FORMS A COMPREHENSIVE DATA SET FOR A RANGE OF FLOW CONDITIONS. SIMPLE AIR JET TO COMBUSTING SPRAY JET.	

TABLE 12. SPRAY EVAPORATION AND COMBUSTION (CONTD.).

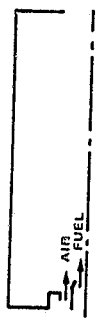
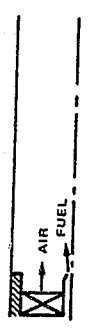

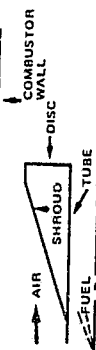
AUTHOR (YEAR)	FLOW DESCRIPTION	FLOW TYPE	FUEL	NUMBER OF CASES	QUANTITIES MEASURED AND MEASUREMENT TECHNIQUE					MEASUREMENT LOCATIONS				REMARKS
					SPRAY FEATURES	TEMPERATURE	COMPOSITION	OTHER	SPRAY FEATURES	TEMPERATURE	COMPOSITION	OTHER		
OHUMA AND OGASAWARA (1975) REF. 174	CYLINDRICAL BURNER WITH AN AIR-ATOMIZING SPRAY NOZZLE AND AIR INTRODUCED THROUGH AN ANNULUS SURROUNDING THE NOZZLE. 	2-D ELLIPTIC	GASEOUS PROPANE AND LIQUID KEROSENE	THREE EDGE-VALENCE RATIOS FOR LIQUID FUEL; ONE FOR GASEOUS FUEL; AND ONE ISO-THERMAL LIQUID FUEL.	DROPLET NO. DENSITY AND SIZE - PLATE COLLECTOR AND MICROPHOTOGRAPHS.	THERMO-COUPLE	O ₂ , CO, CO ₂ , C ₁ H ₄ , COOLED SAMPLING PROBE AND GAS AND GAS CHROMATOGRAPHY	GAS VELOCITY - PITOT TUBE.	RADIAL PROFILE OF DROPLET LET NO. DENSITY AT 3 AXIAL LOCATIONS. DROPLET SIZE DISTRIBUTION AT 4 LOCATIONS.	AXIAL PROFILE ALONG CENTER-LINE. RADIAL PROFILE AT ONE AXIAL LOCATION.	AXIAL PROFILE OF GAS VELOCITY CENTER-LINE. RADIAL PROFILE AT ONE AXIAL LOCATION.	OTHER	COMPARISON BETWEEN GASEOUS AND SPRAY FLAMES FOR SIMILAR CONDITIONS POSSIBLE - HELPS IN ASSESSING SPRAY AND GASEOUS COMBUSTION MODELS.	
SPADACCINI ET AL. (1977) REF. 175	CYLINDRICAL COMBUSTOR WITH CENTRALLY LOCATED PRESSURE ATOMIZING FUEL INJECTOR; AIR INTRODUCED THROUGH AN ANNULUS SWIRLER AROUND FUEL INJECTOR. 	2-D ELLIPTIC	ISO-OCTANE AND B2 DISTILLATE FUEL OIL	TWO SWIRL ANGLES; TWO PRESSURES; TWO INLET TEMPERATURES.	DROPLET VELOCITY - LDV. DROPLET SIZE AND SPRAY TRAJECTORY - LASER HOLOGRAPHY.	THERMO-COUPLE	CO, CO ₂ MONOSPERSIVE INFRA-RED ANALYZER; O ₂ PARAMAGNETIC ANALYZER. C ₁ H ₄ FLAME IONIZATION DETECTOR. COOLED SAMPLING PROBE.	GAS VELOCITY - LDV	CONTOUR PLOT OF DROPLET VELOCITY.	CONTOUR PLOTS	CONTOUR PLOT OF GAS VELOCITY	OTHER	DETAILED DATA SET FOR MODEL ASSESSMENT UNDER DIFFERENT FLOW CONDITIONS.	
WIERZBA (1982) REF. 176	OPPOSED JET COMBUSTOR - RICH KEROSENE-AIR JET WITH A COUNTER-FLOWING AIR STREAM. 	2-D ELLIPTIC	KEROSENE	THREE JET TO AIR VELOCITY RATIOS.	EXTENT OF DROPLET VAPORIZATION USING INDICATOR DYE.	THERMO-COUPLE	CO ₂ , CO, O ₂ SAMPLING PROBE AND GAS CHROMATOGRAPHY AND INFRA-RED ANALYZERS.	GAS VELOCITY	VAPORIZATION REGION.	RADIAL PROFILES AT 8 AXIAL LOCATIONS, CONTOUR PLOTS	CONTOUR PLOTS	OTHER	SOME GEOMETRICAL DETAILS NOT EXACTLY KNOWN	
PROCTOR AND KELLOR (1982) REF. 177	PREVAPORIZING/PREMIKING COMBUSTOR - SHROUDED TUBE AND DISC CONFIGURATION; SIMPLEX PRESSURE ATOMIZING NOZZLE. 	2-D ELLIPTIC	LIQUID PROPANE AND JETA	ONE FOR EACH FUEL	FROM GAS COMPOSITION, INFERING PRESENCE OF H ₂ IN WALL THERMO-COUPLE	FROM GAS COMPOSITION, INFERING PRESENCE OF H ₂ IN WALL THERMO-COUPLE	C ₁ H ₄ , CO, CO ₂ , O ₂ COOLED SAMPLING PROBE AND GAS ANALYSIS		CONTOUR PLOTS	CONTOUR PLOTS	CONTOUR PLOTS	OTHER	SOME PROBLEMS POSED IN MODELING LIQUID FUEL IMPINGEMENT ON INNER TUBE WALLS	

TABLE 12. SPRAY EVAPORATION AND COMBUSTION (CONTD).

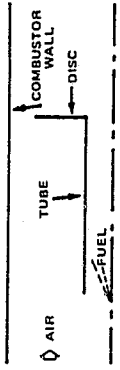
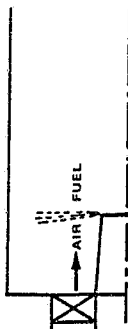
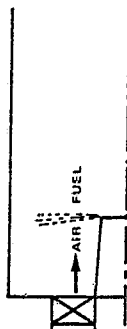
AUTHOR (YEAR)	FLOW DESCRIPTION	FLOW TYPE	FUEL	NUMBER OF CASES	QUANTITIES MEASURED AND MEASUREMENT TECHNIQUE				MEASUREMENT LOCATIONS				REMARKS
					SPRAY FEATURES	TEMPERA- TURE	COMPOSI- TION	OTHER	SPRAY FEATURES	TEMPERA- TURE	COMPOSI- TION	OTHER	
FERGUSON AND MELLOR (1979) REF. 178	PREVAPORIZING/PREHEATING COMBUSTOR-TUBE AND DISC CONFIGURATION; SIMPLE PRESSURE ATOMIZING NOZZLE. 	2-D ELLIPTIC	JETA	ONE	SPRAY FEATURES	THERMO- COUPLE	CO - SAMPLING PROBE; NON-DIS- PERSIVE INFRA-RED ANALYZER; CH ₄ - FLAME IONIZATION DETECTOR.			CONTOUR PLOTS.	CONTOUR PLOTS OF CO AND C ₂ H ₄		SOME PROBLEMS POSED IN MODELING LIQUID FUEL IMPINGEMENT ON INNER TUBE WALLS.
EL-BANHAWY & WHITELAW (1979) REF. 179	CYLINDRICAL COMBUSTOR WITH ROTATING CUP ATOMIZER AND AIR THROUGH A SWIRLER SURROUNDING ATOMIZER. 	2-D ELLIPTIC	KEROSENE	ISO- THERMAL AND COM- BUSTING	SPRAY FEATURES	THERMO- COUPLE	CO ₂ , CO - SAMPLING PROBE, INFRA-RED ANALYZER. O ₂ - PARAMAG- NETIC ANA- LYZER.	ISO- THERMAL AXIAL VELOCITY		RADIAL PROFILES AT 8 AXIAL LOCATIONS	RADIAL PROFILES OF AXIAL VELOCITY AT 3 AXIAL LOCATIONS		DROPLET SIZE DISTRIBUTION AND INJECTION VELOCITY MEASURED - BULET CONDITIONS ACCURATELY KNOWN.
EL-BANHAWY & WHITELAW (1981) REF. 180 SECTION 8.7	AS EL-BANHAWY AND WHITELAW (1979) 	2-D ELLIPTIC	KEROSENE	SIX WITH DIFFERENT SMD AND AIR SWIRL	AXIAL AND TANGEN- TIAL DROP- LET VE- LOCITY - LDV	THERMO- COUPLE WALL TEMP- ERATURE MEASURED.	CO ₂ , CO - SAMPLING PROBE, IN- FRARED ANALYZER. O ₂ - PARAMAG- NETIC ANALYZER.			RADIAL PROFILE OF AXIAL VELOCITY AT 4 AXIAL LOCATIONS AND OF TANGEN- TIAL VE- LOCITY AT ONE AXIAL LOCATION.	CONTOUR PLOTS		ASSESSMENT OF MEASURE- MENT ACCURACY PROVIDED

TABLE 12. SPRAY EVAPORATION AND COMBUSTION (CONTD).

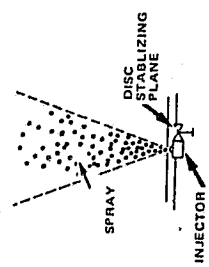
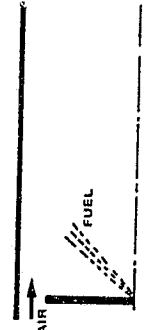
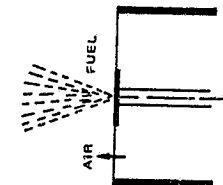
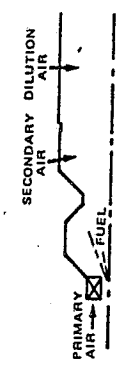
AUTHOR (YEAR)	FLOW DESCRIPTION	FLOW TYPE	FUEL	NUMBER OF CASES	QUANTITIES MEASURED AND MEASUREMENT TECHNIQUE				MEASUREMENT LOCATIONS				REMARKS
					SPRAY FEATURES	TEMPERATURE	COMPOSITION	OTHER	SPRAY FEATURES	TEMPERATURE	COMPOSITION	OTHER	
ATYA AND WHITELAW (1981) REF. 181	VERTICAL SPRAY FLAME IN STILL AIR STABILIZED ON A DISC AT FUEL NOZZLE EXIT PLANE. SOI ID CONE SPRAY WITH TWIN FLUID ATOMIZER 	2-D ELLIPTIC	KEROSENE	TWO DIFFERENT SHOTS.	SPRAY FEATURES DROPLET NUMBER DENSITY - LDV	TEMPERATURE THERMO-COUPLE	COMPOSITION CO, CO ₂ - COOLED SAMPLING PROBE. INFRARED ANALYZER. O ₂ - PARAMAGNETIC ANALYZER. C ₂ H ₄ - FLAME IONIZATION DETECTOR.	OTHER GAS VELOCITY LDV	SPRAY FEATURES RADIAL PROFILE OF DROPLET DENSITY AT 4 AXIAL LOCATIONS	TEMPERATURE AXIAL PROFILE ALONG CENTER LINE. RADIAL PROFILE AT 3 AXIAL LOCATIONS	COMPOSITION AXIAL PROFILE ALONG CENTER LINE. RADIAL PROFILE AT 5 AXIAL LOCATIONS.	OTHER RADIAL PROFILES OF GAS VELOCITY AT 5 AXIAL LOCATIONS.	ASSESSMENT OF MEASUREMENT ACCURACY PROVIDED
TUTTLE, SHIGLER AND MELLOR (1976) REF. 182	SIMPLEX PRESSURE ATOMIZER 	2-D ELLIPTIC	LIQUID PROPANE	ONE		TEMPERATURE THERMO-COUPLE	COMPOSITION CO, C ₂ H ₄			RADIAL PROFILES AT 5 AXIAL LOCATIONS.	RADIAL PROFILES AT 5 AXIAL LOCATIONS.		LIMITED AMOUNT OF DATA FOR DETAILED MODEL ASSESSMENT.
STYLES AND CRIBBER (1977) REF. 183	TWIN FLUID ATOMIZER UNCONFINED FLAME STABILIZED IN A COFLOWING AIR STREAM ON A DISC AT ATOMIZER EXIT 	2-D ELLIPTIC	KEROSENE	HOT AND COLD FLOW.	SPRAY FEATURES DROPLET SIZE AND VELOCITY - LASER DIFFRACTION TECHNIQUE AND LASER ANEMOMETER	TEMPERATURE THERMO-COUPLE	COMPOSITION CO, CO ₂ , H ₂ , CH ₄ QUARTZ MICRO-PROBE AND GAS CHROMATOGRAPHY	AXIAL VELOCITY - LDV	RADIAL PROFILES OF DROPLET SIZE AND VELOCITY AT 2 AXIAL LOCATIONS. AXIAL PROFILE ALONG CENTER LINE.	RADIAL PROFILES AT 5 AXIAL LOCATIONS.	RADIAL PROFILES AT 2 AXIAL LOCATIONS. AXIAL PROFILE ALONG CENTER LINE.	CONTOUR PLOTS OF AXIAL VELOCITY	DROPLET SIZE AND VELOCITY DATA PROVIDED FOR ASSESSMENT OF SPRAY MODEL FEATURES.

TABLE 12. SPRAY EVAPORATION AND COMBUSTION (CONTD).

AUTHOR (YEAR)	FLOW DESCRIPTION	FLOW TYPE	FUEL	NUMBER OF CASES	QUANTITIES MEASURED AND MEASUREMENT TECHNIQUE				MEASUREMENT LOCATIONS				REMARKS
					SPRAY FEATURES	TEMPERA- TURE	COMPOSI- TION	OTHER	SPRAY FEATURES	TEMPERA- TURE	COMPOSI- TION	OTHER	
KAWAGUCHI ET AL. (1981) REF. 184	CAN COMBUSTOR WITH AIRBLAST ATOMIZER AND AIR INTRO- DUCED THROUGH PRIMARY RADIAL SWIRLER, SECONDARY AND DILUTION HOLES. 	3-D ELLIPTIC	KEROSENE	4 CASES WITH DI- FERENT INLET TEMPERA- TURES AND DIFFERENT AIR-FLOW SPLITS.	SPRAY FEATURES	TEMPERA- TURE COUPLE.	COMPOSI- TION CO - WATER COOLED PROBE, NORRIS- PERSIVE INFRARED ANALYZER, C ₂ H ₄ - FLAME IONIZATION DETECTOR.	OTHER	SPRAY FEATURES	TEMPERA- TURE RADIAL PROFILES AT 3 AXIAL LOCATIONS	COMPOSI- TION RADIAL PROFILES AT 3 AXIAL LOCATIONS.	OTHER	DATA PROVIDES FOR MODEL ASSESSMENT UNDER CONDI- TIONS CLOSE TO GAS- TURBINE COMBUSTORS.

5.1.4 Soot Formation and Oxidation

In this paragraph, a data base for assessing soot formation and oxidation models is provided. The assessment procedure will consist of comparing the predicted soot concentration, temperature, concentrations of species (unburnt fuel, CO, CO₂, H₂, H₂O, O₂, N₂) against the experimentally measured values of these quantities. The comparison of predicted and measured soot concentrations is a direct indication of the accuracy of the soot model. Temperature and gas composition are affected by the presence of soot to an extent depending on its concentration. Therefore, assessing the accuracy of the predictions of temperature and gas composition serves to indirectly assess the soot model.

The data base for the soot models is rather inadequate since very few measurements under controlled conditions have been reported in the literature. The reason is the difficulty in accurately measuring soot concentration profiles in a combustor. Quite often, only the exhaust smoke concentration is measured and soot profiles have been measured in only simple flames.

As in the preceding sections, several sources of data (e.g. References 185-194) were found that were not suitable for model assessment due to incomplete specification of the boundary and initial conditions. These have not been included here. Also, measurements related only to gas turbine type fuels have been considered, since it is practically impossible to validate the model and obtain a set of model constants for all types of hydrocarbons. The data base for soot formation and oxidation is presented in Table 13.

TABLE 13. SOOT DATA.

AUTHOR (YEAR)	FLOW DESCRIPTION	FLOW TYPE	FUEL	NUMBER OF CASES	QUANTITIES MEASURED AND MEASUREMENT TECHNIQUE				MEASUREMENT LOCATIONS				REMARKS
					SOOT FEATURES	TEMPERATURE	COMPOSITION	OTHER	SOOT FEATURES	TEMPERATURE	COMPOSITION	OTHER	
PRADO ET AL. (1961) REF. 195	PREHEATED FLAT LAMINAR FLAME STABILIZED BETWEEN A WATER-COOLED SINTERED BRASS PLATE AND A STAINLESS DISC PLATE ABOVE THE BURNER.	1-D PARABOLIC	CH ₄ -O ₂ AND C ₃ H ₈ -O ₂	THREE EQUIVALENCE RATIOS; THREE GAS VELOCITIES.	SOOT VOLUME FRACTION AND PARTICLE SIZE — SAMPLING PROBE AND LASER- LIGHT SCATTERING AND ABSORPTION TECHNIQUES.	THERMOCOUPLE.			SOOT VOLUME FRACTION AND PARTICLE SIZE ALONG FLAME AXIS.	ALONG FLAME AXIS.			THIS DATA CAN BE USED TO ESTABLISH RATE CONSTANTS IN SOOT FORMATION/OXIDATION SINCE UNCERTAINTIES IN FLOW AND TURBULENCE ARE INSIGNIFICANT.
ROCKHORN ET AL. (1961) REF. 196	WATER-COOLED POROUS PLATE FLAT FLAME BURNER. FLAME ENCLOSED IN SHORT CYLINDER PLACED ABOVE BURNER PLATE.	1-D PARABOLIC	C ₃ H ₈ -O ₂ AND C ₃ H ₈ -H ₂ -O ₂	DIFFERENT C/O RATIOS.	SOOT CONCENTRATION AND PARTICLE SIZE — SAMPLING PROBE AND LIGHT SCATTERING TECHNIQUE.				SOOT CONCENTRATION AND PARTICLE SIZE IN BURNER GAS REGION AT 4 AXIAL LOCATIONS. ALSO AS A FUNCTION OF C/O RATIO AT ONE AXIAL LOCATION.				THIS DATA CAN BE USED TO ESTABLISH RATE CONSTANTS IN SOOT FORMATION/OXIDATION SINCE UNCERTAINTIES IN FLOW AND TURBULENCE ARE INSIGNIFICANT.
FLOWER (1962) REF. 197	FUEL-RICH PREMIXED LAMINAR FLAT FLAME ABOVE A COOLED POROUS-PLUG BURNER.	1-D PARABOLIC	CH ₄ -O ₂	THREE DIFFERENT EQUIVALENCE RATIOS.	PARTICLE DIAMETER, PARTICLE NUMBER DENSITY, SOOT VOLUME FRACTION — DIFFUSION BROADENING SPECTROSCOPY OR HOLOGRAPHY TECHNIQUE.				PARTICLE DIAMETER, NUMBER DENSITY AND SOOT VOLUME FRACTION ALONG FLAME AXIS.				DATA CAN BE USED FOR ESTABLISHING RATE CONSTANTS IN SOOT FORMATION/OXIDATION

ORIGINAL PAGE IS
OF POOR QUALITY

TABLE 13. SOOT DATA (CONTD).

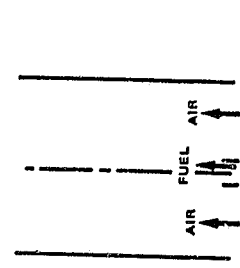
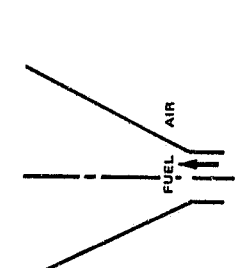
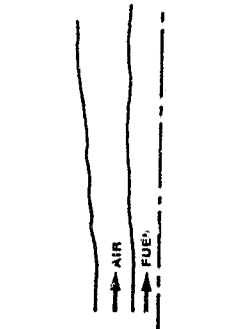
AUTHOR (YEAR)	FLOW DESCRIPTION	FLOW TYPE	FUEL	NUMBERS OF CASES	QUANTITIES MEASURED AND MEASUREMENT TECHNIQUE				MEASUREMENT LOCATIONS				REMARKS	
					SOOT FEATURES	TEMPERA- TURE	COMPOSI- TION	OTHER	SOOT FEATURES	TEMPERA- TURE	COMPOSI- TION	OTHER		
ROPER AND SMITH (1979) REF. 198	COAXIAL FUEL/AIR JETS - LAMINAR DIFFUSION FLAME 	2-D PARABOLIC	CH ₄	FOUR VALUES OF EQUIVAL- ENCE RATIO.	SOOT CON- CENTRA- TION - OPTICAL ABSORP- TION USING A SENSI- TIVE DUAL- BEAM DENSI- TOMETER.				CONTOURS OF SOOT CONCENTR- ATION				SOOT CONCENTRATION MEASURED MAY BE WIDER BY A FACTOR OF 1.5-2.0.	
DALZELL ET AL (1970) REF. 199	FREE TURBULENT ACETYLENE DIFFUSION FLAME IN STAGNANT AIR 	2-D PARABOLIC	C ₂ H ₂	ONE	SOOT CON- CENTRA- TION - LIGHT SCATTER- ING METHOD.				RADIAL PROFILES OF SOOT CONCENTR- ATION AT 10 AXIAL LOCATIONS.				SOOT PARTICLE SIZE FOUND TO BE ABOUT UNIFORM THROUGHOUT BURNOFF REGION.	
KENT ET AL (1981) REF. 200	MODIFIED WOLFRARD-PARKER BURNER - LAMINAR DIFFUSION FLAME 	2-D PARABOLIC	C ₂ H ₄	ONE	SOOT VOLUME FRACTION, PARTICLE NUMBER DENSITY AND AVERAGE PARTICLE SIZE - LIGHT SCATTERING METHOD.	THERMO- COUPLE			TRANS- VERSE PROFILES OF SOOT CONCENTR- ATION AT 6 HEIGHTS ABOVE BURNER LIP.				TRANS- VERSE PROFILES OF AXIAL VELOCITY AT 6 HEIGHTS ABOVE BURNER LIP.	CH ₄ FUEL, NOT OF DIRECT INTEREST FOR GAS-TURBINE COMBUSTORS.

TABLE 13. SOOT DATA (CONTD).

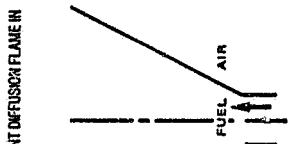
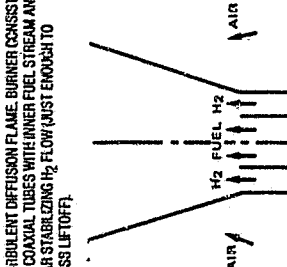
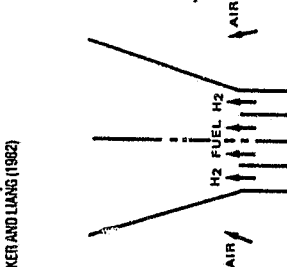

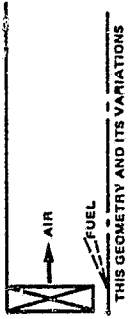

AUTHOR (YEAR)	FLOW DESCRIPTION	FLOW TYPE	FUEL	NUMBER OF CASES	QUANTITIES MEASURED AND MEASUREMENT TECHNIQUE			MEASUREMENT LOCATIONS			REMARKS
					SOOT FEATURES	TEMPERATURE	COMPOSITION	OTHER	SOOT FEATURES	TEMPERATURE	
MAGNUSSEN ET AL. (1979) REF. 201	VERTICAL FREE TURBULENT DIFFUSION FLAME IN STAGNANT AIR 	2-D PARABOLIC	C ₂ H ₂	8 CASES	SOOT CONCENTRATION - LIGHT SCATTERING METHOD.				AXIAL PROFILE OF SOOT CONCENTRATION ALONG CENTERLINE.		INLET VELOCITY AND TEMPERATURE PROFILE MEASURED. FUEL DILUTED WITH H ₂ AND H ₂ O.
BECKER AND LANG (1982) REF. 202	FREE TURBULENT DIFFUSION FLAME. BURNER CONSISTS OF PAIR OF COAXIAL TUBES WITH INNER FUEL STREAM AND ANNULAR STABILIZING H ₂ FLOW (JUST ENOUGH TO SUPPRESS LIFTOFF). 	2-D PARABOLIC	CH ₄ , C ₂ H ₂ , C ₂ H ₄ , C ₂ H ₆ , C ₃ H ₈	MEASUREMENTS ON A RANGE OF JETVELOCITIES AND DIFFERENT FUELJET DIAMETERS.	SOOT CONCENTRATION - AEROSOL SAMPLING FILTER.			FLAME RADIATION - WATER-COOLED TO ELIMINATE RADIATION-DIAPHRAGM.	SMOKE EMISSIONS AT EXIT FLAME.		RADIATION MEASUREMENTS PROVIDED FOR ASSESSMENT OF RADIATION MODEL ALSO.
BECKER AND YANHAZART (1977) REF. 203	AS BECKER AND LANG (1982) 	2-D PARABOLIC	C ₂ H ₆ , C ₂ H ₂	ONE FOR EACH FUEL.	SOOT CONCENTRATION - LIGHT SCATTERING TECHNIQUE.				SOOT CONCENTRATION ALONG FLAME AXIS.		C ₂ H ₂ FUEL NOT OF DIRECT INTEREST FOR GAS-TURBINE COMBUSTORS.

TABLE 13. SOOT DATA (CONTD).

AUTHOR(S) (YEAR)	FLOW DESCRIPTION	FLOW TYPE	FUEL	NUMBER OF CASES	QUANTITIES MEASURED AND MEASUREMENT TECHNIQUE				MEASUREMENT LOCATIONS				REMARKS
					SOOT FEATURES	TEMPERATURE	COMPOSITION	OTHER	SOOT FEATURES	TEMPERATURE	COMPOSITION	OTHER	
PRADO ET AL. (1977) REF. 204	CYLINDRICAL BURNER WITH AIR-ASSISTED FUEL SPRAY NOZZLE AND AIR INTRODUCED THROUGH SWIRLER SURROUNDING THE NOZZLE. 	2-D ELLIPTIC	AVIATION KEROSENE AND BENZENE	5 VALUES OF EQUIVALENCE RATIO; 3 ATOMIZING AIR PRESSURES; 2 COLD GAS VELOCITIES	SOOT CONCENTRATION - WATER COOLED PROBE AND SAMPLING FILTER				AXIAL PROFILE OF SOOT CONCENTRATION ALONG CENTERLINE				DISCUSSION OF SAMPLING ERROR PROVIDED.
HOULT (1979) REF. 205	FLAME TUBE BURNER CONSISTING OF A CIRCULAR TUBE WITH A CENTRALLY PLACED FUEL INJECTOR SURROUNDED BY AN AIR SWIRLER. 	2-D ELLIPTIC	VARIOUS BLENDS OF DIFFERENT FUELS	FOUR GEOMETRIES AND THREE ATOMIZING AIR PRESSURES	SOOT CONCENTRATION - WATER-FLUSHED PROBE AND A FIBER-GLOSS FILTER				AXIAL PROFILE OF SOOT CONCENTRATION ALONG CENTERLINE				DATA PROVIDES FOR ASSESSMENT UNDER DIFFERENT FLOW CONDITIONS.
JANOTA ET AL. (1977) REF. 206	CYLINDRICAL COMBUSTOR WITH A CENTRAL FUEL INJECTOR AND A COAXIAL ANNULAR AIR-STREAM. 	2-D ELLIPTIC	DIESEL FUEL	ONE	SOOT CONCENTRATION - QUENCHED STAINLESS STEEL PROBE AND COLLECTING FILTER		CO, CO ₂ - QUENCHED STAINLESS STEEL PROBE AND GAS ANALYSIS.		CONTOUR PLOT OF SOOT CONCENTRATION		CONTOUR PLOTS OF CO, CO ₂		RATE CONSTANTS FOR DIESEL FUEL PROBABLY DIFFERENT FROM THOSE OF AVIATION FUELS.

5.2 Data Base from Garrett Gas Turbine Combustors

A number of gas turbine combustors have been mapped at Garrett over the last ten years. A brief description of the Garrett data base is given in the following paragraphs.

5.2.1 Can Combustor Mapping

A nonreacting can combustor with swirlers at the dome was mapped²⁰⁷ in 1973 for comparison with the k- ϵ turbulence model. A schematic of the burner along with the flow split is shown in Figure 5.2-1. A calibrated three-hole wedge probe and liquid micro-manometer were used to measure the radial distribution of the yaw angle, static and total pressures at different axial stations.

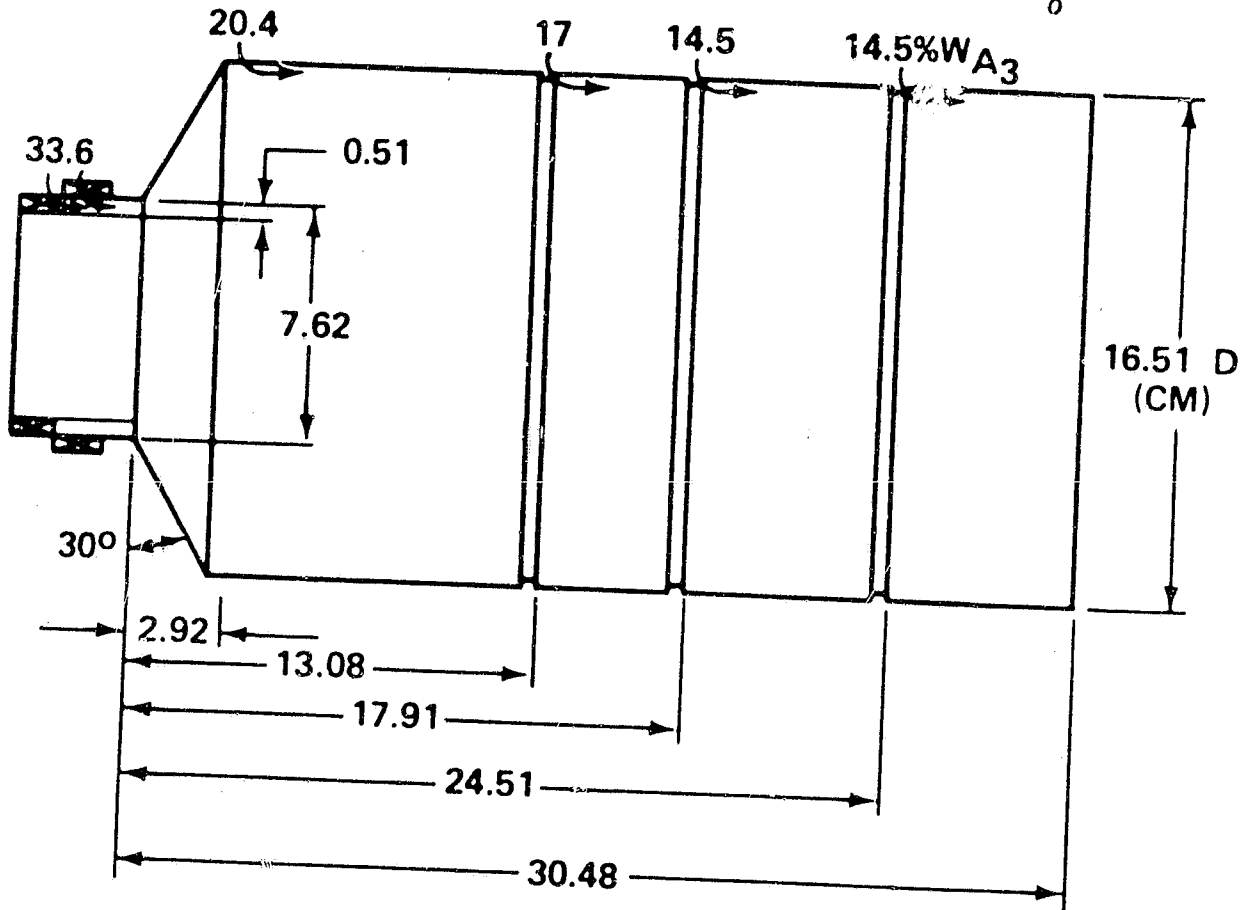
As part of model validation under the USARTL Design Criteria Program, another can combustor nonreacting flow was mapped at different throughflow rates. This combustor was filled with 21 measurement ports.

A calibrated five-hole pyramid probe was traversed across the can combustor at three circumferential locations and seven axial stations. Four traverses were made in the primary zone, seven in the intermediate, and ten in the dilution zone. The probe mounts and the test conditions are shown in Figure 5.2-2.

Reacting flow mapping was accomplished on a similar can combustor, shown in Figure 5.2-3. Radial profiles of CO, CO₂, NO_x, and unburned hydrocarbons were measured at axial stations 6.0, 8.5, 10.4, 12.9, 15.4, 18.8, 21.3, and 26.2 cm downstream from the fuel nozzle face. Five circumferential stations were mapped to determine the profile variations in the circumferential direction. The mapping was conducted for both gaseous (natural gas) and liquid fuels (Jet A) over a wide range of operating conditions. The fuel nozzles used for each fuel are shown in Figure 5.2-4.

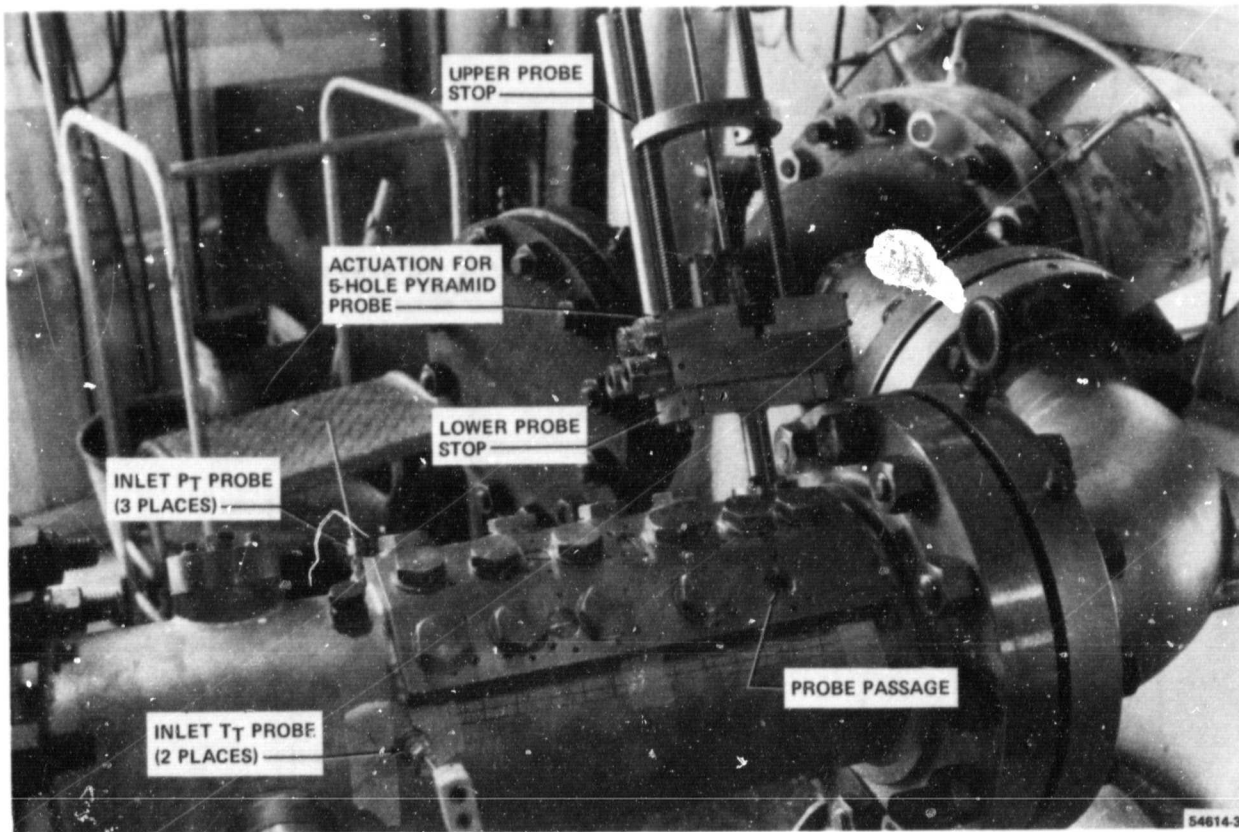
ORIGINAL PAGE IS
OF POOR QUALITY

$P_3 = .984 \text{ ATM}$ $T_3 = 723^\circ\text{R}$ $W_{A_3} = .7297 \text{ PPS}$ $\frac{W\sqrt{\theta}}{\delta} = .874$



$$\frac{\Delta P}{P} = 4.1\%$$

Figure 5.2-1. Nonreacting Swirling Combustor Flow Validation.

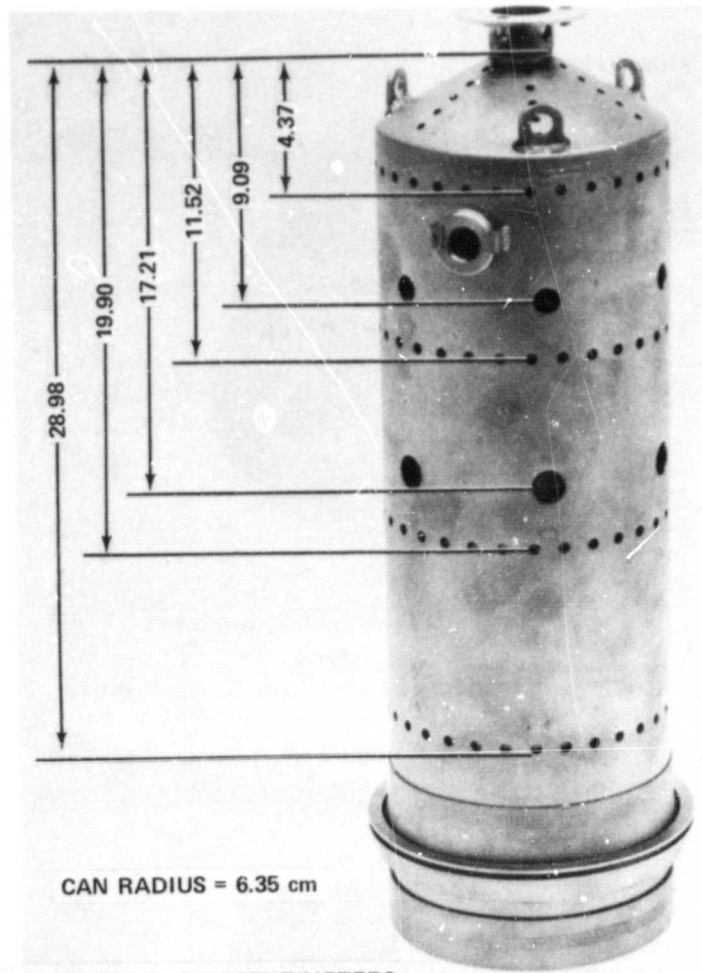


○ TEST CONDITIONS

COND #	P ₃ (ATM)	T ₃ (K)	W _{a3} (Kg/s)	$\frac{\Delta P}{P}$ (%)
1	10.00	288	1.818	3.25
2	10.03	288	2.263	5.01
3	9.98	288	2.736	7.39

Figure 5.2-2. Cold Flow Can Combustor Mapping Setup and Test Conditions.

ORIGINAL PAGE IS
OF POOR QUALITY



ALL DIMENSIONS IN CENTIMETERS

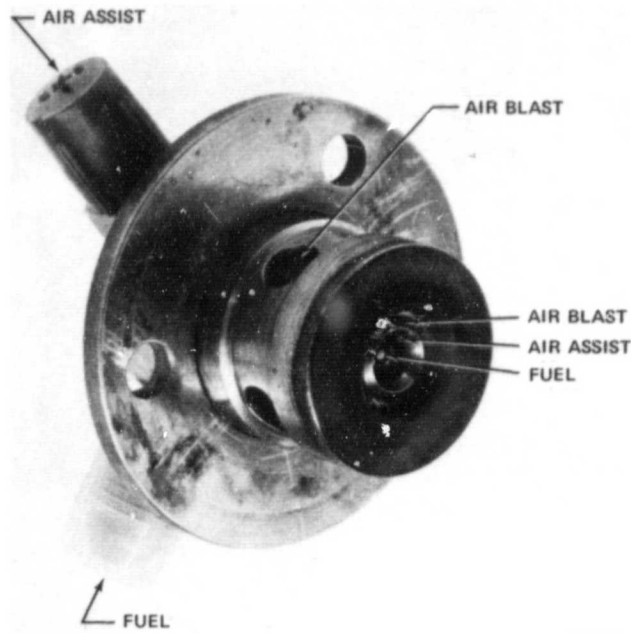
54122-1

REACTING FLOW CAN COMBUSTOR GEOMETRICAL DETAILS

ORIFICE TYPE	NO. OF ORIFICES	SIZE (cm)	GEOMETRIC AREA, cm ²	AXIAL DISTANCE (cm)
DOME LOUVERS	30	0.36	3.02	—
PRIMARY	6	1.12	5.89	9.09
DILUTION	6	1.42	9.53	17.21
COOLING SLOT LIP				
#1	30	0.44	4.6	5.05
#2	30	0.48	5.43	12.20
#3	30	0.48	5.43	20.59
#4	30	0.48	5.43	29.67

Figure 5.2-3. Can Combustor for Reacting Flow Mapping.

ORIGINAL PAGE IS
OF POOR QUALITY



54113-1

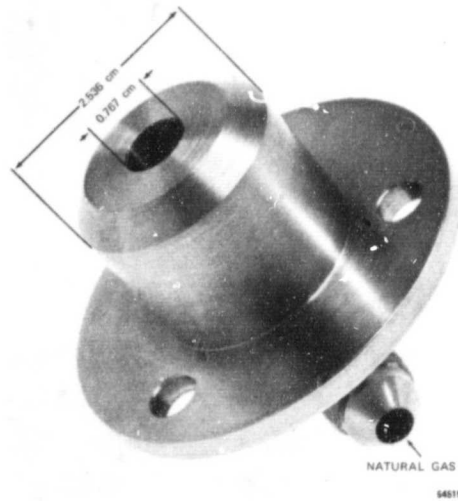


Figure 5.2-4. Natural Gas Nozzle and Airblast Nozzle Used for the Can Combustor Mapping.

A water/steam-cooled stainless steel emissions probe with ten individual radial sampling points was used for the combustion emissions mapping.

5.2.2 Annular Combustor Mapping

A reverse-flow premix/prevaporizing (PM/PV) annular combustion system that is compatible with the Garrett TFE731-2 turbofan engine envelope was designed and tested to demonstrate combustor technology capable of meeting the 1979 EPA emission standards for TI class engines as part of the NASA Pollution Reduction Technology Program. To better understand the performance characteristics of this combustion system, internal radial profiles of gaseous emissions were measured in an atmospheric test rig.

The piloted PM/PV combustion system incorporates two axially staged burning zones, as shown in Figure 5.2-5. The radial profiles of CO, CO₂, UHC, and NO_x were measured at four different axial-stations and six circumferential (θ) planes within the main combustion zone. A water/steam-cooled probe was used to obtain radial profiles. The internal emissions mapping was conducted at one atmosphere in a combustor rig without the transition liner. The effect of different parameters including combustor inlet temperature (T_3), overall fuel/air ratio, and fuel-flow splits between the pilot and PM/PV combustion zones on the emissions profiles were studied. The mapping was conducted with propane as PM/PV fuel to simulate complete evaporation; however, Jet A fuel was used for the pilot.

Information concerning the internal flow field of a TFE731 production combustor (Figure 5.2-6) was provided through measurements of CO₂, CO, UHC, and NO_x taken inside the combustor primary, intermediate, and dilution zones at atmospheric test conditions.

ORIGINAL PAGE IS
OF POOR QUALITY

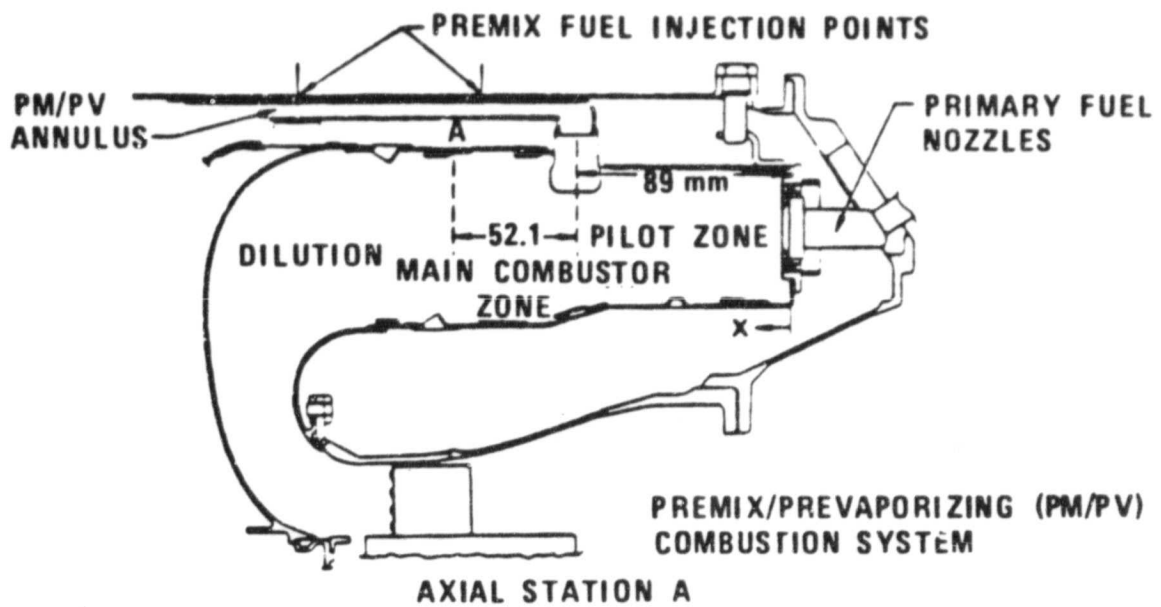


Figure 5.2-5. Axially Staged Burning Zones of the Piloted PM/PV Combustion System.

ORIGINAL PAGE IS
OF POOR QUALITY

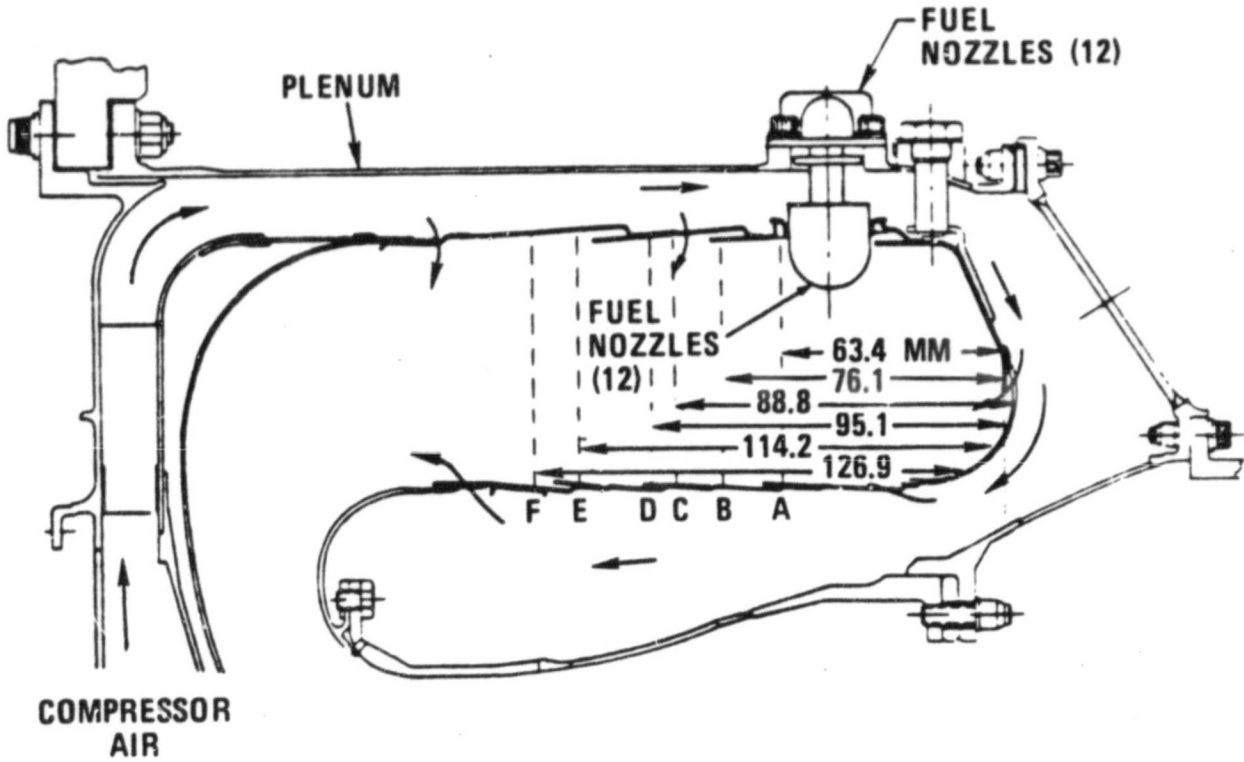


Figure 5.2-6. Emission Sampling Probe Stations Inside the TFE731 Combustor.

The emissions probe used for the internal mapping was the same as the one used earlier to map the PM/PV Concept 3 combustor. The eight individual sampling ports of the probe were manifolded together to obtain only averages in the radial direction. The measurements were taken at different axial stations (as shown in Figure 5.2-6) in the primary and secondary regions.

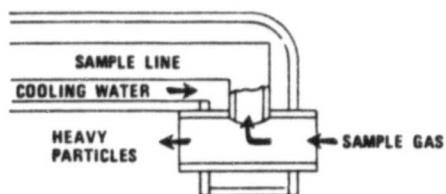
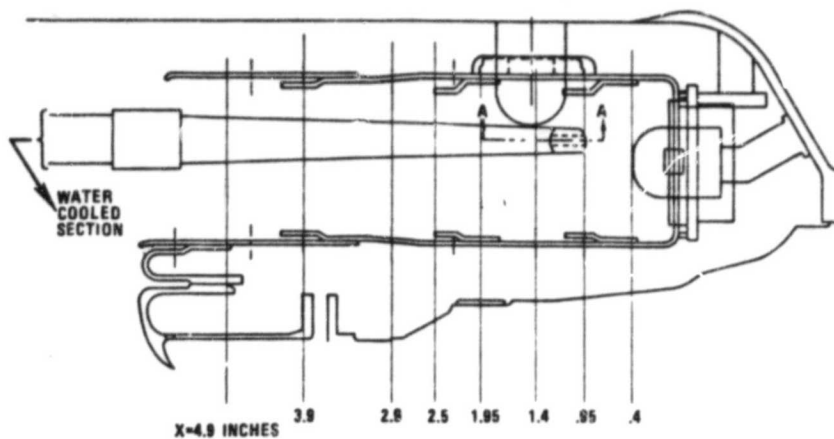
Detailed internal gaseous emissions and temperature measurements inside the Uprate T76 combustor primary zone have been conducted at various axial locations.

A single-point, water-cooled, emissions probe with an end cap (Figure 5.2-7) was designed for use in the primary zone. This probe is intended to separate relatively large liquid fuel droplets from the gas sample. The end-cap feature was also used in the construction of a ceramic radiation shield for the aspirated thermocouple used to measure primary zone temperatures.

Emissions samples were taken at five different axial positions from 1.016 to 6.35 cm from the dome. Temperature measurements were taken from the dome to the dilution zone. The measured sector extended over 36 degrees and was centered on a main fuel nozzle. Seven circumferential stations were selected to correspond with areas of carbon deposition in the Uprate T76 combustor.

Most of the data was taken at an altitude idle-engine condition and also at the sea-level design condition. Two combustors of the same part number were measured. Fuel/air ratios nearly twice the stoichiometric values were measured at the discharge of the primary zone for the design condition, indicating poor primary zone mixing.

ORIGINAL PAGE IS
OF POOR QUALITY



DETAIL OF EMISSIONS PROBE END CAP - SECTION A-A

Figure 5.2-7. Schematic of Emissions Probe and Measurement Locations for Fuel/Air Rate Profiles in the UT76 Combustor.

SECTION VI

6.0 SIMPLE FLOWS

The results for the benchmark test cases (shown in Table 3) are presented in the following four categories:

- o Model evaluation for simple flows
- o Model evaluation for complex nonswirling flows
- o Model evaluation for swirling flows
- o 3-D jet-mixing flow validation

These categories are selected in increasing order of complexity and, for each category, the results will be presented for nonreacting and reacting flows. In this section, discussion of results and model evaluation for simple flows are presented. To present the results, the predictions will be shown by lines and the data will be represented by symbols throughout this report.

6.1 Flow Over a Flat Plate

One of the benchmark test cases selected from the assembled data base is the flow over a flat plate, for which measurements were made by Watts and Brundrett⁶⁷. Their test plate was 2.44 m long with boundary layer trips placed near the leading edge to make the boundary layer fully turbulent. The mean velocity and the turbulence velocity fluctuations were measured with a hot-wire probe at $x = 0.244, 0.462, 0.8466, 1.163, 1.4656$ and 2.2743 m. The free stream velocity for this test case was 20.8 m/s. A schematic of this flow geometry is shown in Figure 6.1-1.

Computations for this case were made using the Garrett 2-D parabolic code, and predictions were obtained with the following models:

- o Standard $k-\epsilon$ model
- o Standard $k-\epsilon$ model with near-wall low Reynolds number correction
- o Algebraic stress model (ASM)
- o ASM with low Reynolds number correction

For all these cases, the initial conditions were applied at $x = 0.244$ using the measured profiles. One hundred cross-stream grid points were used in these computations. The grid distributions were selected so that the nodes were closely spaced near the wall and are farther apart near the edge of the boundary layer. For the standard $k-\epsilon$ model, the wall function treatment outlined in Section 4.2 was used to specify the wall boundary conditions.

The predicted mean velocity profiles using the standard $k-\epsilon$ model are shown in Figure 6.1-2. This figure shows that the agreement between data and predictions was poor. Problems in this computation were associated with the wall function approach for prescribing the boundary conditions at the near-wall nodes.

One way to circumvent the application of the wall functions is to apply low Reynolds number corrections to the k and ϵ equations that will enable k and ϵ to be zero at the wall in a consistent manner. From the survey of literature for low Reynolds number corrections, the model of Chien¹⁷ was selected for these computations. In Chien's model, the source terms and exchange coefficients in the k and ϵ equations have been modified. The governing equations for k and ϵ , still retain the form shown in Equation (1). The difference arises in equations (2) and (4). The modified terms in Chien's model are

$$S_k = G_k - \rho \epsilon - 2\mu \frac{k}{y^2} \quad (133)$$

and,

$$S_\epsilon = (C_1 G_k - C_2 f_2 \rho \epsilon) \frac{\epsilon}{k} + E \quad (134)$$

$$\Gamma_{\text{eff},k} = \mu + \mu_t f_\mu \quad (135)$$

where,

$$f_\mu = 1.0 - \exp(-0.0115 y^+), \quad (136)$$

$$y^+ = \frac{\rho u_* y}{\mu}$$

$$f_2 = 1.0 - 0.2 \left[\frac{\Gamma / \left(\frac{\rho k^2}{6\mu\epsilon} \right)^2}{\left(\frac{\rho k^2}{6\mu\epsilon} \right)^2} \right] \quad (137)$$

$$E = -2\mu \frac{\epsilon}{y^2} \exp[-0.5 y_+] \quad (138)$$

$$\Gamma_{\text{eff},\epsilon} = (\mu + \mu_t) / \sigma_\epsilon \quad (139)$$

Here, u_* is determined by using the linear part of the law of the wall,

$$u = u_* y_+, \quad 0 \leq y_+ \leq 11.5 \quad (140)$$

With the modified terms in the k and ϵ equations, the wall boundary conditions at the wall ($y=0$) are:

$$k = 0$$

$$\epsilon = 0$$

It should be recognized that for improving near-wall solution accuracy with Chien's modification, one must employ a number of grid points inside the viscous sublayer. This is not always possible for elliptic flows. Consequently, in this report, Chien's corrections are applied only for parabolic flows. In all the computations with Chien's correction, approximately 10 nodes were distributed in the viscous sublayer.

A comparison between the data and the predicted results using Chien's correction are shown in Figure 6.1-3. A significant improvement in the agreement and predictions is obtained with the low Reynolds number correction over the wall function approach in the standard $k-\epsilon$ model.

Figure 6.1-4 illustrates the predicted results for mean velocity using the algebraic Reynolds stress model. In the ASM the value of the coefficient C_D is computed from equation (23) while the standard $k-\epsilon$ model assumes a constant value of C_D . This parameter, C_D , is used for calculating the turbulence diffusion rate. Figure 6.1-4 shows that the ASM is in excellent agreement with the data of Watts and Brundrett. Application of the low Reynolds number correction on the ASM does not appreciably improve the mean velocity predictions. These results are presented in Figure 6.1-5. However, the application of Chien's low Reynolds number correction substantially improves the prediction of turbulence kinetic energy components. A comparison of the predicted turbulence kinetic energy profiles at $x = 1.8735$ m using the four models are presented in Figure 6.1-6. The predicted turbulence kinetic energy values, using the standard $k-\epsilon$ model, are slightly higher than the measured values. The peak k value near the wall is significantly higher than the measurements. When Chien's low Reynolds number correction is applied to the $k-\epsilon$ model, the near-wall kinetic energy values are in better agreement with the data. The ASM predictions for k are also higher than the data, but is slightly better in comparison

with the $k-\epsilon$ model predictions. The application of the low Reynolds number correction significantly improves the predicted k values.

A comparison between data and predicted time mean fluctuating velocity components at $x = 1.8735$ is shown in Figure 6.1-7. The ASM predicts much higher peak values for u' , v' , and w' components compared to the data. Application of the low Reynolds number correction yields good agreement with the data.

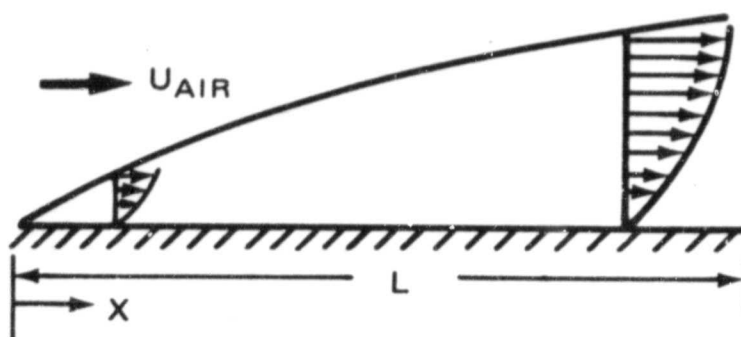
Based on the comparison between predictions and data on a flat plate turbulent boundary layer, the following conclusions can be made:

- o The standard $k-\epsilon$ model gives qualitatively good results. Significant improvements in mean velocity profiles are achieved by applying Chien's low Reynolds number correction to the $k-\epsilon$ model (low Reynolds $k-\epsilon$).
- o Algebraic stress model results are as good as the low Reynolds $k-\epsilon$ model in regard to mean velocity profile.
- o The low Reynolds number correction is required for achieving good near-wall turbulent kinetic energy profiles with both $k-\epsilon$ and ASM models.
- o Individual fluctuating velocity components are reasonably well correlated by ASM except in the viscous sub-layer, where significant improvements are obtained by applying the low Reynolds number correction.

ORIGINAL PAGE IS
OF POOR QUALITY.

WATTS AND BRUNDRETT

FLOW OVER A FLAT PLATE



$L = 0.23 \text{ M}$
 $(U_{AIR} = 20.8 \text{ M/S})$
 $L = 2.44 \text{ M}$

Figure 6.1-1. Watts and Brundrett⁶⁷ Setup for Turbulent Flow over a Flat Plate.

ORIGINAL PAGE IS
OF POOR QUALITY

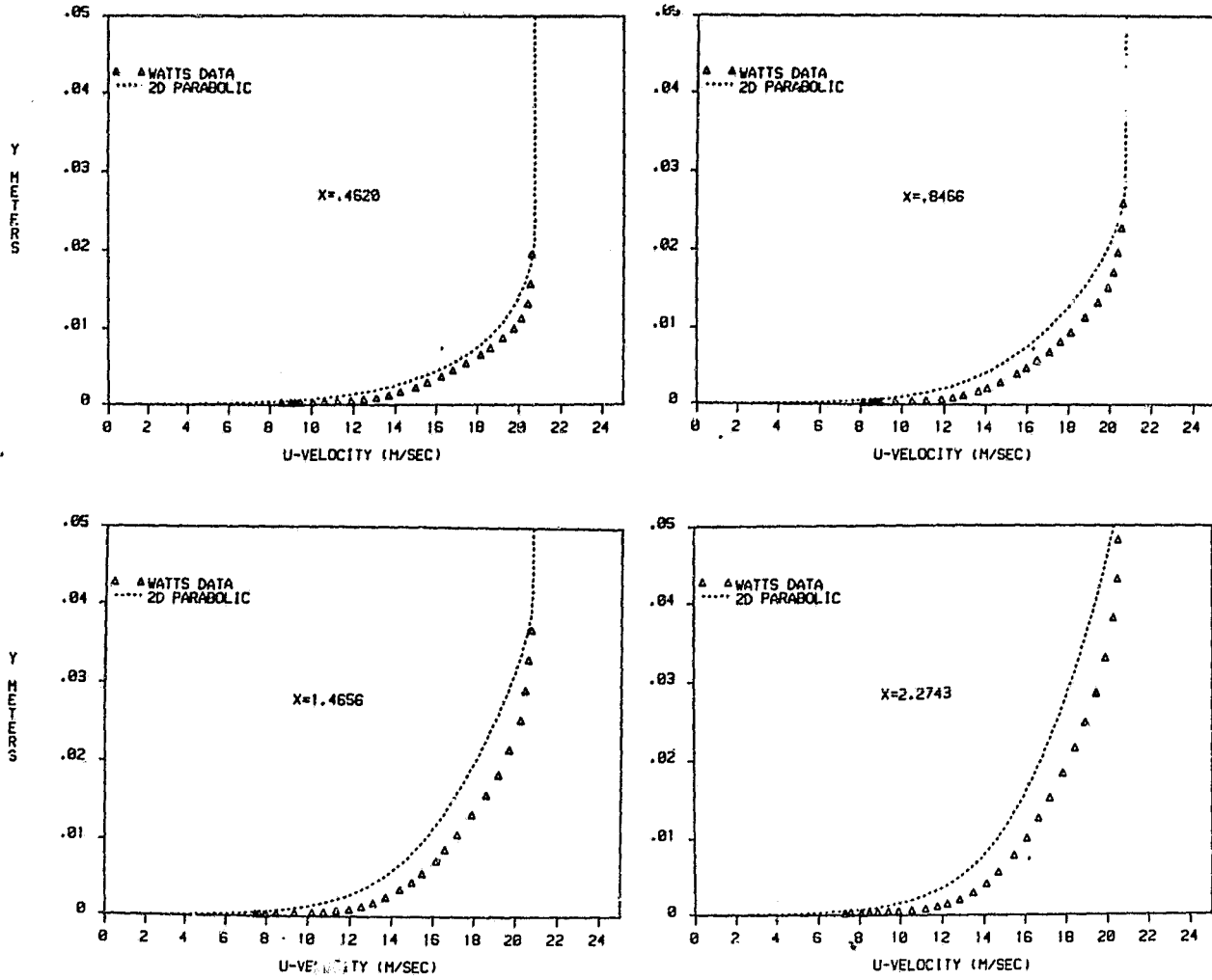


Figure 6.1-2. Turbulent Boundary Layer Mean Velocity Profiles with the Standard k- ϵ Model.

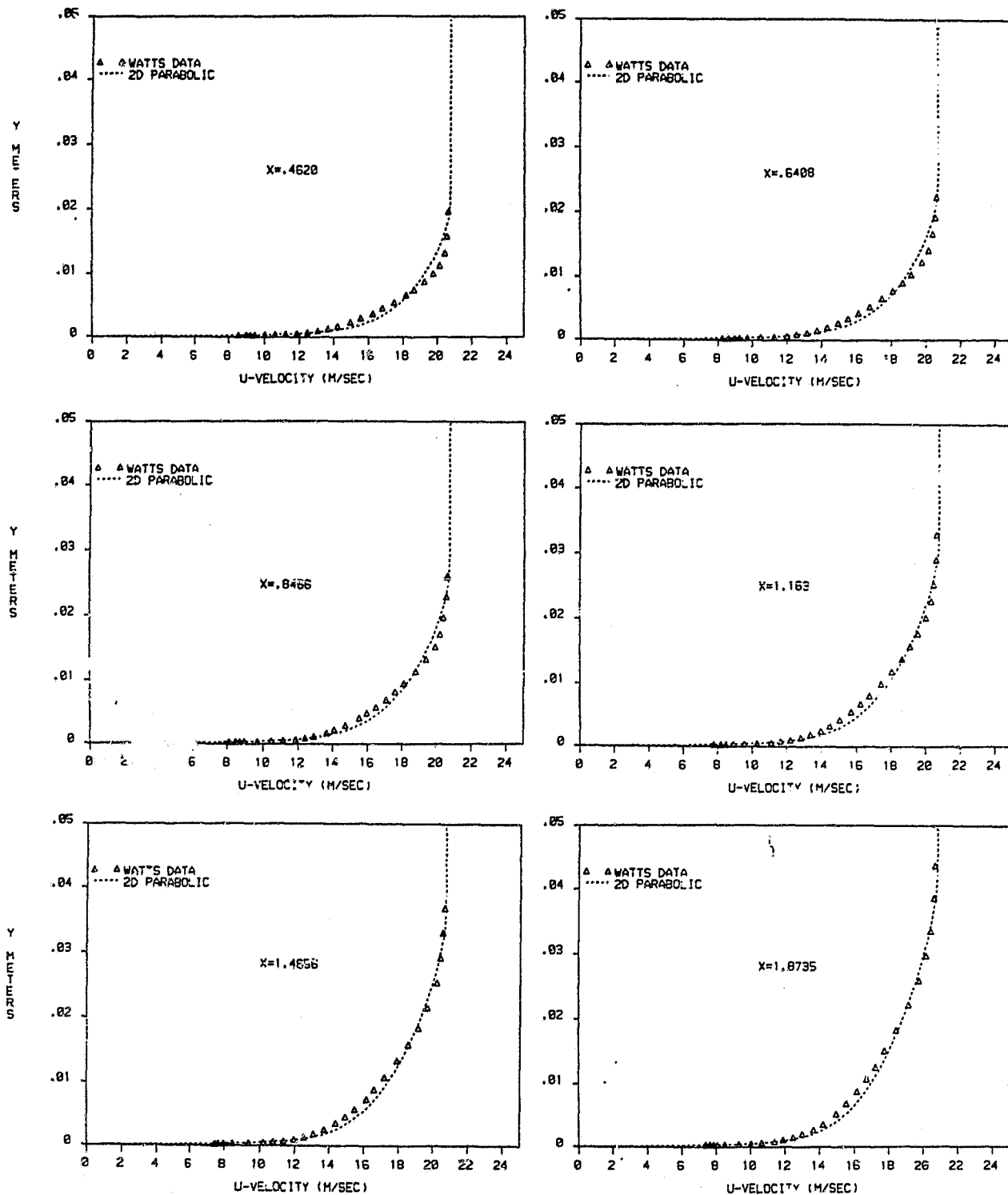


Figure 6.1-3. Turbulent Boundary Layer Mean Velocity Profiles with the $k-\epsilon$ Model and Chien's Low Reynolds Number Correction (Low Reynolds Number $k-\epsilon$ Model).

ORIGINAL PAGE 10
OF POOR QUALITY

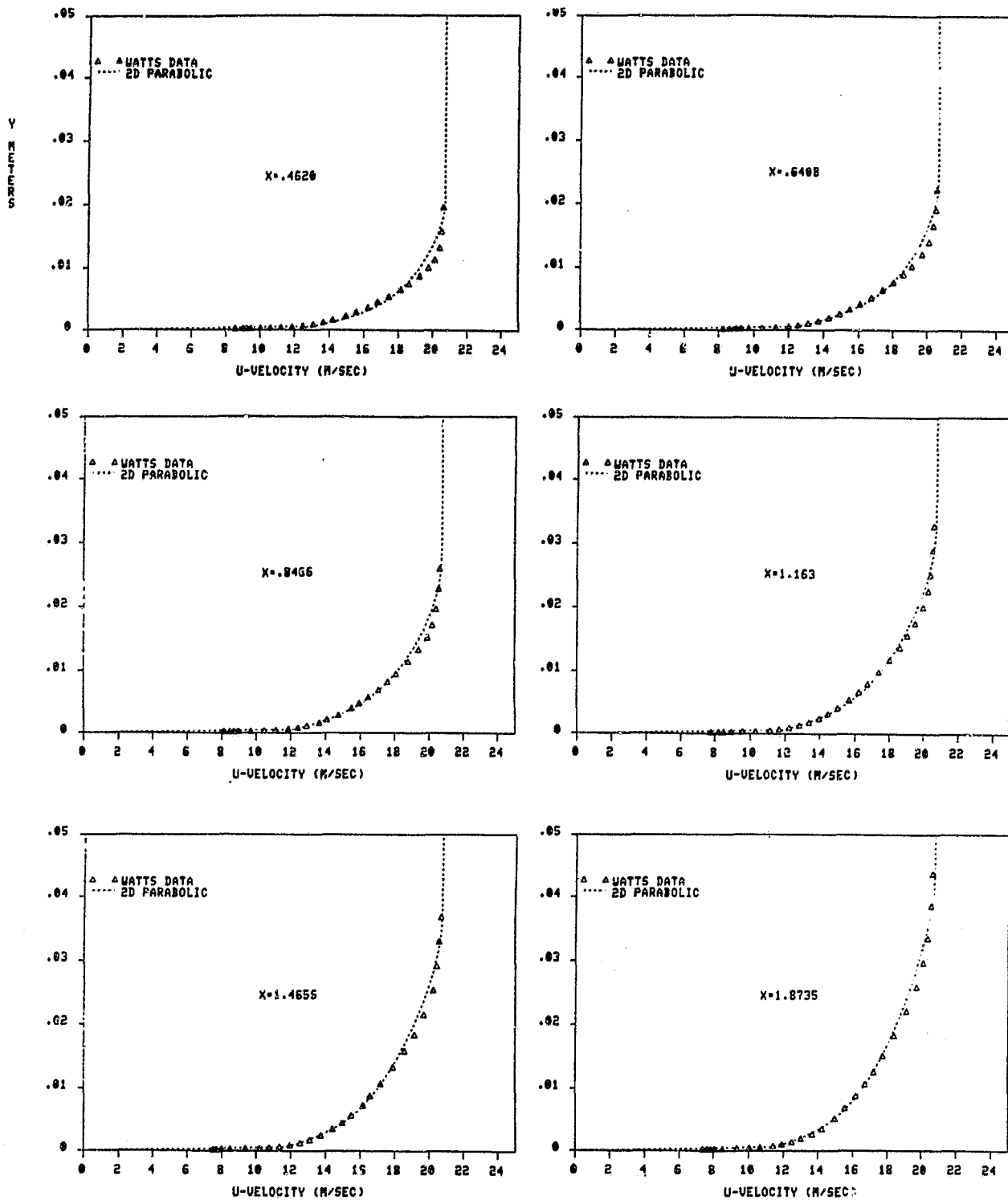


Figure 6.1-4. Turbulent Boundary Layer Mean Velocity Profiles With the Algebraic Stress Model (ASM).

ORIGINAL PAGE IS
OF POOR QUALITY

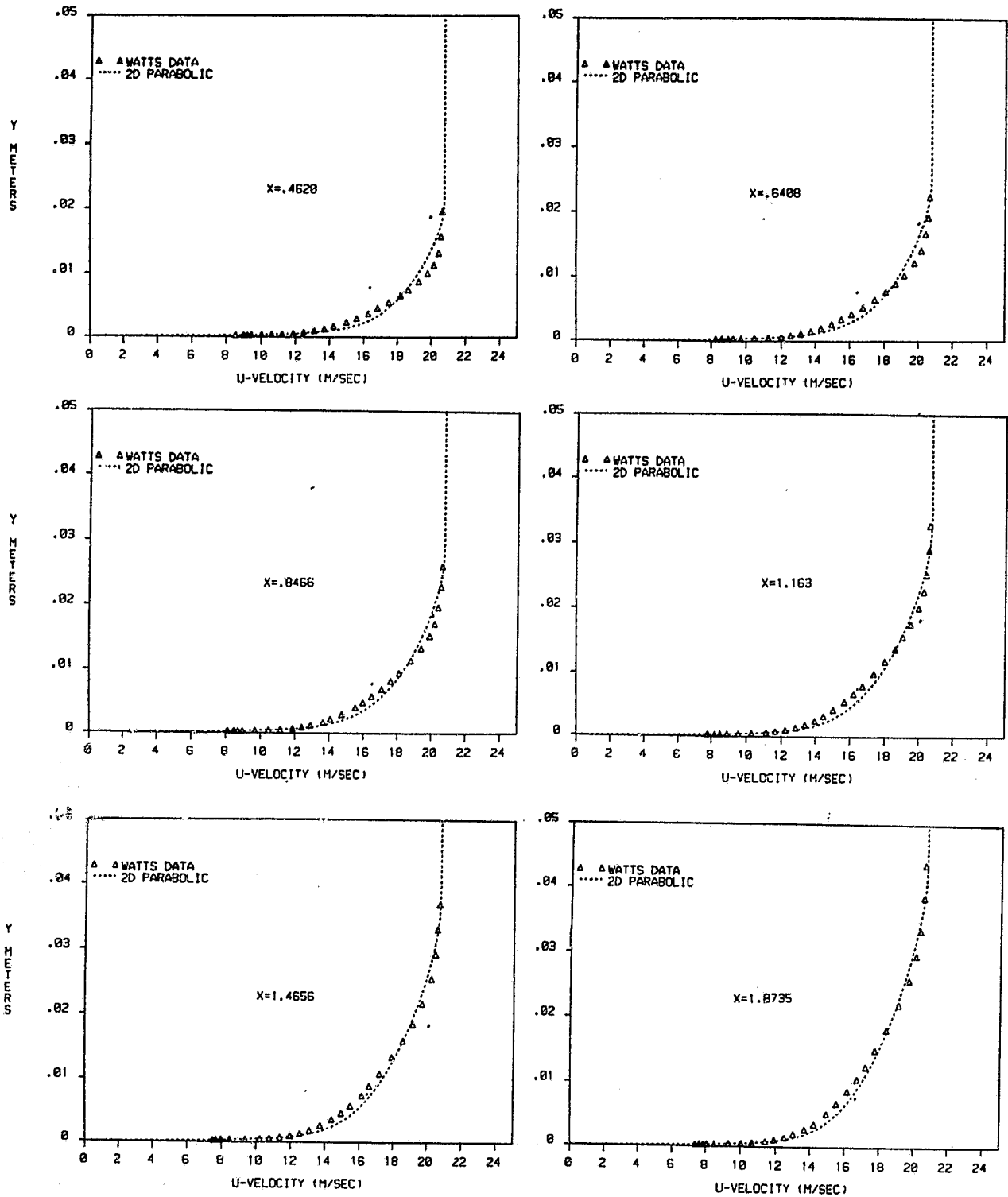


Figure 6.1-5. Turbulent Boundary Layer Mean Velocity Profiles With ASM Modified By Low Reynolds Number Correction.

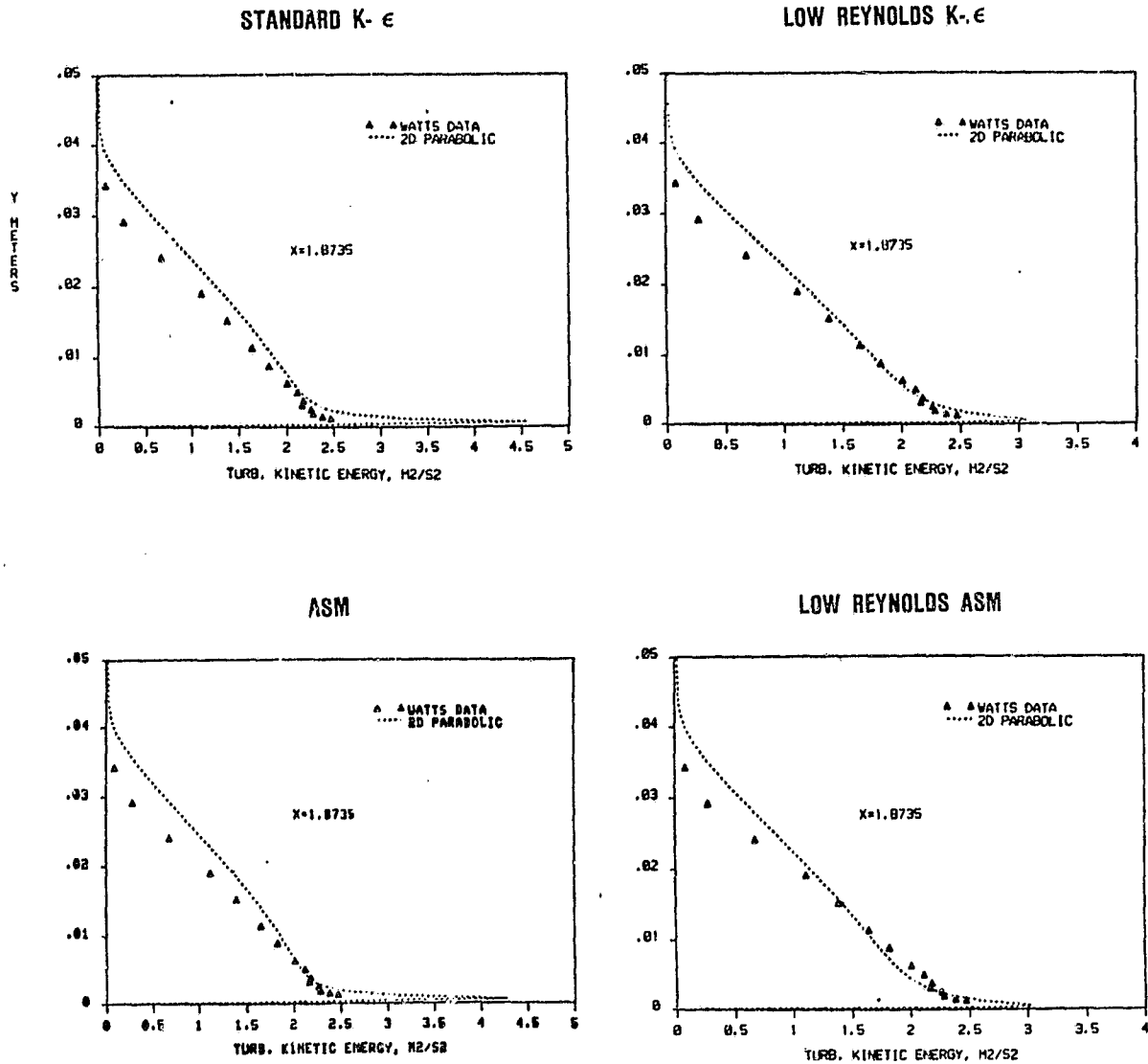


Figure 6.1-6. Turbulent Kinetic Energy Profiles Predicted By the Four Turbulence Models.

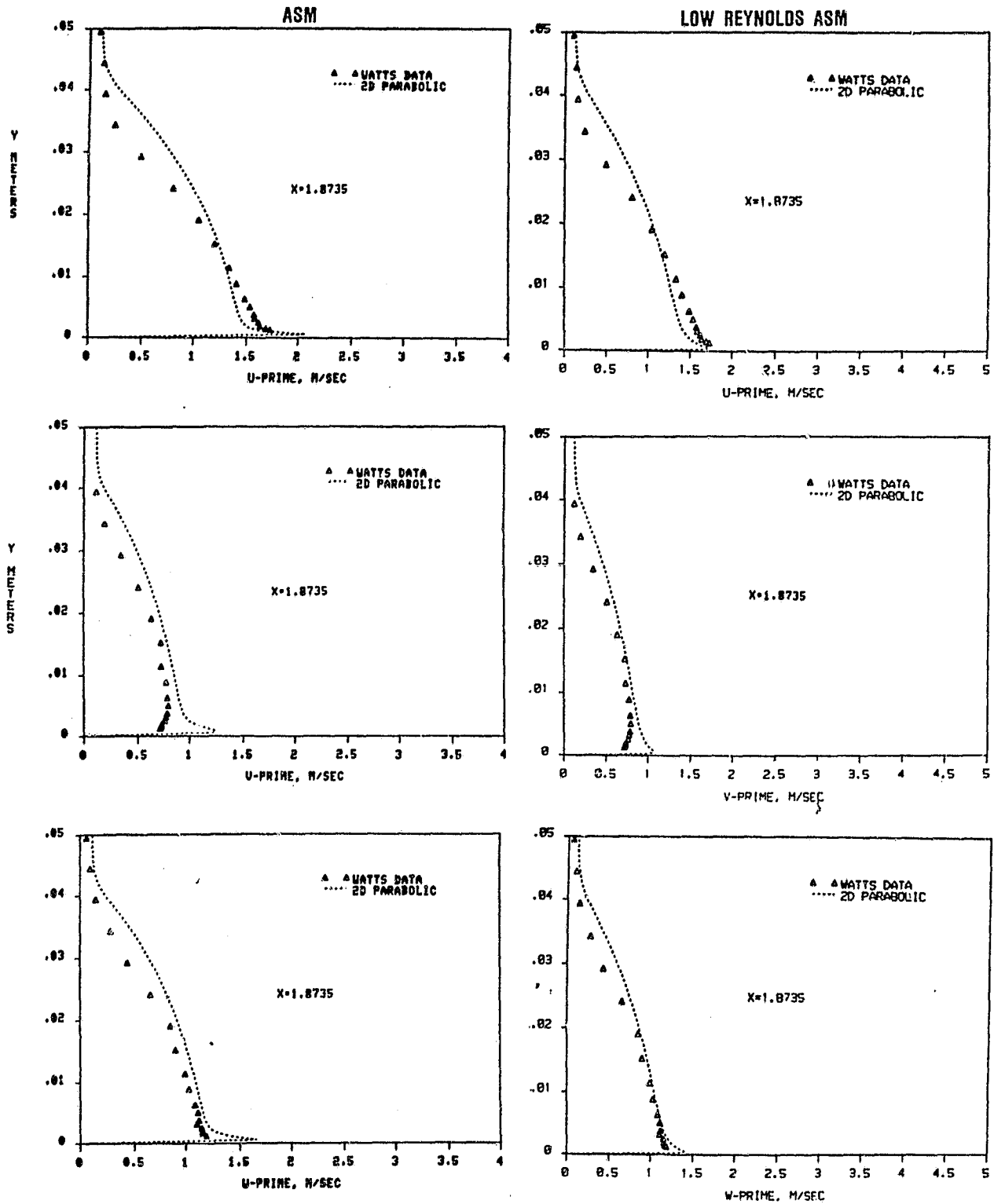


Figure 6.1-7. Fluctuating Components of Axial, Radial and Transverse Velocities (u' , v' and w') Predicted by ASM, and ASM With Low Reynolds Number Correction.

6.2 Plane Couette Flow

The plane Couette flow is a well defined flow for which analytical solutions and good experimental measurements are available for evaluating the turbulence models. The test data selected for validating the models in this report were obtained by El Telbany and Reynolds²⁰⁸ in a test setup shown schematically in Figure 6.2-1. In this setup, the bottom wall was stationary and the top wall was moved at a velocity of 17.08 m/s, which corresponds to a Reynolds number of 12,640. The distance between the walls was 44 mm.

Computations for this flow were made with the standard k- ϵ model and the algebraic stress model using a 2-D parabolic code. The standard k- ϵ model predictions and the data for mean velocity are shown in Figure 6.2-2. The agreement between data and predictions is very good. The non-dimensionalized Reynolds shear stress profile predicted by the standard k- ϵ model is also in good agreement with the data, as seen in Figure 6.2-3. However, the profile of Reynolds stress normalized by the turbulence kinetic energy predicted by standard k- ϵ model is not in agreement with the data (Figure 6.2-4). In the standard k- ϵ model, in the regions where the shear stress is a constant, the turbulence kinetic energy is also a constant. However, the data shows a gradual reduction in the k values away from the wall with the minimum value at the plane of symmetry. Consequently, the predicted \overline{uv}/k profile is constant in the core of the flow, while the data shows a gradual increase in its value away from the wall. It is possible to match the predicted and measured values of \overline{uv}/k at the plane of symmetry by increasing the turbulence model constant, C_D , from 0.09 to 0.144. A significant improvement is obtained in the \overline{uv}/k profile, which is shown in Figure 6.2-5. However with $C_D = 0.144$ used in the standard k- ϵ model, the predicted mean velocity profile was not in agreement with the data, as seen in Figure 6.2-6.

The ASM predictions are illustrated in Figures 6.2-7 through 6.2-13. The comparison between ASM prediction and the data for mean axial velocity is shown in Figure 6.2-7. The agreement between the two is very good. The ASM prediction for \overline{uv} , normalized by the wall shear stress is in good agreement with the data, as shown in Figure 6.2-8. However, when the Reynolds stress profiles are normalized by the local turbulence kinetic energy, shown in Figure 6.2-9, the predicted profile underestimates the values in the core of the flow. However, the ASM predictions for the centerline \overline{uv}/k values are closer to the data than that predicted by standard $k-\epsilon$ model. A very similar profile is obtained for the correlation coefficient, $\overline{uv}/(u'v')$, which is shown in Figure 6.2-10. These two figures demonstrate that the ASM slightly overestimates the turbulence kinetic energy components.

The ASM prediction for the axial turbulence intensity, u' , is shown in Figure 6.2-11. The predicted peak u' value is slightly smaller than the data. However, in the core of the flow, the ASM predictions are in good agreement with the data. The predicted and measured cross-stream turbulence intensity profiles are illustrated in Figure 6.2-12. The predicted v' values are about 20 percent higher than the data. The predicted w' values are also higher than the data by about 15 percent in the region near the plane of symmetry as shown in Figure 6.2-13.

The Couette flow calculations may be summarized as follows:

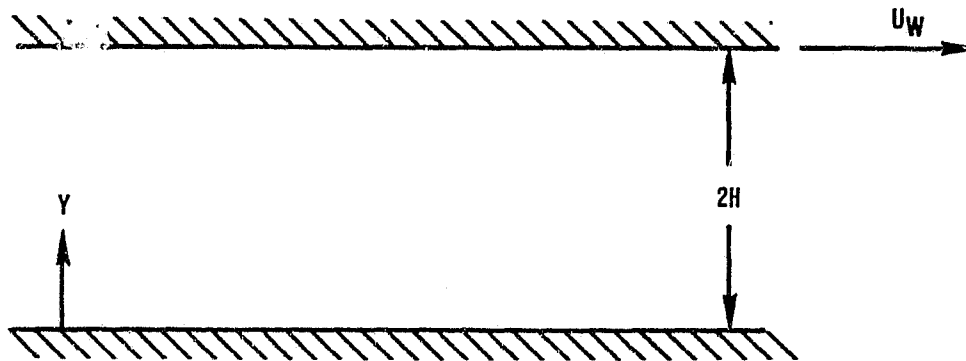
- o The standard $k-\epsilon$ model predicts the mean velocity profile accurately, but underpredicts the centerline \overline{uv}/k value by about 20 percent.
- o When the centerline \overline{uv}/k value is matched with the data, (using $C_D = 0.144$), the predicted mean velocity profile is in poor agreement with data.

- o The algebraic stress model correctly predicts the mean velocity profile and underpredicts the centerline \overline{uv}/k , but the centerline \overline{uv}/k values are in better agreement with the data than the standard $k-\epsilon$ model. The basic reason for this deficiency is because of the overestimation of v' and w' by the ASM. Overall individual turbulence components are predicted well by the ASM.

ORIGINAL PAGE IS
OF POOR QUALITY

EL TELBANY AND REYNOLDS

COUETTE FLOW



$$\begin{aligned}2H &= 0.044 \text{ M} \\U_w &= 17.08 \text{ M/S} \\Re &= U_w H / \nu = 12,640\end{aligned}$$

Figure 6.2-1. Geometry of Plane Couette Flow.

ORIGINAL PAGE IS
OF POOR QUALITY

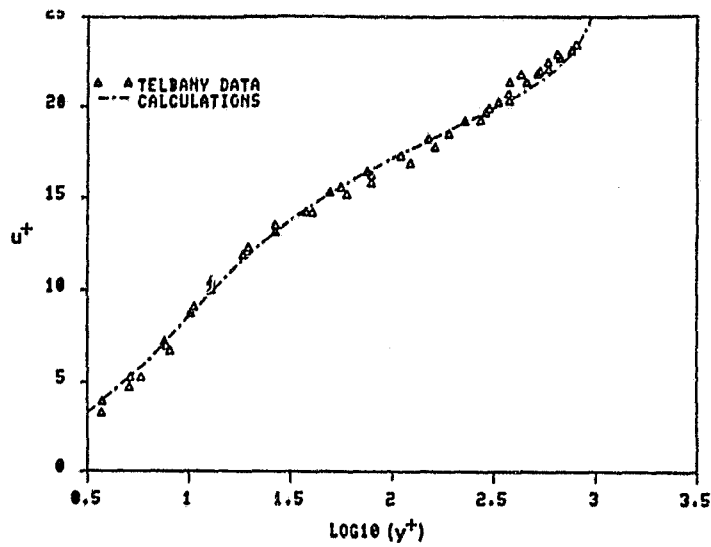


Figure 6.2-2. Comparison Between $k-\epsilon$ Predictions and Measured Couette Flow Axial Velocity Profile (u_+ versus Y_+).

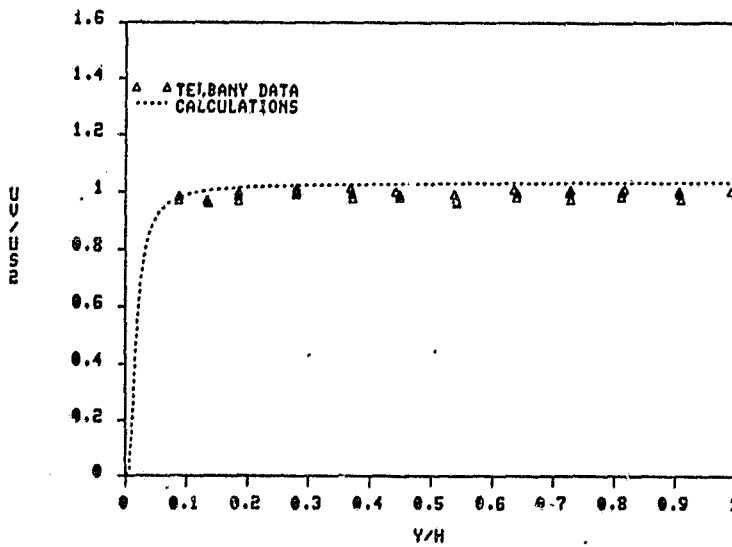


Figure 6.2-3. Comparison Between $k-\epsilon$ Model Predictions and Measured Shear Stress Profile (normalized by wall shear value).

ORIGINAL PAGE IS
OF POOR QUALITY.

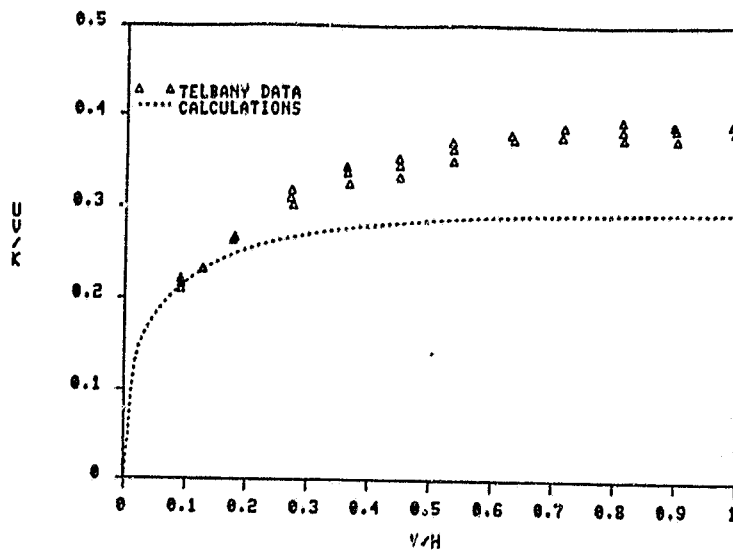


Figure 6.2-4. Shear Stress Normalized by Turbulence Kinetic Energy (τ/K) Standard $k-\epsilon$ Model With $C_D = 0.09$.

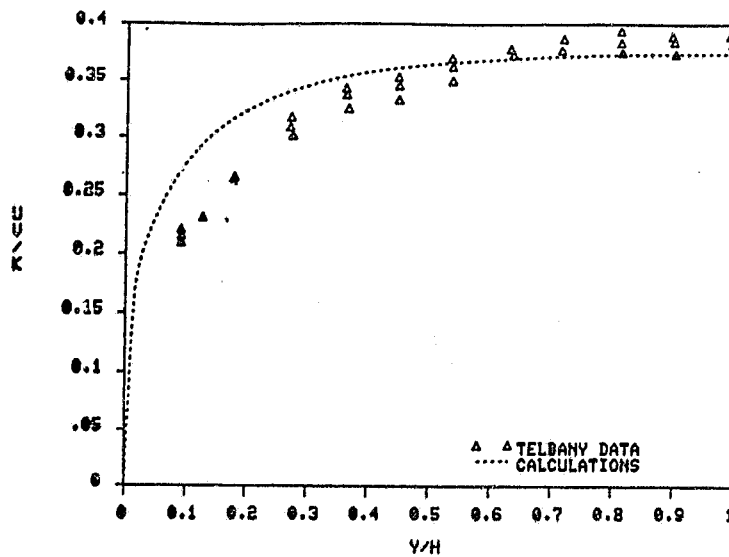


Figure 6.2-5. $k-\epsilon$ Model Predicted τ/K with $C_D = 0.144$.

ORIGINAL PAGE IS
OF POOR QUALITY

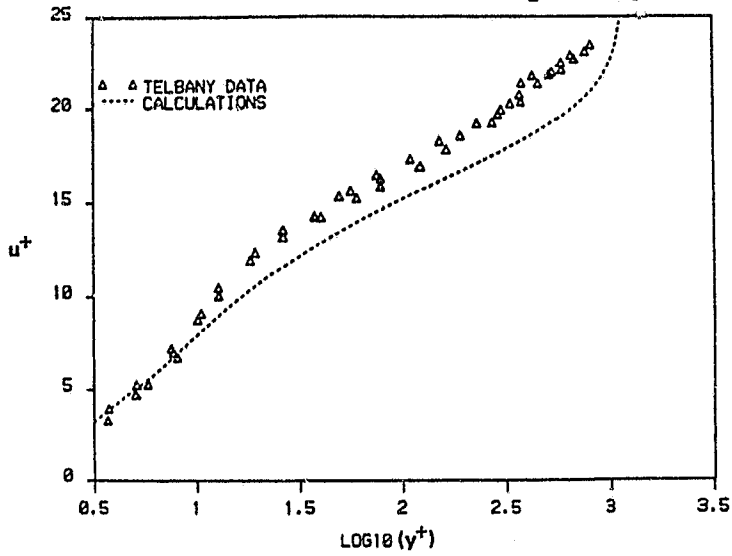


Figure 6.2-6. $k-\epsilon$ Model Predicted U_+ Profiles with $C_D = 0.144$.

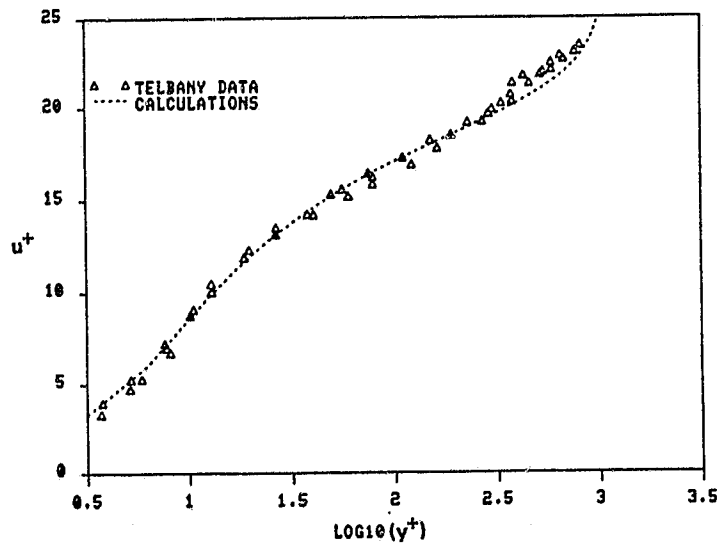


Figure 6.2-7. ASM Prediction and Measured u_+ Versus y_+ Profiles.

C-3

ORIGINAL PAGE IS
OF POOR QUALITY

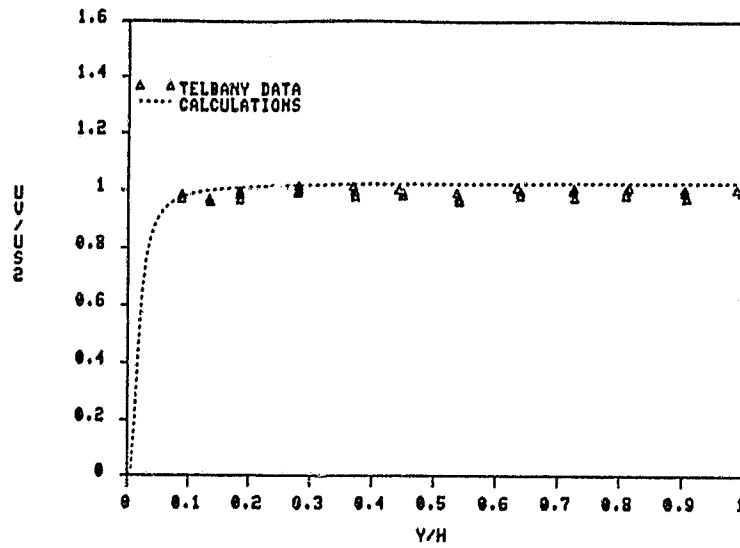


Figure 6.2-8. ASM Prediction and Measured Normalized Shear Stress Profile.

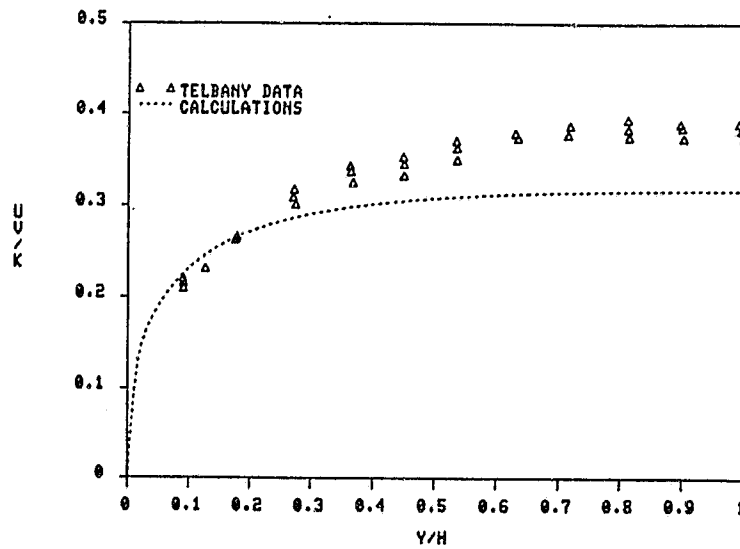


Figure 6.2-9. Shear Stress (\overline{uv}) Normalized by Turbulence Kinetic Energy Predicted By ASM Versus Increased Data.

ORIGINAL PAGE IS
OF POOR QUALITY

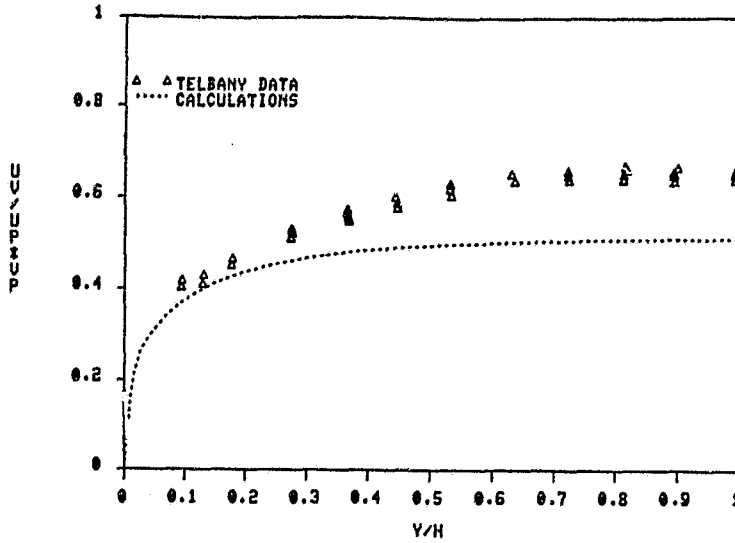


Figure 6.2-10. Correlation Coefficient $(\overline{uv} / (\overline{uv}/u' \times v'))$ Predicted By ASM Versus Measurements.

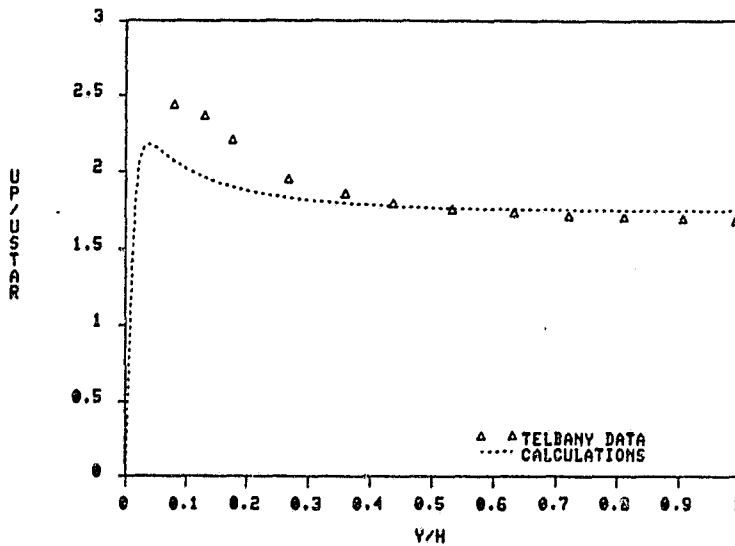


Figure 6.2-11. ASM Predictions and Measured Axial Turbulence Intensity (u'/u^*) .

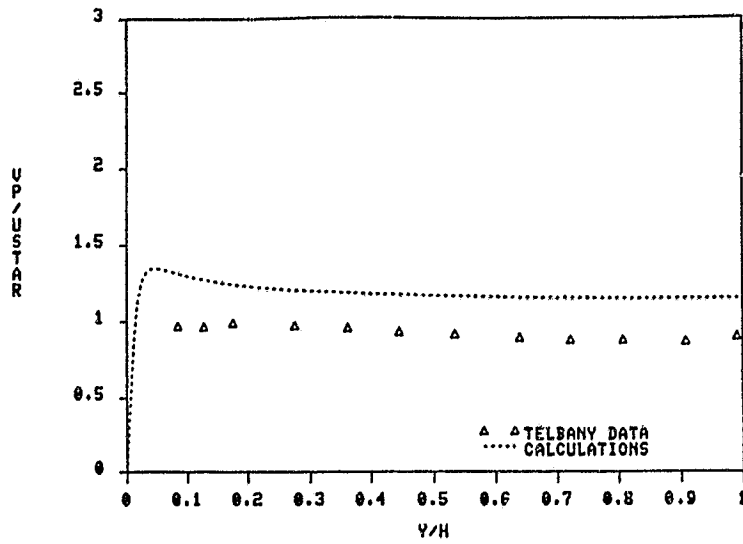


Figure 6.2-12. ASM Predictions and Measured Radial Turbulence Intensity.

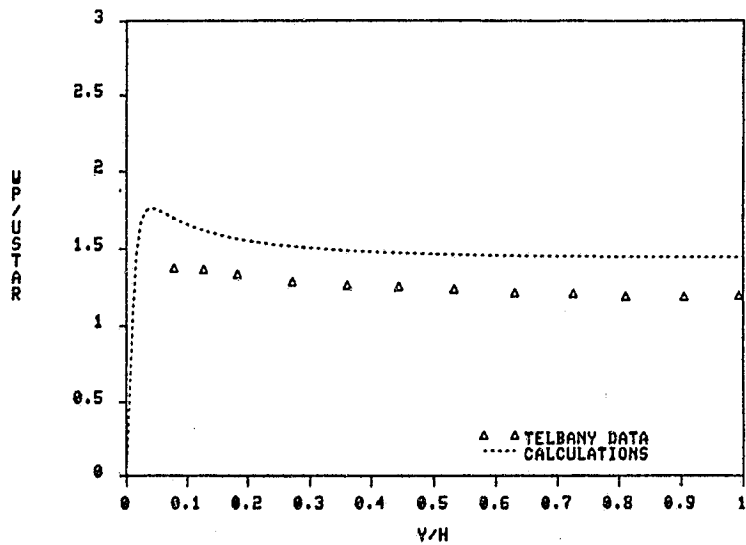


Figure 6.2-13. ASM Predictions and Measured w' .

6.3 Developing Flow in a Two-Dimensional Channel

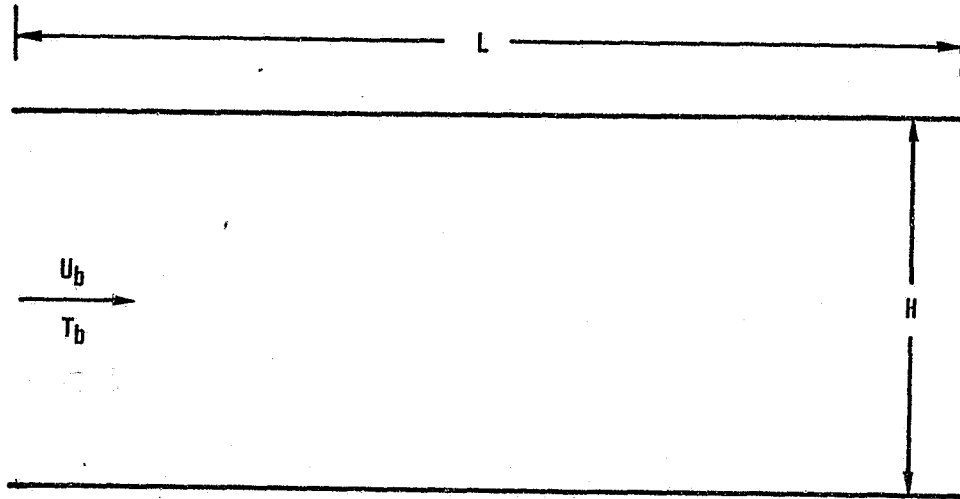
One of the simple flows considered for validating the $k-\epsilon$ turbulence model was the developing flow in a two-dimensional channel. Analysis of the entrance flow problem provides a means of evaluating the accuracy of the numerical scheme. Detailed mean flow measurements in the entrance region of a parallel plate were made by Emery and Gessner⁶⁵. The geometry of their test setup is shown in Figure 6.3-1. Predictions for this flow were obtained using a 2-D elliptic code with the standard $k-\epsilon$ model with 2200 grid nodes. Computations were performed until the total mass source error was less than 0.01 percent. Comparison between predicted and measured axial velocity variation along the centerline of the channel is shown in Figure 6.3-2. The difference between the two results is comparable to the measurement accuracy. Figure 6.3-3 illustrates the predicted and measured profiles of the axial velocity component at different axial stations. The agreement between data and predictions is very good.

The predicted and measured wall shear stress distributions are presented in Figure 6.3-4. The predictions and the measurements are within about 7 percent of the data, which is within the accuracy of the wall shear stress measurements. The agreement between measured and predicted results demonstrates that the standard $k-\epsilon$ model is sufficiently accurate for predicting mean flow field in a two-dimensional channel.

ORIGINAL PAGE IS
OF POOR QUALITY

EMERY AND GESSNER

2-D CHANNEL FLOW



$H = 0.127 \text{ M}$
 $L = 10.16 \text{ M}$
 $U_b = 17.85 \text{ M/S}$
 $T_b = 300^\circ \text{ K}$
 $Re = 100,000$

Figure 6.3-1. Geometry of Developing Flow in a Two-Dimensional Duet.

ORIGINAL PAGE IS
OF POOR QUALITY

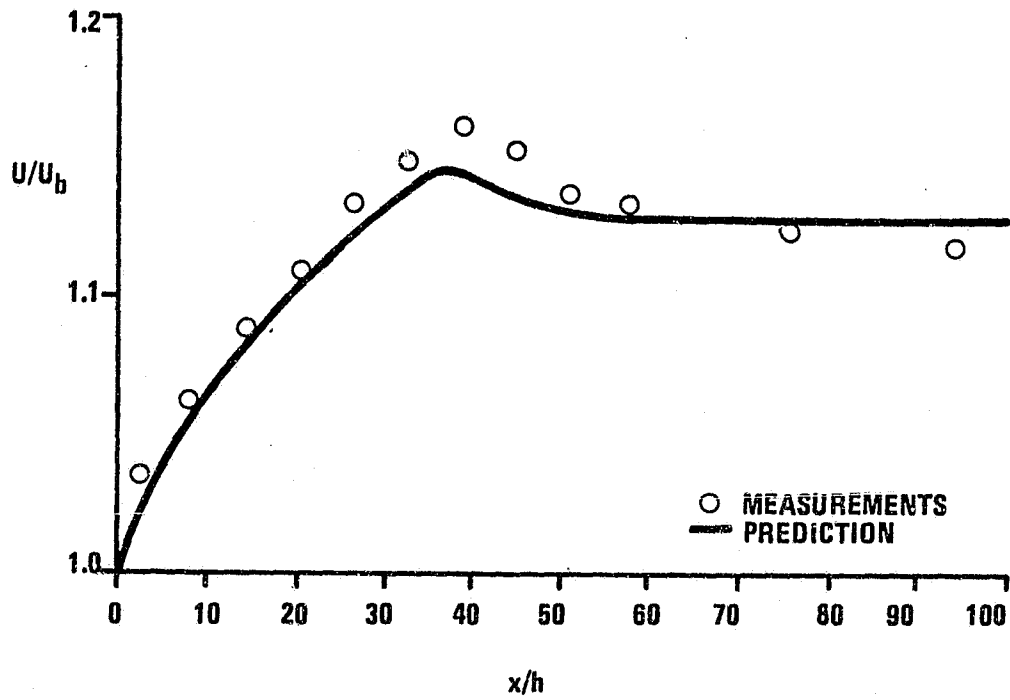


Figure 6.3-2. Predicted and Measured Distributions of Centerline Axial Velocity for Developing Flow in a Two-Dimensional Duct.

ORIGINAL PAGE IS
OF POOR QUALITY

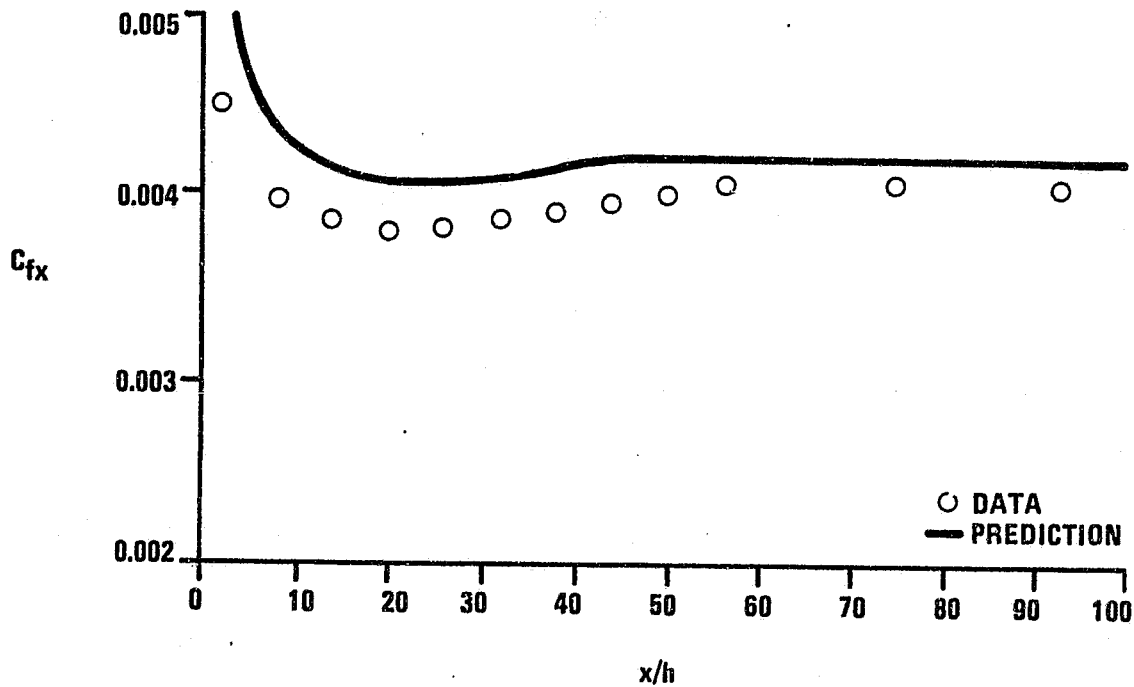


Figure 6.3-4. Predicted and Measured Wall Shear Stress Distributions for Developing Flow in a Two-Dimensional Duct.

6.4 Developing Pipe Flow

The next benchmark test case considered was the developing flow in a circular pipe. The test case selected for this problem corresponds to the measurements by Barbin and Jones⁶⁸. The geometry of their test setup is shown in Figure 6.4-1.

The bulk flow velocity at the inlet in the test case was 33.174 m/s and the Reynolds number, based upon the bulk velocity, was 388,000. The mean velocity measurements were made using pilot tubes and the turbulence velocity components were measured using an x-wire probe. Computations for this case were made using a 2-D parabolic program. The computational domain extended from $x = 0.3$ meters to $x = 8.1$ meters in the axial direction and from $r = 0$ to $r = 0.1$ meters in the radial direction. Along the axis of the tube, symmetry boundary conditions were specified, and along the pipe wall, standard wall functions were used to specify near-wall boundary conditions. In the computations, 100 grid nodal points were used in the radial direction. At $x = 0.3$ meters, the measured profiles were used as initial profiles. Computations were made with standard $k-\epsilon$ model and ASM.

Comparison between standard $k-\epsilon$ model predictions and the data of Barbin and Jones for mean axial velocity is shown in Figure 6.4-2. The mean velocity profiles are nondimensionalized by the average bulk velocity, $U_b = 33.17$ m/s. The predicted mean velocity profiles are in very good agreement with the data.

The mean axial velocity profile comparison between the data and ASM predictions is presented in Figure 6.4-3. The ASM predictions are in good agreement with the measurements. The predicted and measured root mean square (RMS) axial velocity fluctuations, u' , are illustrated in Figure 6.4-4. The ASM correctly predicts the axial turbulence intensity near the axis of the pipe. Near the

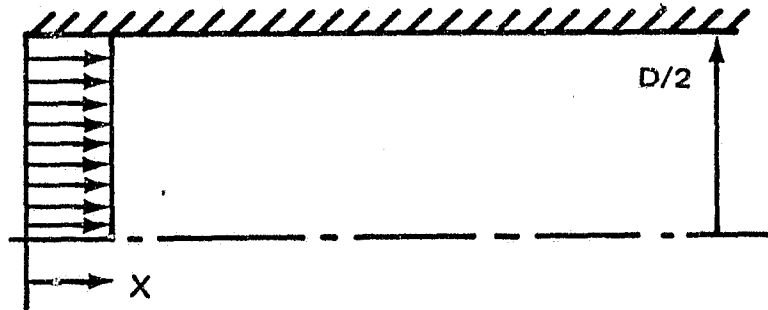
wall of the pipe, predicted peak values of u' are apparently higher than the data. However, the measurements near the wall do not have sufficient resolution. The boundary conditions near the wall were specified using wall functions, which have been shown (Paragraph 6.1) to overestimate the peak turbulence kinetic energy in the case of a flat-plate boundary layer. By using an improved near-wall model, improvements in the peak turbulence intensity can be obtained. The comparison between the predicted and measured circumferential turbulence intensity component, w' , is illustrated in Figure 6.4-5. These profiles have characteristics very similar to the u' profiles. The w' peak values are slightly overestimated. The near-wall model deficiencies are responsible for the overestimation of the peak w' values.

The results presented in this paragraph demonstrate that the $k-\epsilon$ and ASM accurately predict the mean velocity profiles and that further improvements in turbulence structure and pressure drops can be achieved with an improved near-wall model.

ORIGINAL PAGE IS
OF POOR QUALITY

BARBIN AND JONES

DEVELOPING PIPE FLOW



$D = 0.2 \text{ M}$
 $Re = 355,000$
 $U = 33.17 \text{ M/S}$

Figure 6.4-1. Developing Pipe Flow Setup of Barbin and Jones.⁶⁸

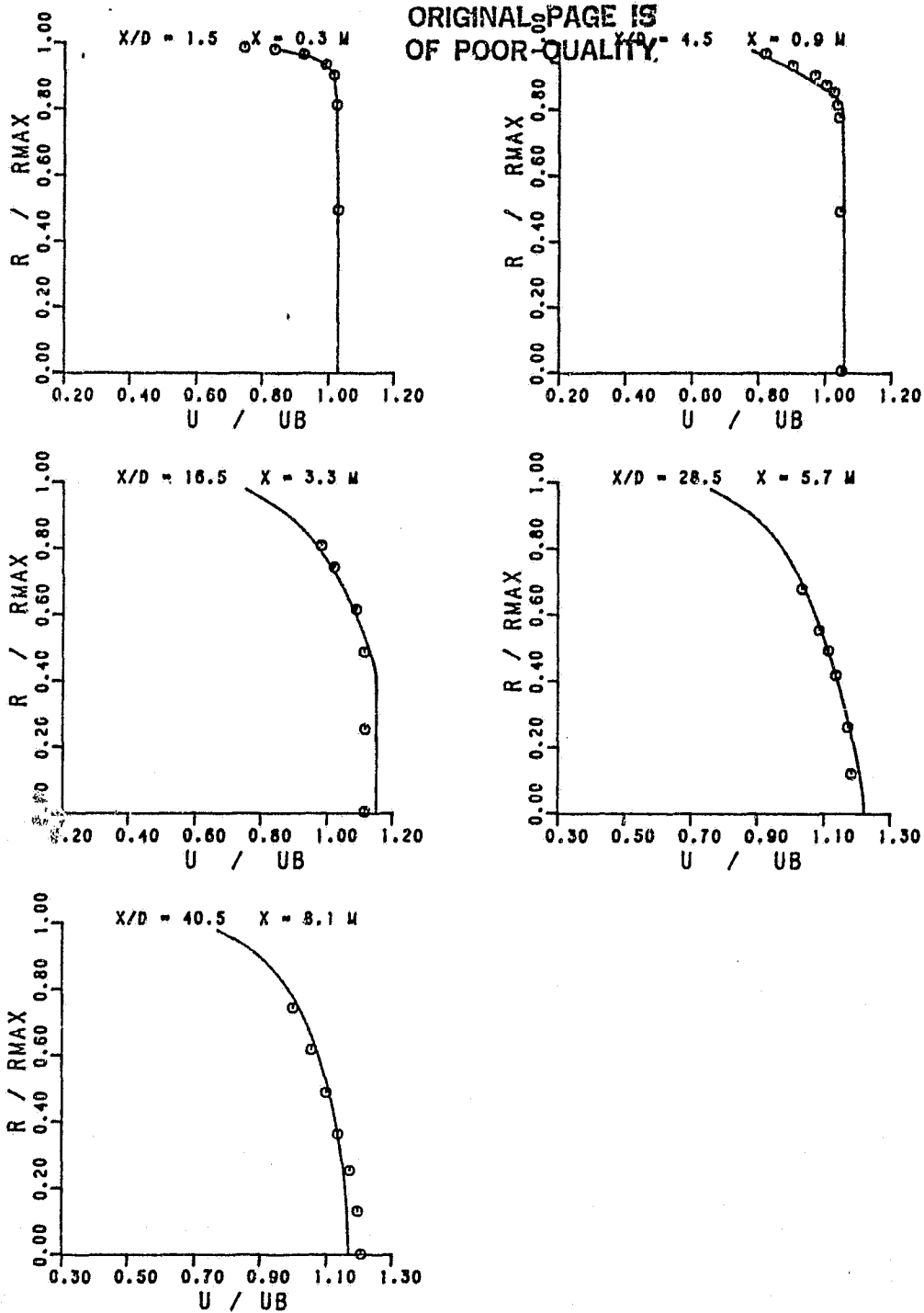


Figure 6.4-2. Comparison Between $k-\epsilon$ Model Predictions and Profiles of Axial Velocity at Different Axial Stations in a Developing Pipe Flow (U_b = The Average Flow Velocity).

ORIGINAL PAGE IS
OF POOR QUALITY

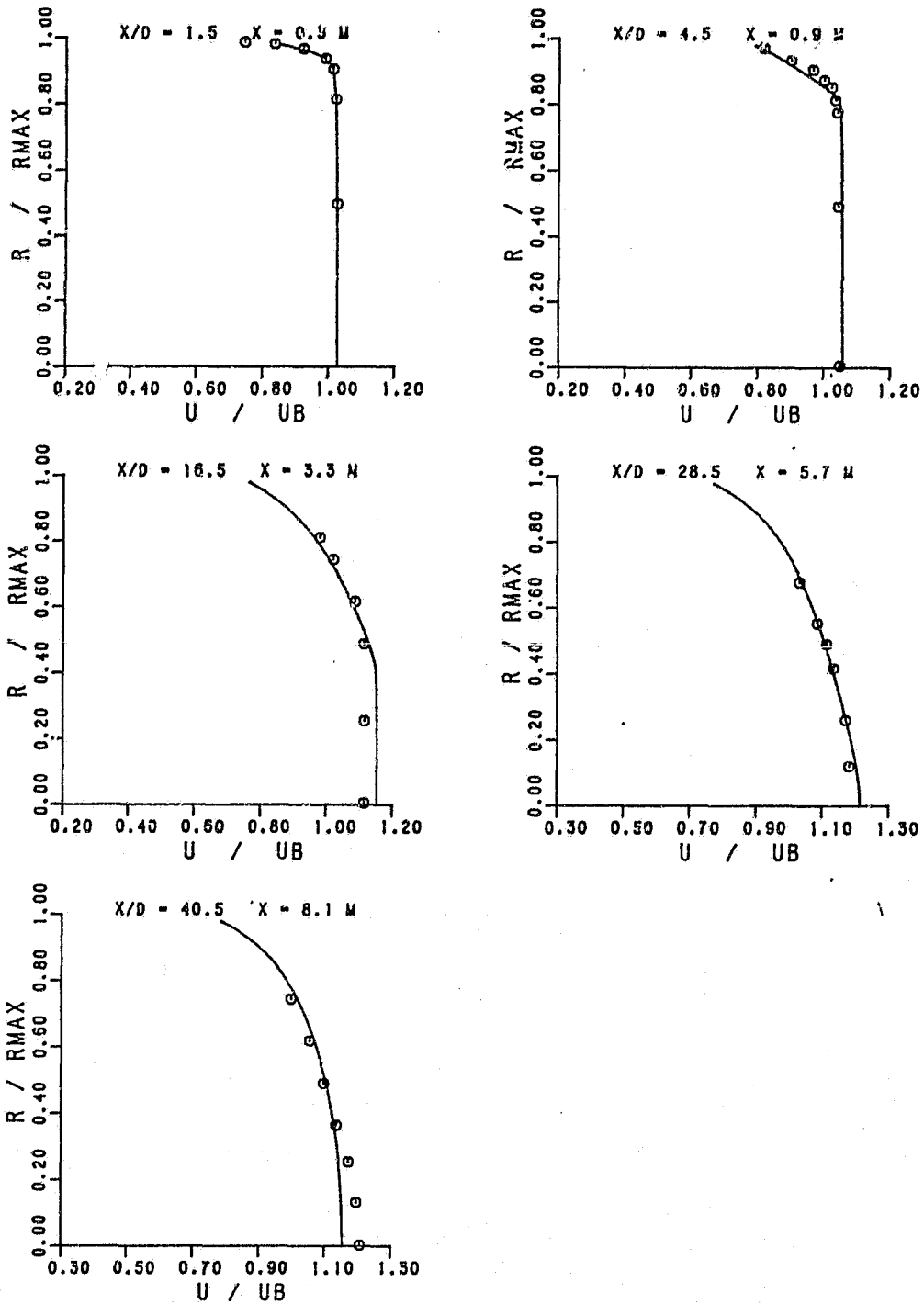


Figure 6.4-3. Comparison Between ASM Predictions and Measured Axial Velocity Profiles; $D = 20$ cm, $U_b = 33.17$ m/s.

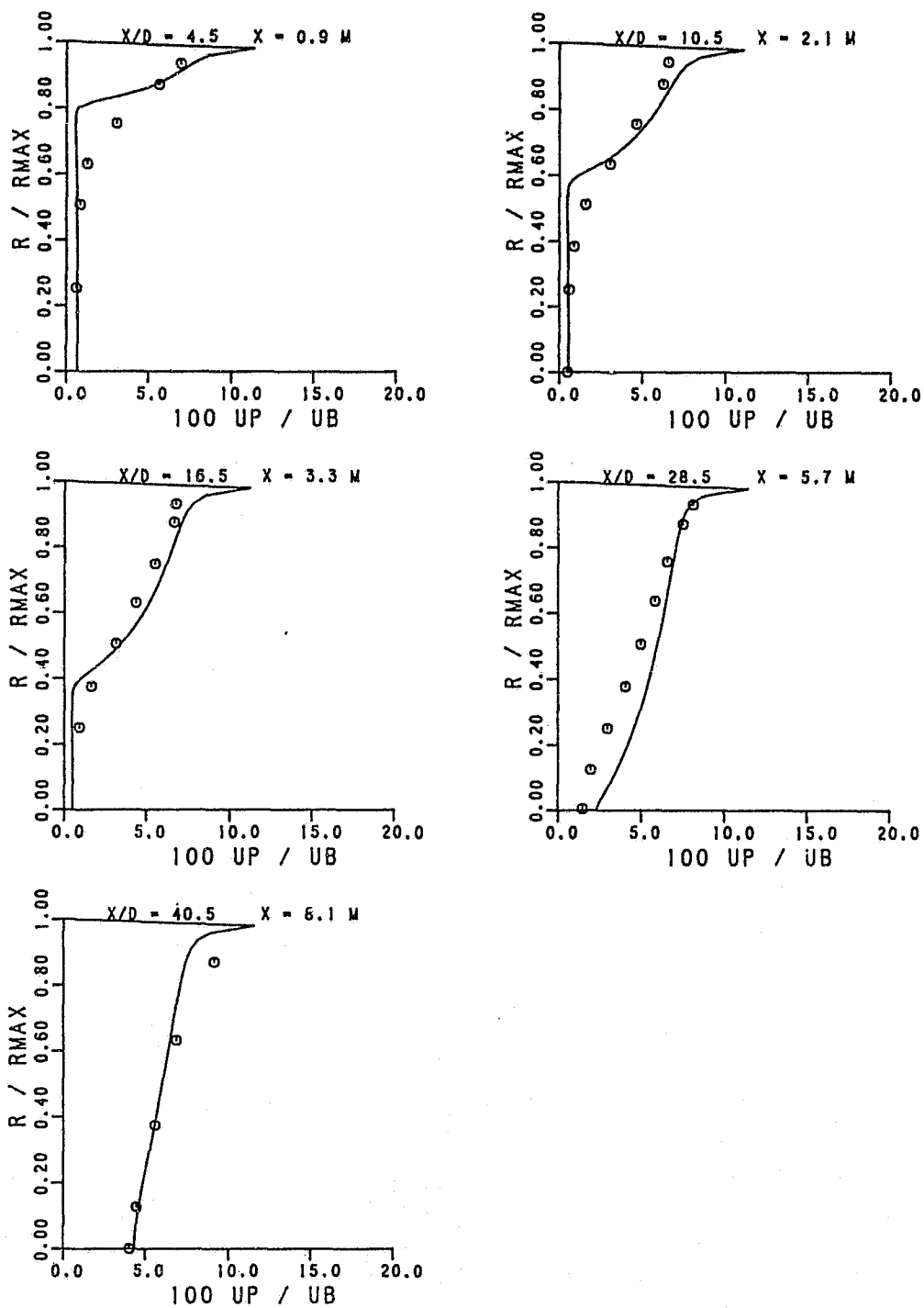


Figure 6.4-4. Comparison Between ASM Predictions and Measurements for Nondimensionalized Axial Turbulence Velocity Fluctuations.

ORIGINAL PAGE IS
OF POOR QUALITY

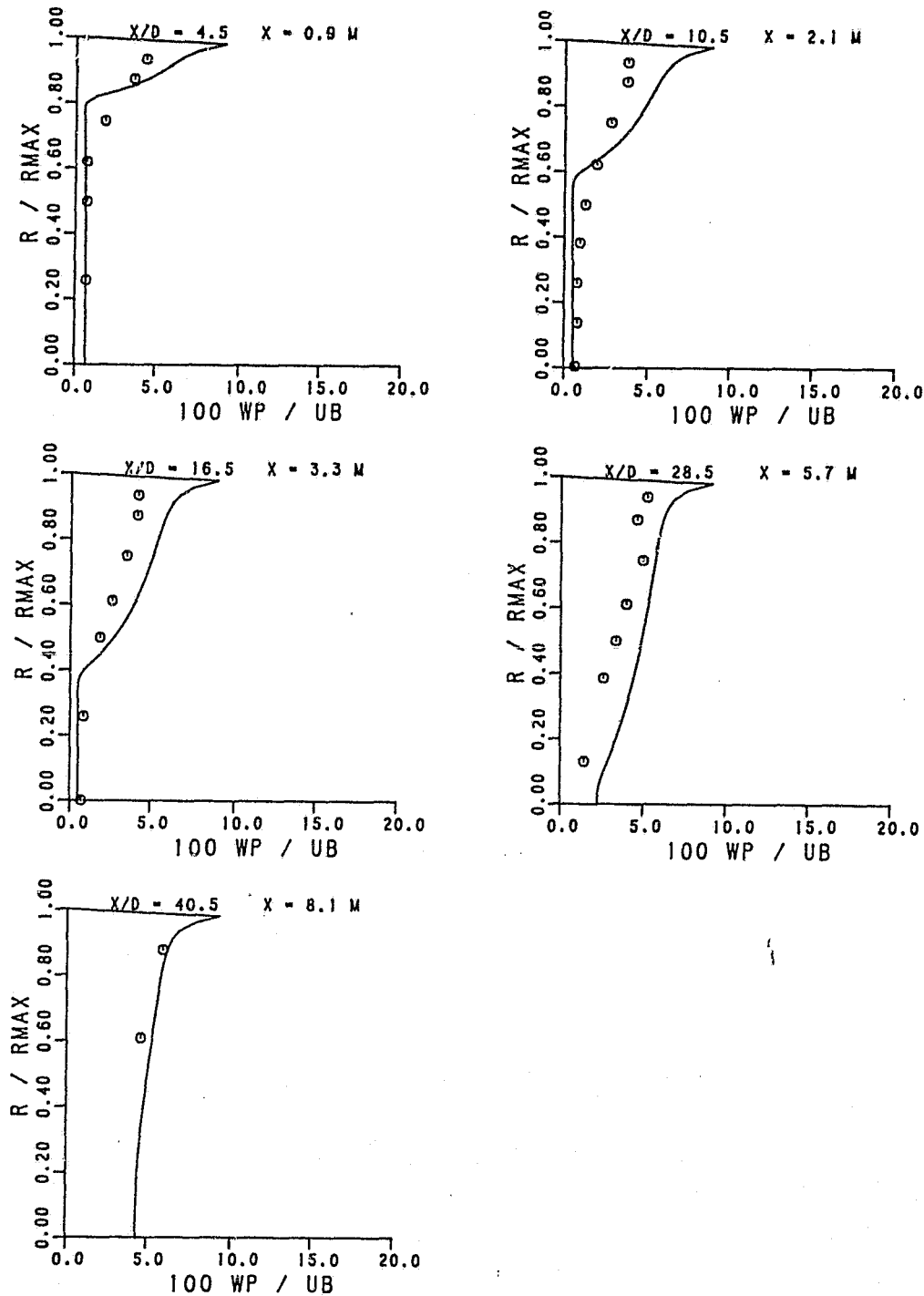


Figure 6.4-5. Comparison Between ASM Predictions and Measurements for Nondimensionalized Circumferential Turbulence Velocity Fluctuations.

6.5 Fully Developed Pipe Flow

The fully developed pipe flow is another case of simple flow where the turbulence models can be evaluated. The test measurement selected for this case was that of Laufer²⁰⁹, at a Reynolds number, R_e , of 500,000. The geometry of the flow field is illustrated in Figure 6.5-1. Computations for this case were made with a 2-D parabolic program, starting with a plug flow profile at $x = 0$. The calculations were performed up to $x = 10$ meters, where fully developed flow field was established. Predictions were obtained using the $k-\epsilon$ model and the ASM with Chien's low Reynolds number correction. A comparison between Laufer's data and the $k-\epsilon$ model predictions are shown in Figure 6.5-2. The agreement between data and predictions is very good. The predicted and measured turbulence kinetic energy profiles are shown in Figure 6.5-3. The standard $k-\epsilon$ model predicts a higher value of peak turbulence kinetic energy near the wall compared to the data. Similarly, at the centerline, the $k-\epsilon$ model predicts about 40 percent higher value for k than the data.

The ASM prediction for mean velocity profile is shown in Figure 6.5-4. The predicted results and the data are in good agreement. The ASM prediction for turbulence kinetic energy is illustrated in Figure 6.5-5. The predicted peak as well as the centerline values of the turbulence kinetic energy are in good agreement with the data. The ASM predicts a faster decay of turbulence kinetic energy (k), away from the wall, but the predicted variation of k in the core of the flow is slightly smaller than the measurements.

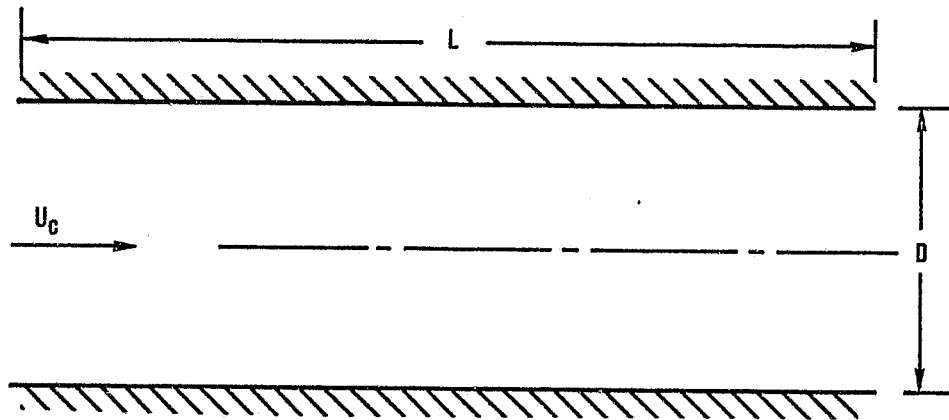
The ASM predictions for axial turbulence intensity, u' , and the data are presented in nondimensional form in Figure 6.5-6. The predicted u' peak value near the wall is slightly smaller than the data. However, the agreement with data in the core of the flow is

very good. The predicted and measured v' profile is shown in Figure 6.5-7. The predicted profile is in good agreement with the data. However, the peak value of v' predicted by the model is slightly higher than the data. The predicted and measured w' profiles, shown in Figure 6.5-8, are in good agreement in the entire flow field. At the axis of the pipe, the predicted w' value is slightly higher than the data. The comparison between data and predictions for the Reynolds shear stress, \overline{uv} , is shown in Figure 6.5-9. The data and predicted values are in excellent agreement.

The low Reynolds number $k-\epsilon$ model predicts the mean velocity profiles in a fully developed pipe flow accurately. It predicts a higher value of turbulence kinetic energy near the wall and at the centerline compared to the data. The ASM predicts the mean velocity profile accurately and significantly improves the turbulence kinetic energy over the $k-\epsilon$ model results.

ORIGINAL PAGE IS
OF POOR QUALITY

LAUFER PIPE FLOW



$$\begin{aligned} D &= 0.247 \text{ M} \\ L &= 4.88 \text{ M} \\ U_c &= 30.48 \text{ M} \\ Re &= U_c D / \nu = 500,000 \end{aligned}$$

Figure 6.5-1. Geometry of the Pipe Flow.

ORIGINAL PAGE IS
OF POOR QUALITY

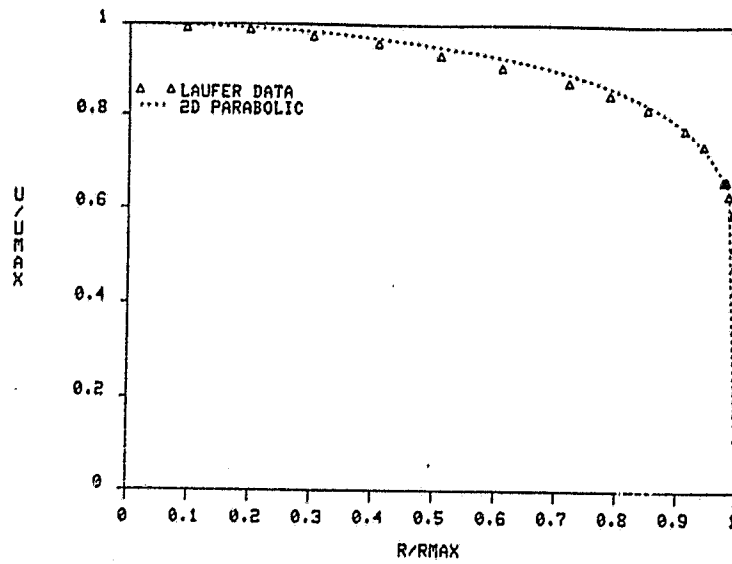


Figure 6.5-2. Low Reynolds $k-\epsilon$ Model Axial Velocity Profile.

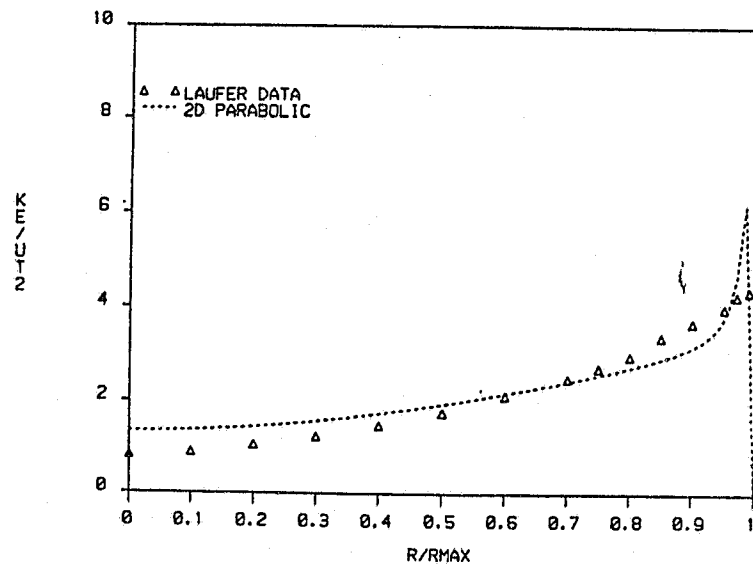


Figure 6.5-3. Low Reynolds $k-\epsilon$ Model Turbulence Kinetic Energy Profile.

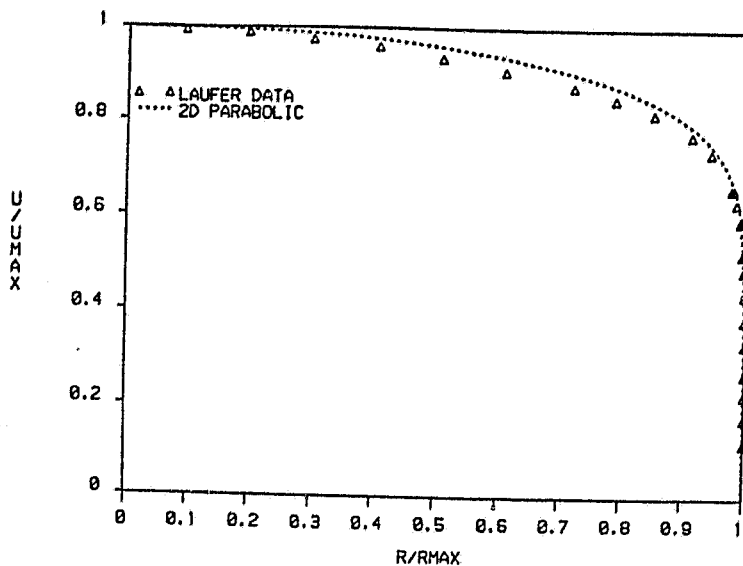


Figure 6.5-4. ASM With Low Reynolds Number Correction -- Axial Velocity Profile.

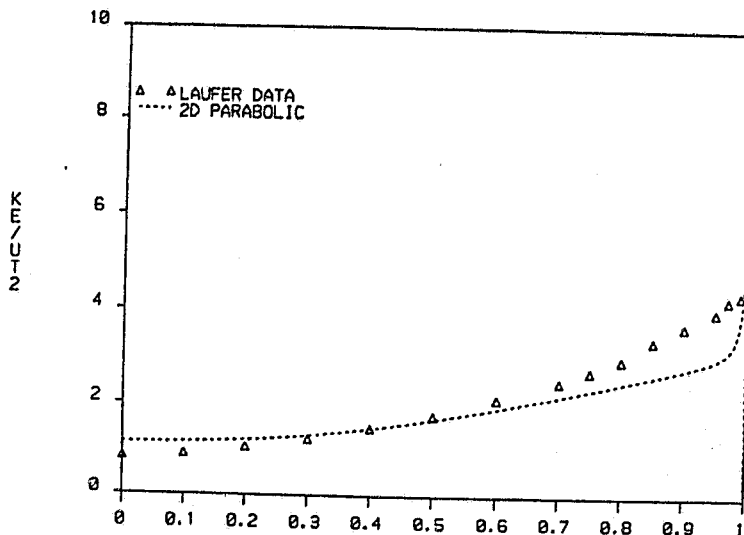


Figure 6.5-5. ASM With Low Reynolds Number Correction -- Turbulence Kinetic Energy Profile.

ORIGINAL PAGE IS
OF POOR QUALITY

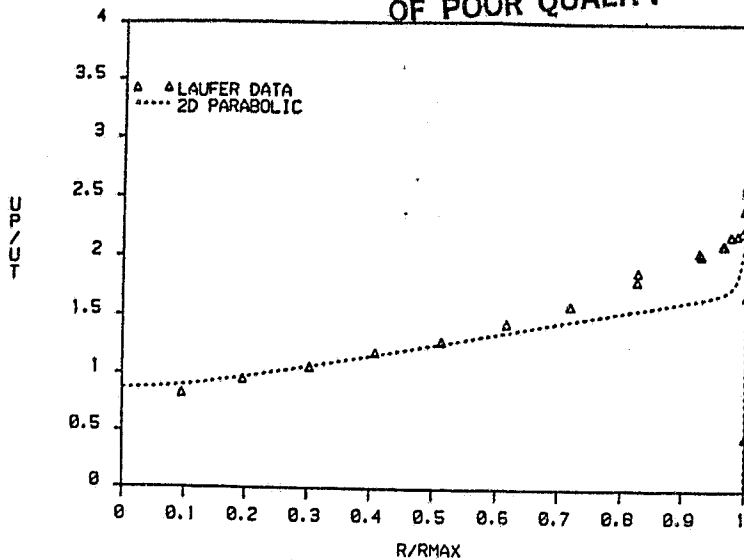


Figure 6.5-6. u'/u^* Profile.

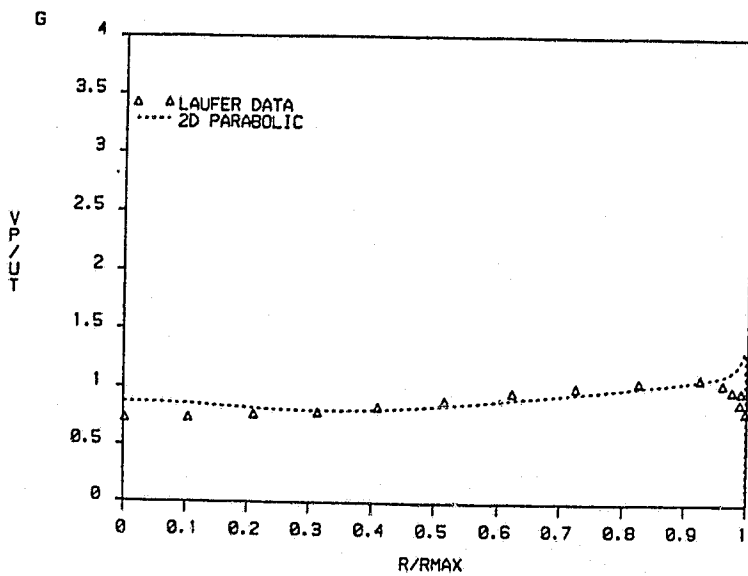


Figure 6.5-7. v'/u^* Profile.

ORIGINAL PAGE IS
OF POOR QUALITY

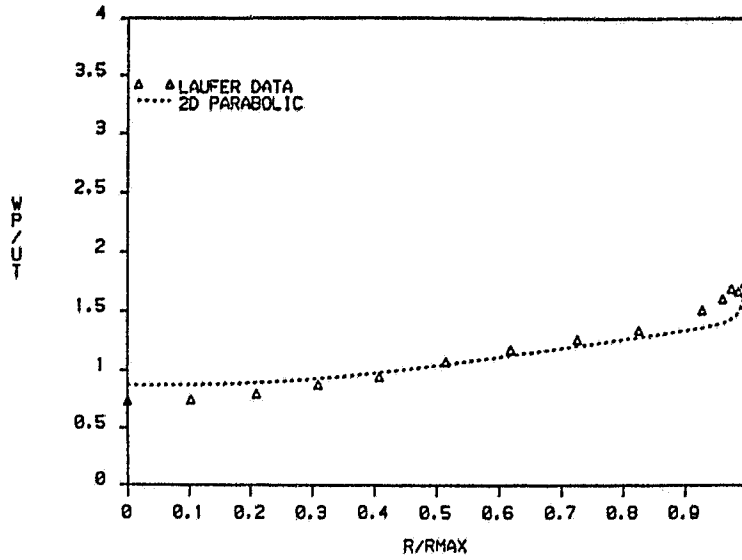


Figure 6.5-8. w'/u^* Profile.

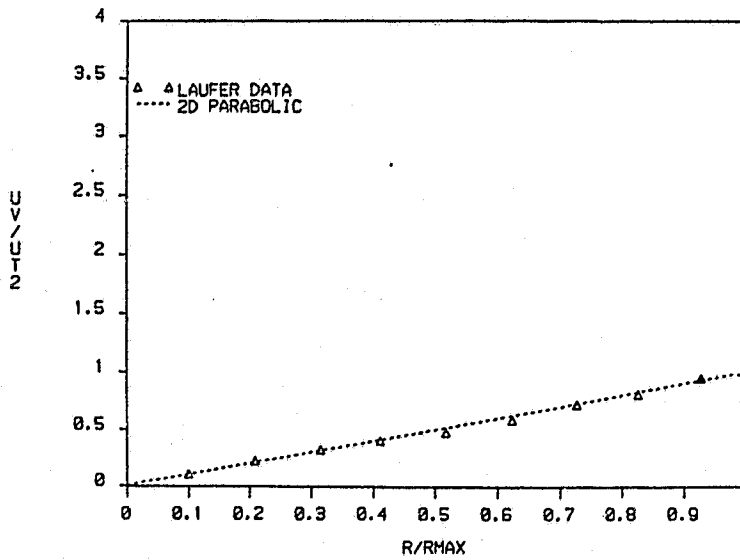


Figure 6.5-9. \overline{uv}/u_*^2 Profile.

6.6 Two-Stream Mixing Layer

Another benchmark test case selected from the data base for turbulence model validation is the flow in the mixing layer between two streams. Measurements for this case were made by Saiy and Peerless⁶⁰ using a hot-wire probe and pitot tubes. A schematic of their flow test setup is shown in Figure 6.6-1.

Computations for this case were made using the 2-D Parabolic Program. Since this flow field does not involve a wall boundary layer, low Reynolds number correction is not needed. Predictions for this case were obtained with the standard $k-\epsilon$ model and the ASM. Initial conditions for these computations were applied at $x = 12.5$ cm using measured data. A total of 100 cross-stream nodes were used in the computations. The nodes were closely distributed in the mixing region where gradients are higher and are sparsely spaced in the outer regions. For the test conditions, the velocities of the two streams are;

$$U_E = 16.5 \text{ m/s}; \quad U_I = 38.37 \text{ m/s}$$

The predicted mean velocity and turbulence kinetic energy profiles using the standard $k-\epsilon$ model are presented in Figure 6.6-2. The predicted mean velocity profiles are in very good agreement with the measurements. The predicted turbulence kinetic energy (TKE) values are slightly smaller than the data. However, the width of the shear layer is correctly predicted. Overall agreement between $k-\epsilon$ model predictions and data is good.

Figure 6.6-3 shows the comparison between data and predictions obtained from the algebraic Reynolds stress model for the mean velocity. The ASM predictions, similar to the $k-\epsilon$ results, are in very good agreement with data. A typical comparison between data and predicted turbulence velocity components at $x = 15$ cm and $x =$

20 cm is presented in Figure 6.6-4. The u' profiles are in very good agreement with the data. The predicted and measured v' data are in good agreement. A similar conclusion can be drawn for the w' component, with the exception that the predicted w' peak values are slightly larger than the data.

The measured data of v' and w' indicate that the peak values occur at $y > 0$; i.e., they have shifted toward the low-velocity stream side of the mixing layer. The ASM model predicts them to lie along $y = 0$.

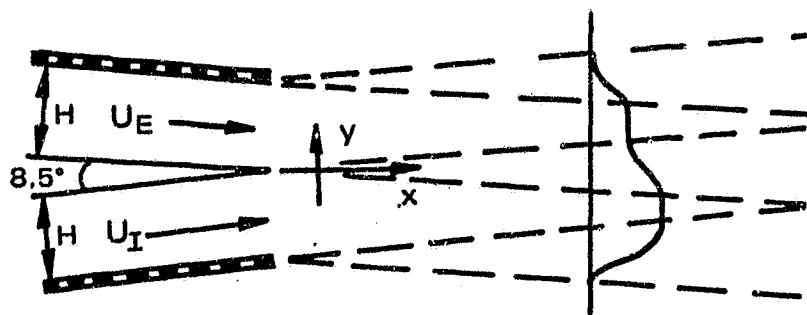
Figure 6.6-5 illustrates the comparison between data and predicted turbulence kinetic energy and shear stress (\overline{uv}) profiles at $x = 15$ cm and $x = 20$ cm. The predicted turbulence $k-\epsilon$ values are slightly smaller than the data. This is consistent with the results shown for the $k-\epsilon$ model in Figure 6.6-2. The predicted \overline{uv} profiles are in good agreement with data except for a slight discrepancy at $y = 0$.

Major conclusions from the mixing layer work reported here are:

- o Both $k-\epsilon$ and ASM models give equally good mean velocity profiles as well as turbulent kinetic energy profiles. The measured peak values of the turbulent kinetic energy (KE) are slightly higher than predictions; the ASM gives a little better correlation.
- o The ASM model gives good correlation for the fluctuating velocity components (u' , v' , and w') as well as shear stress ($\overline{u'v'}$). There is slight discrepancy in regard to the radial location of the v' and w' peaks.

SAIY AND PEERLESS

TWO STREAM MIXING LAYER



$H = 0.06M$
DUCT DEPTH = 0.30M

$U_E = 10.7 \text{ M/S}$
 $U_I = 25 \text{ M/S}$
TURBULENCE INTENSITY = 0.6%

Figure 6.6-1. Two-Stream Mixing-Layer Setup of Saiy and Peerless⁶⁰.

ORIGINAL PAGE IS
OF POOR QUALITY

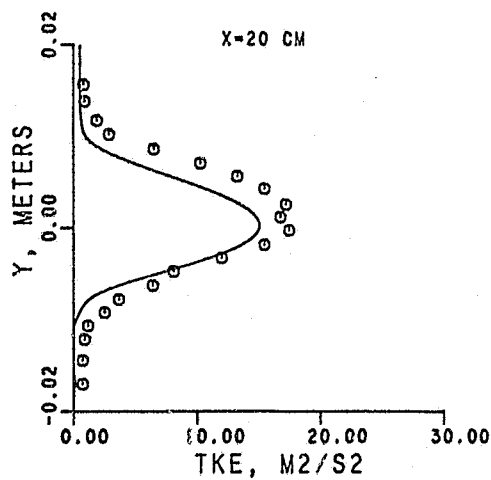
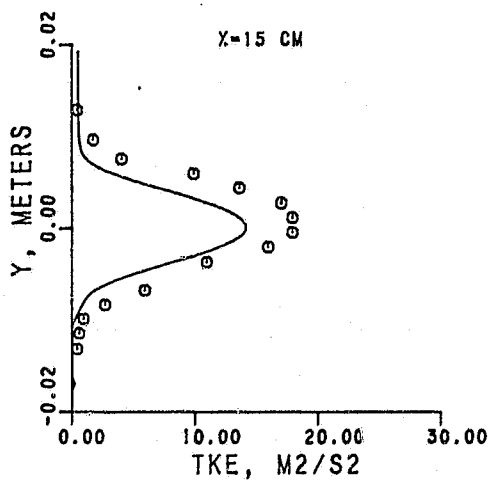
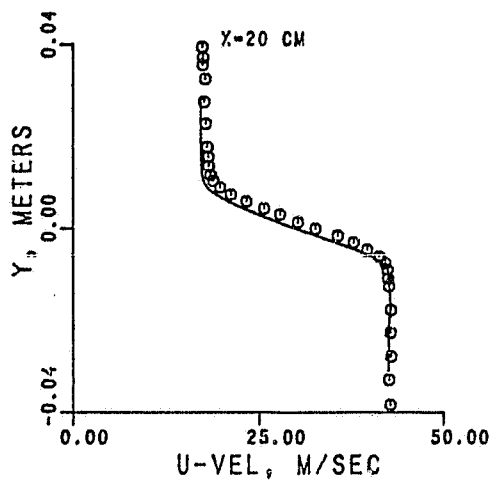
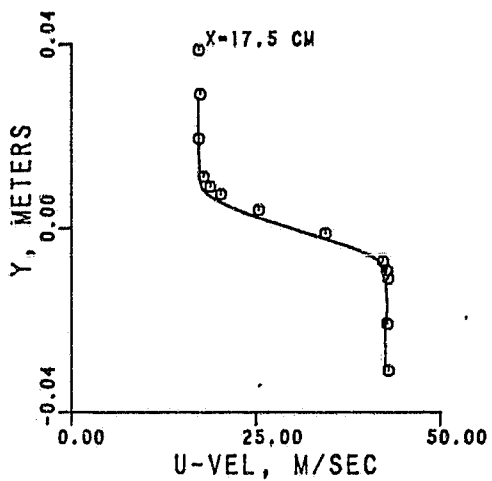
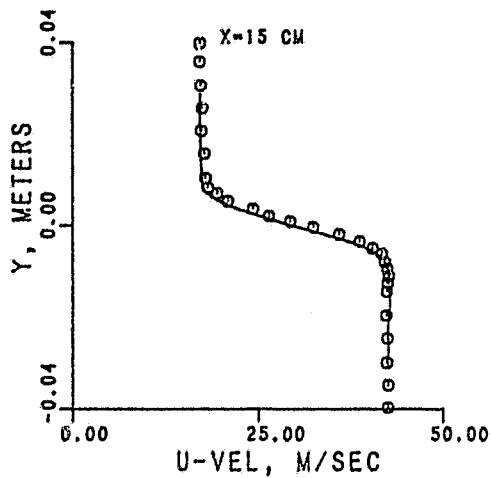
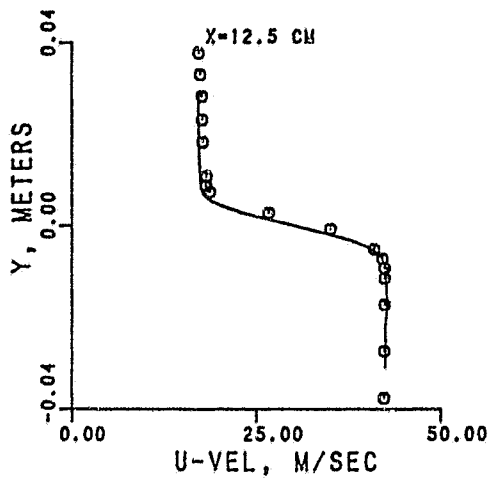


Figure 6.6-2. Mixing Layer Mean Axial Velocity and Turbulent Kinetic Energy (TKE) Profiles Predicted by the Standard k- ϵ Model.

ORIGINAL PAGE IS
OF POOR QUALITY

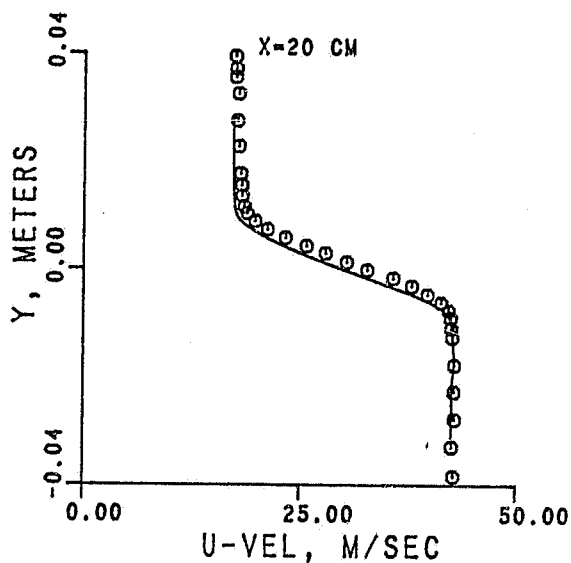
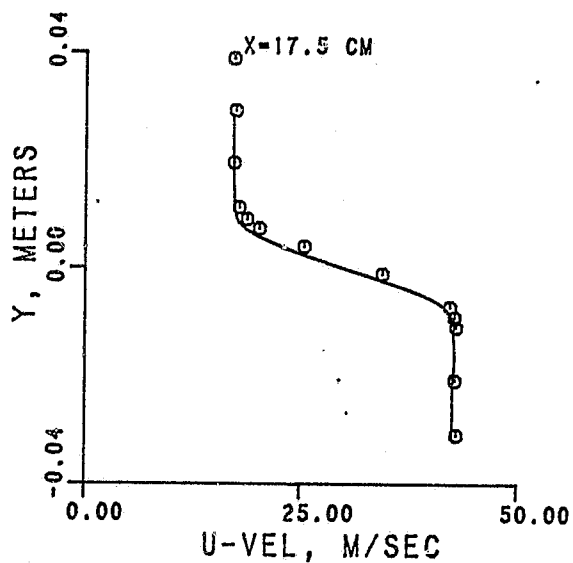
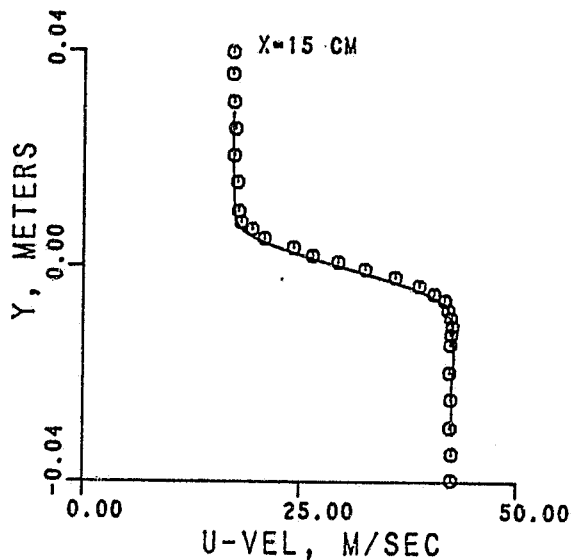
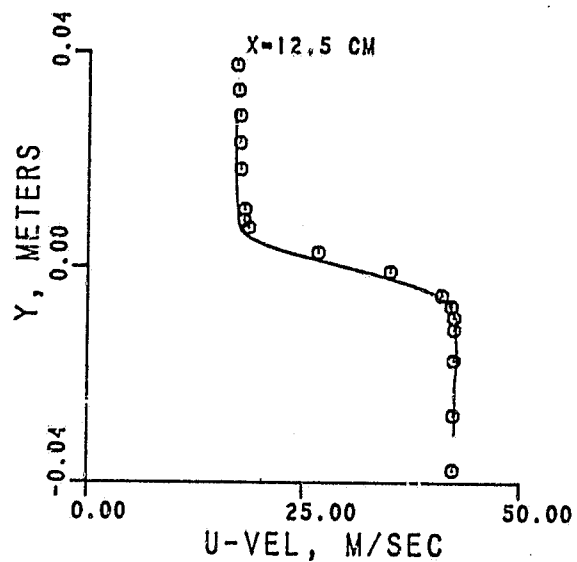


Figure 6.6-3. Mixing Layer Mean Axial Velocity Profiles Predicted by the Algebraic Stress Model (ASM).

ORIGINAL PAGE IS
OF POOR QUALITY

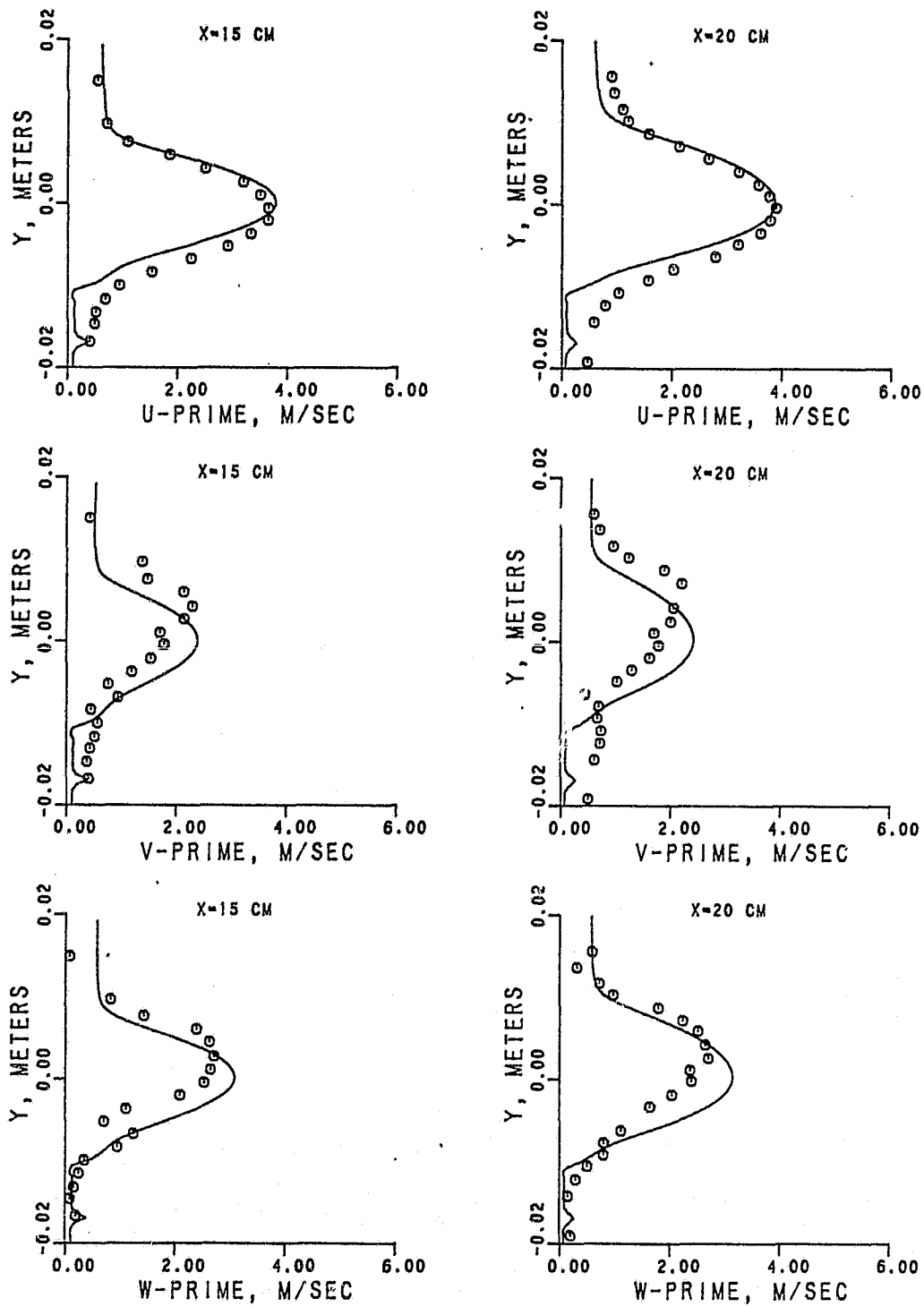


Figure 6.6-4. Mixing Layer Fluctuating Velocity Components (u' , v' and w') Predicted by ASM.

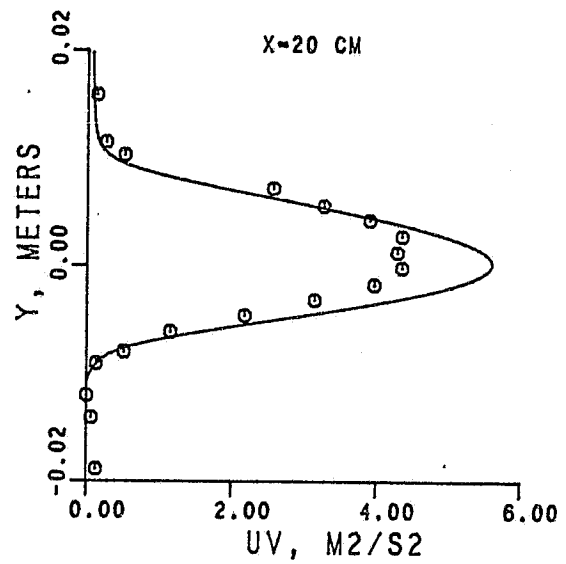
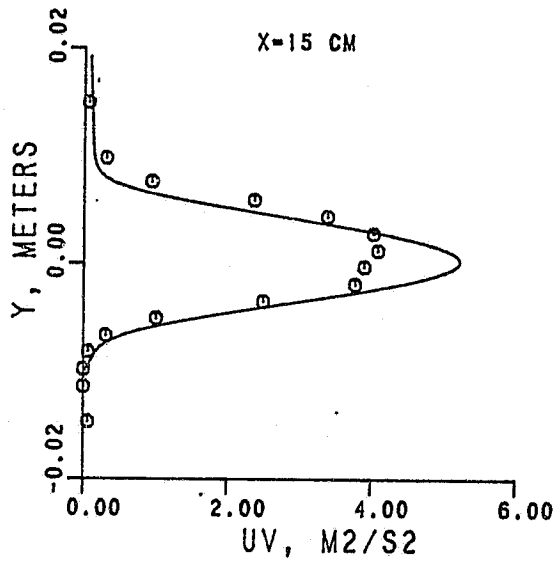
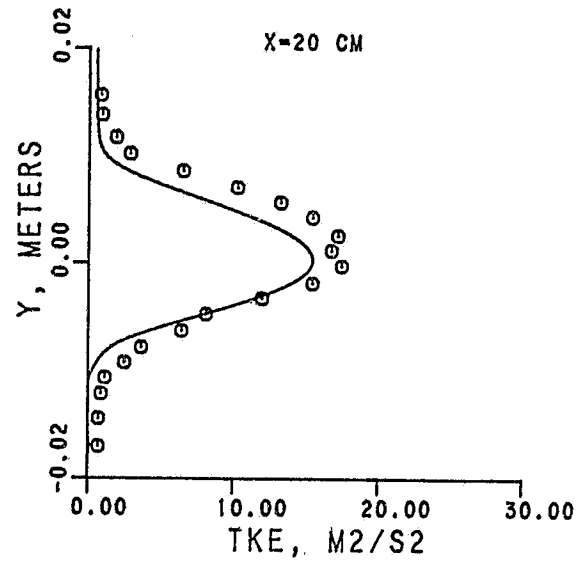
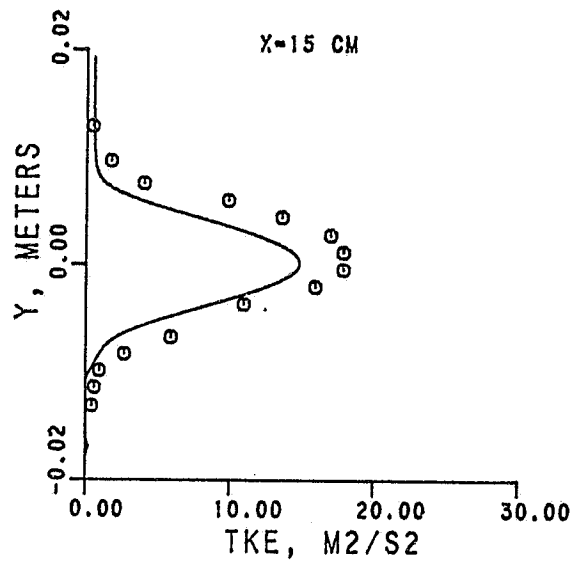


Figure 6.6-5. Mixing Layer Turbulent Kinetic Energy and Shear Stress Profiles Predicted by ASM.

6.7 Mixing of Coaxial Jets in Ambient Air

Another benchmark test case selected from the data base for turbulence model evaluations is the flow in the near field unconfined mixing region of two coaxial jets. Measurements for the selected test case were made by Champagne et al.⁶⁴ using a hot-wire probe. A schematic of their test set-up is shown in Figure 6.7-1. For the test case studied, the ratio of outer to inner velocity at the nozzle exit was 5.0 with the area ratio, $A_o/A_i = 2.94$.

Computations for this flow were performed using the 2-D parabolic stream with the measured inlet velocity profile at $x/D_o = 1.16$, where the maximum velocity, U_{max} was 18.29 m/s. The inlet kinetic energy profiles were obtained from measurements and a uniform inlet length scale of $0.01 D_o$ was prescribed. Computations were made with the standard $k-\epsilon$ model and ASM.

The predicted mean axial velocity profiles with the $k-\epsilon$ model and data are presented in Figure 6.7-2 at $x/D_o = 1.16, 2.14, 3.09, 4.7, 6.05$ and 8.02 . The profiles shown at $x/D_o = 1.16$ are the initial profiles used in the computation. Here $YM2$ represents the local half width of the jet. These results show that the data and $k-\epsilon$ model predictions are in good agreement with each other. Figure 6.7-3 show the comparison between data and ASM predictions for mean axial velocity. These profiles are in good agreement with the data, and a slight improvement over the $k-\epsilon$ results can be seen.

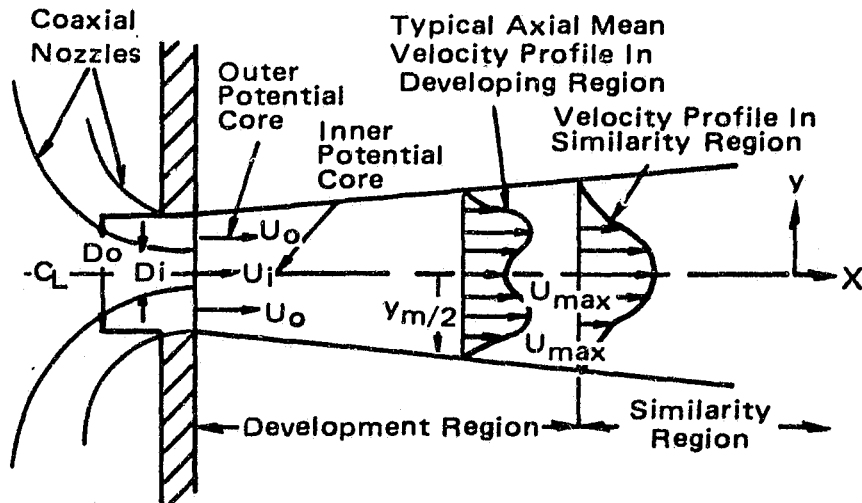
Figure 6.7-4 show the comparison between the data and ASM predictions for u' . The predicted u' values are slightly higher than the data. However, the radial locations of the peak values are in good agreement with the data. Figures 6.7-5 presents the comparison of the v' profiles. The predicted results and measurements are again in good agreement. The comparison between predicted \overline{uv} and measured values are illustrated in Figure 6.7-6. These two results

are in very good agreement with each other up to $x/D = 4.07$. Beyond this station, the predicted \overline{uv} values are slightly larger in magnitude compared to the data.

The $k-\epsilon$ and ASM predictions are in good agreement with measurements. Further improvements in ASM predictions can be achieved by fine tuning the empirical constants in the model.

CHAMPAGNE AND WYGNANSKI

MIXING OF TWO COAXIAL JETS IN AMBIENT AIR



$D_i = 0.0254M$
 $D_o = 0.0435M$
 $U_o = 37.4 M/S$
 $U_i = 7.5 M/S$

Figure 6.7-1. Coaxial-Jets Mixing Setup of Champagne et al.59

ORIGINAL PAGE IS
OF POOR QUALITY

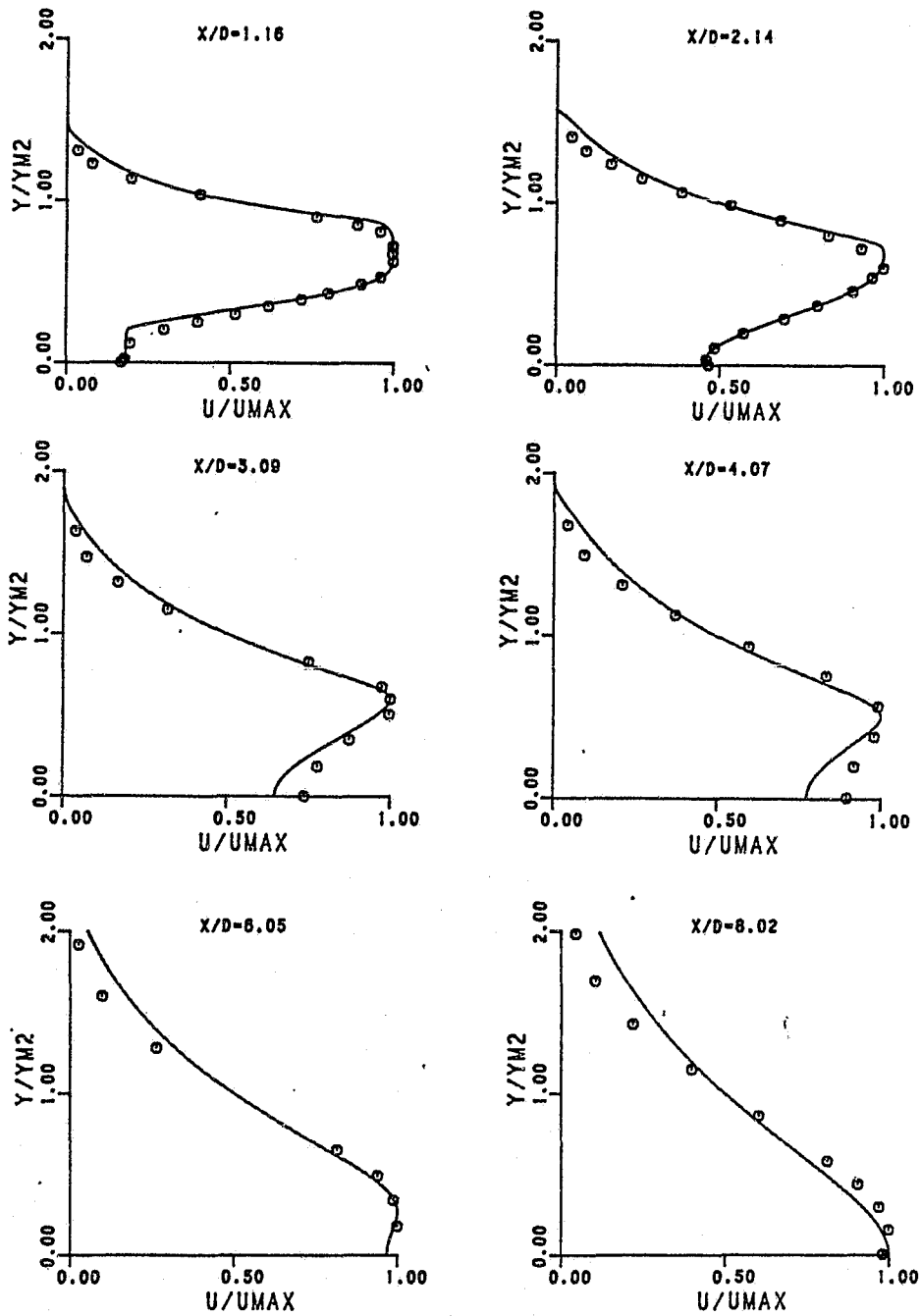


Figure 6.7-2. Comparison Between $k-\epsilon$ Model Predictions and Measured Axial Velocity Profiles of Coaxial Jets in Ambient Air.

ORIGINAL PAGE IS
OF POOR QUALITY

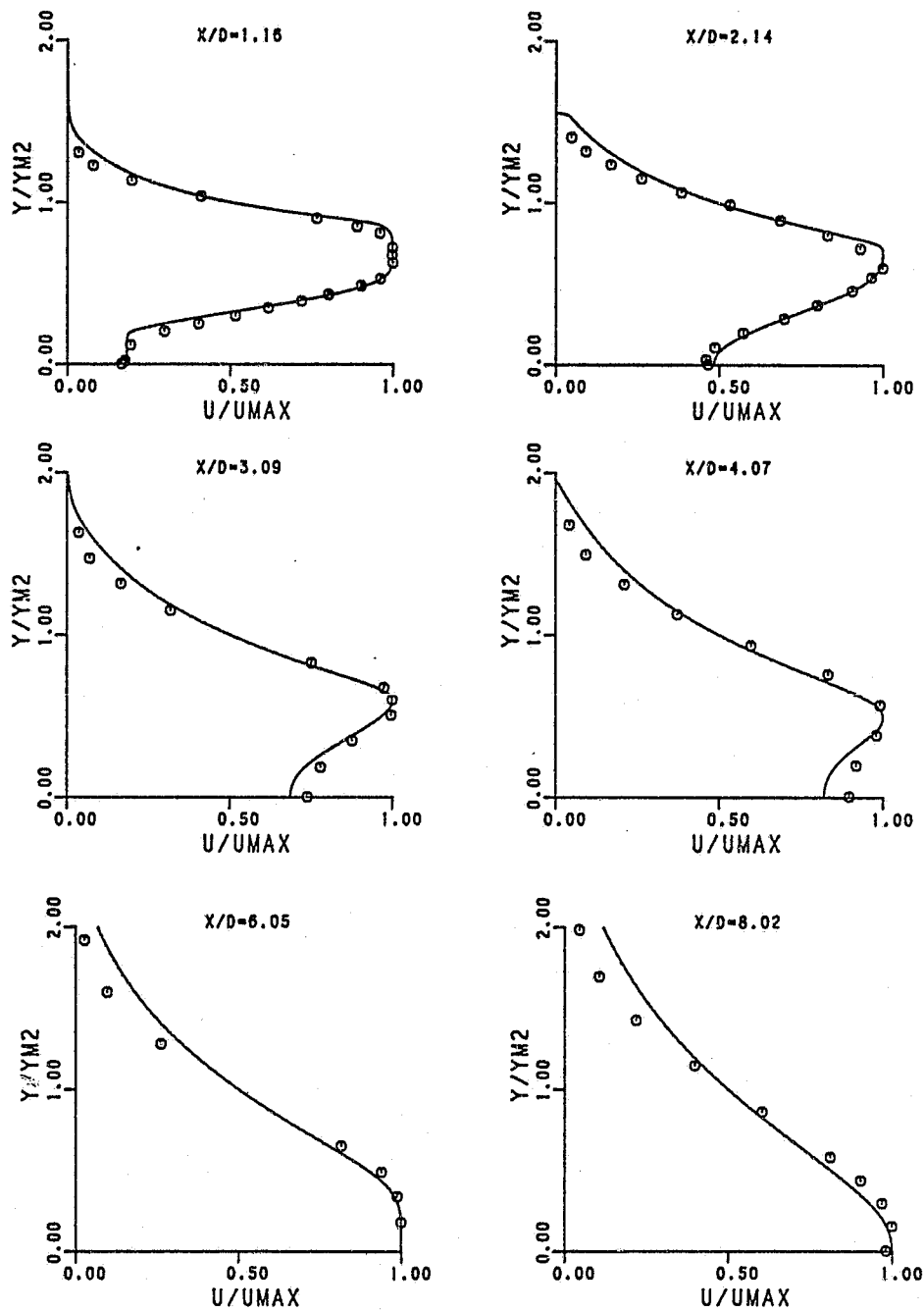


Figure 6.7-3. Comparison Between ASM Predictions and Measured Axial Velocity Profiles of Coaxial Jets in Ambient Air.

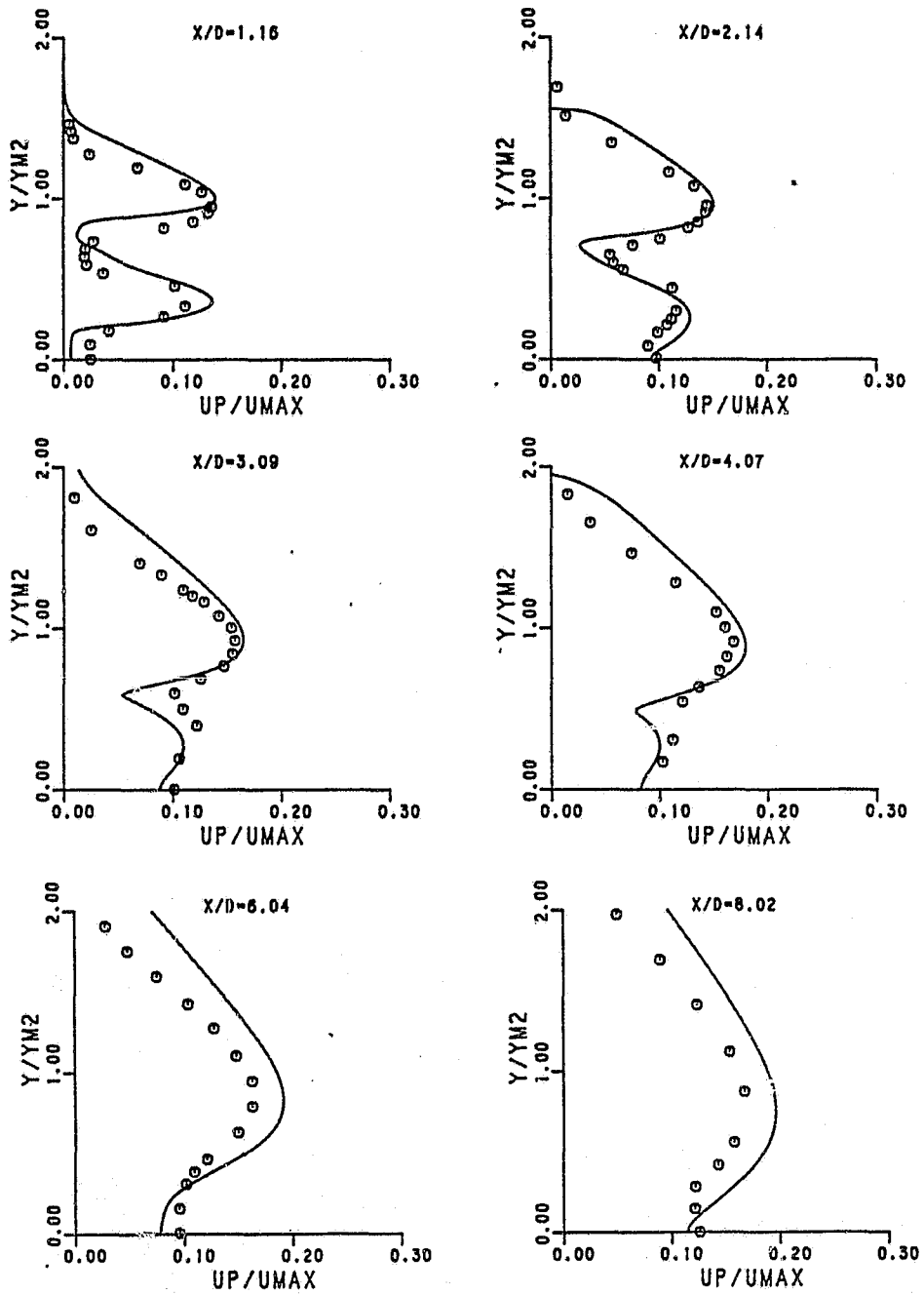


Figure 6.7-4. Predicted and Measured Profiles of RMS Axial Velocity (u') for Coaxial Jets in Ambient Air.

ORIGINAL PAGE IS
OF POOR QUALITY.

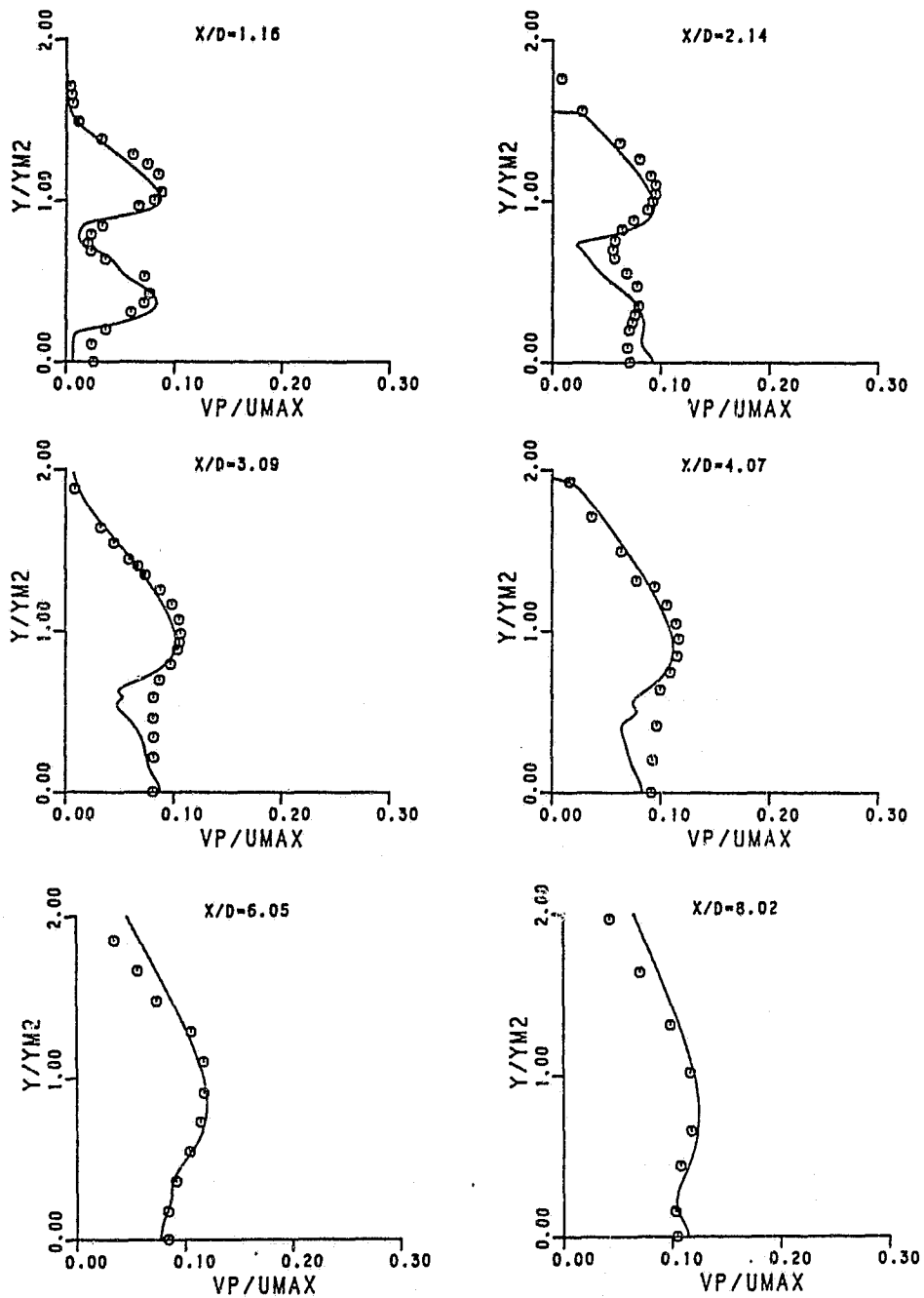


Figure 6.7-5. Predicted and Measured Profiles of Fluctuating Radial Velocity Component (v').

ORIGINAL PAGE IS
OF POOR QUALITY

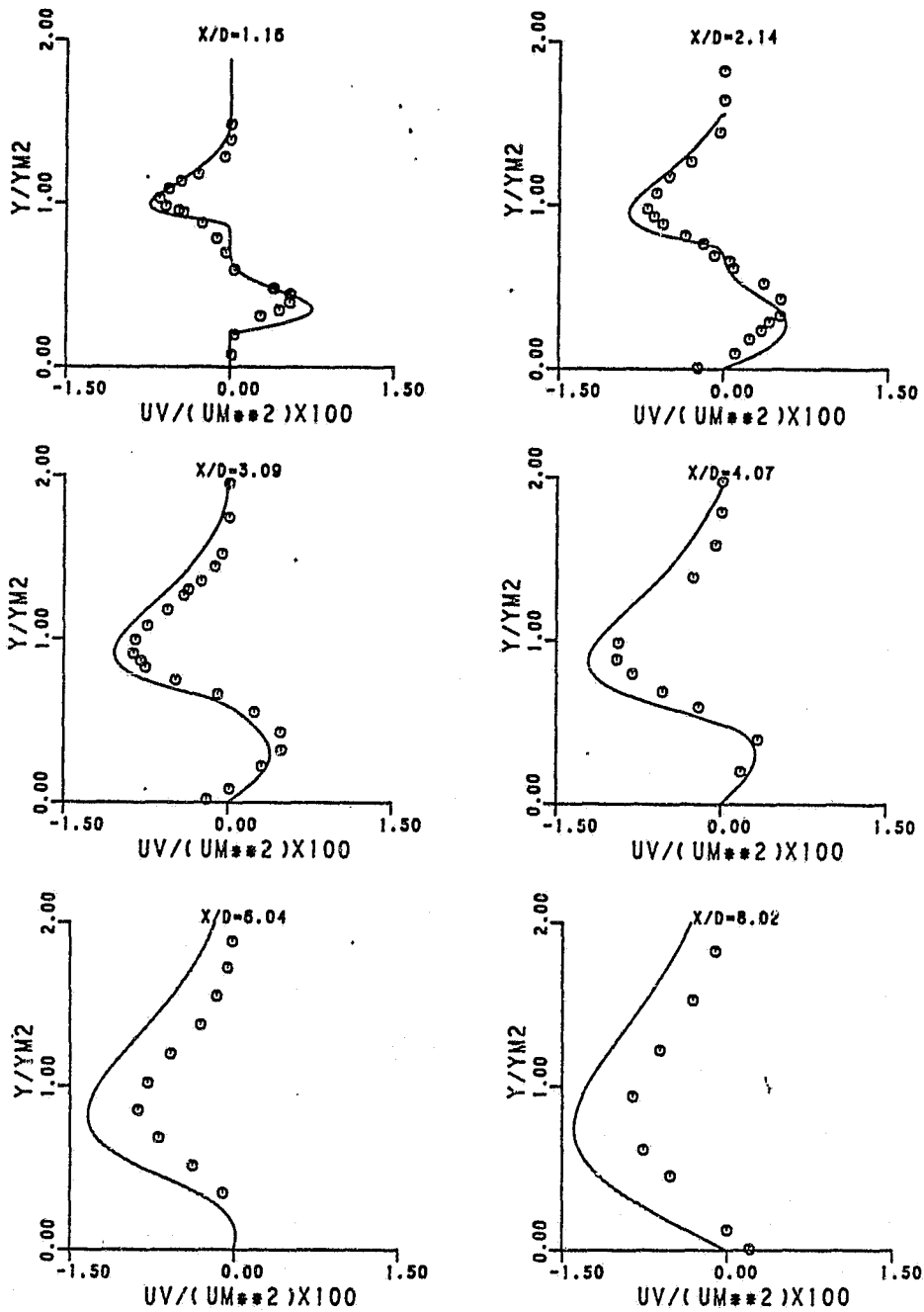


Figure 6.7-6. Predicted and Measured Shear Stress (\overline{uv}) Profiles for the Coaxial Jets in Ambient Air.

6.8 Free Circular Jet

In partial support of the free swirling jet correlation and to further elucidate the coaxial jet mixing, a simpler case of free circular jet was selected for model validation. The benchmark case selected for this flow was that of Wagnanski and Fiedler²¹⁰. They have reported accurate measurements of mean and turbulence velocity components using a hot-wire anemometer in a test setup shown schematically in Figure 6.8-1. Their jet diameter at the nozzle exit was 26.4 mm with a jet exit velocity of 51 m/s. Measurements were made at $x/D = 40, 50, 60, 75,$ and 97.5 . Computations for this case were made with a 2-D parabolic program using initial profile obtained from measurements at $X/D = 40$. Along the axis of the tube, symmetry conditions were applied. A total of 100 cross-stream points were used in the computations.

The mean axial velocity profiles obtained from measurements and standard $k-\epsilon$ model predictions are shown in Figure 6.8-2. The top left corner figure shows the initial profiles used in the computations. The predicted axial velocity results show a slower decay of centerline velocity than the measurements do. This may be due to under-estimated diffusion rates. Launder²¹¹ has recommended modifying the turbulence model constants C_D and C_2 for round jets in stagnant surroundings according to the relation

$$C_D = 0.09 - 0.04 f \quad (141)$$

$$C_2 = 1.92 - 0.067 f \quad (142)$$

where

$$f = \frac{\Delta y}{2U} \left| \left(\frac{\partial U_c}{\partial x} - \left| \frac{\partial U_c}{\partial x} \right| \right) \right|^{0.2} \quad (143)$$

These modifications were used to predict the structure of Wagnanski and Fiedler's free jet. Comparison between the data and predictions for mean axial velocity are shown in Figure 6.8-3. The

predicted centerline velocity decay rate shown in this figure is smaller than the standard k- ϵ model results.

The correction factor f is always positive and equations (141) and (142) would tend to reduce the magnitudes of C_D and C_2 . Reduction of C_D value would tend to reduce the eddy viscosity with attendant decrease in mixing rate.

The present approach is to increase the C_D value by the expression

$$C_D = 0.09 + 0.04 f \quad (144)$$

Furthermore, it was considered necessary to evaluate separating the effects of changing C_C and C_2 . Application of equation (144) alone on the k- ϵ model will be denoted as the k- ϵ 1 model and the use of equation (144) and (142) will be denoted as the k- ϵ 2 model in this report.

The predicted axial velocity profiles using the k- ϵ 1 model and the measurements are presented in Figure 6.8-4. The agreement between data and the k- ϵ 1 model is excellent. Figure 6.8-5 allows the k- ϵ 2 model predictions for axial velocity. These results demonstrate that the k- ϵ 2 model tends to overestimate the mixing, which is responsible for the fast decay of the centerline velocity of the jet.

The predicted mean velocity using the standard ASM is presented in Figure 6.8-6. The ASM tends to slightly underestimate the mixing of the jet compared to the k- ϵ 1 model, but is significantly better than the standard k- ϵ model. Comparison of the predicted u' profiles and measurements, as shown in Figure 6.8-7, illustrates that u' is underpredicted up to $x/D = 60$ and beyond that station the agreement between data and ASM predictions is very good. This is a consequence of the underestimated mixing

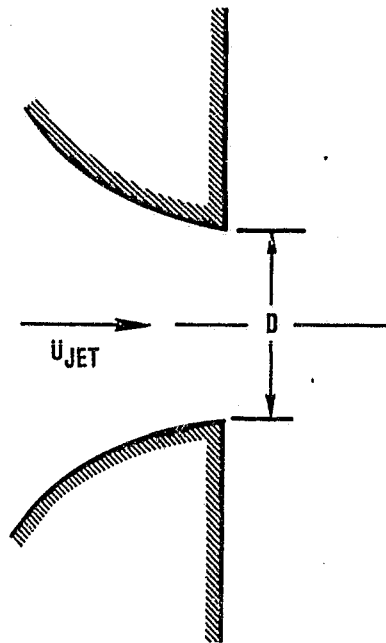
rates in the model. Figure 6.8-8 shows the comparison of the predicted and measured v' component at three axial stations. The agreement between these two is quite good. However, some disagreements can be seen close to the axis of the jet. The predicted w' velocity profiles are in good agreement with the data, as seen in Figure 6.8-9. The predicted \overline{uv} profiles are compared with the measurements in Figure 6.8-10. The \overline{uv} values are initially under-predicted and are slightly overestimated at $x/d = 75$.

For the case of the round free jet, the standard $k-\epsilon$ model tends to underestimate the turbulent diffusion rates. Modifications of the empirical constants are necessary to improve these results. The $k-\epsilon_1$ model accurately predicts the mean velocity profiles, while the $k-\epsilon_2$ model tends to overestimate the jet center-line decay rate. The ASM shows a substantial improvement over the standard $k-\epsilon$ model and no ad hoc modification of the empirical constants is necessary. The turbulence structure is well predicted by the ASM, and further refinement of the ASM is necessary to improve the quantitative predictions.

ORIGINAL PAGE IS
OF POOR QUALITY

WYGNANSKI AND FIEDLER

AXISYMMETRIC FREE JET



$D = 0.0264 \text{ M}$

$U_{JET} = 51 \text{ M/S}$

$T_{JET} = 300^\circ\text{K}$

Figure 6.8-1. Geometry of Single Free Jet Setup Studied by Wagnanski and Fiedler.

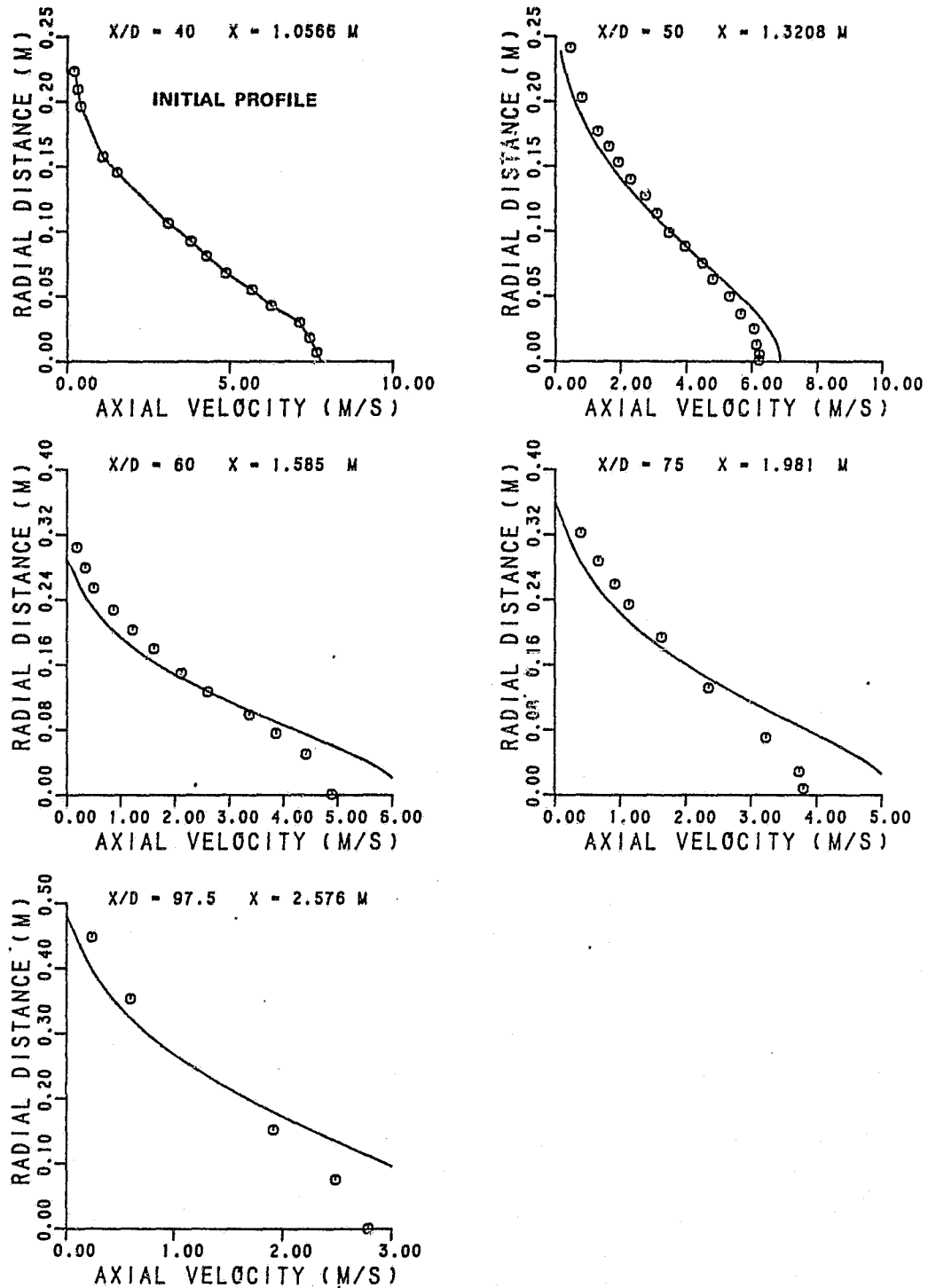


Figure 6.8-2. Comparison Between $k-\epsilon$ Model Predictions and Measured Axial Velocity Profiles, Initial Jet Velocity = 51 m/s Initial Jet Diameter $D = 26.4$ mm.

ORIGINAL PAGE IS
OF POOR QUALITY

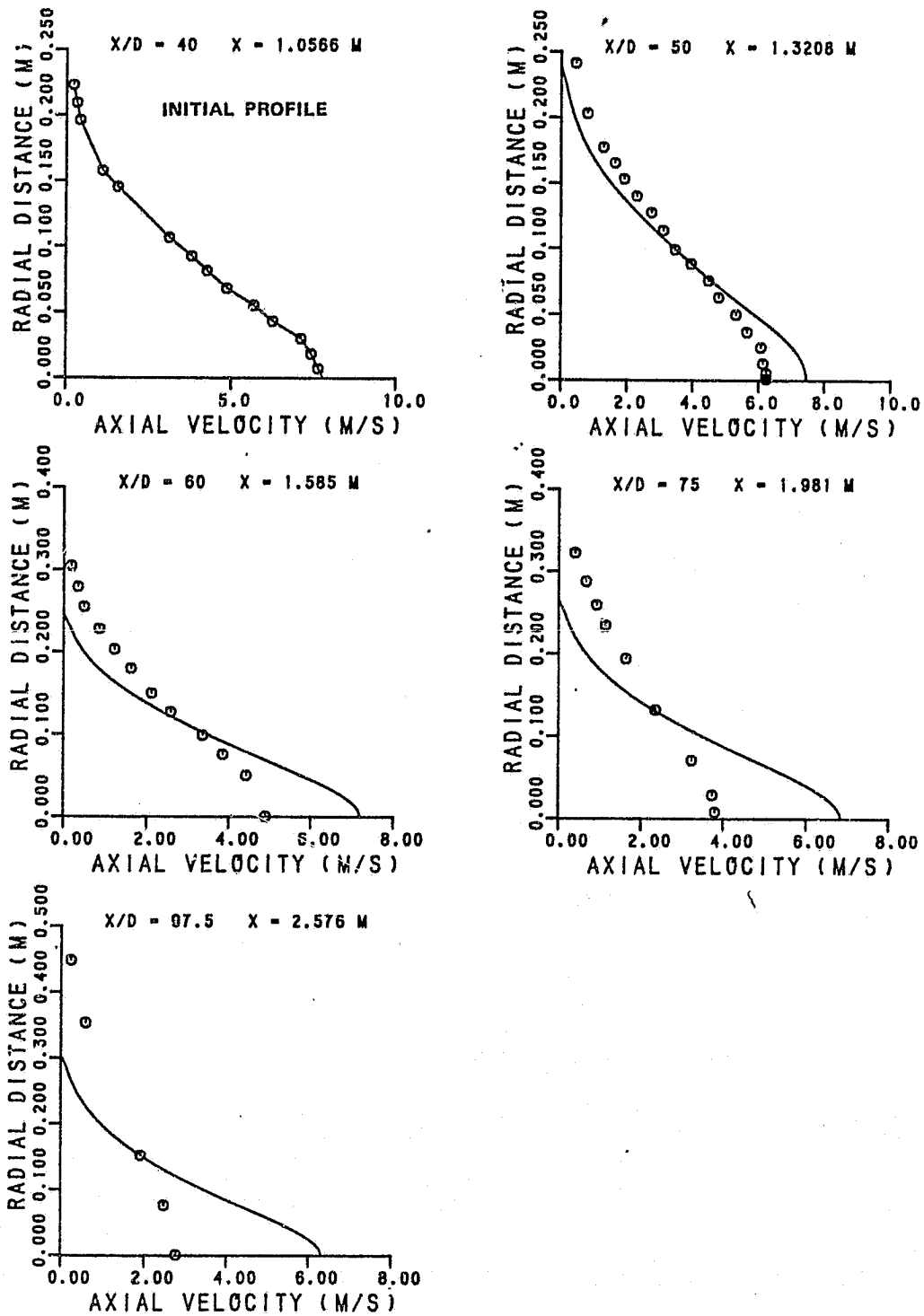


Figure 6.8-3. Modified $k-\epsilon$ Model Predictions with C_D and C_2 Constants Given by Equations (141) and (142).

ORIGINAL PAGE IS
OF POOR QUALITY

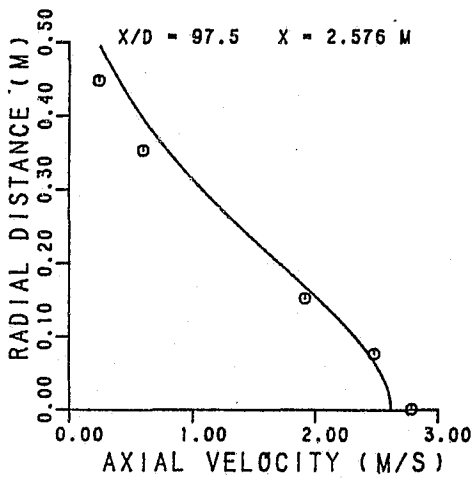
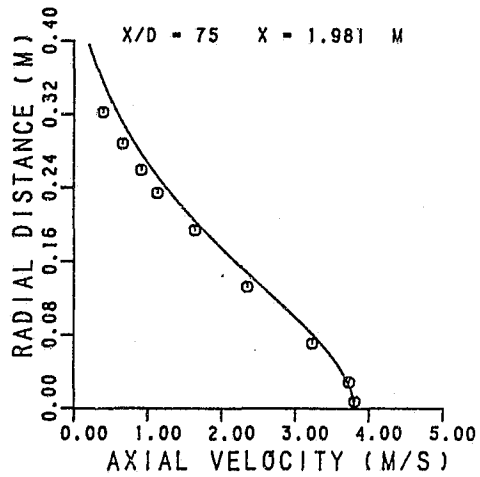
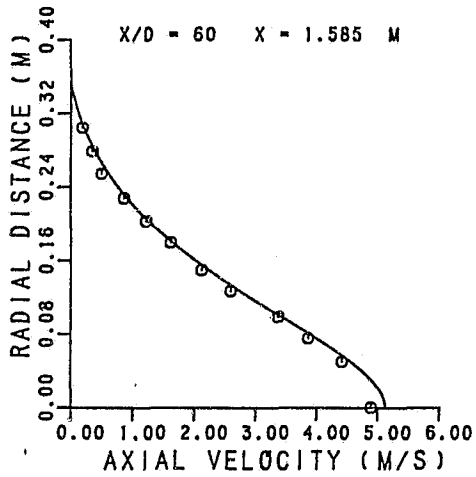
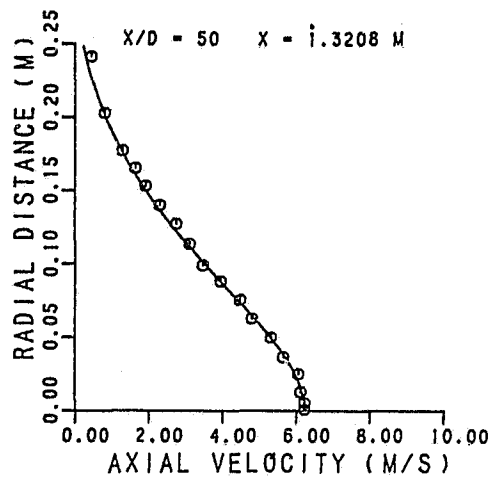
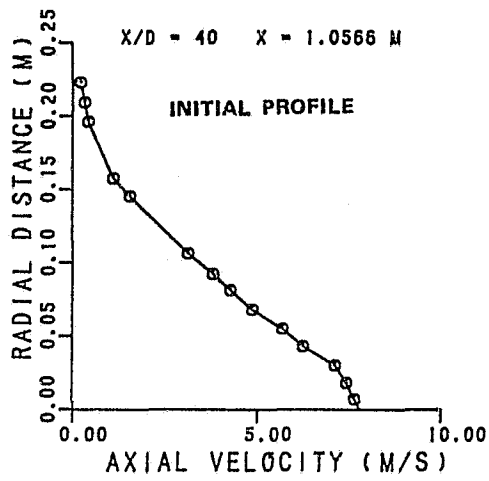


Figure 6.8-4. Modified $k-\epsilon$ Model ($k-\epsilon_l$) Predictions With C_D as given by Equation 62.

ORIGINAL PAGE IS
OF POOR QUALITY

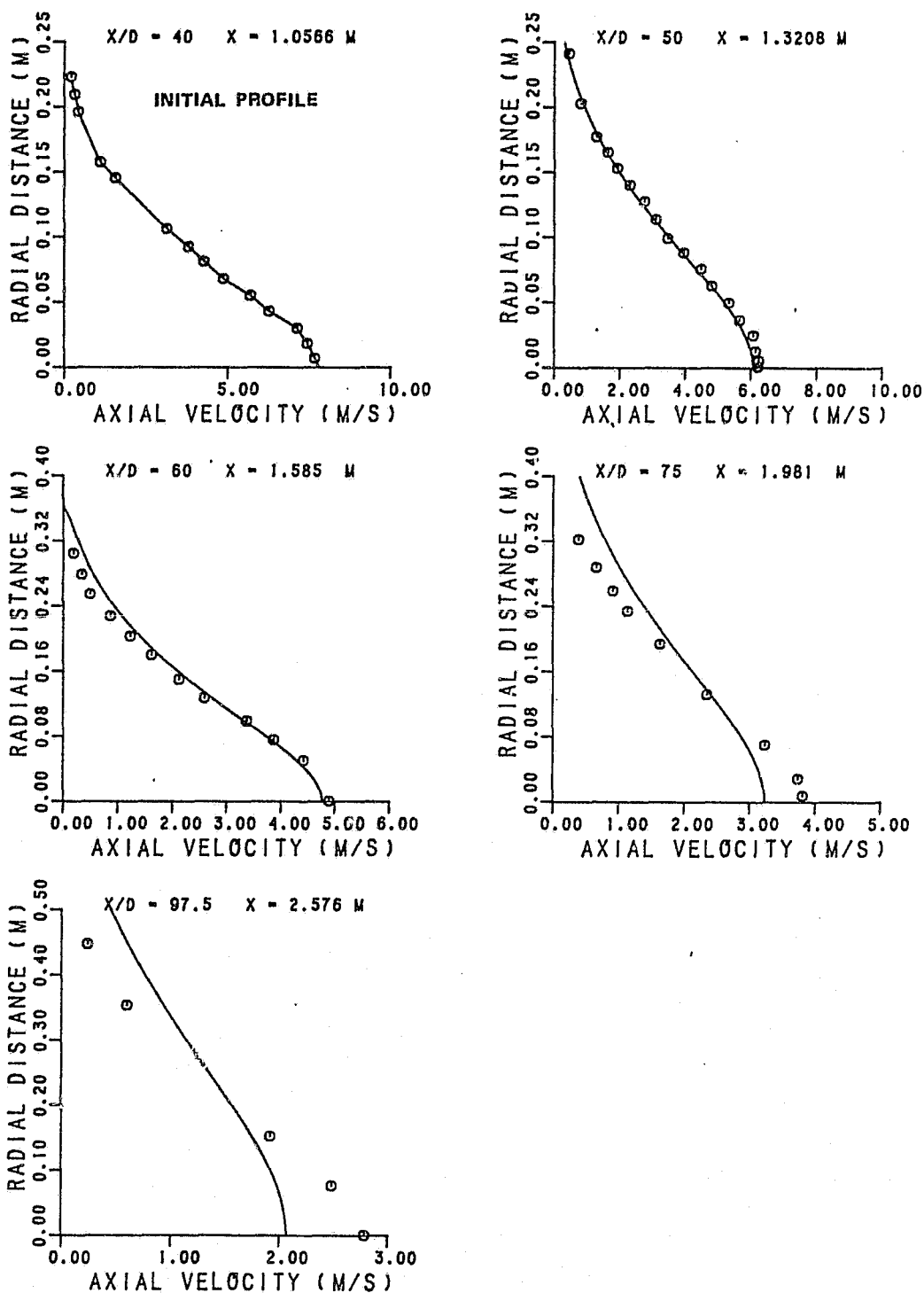


Figure 6.8-5. Modified $k-\epsilon$ Model ($k-\epsilon_2$) Predictions with C_2 and C_D As Given by Equations 60 and 62.

ORIGINAL PAGE IS
OF POOR QUALITY

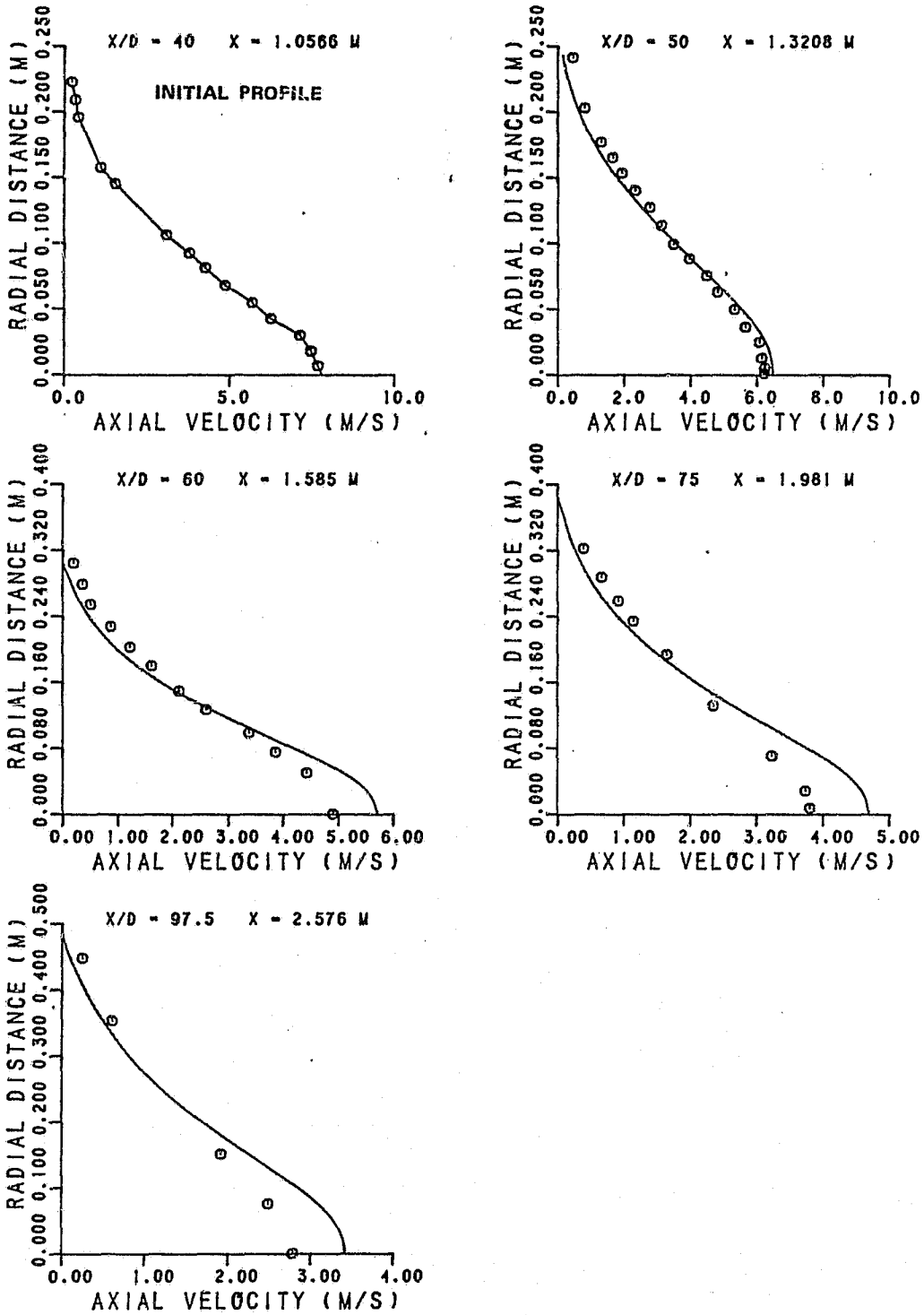


Figure 6.8-6. Comparison Between ASM Predictions and Measured Axial Velocity Profiles of a Free Jet.

ORIGINAL PAGE IS
OF POOR QUALITY

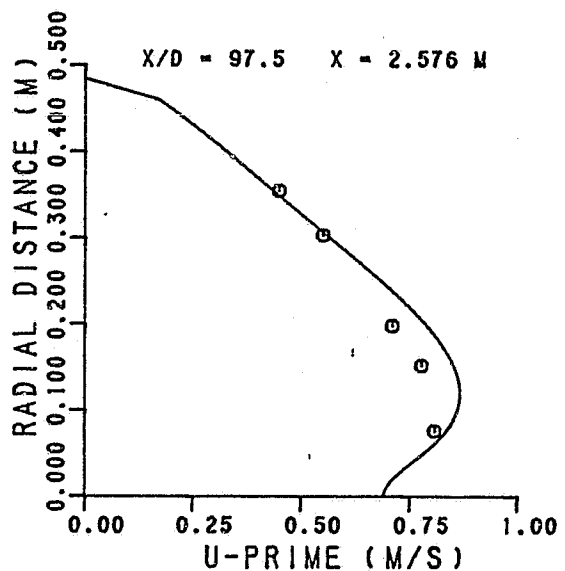
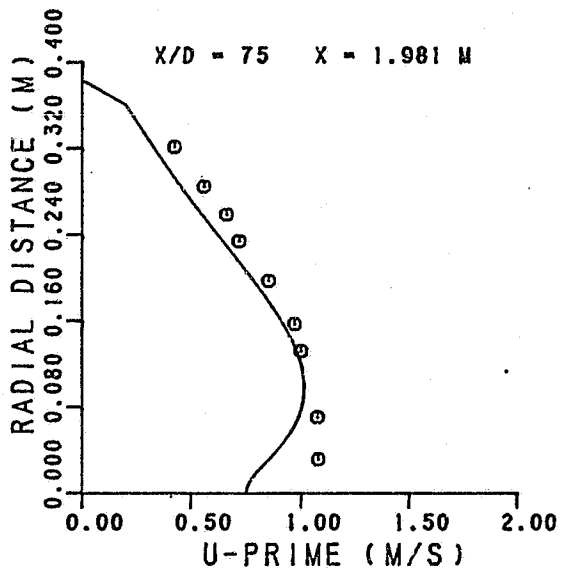
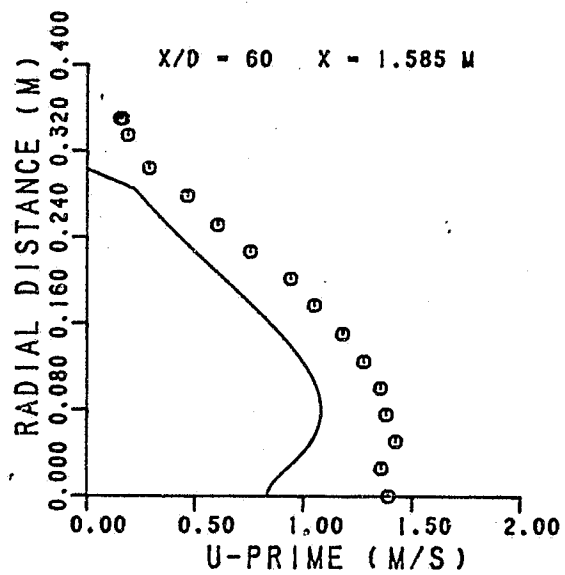
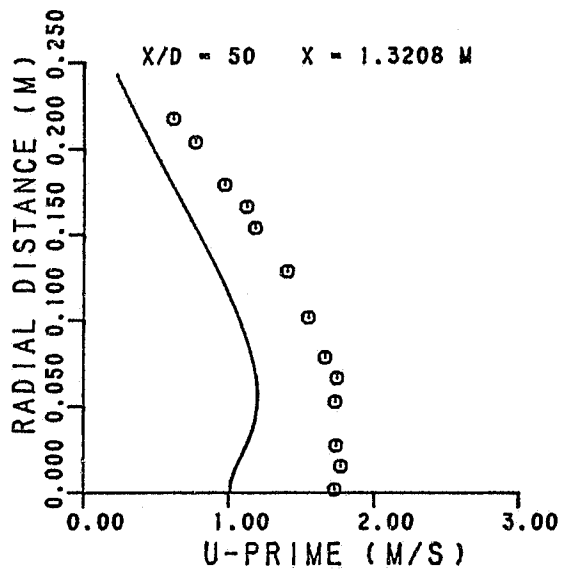


Figure 6.8-7. Comparison Between ASM Predictions and Measurements for Axial RMS Turbulence Velocity Fluctuations.

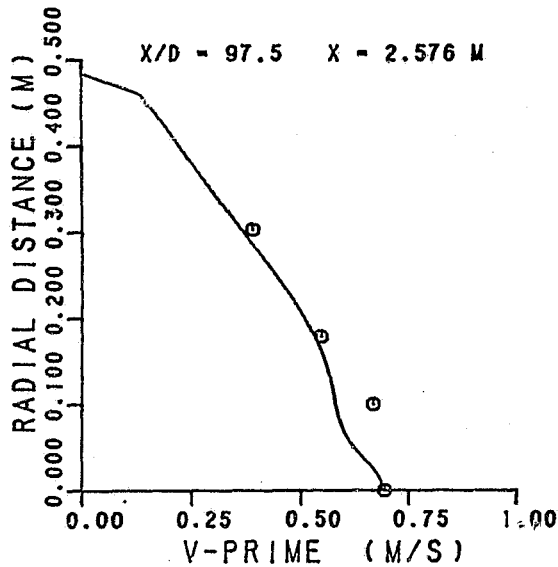
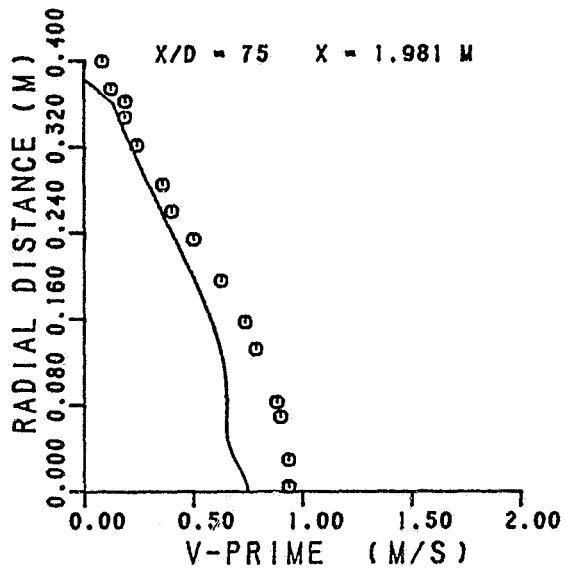
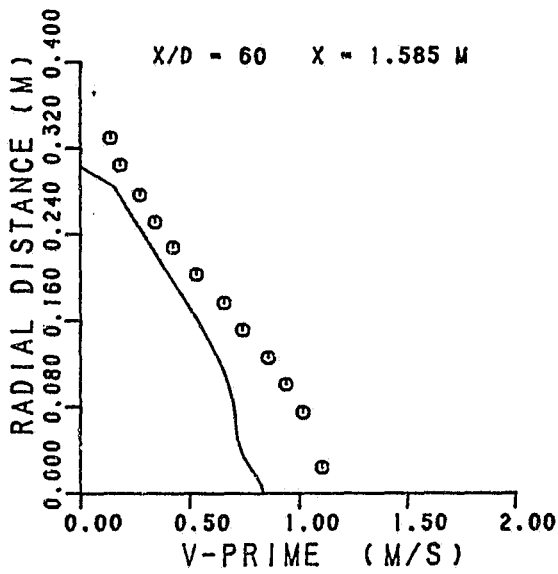


Figure 6.8-8. Comparison Between ASM Predictions and Measurements for Radial RMS Turbulence Velocity Fluctuations.

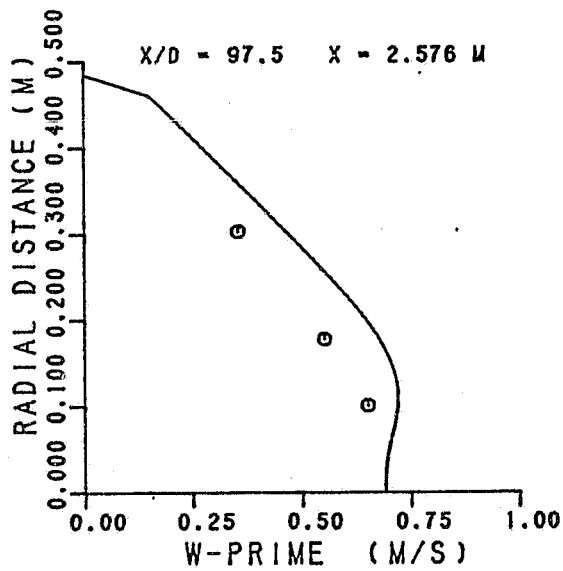
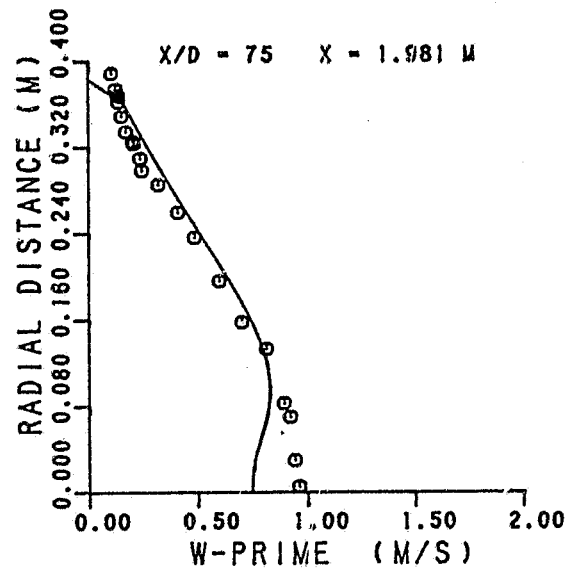
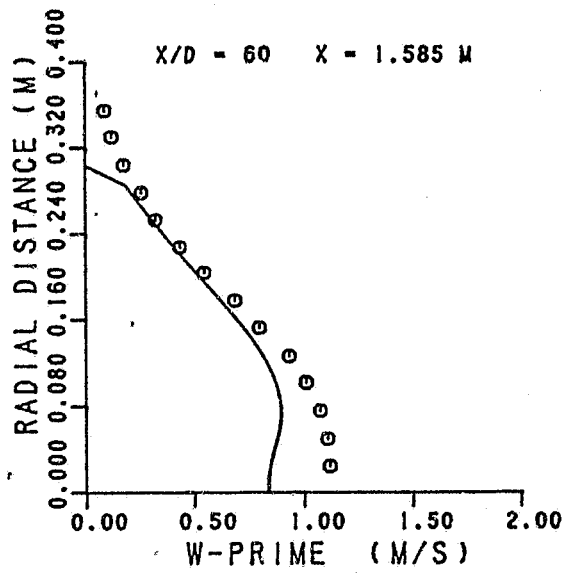


Figure 6.8-9. Comparison Between ASM Predictions and Measurements for Circumferential RMS Turbulence Velocity Fluctuations.

ORIGINAL PAGE IS
OF POOR QUALITY

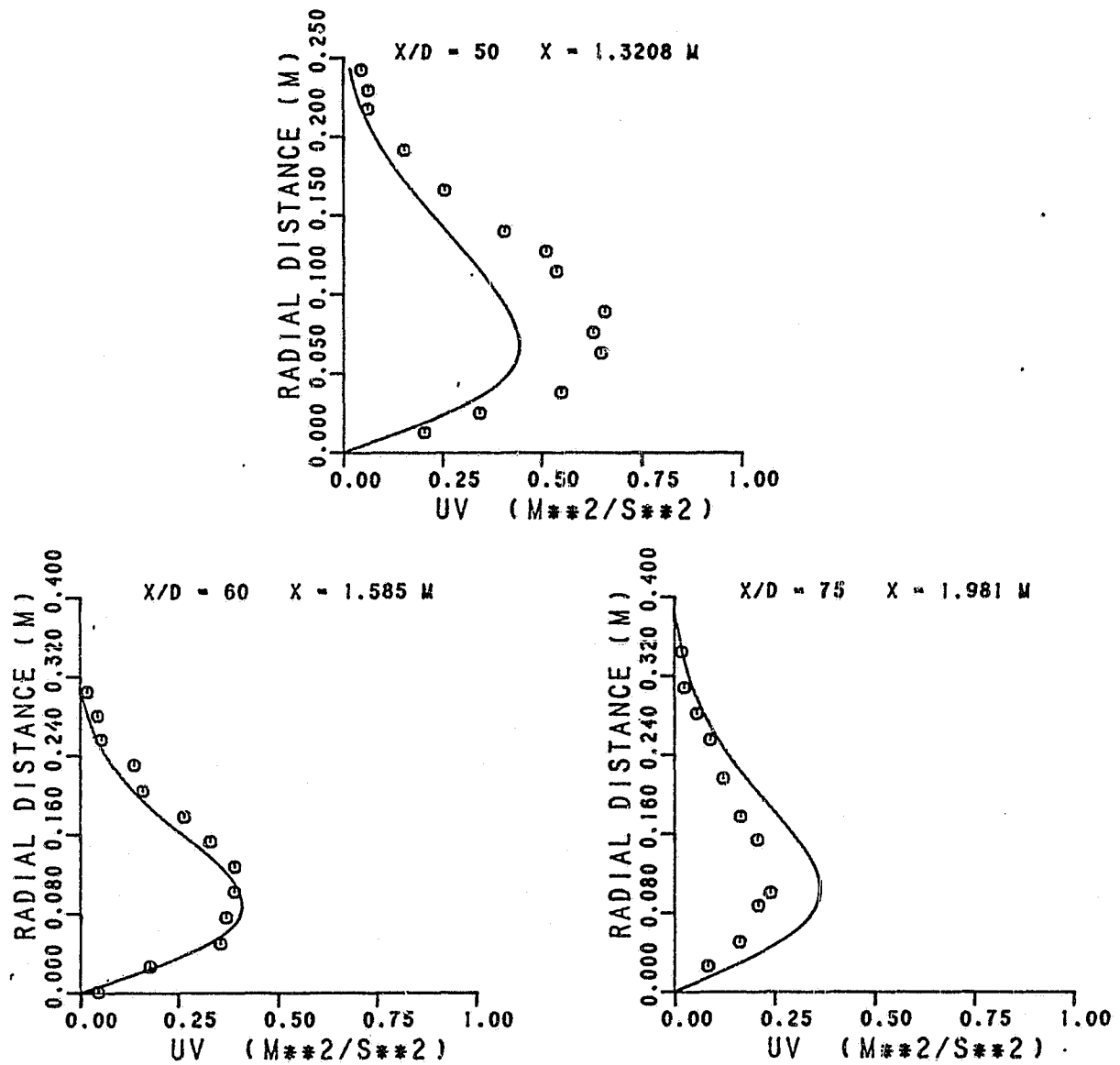


Figure 6.8-10. Comparison Between ASM Predictions and Measurements for Turbulent Shear Stress.

6.9 Flow Over a Heated Flat Plate

The $k-\epsilon$ and the ASM seem to predict the momentum transport reasonably well for simple flows. It was deemed essential to evaluate these models on the transport of scalar quantities such as temperature. The benchmark test case that was selected for this purpose was the flow over a heated flat plate. Measurements of mean and fluctuations of temperature were made for this case by Charnay¹¹⁰ et al. A schematic of their setup is shown in Figure 6.9-1. The flat plate was heated from the leading edge up to $x = 0.7$ m and maintained at a uniform temperature of 313°K. Beyond $x = 0.7$ m, the wall temperature was abruptly changed and maintained at 290°K. The free stream temperature of air during the test was 293°K. Measurements of \bar{T} , T'^2 and $\overline{vT'}$ were made at $x = 0.7, 0.8, 0.9, 1.05,$ and 1.4 m.

Computations for this case were made using the 2-D parabolic program with the initial conditions specified at $x = 0.7$ m from the measured profiles. At $x = 0.7$ m, only the measured temperature profiles were reported. The inlet velocity profiles were assumed to conform to the law of the wall. The unknown wall mean stress was calculated by assuming the temperature distribution to also follow a logarithmic law. The details of this calculation procedure are as follows:

For a flat plate with constant free stream velocity and surface temperature, the local Stanton number $(\frac{h}{\rho_{\infty} U_{\infty} C_p})$ is given by Kays²¹² as

$$St = \frac{0.0287 Re_x^{-0.2}}{0.169 Re_x^{-0.1} (13.2 Pr - 10.16) + 0.9} \quad (145)$$

where $Re_x = \rho_{\infty} U_{\infty} x / \mu$

For the given free stream conditions, St was computed. The local wall heat flux, q_w was obtained from ²¹²

$$q_w = \rho_\infty C_p U (T_w - T_\infty) St \quad (146)$$

The logarithmic law for temperature is given by Kays²¹² as

$$t_+ = 2.195 \ln y^+ + 13.2 Pr - 5.66 \quad (147)$$

where,

$$t^+ = \frac{(T_w - T) u_*}{(q_w / \rho_\infty C_p)} \quad (148)$$

and

$$y = \frac{\rho_\infty u_* y}{\mu} \quad (149)$$

From the prescribed temperature profile (T vs. y), using equation (148), the value of u_* was computed. Knowing u_* , the velocity profile was constructed from the law of the wall for mean velocity. This profile was used as the initial velocity profile. The turbulence kinetic energy was assumed to be a constant with $k = 0.003 U^2$. The length scale was assumed to be linear, $l = \kappa y$ up to $y = \delta$. Beyond that point, l was set equal to $\kappa \delta$.

The boundary condition on the boundary layer edge was specified through the computed entrainment rate. Along the wall boundaries, Chien's low Reynolds number correction to the $k-\epsilon$ model was applied. Across the boundary layer, a total of 100 nodes were distributed with the nodes closely spaced near the wall and further apart near the boundary layer edge. Computations were made using

- o $k-\epsilon$ model with gradient transport model
- o ASM with gradient transport model

o Algebraic scalar transport model (ASTM)

The standard k- ϵ model predictions with gradient scalar transport model are presented in Figures 6.9-2 through 6.9-4. In gradient transport assumption, the following expressions were used for the turbulent transports:

$$\rho \overline{u\theta'} = - \Gamma_{\text{eff},\theta} \frac{\partial \theta}{\partial x} \quad (150)$$

$$\rho \overline{v\theta'} = - \Gamma_{\text{eff},\theta} \frac{\partial \theta}{\partial r} \quad (151)$$

$$\overline{\theta'^2} = \frac{2}{a_\theta} \frac{k}{\epsilon} \Gamma_{\text{eff},\theta} \left\{ \left(\frac{\partial \bar{\theta}}{\partial x} \right)^2 + \left(\frac{\partial \bar{\theta}}{\partial r} \right)^2 \right\} \quad (152)$$

$$\Gamma_{\text{eff},\theta} = \frac{\mu_{\text{eff}}}{\text{Pr}_{\text{eff}}}$$

where

$$\text{Pr}_{\text{eff}} = 0.9$$

Figure 6.9-2 shows the comparison between measured and predicted mean temperature profiles across the boundary layer. In these figures, the abscissa represents the temperature difference, $(T - T_{W_0}) / (T_\infty - T_{W_0})$, where T_{W_0} is the wall temperature upstream of $X = 0.7$ m. (313°K). At $X = 0.7$, the nondimensional temperature profile would be similar to the velocity profile with a monotonic variation between zero at the wall to 1.0 at face stream edge. Just downstream of $X = 0.7$, the value of the nondimensional temperature at the wall jumps to 1.15. The mean temperature profiles gradually recover from a hot wall condition to a cold wall profile. The k- ϵ model predictions for temperature differences are smaller than the data as seen in Figure 6.9-2. In other words, the model underestimates the heat transfer rate to the wall.

The root mean square (RMS) value of the temperature fluctuations obtained from the k- ϵ model are shown in Figure 6.9-3. In

these figures, the T' values are nondimensionalized by $(T_{w_0} - T_{\infty})$, (20°K in the present case). The $k-\epsilon$ model predicts high values of T' near the wall. At the outer edge of the boundary layer, the $k-\epsilon$ model predictions are in reasonably good agreement with data. At $x = 140$ cm, the peak T' values tend to approach the measured values. This indicates that the gradient diffusion assumption is valid for equilibrium boundary layers.

Figure 6.9-4 illustrates the comparison between data and $k-\epsilon$ model predictions for the turbulent transport $\overline{vT'}$. In these figures, the quantity $\overline{vT'}$ is nondimensionalized by $U (T_{w_0} - T_{\infty})$, with T_{w_0} being the wall temperature upstream of $x = 0.7$ m. The $k-\epsilon$ model underestimates the heat flux component $\overline{vT'}$, especially in the region close to the wall.

The predicted mean temperature profiles obtained from the ASM and gradient transport assumption are shown in Figure 6.9-5. These profiles are almost identical to those obtained from the $k-\epsilon$ model, and the temperature differences are overestimated. The ASM predictions for RMS temperature fluctuations are shown in Figure 6.9-6. These profiles are also identical to those obtained from $k-\epsilon$ model. A similar conclusion may be drawn for the $\overline{vT'}$ profiles obtained from ASM, as seen in Figure 6.9-7. These figures illustrate that the gradient transport model underestimated the heat flux, and the ASM does not significantly improve the heat estimation.

The predicted results using the ASTM are presented in Figure 6.9-8 through 6.9-10. The ASTM uses the expressions given in Section 4.0 for the various turbulent transports. The ASTM predictions for mean temperature are shown in Figure 6.9-8. Comparison with the $k-\epsilon$ model results (Figure 6.9-2) shows that the ASTM significantly improves the predictions for mean temperature, and at $x = 140$ cm, the predicted mean temperature profile agrees very well with the data.

The ASTM predictions for RMS temperature fluctuations are illustrated in Figure 6.9-9. The ASTM tends to overestimate the T' values near the boundary layer edge. In the near-wall region, some differences between the data and ASTM predictions are present. These differences are mainly due to the estimated turbulence structure, namely, u^2 and v^2 profiles.

The ASTM predictions for the heat transport $\overline{vT'}$ are presented in Figure 6.9-10. These profiles are in good agreement with the data near the edge of the boundary layer. However, some differences exist in the near-wall region. These are due to the differences between estimated values and test conditions. The test results for the turbulence velocities were not reported. Further improvements in the ASTM predictions can be achieved if the turbulence structure predictions are refined.

The results presented in this paragraph show that even for a simple flow case of boundary layer with sudden changes in wall temperature, the gradient transport assumption is not valid. The ASTM gives significantly improved predictions. Further improvements in the Reynolds stress predictions are needed to obtain quantitatively accurate results from ASTM.

Comparisons of mean temperature ($T-T_{w0}$), the RMS temperature fluctuations (T'), and the heat transport ($\overline{vT'}$) calculated using the various models can be made from the following figures:

	<u>Figures</u>
$T-T_{w0}$	6.9-2 6.9-5 6.9-8
$\frac{T'}{T_{w0}-T_{\infty}}$	6.9-3 6.9-6 6.9-9
$\frac{\overline{vT'}}{U_{\infty}(T_{w0}-T_{\infty})}$	6.9-4 6.9-7 6.9-10

CHARNAY ET AL

FLOW OVER A HEATED FLAT PLATE

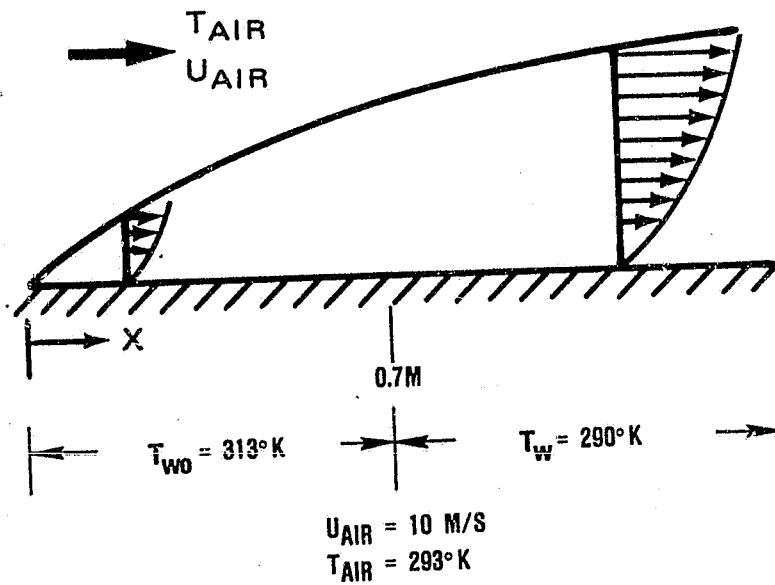


Figure 6.9-1. Geometry of Flow Over a Flat Plate with Step Change in Temperature.

ORIGINAL PAGE IS
OF POOR QUALITY.

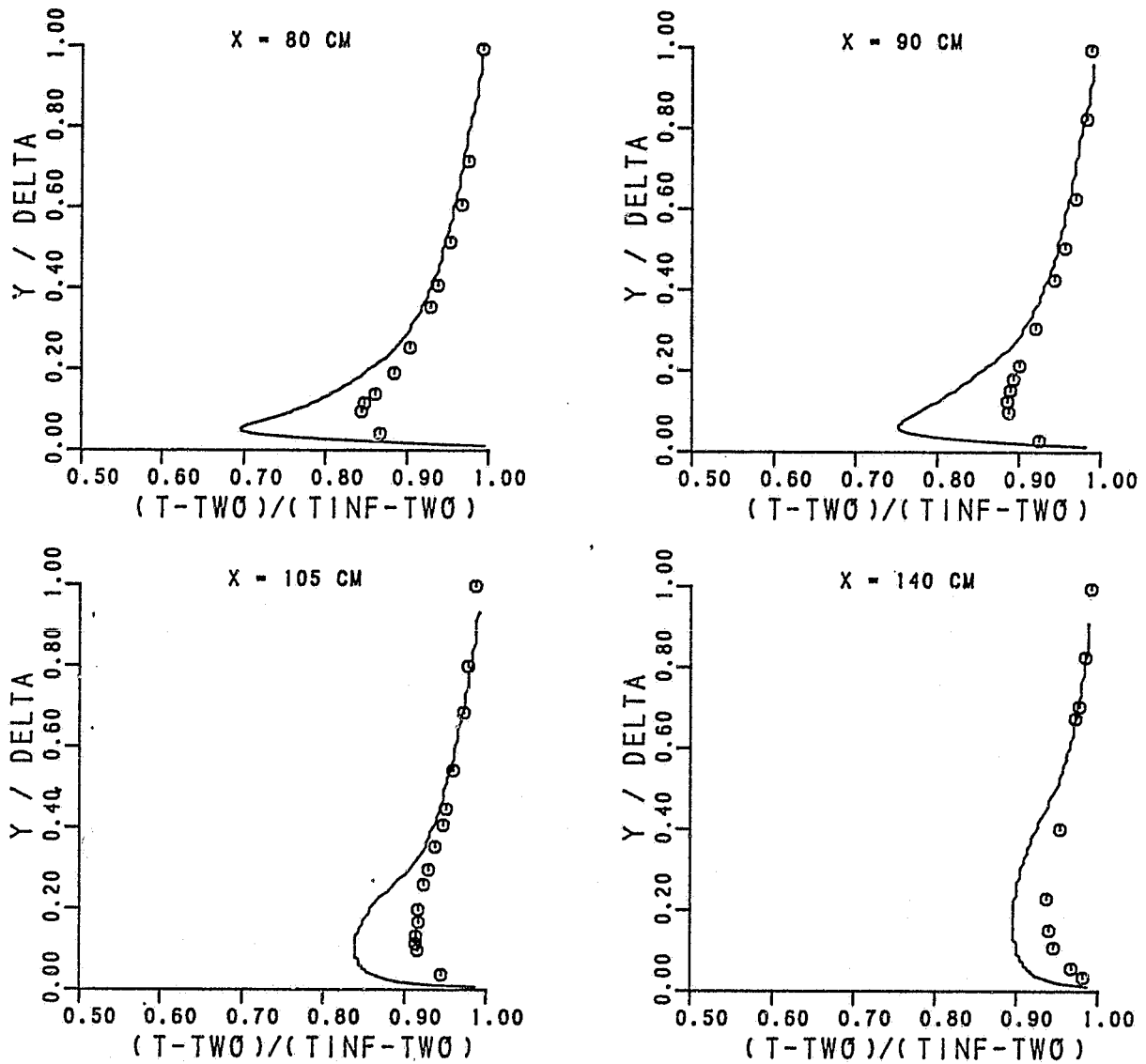


Figure 6.9-2. $k-\epsilon$ Model Predictions and Measured Mean Temperature Profile on a Flat Plate with Step Change in Temperature.

ORIGINAL PAGE IS
OF POOR QUALITY

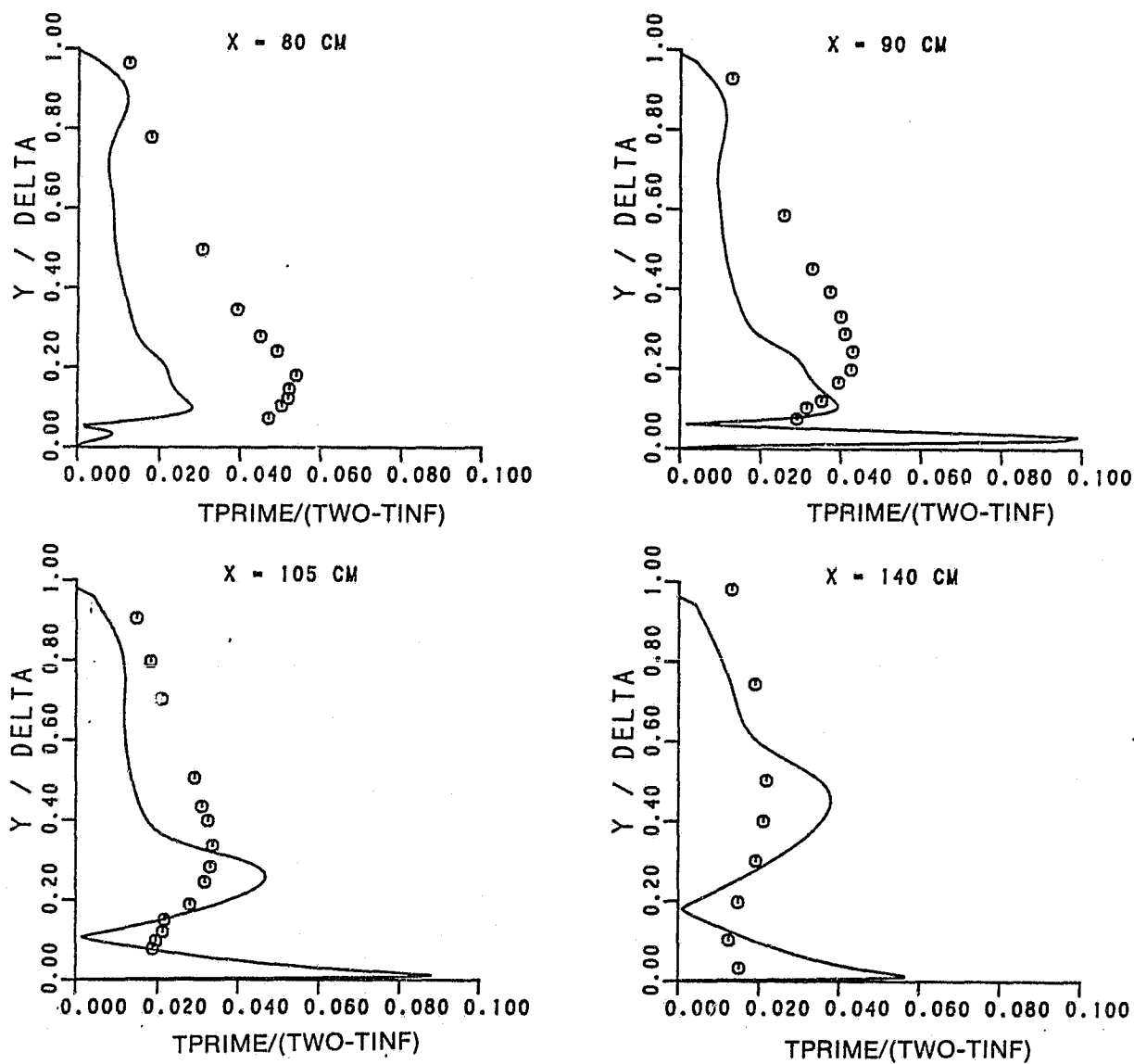


Figure 6.9-3. $k-\epsilon$ Model Prediction, and Measured RMS Temperature Normalized by $(T_{w0} - T_{\infty})$.

ORIGINAL PAGE IS
OF POOR QUALITY

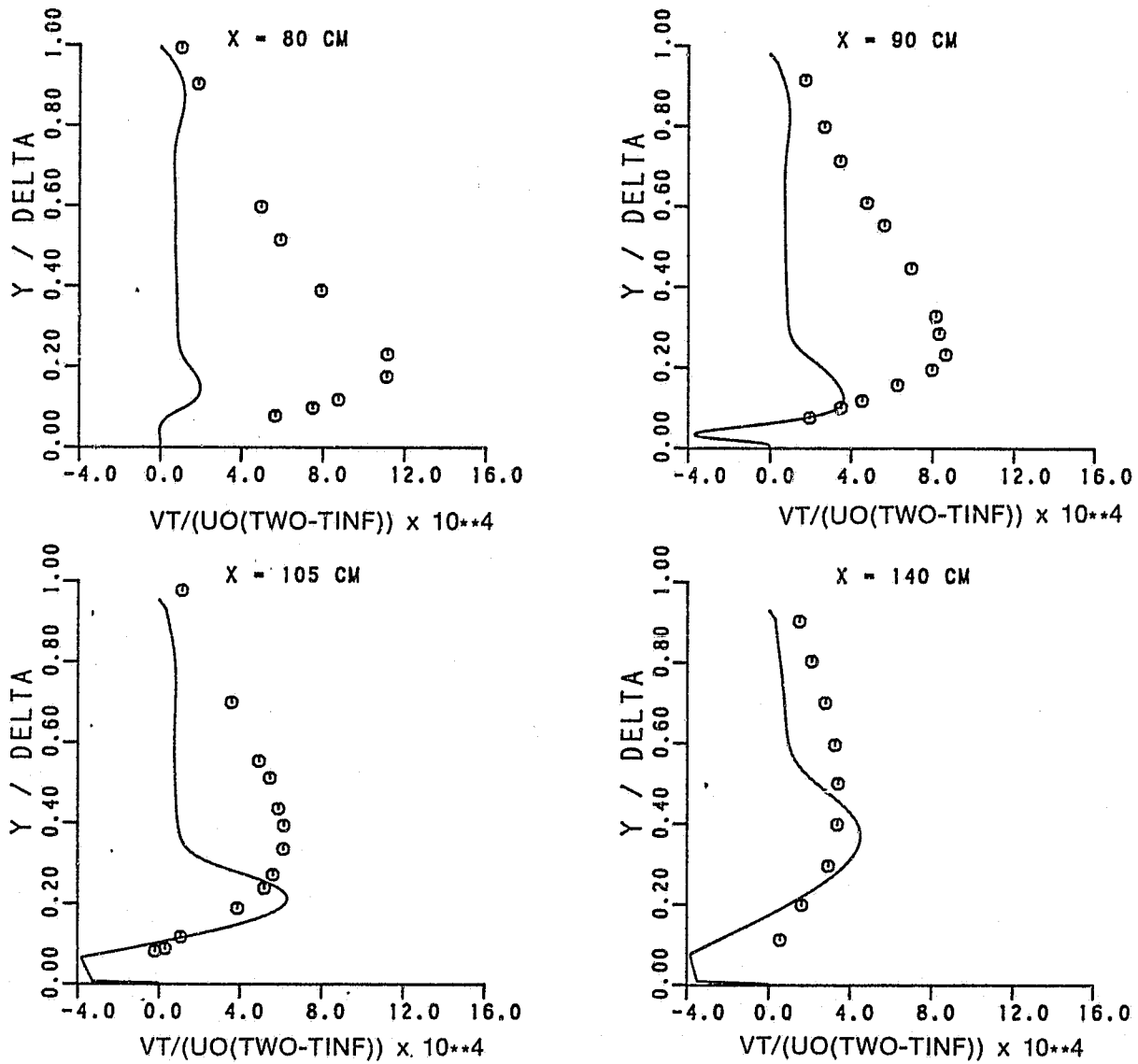


Figure 6.9-4. $k-\epsilon$ Model Predictions and Measured $\overline{vT'}$ Normalized by $U_\infty (T_{w0} - T_\infty)$.

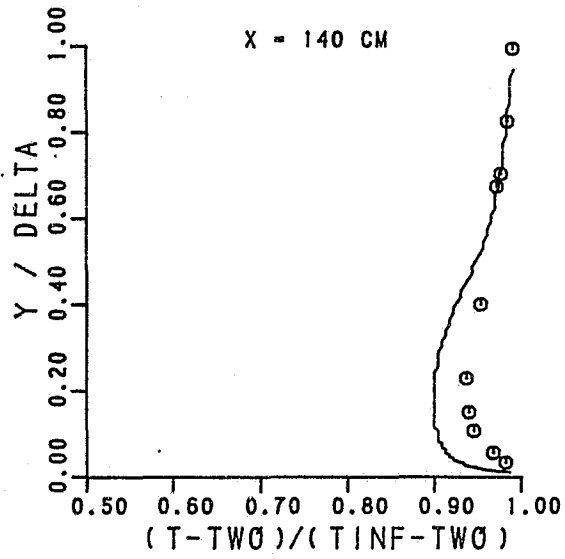
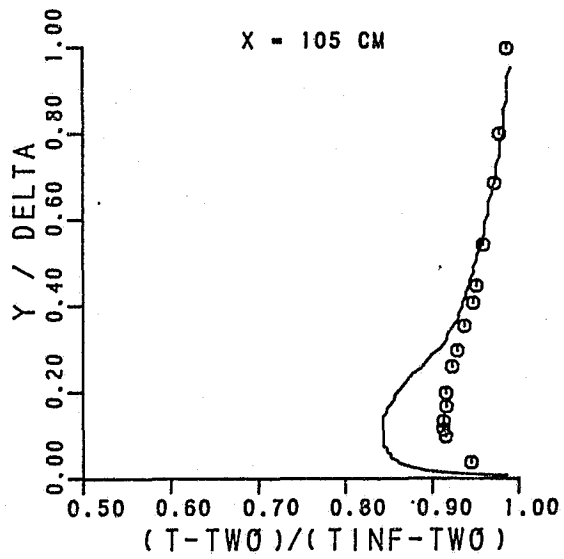
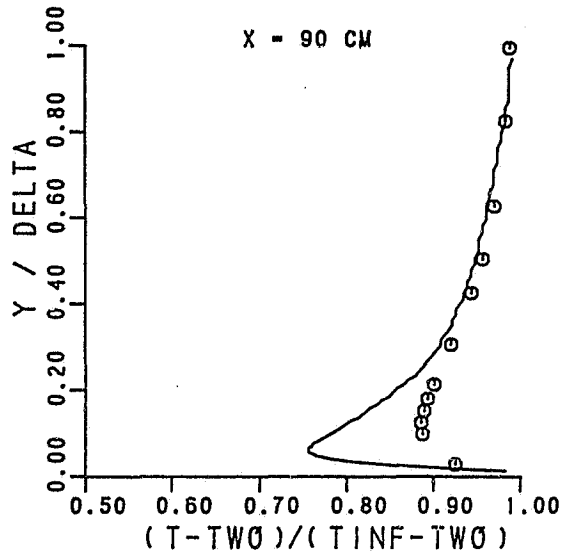
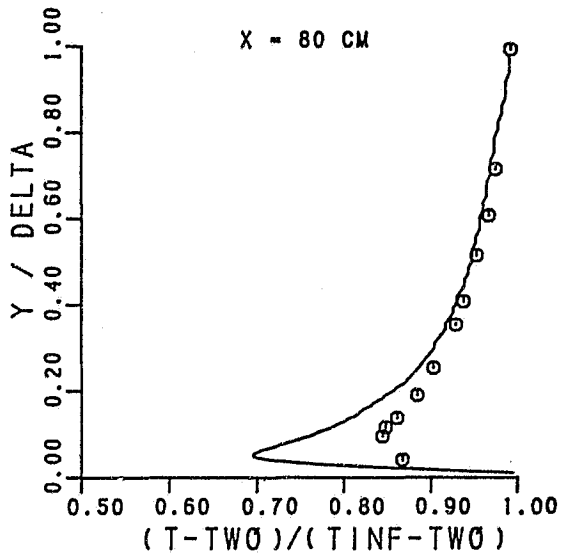


Figure 6.9-5. ASM Predictions of Mean Temperature Profile.

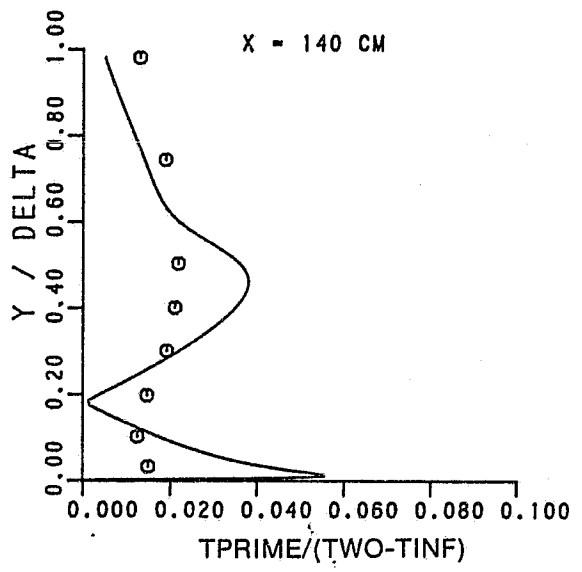
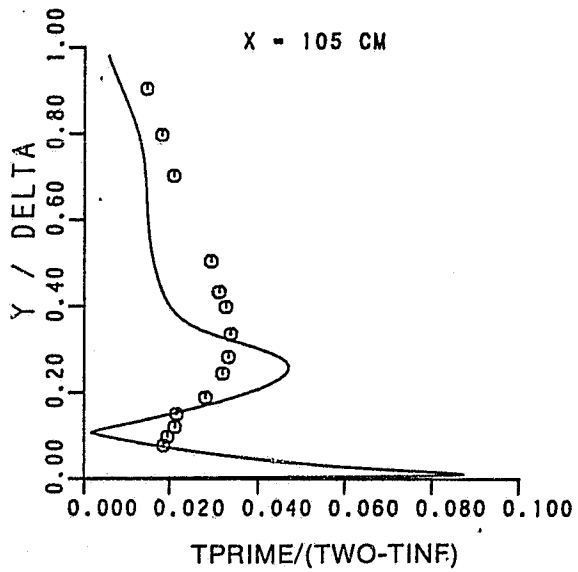
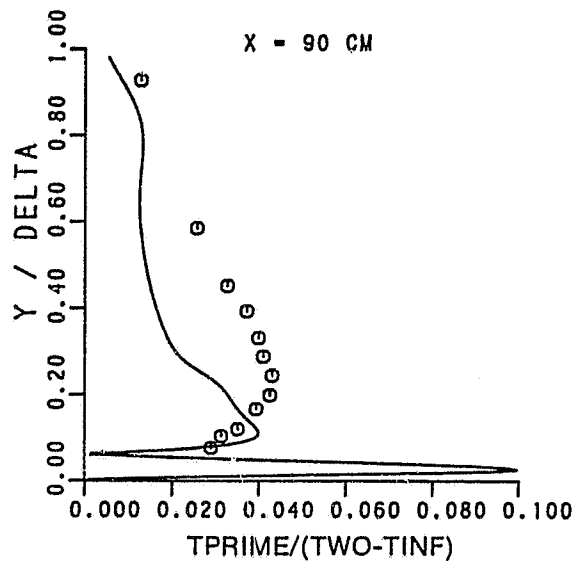
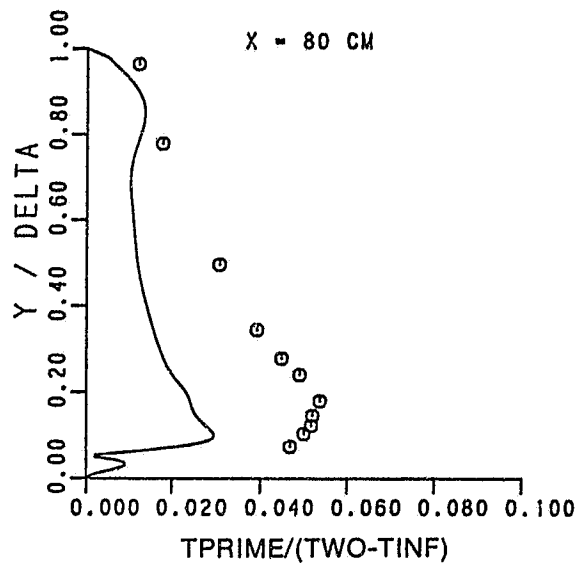


Figure 6.9-6. ASM Predictions of RMS Temperature Profile.

ORIGINAL PAGE IS
OF POOR QUALITY

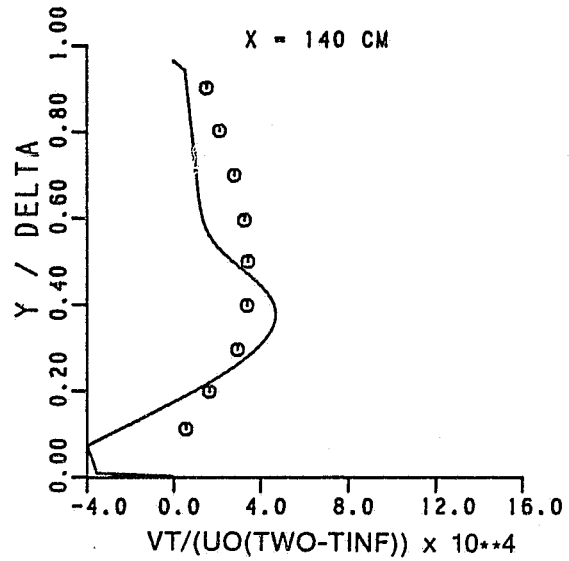
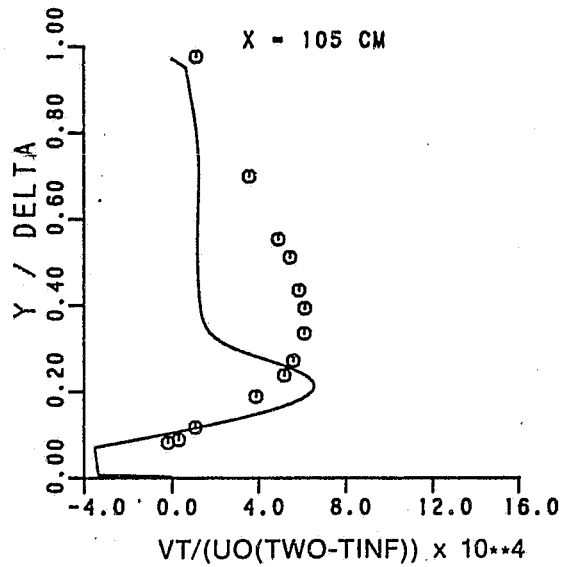
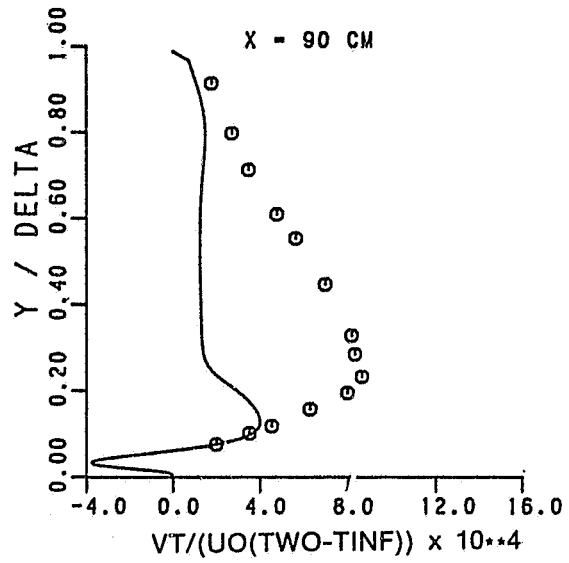
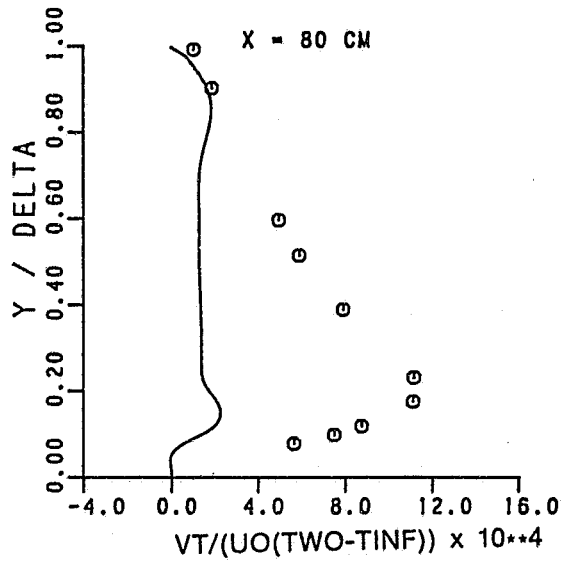


Figure 6.9-7. ASM Predictions of $\overline{vT'}$.

ORIGINAL PAGE IS
OF POOR QUALITY

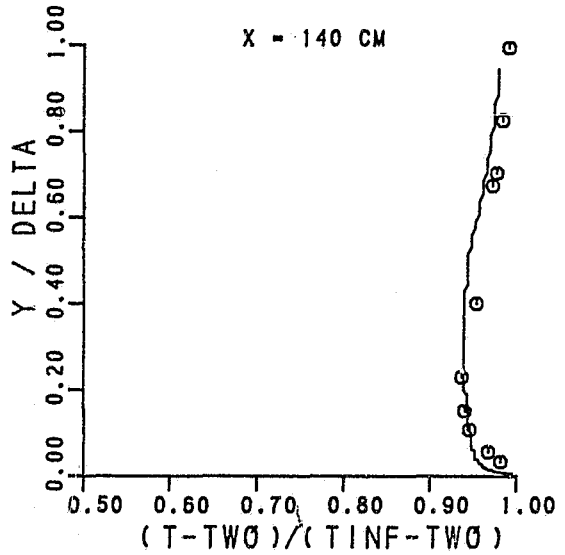
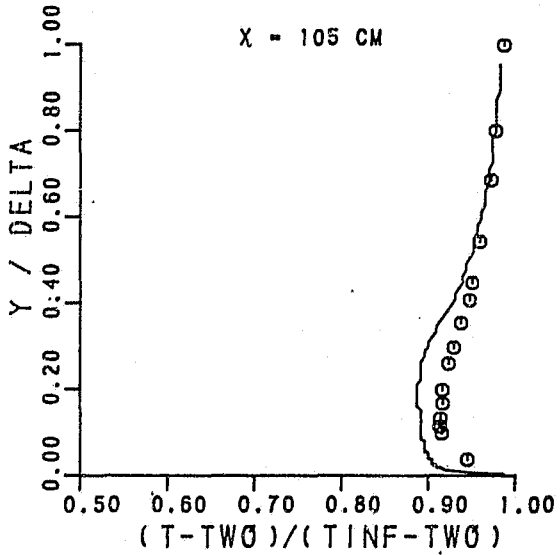
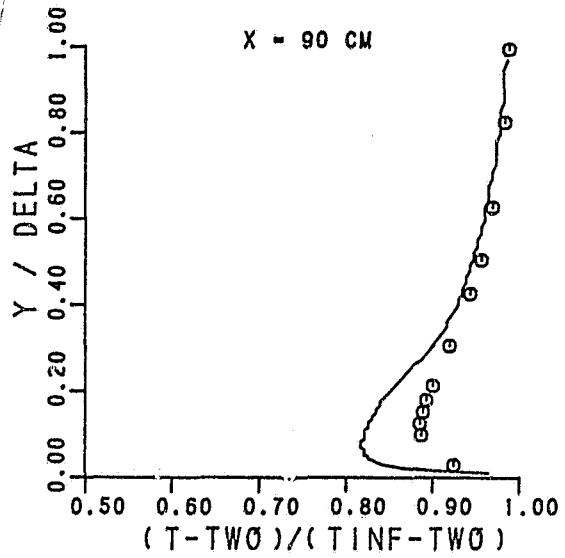
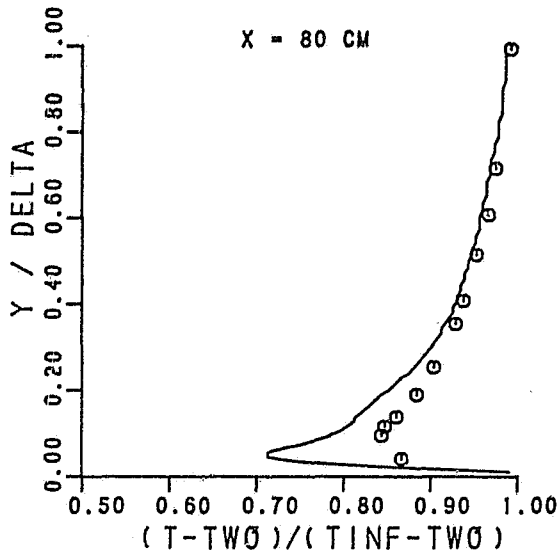


Figure 6.9-8. ASTM Predictions of Mean Temperature Profiles.

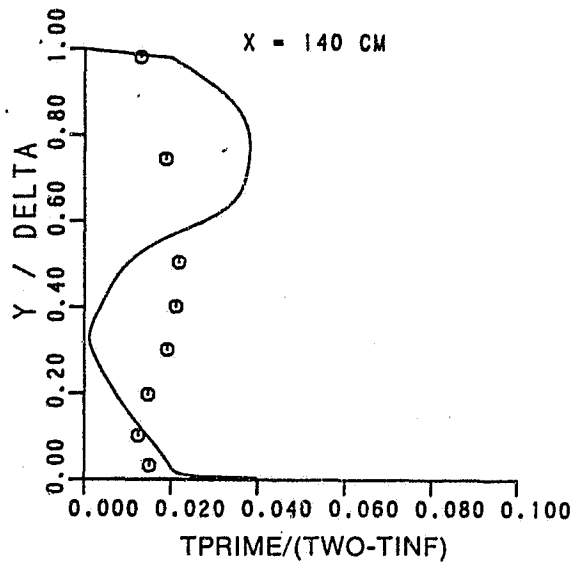
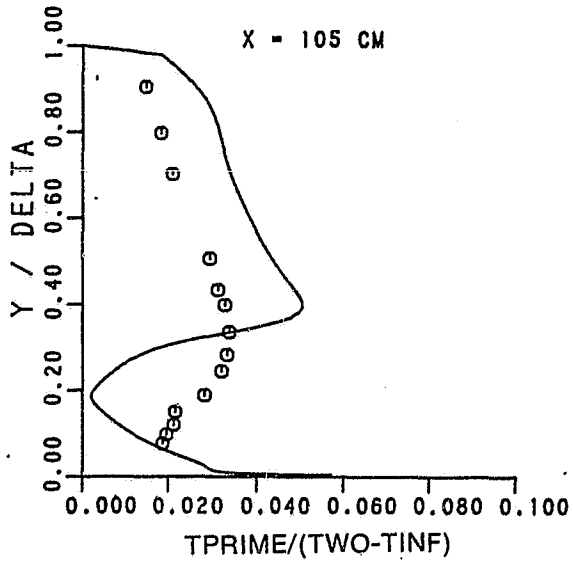
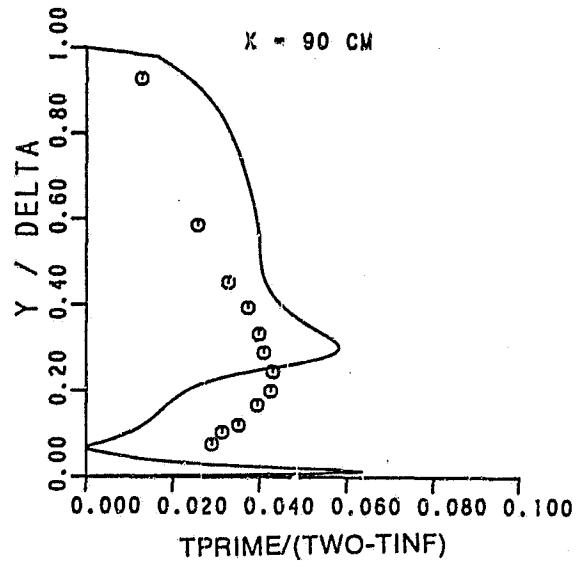
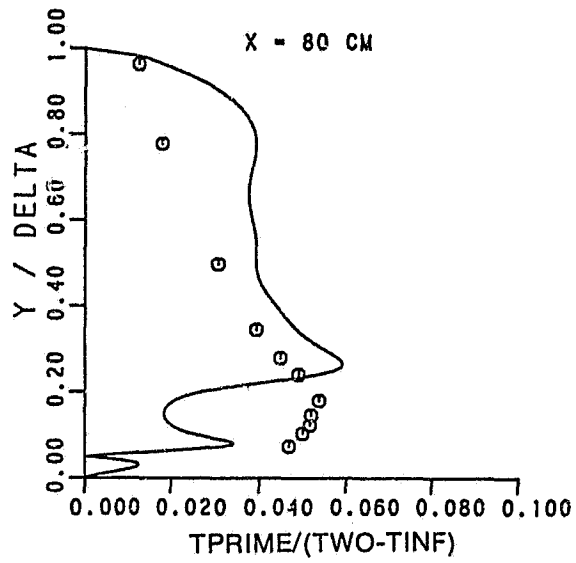


Figure 6.9-9. ASTM Predictions of the RMS Temperature Profile.

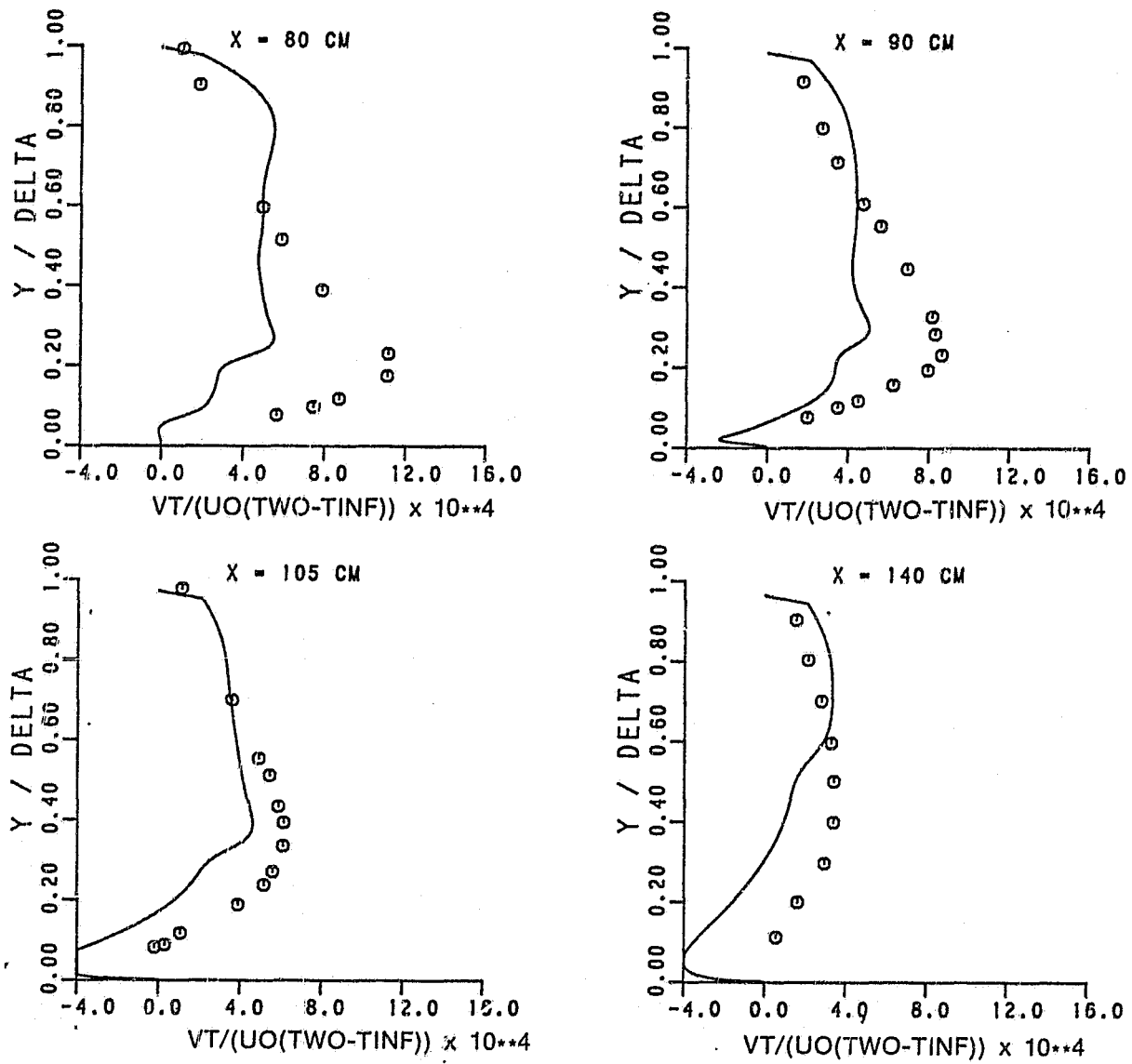


Figure 6.9-10. ASTM Predictions of $(\overline{vT'})$ Profiles.

6.10 Plug Flow Reactor

In reacting flows, the validation of the kinetic scheme is as important as the turbulence/chemistry interaction model. To validate the kinetic scheme, computations were made for the plug flow reactor shown schematically in Figure 6.10-1.

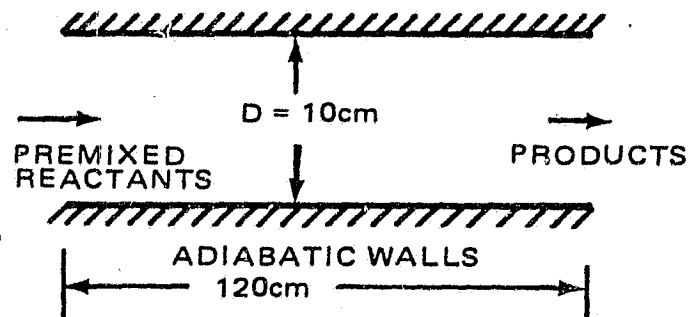
Measurements in a plug flow reactor were conducted by Hautman, et al.,¹⁹ for lean, stoichiometric, and rich propane flames. These measurements were used to test the validity of the four-step scheme that has been proposed by Glassman and his associates based upon detailed species and temperature measurements under a well-controlled low-pressure and high inlet temperature environment. The Glassman four-step scheme has been incorporated into the Garrett Combustion Codes, both parabolic and elliptic.

Computations were performed for lean, stoichiometric, and rich propane flames with both the two-step and the four-step schemes. Comparisons of these results with the measurements are shown in Figure 6.10-2 for the case of lean mixture. From Figure 6.10-1, it is clear that the four-step scheme is far superior to the two-step scheme in predicting the salient features of hydrocarbon combustion in the Princeton reactor.

It should be noted that the four-step scheme as proposed by Glassman and his associates was based upon data from their plug flow reactor. This scheme probably represents a closer approximation to actual hydrocarbon oxidation processes in a high temperature environment than the simpler two-step scheme does. How four-step correlates other reacting flow situations, such as a laminar diffusion flame, premixed turbulent flames, and jet flames, is covered in Paragraphs 6.11, 6.12 and 6.13, respectively.

HAUTMAN ET AL

PLUG FLOW REACTOR



$U = 10.3465\text{ M/S}$
EQUIVALENCE RATIO = 0.12
 $T = 1021^\circ\text{K}$
 $P = 1\text{ ATM}$

Figure 6.10-1. Princeton High Temperature Plug Flow Reactor.

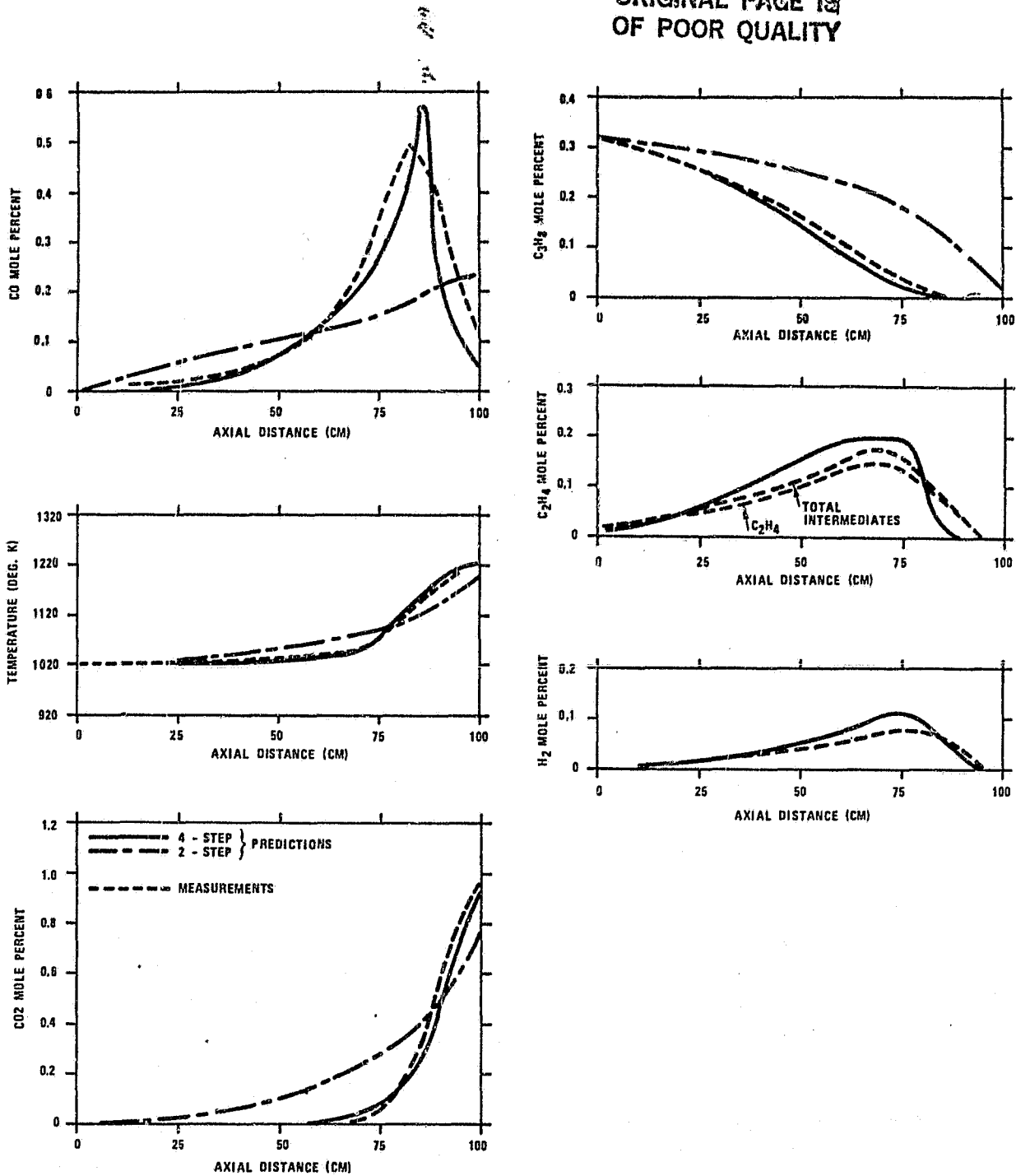


Figure 6.10-2. Comparison of 2-Step and 4-Step Kinetic Scheme With Lean Propane Premixed Flame Data From High Temperature Plug Flow Reactor.

6.11 Laminar Diffusion Flame

Another benchmark test case selected for validating the kinetic schemes is the laminar diffusion flame. Measurements for a laminar diffusion flame have been reported by Mitchell, et al.¹²⁹ for the setup shown in Figure 6.11-1. This flow was computed with the 2-D elliptic CPM. Runs of this type are useful in the validation of reaction mechanisms and establishing rate constant values since uncertainties due to turbulent interactions are absent.

Comparisons between the measured and predicted species concentration, temperature, and velocity at different axial locations are shown in Figures 6.11-2 through 6.11-8, respectively, at three axial stations. The predictions were obtained with both kinetic schemes and include the influence of buoyancy and variable thermodynamic and transport properties. Overall, the agreement between the predictions and measurements is fairly good.

Results with the two-step scheme for the first axial station ($x = 1.2$ cm) are presented in Figures 6.11-2 through 6.11-4. The overall heat release rate as indicated by axial velocity (V) correlation is in good agreement with data. Stable species profiles (e.g. CO_2 , H_2O , O_2 and unburned fuel) are also well correlated. The CO levels are predicted to be significantly lower than measurements by a factor of two to three. This is consistent with the two-step results on the plug flow reactor. Similar observation can be made for the comparison shown in Figures 6.11-5 and 6.11-6 at $x = 2.4$ cm. The temperature is slightly overpredicted (perhaps due to neglect of radiation losses in calculations) at $x = 5$ cm. The new CO prediction correlates well with the data.

The overall agreement between the two-step predictions and data is reasonable. The slight discrepancies are due to the following:

- (a) The presence of H_2 and intermediate hydrocarbons has been ignored in the two-step scheme. This results in over-prediction of H_2O , CH_4 , and temperature. Some of these differences can be overcome with an improved scheme.
- (b) Differential diffusion of species has been ignored. This will be significant for H_2 diffusion due to its low molecular weight.
- (c) Radiation was not considered in these computations.

The four-step results with the rate constants suggested by Hautman et al. are presented in Figures 6.11-9 through 6.11-15. Except for the velocity profile at $x = 1.2$ cm, the scheme indicates good comparison with data as shown in Figure 6.11-9. The general shape of the temperature profile is well predicted as shown in Figure 6.11-10. Near the flame centerline at $x = 1.2$ cm, the model underpredicts temperature levels by approximately 50 percent. The agreement improves further downstream, and by $x = 5$ cm, the comparison is good. The fuel breakdown near the center is underpredicted by a factor of two as shown in Figure 6.11-11 for both $x = 1.2$ and 2.4 cm. Similarly, for the initial portion of the flame, the CO_2 levels near the center are considerably different from data. The same is true of the other stable species; for example, O_2 and H_2O as shown in Figures 6.11-14 and 6.11-15.

The four-step predictions in regard to CO are considerably better than the two-step results shown in Figures 6.11-4 through 6.11-8. As shown in Figure 6.11-13, the CO peaks are similar in magnitude, as the data shows. Some improvement is desirable for the radial profile shape. Overall, the four-step correlates well with the data. Deficiencies are in regard to correlation in the initial portion of the flame centerline where the model underpredicts fuel breakdown and the levels of temperature, CO_2 , CO, O_2 and H_2O .

ORIGINAL PAGE IS
OF POOR QUALITY

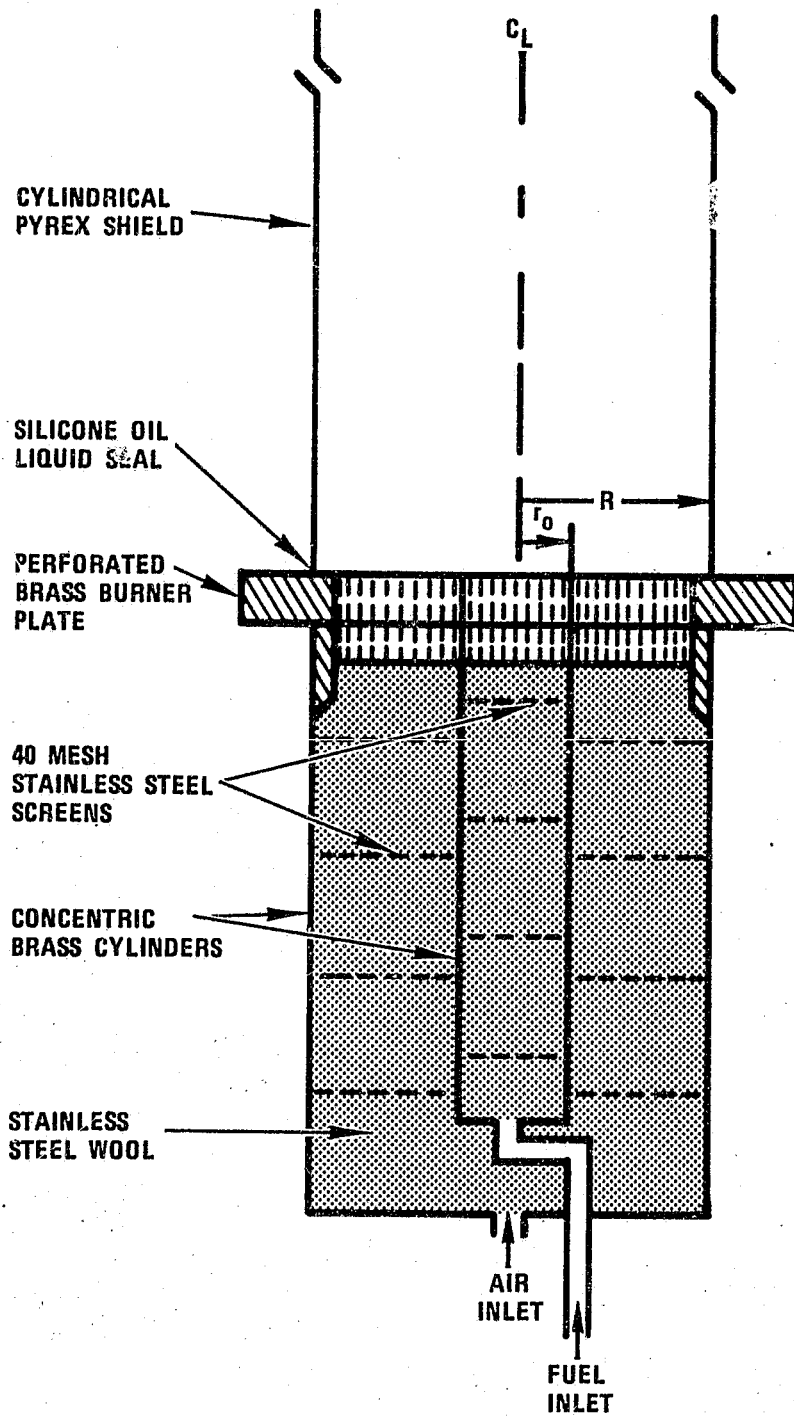


Figure 6.11-1. Schematic of Laminar Diffusion Flame Setup Used By Mitchell.

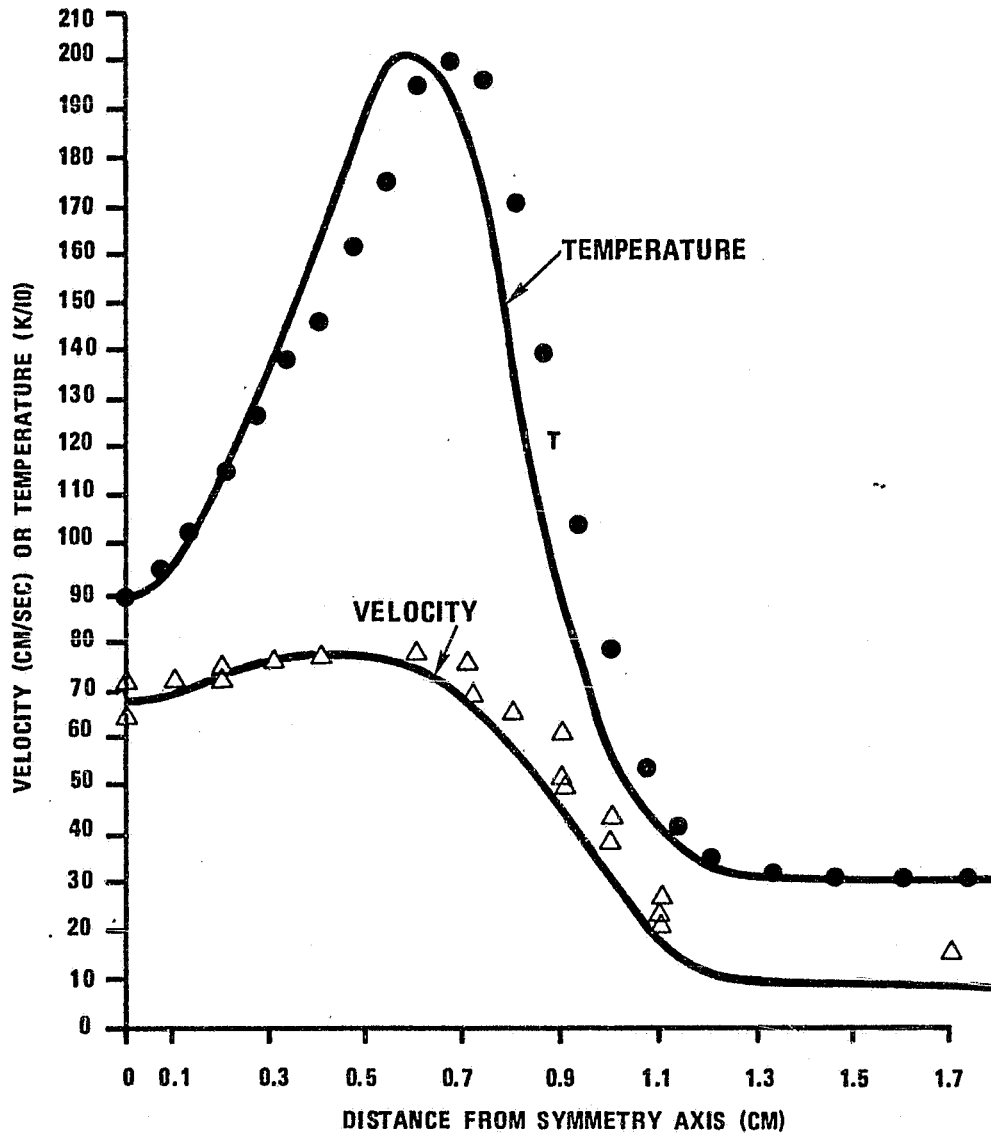


Figure 6.11.2. Comparison Between Two-Step Model Predictions and Measurements for Axial Velocity and Temperature Profiles of the Mitchell's Laminar Diffusion Flame at 1.2 cm Above the Burner Plate.

ORIGINAL PAGE IS
OF POOR QUALITY

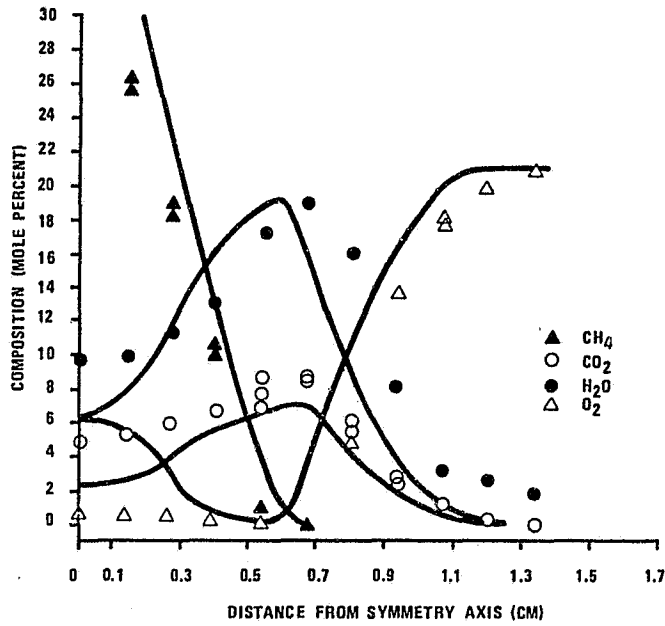


Figure 6.11-3. Two-Step Predictions and Measurements for CH₄, CO₂, H₂O and O₂ Profiles, X = 1.2 cm.

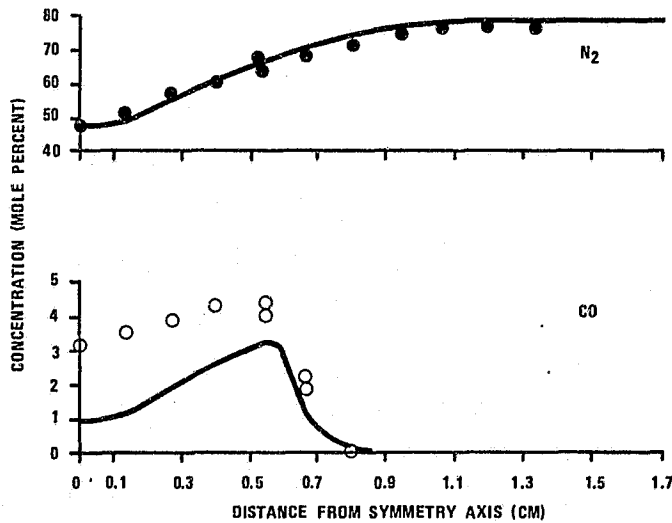


Figure 6.11-4. Two-Step Predictions and Measurements for N₂ and CO Profiles, X = 1.2 cm.

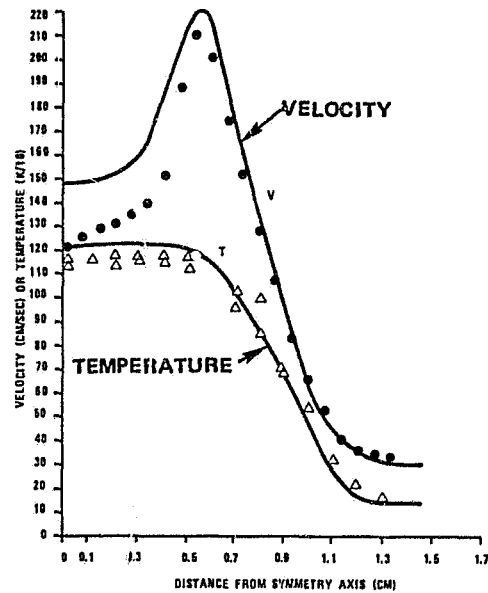


Figure 6.11-5. Comparison Between Two-Step Predictions and Measurements of Velocity and Temperature Profiles of the Mitchell's Laminar Diffusion Flame at $X = 2.4$ cm.

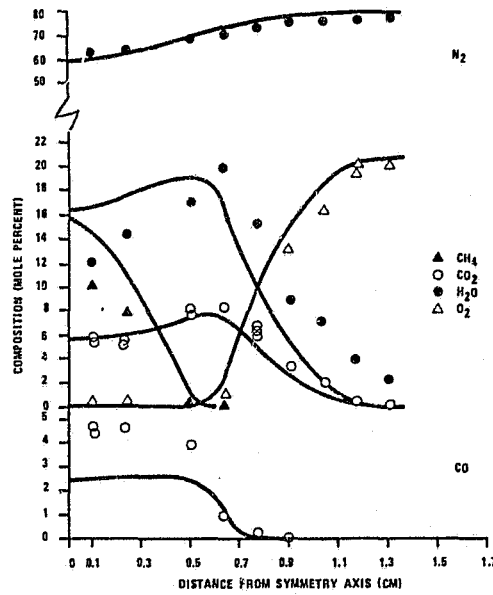


Figure 6.11-6. Predicted and Measured Species Profiles at $X = 2.4$ cm. (Two-Step)

ORIGINAL PAGE IS
OF POOR QUALITY

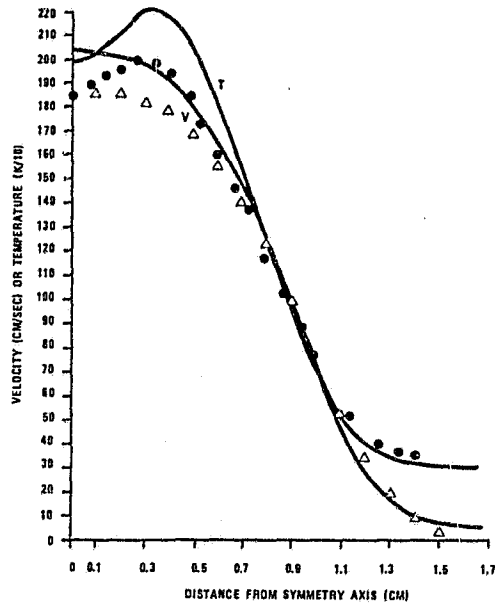


Figure 6.11-7. Comparison Between Predicted and Measured Axial Velocity and Temperature Profiles and Mitchell's Laminar Diffusion Flame at $X = 5.0$ cm. (Two-Step)

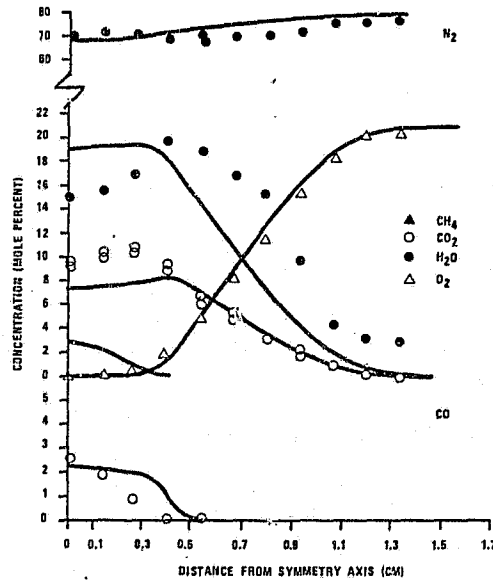


Figure 6.11-8. Predicted and Measured Species Profiles at $X = 5.0$ cm. (Two-Step)

ORIGINAL PAGE IS
OF POOR QUALITY

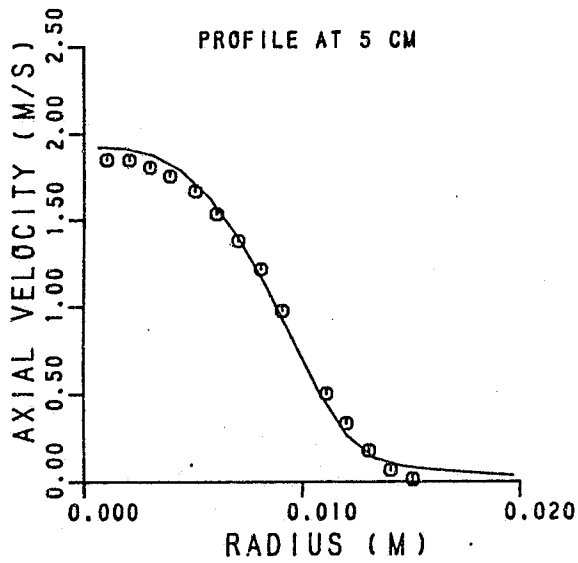
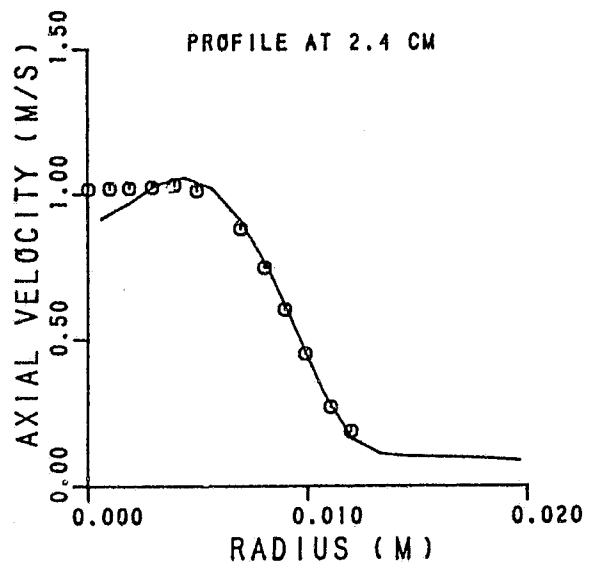
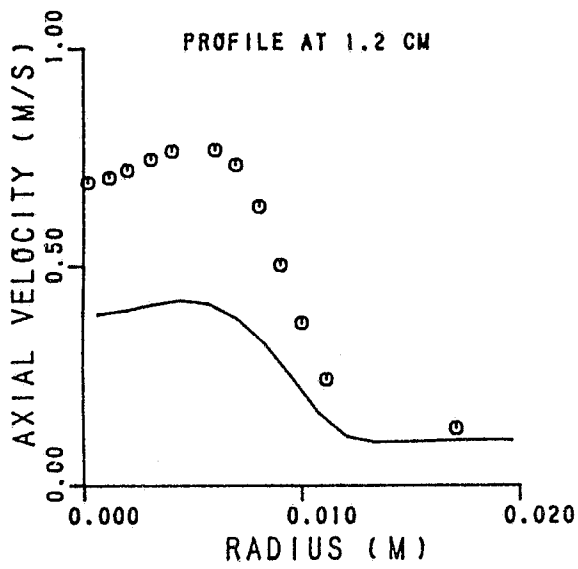


Figure 6.11-9. 4-Step Scheme, Axial Velocity Profiles.

ORIGINAL PAGE IS
OF POOR QUALITY

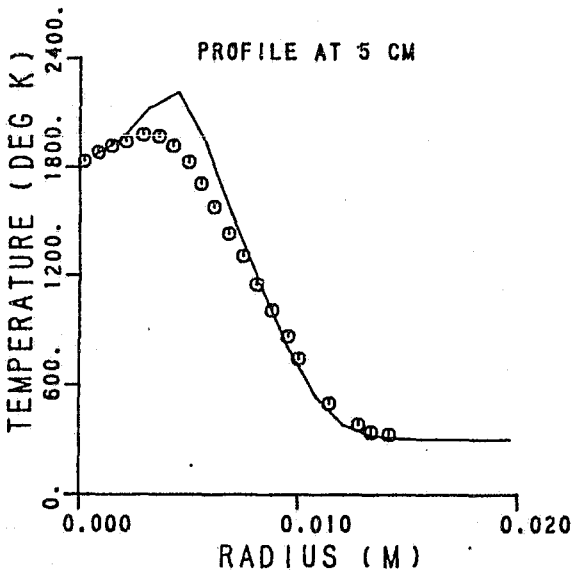
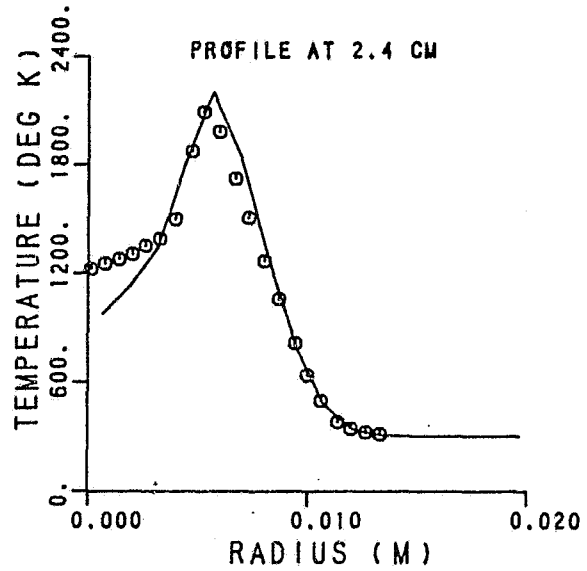
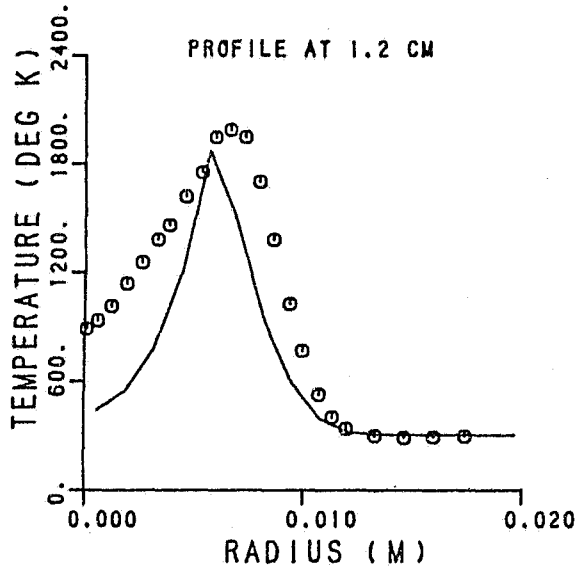


Figure 6.11-10. 4-Step Scheme, Temperature Profiles

ORIGINAL PAGE IS
OF POOR QUALITY

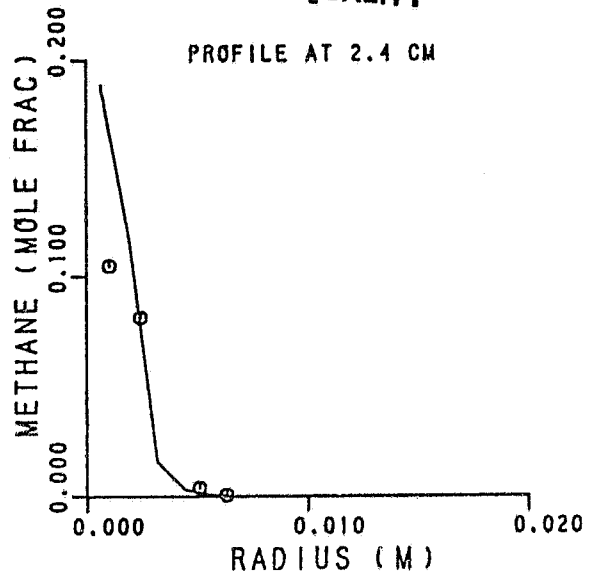
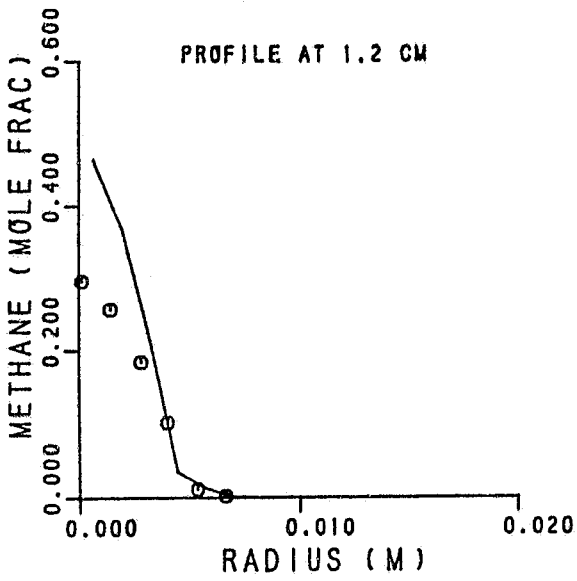


Figure 6.11-11. 4-Step Scheme, Methane Profiles.

ORIGINAL PAGE IS
OF POOR QUALITY

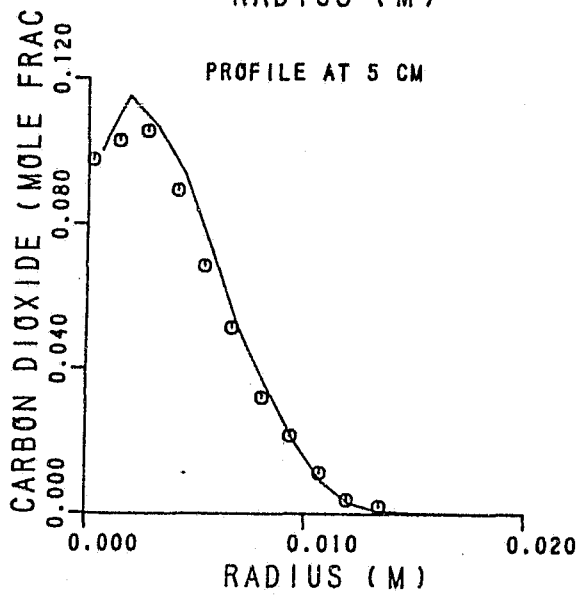
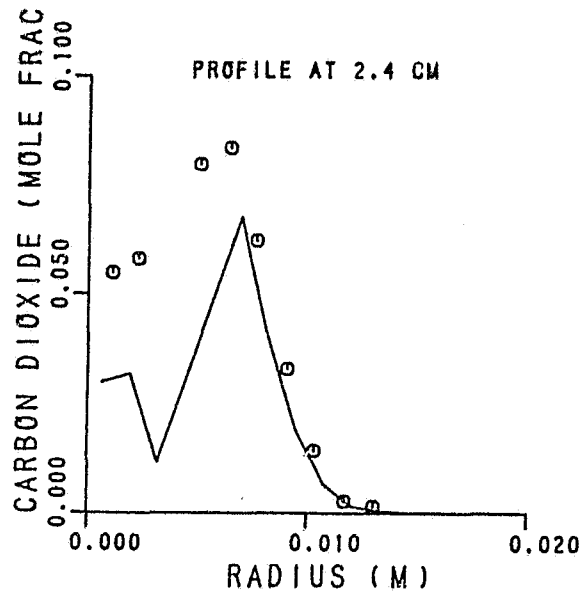
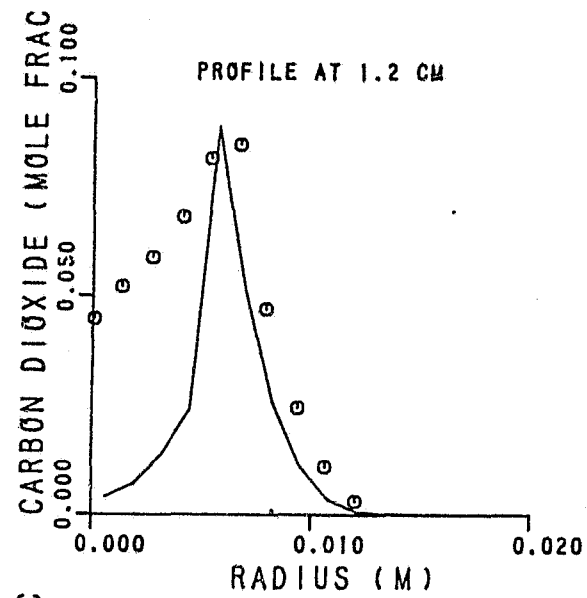


Figure 6.11-12. 4-Step Scheme, CO₂ Profiles.

ORIGINAL PAGE IS
OF POOR QUALITY

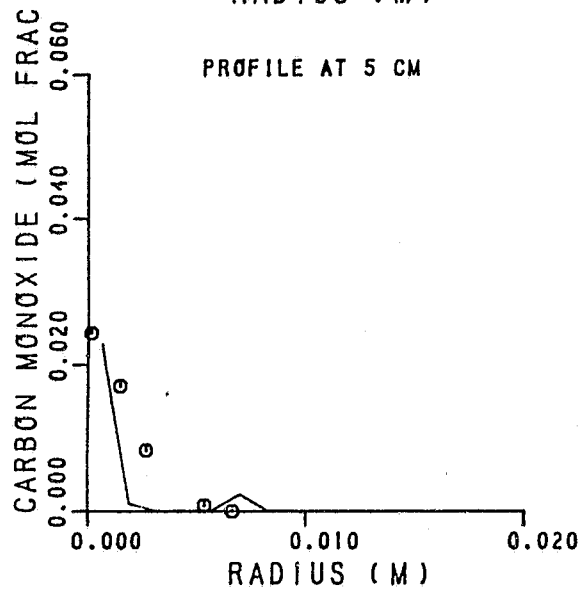
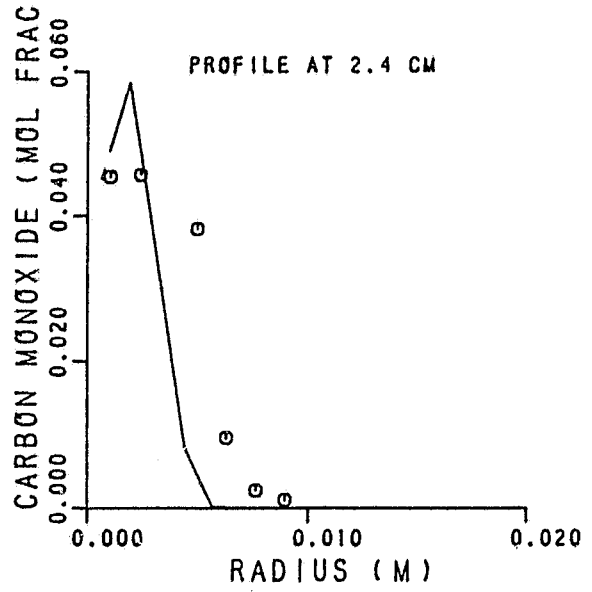
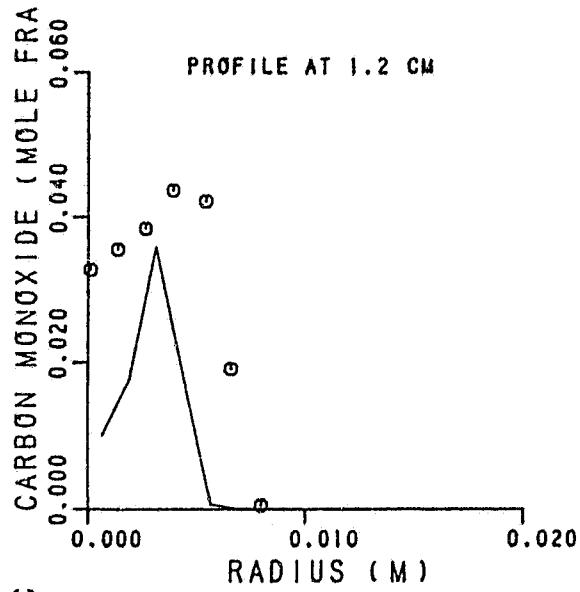


Figure 6.11-13. 4-Step Scheme, CO Profiles.

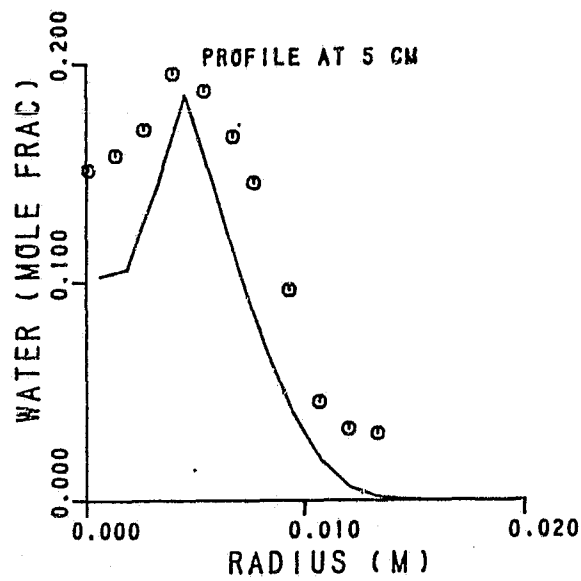
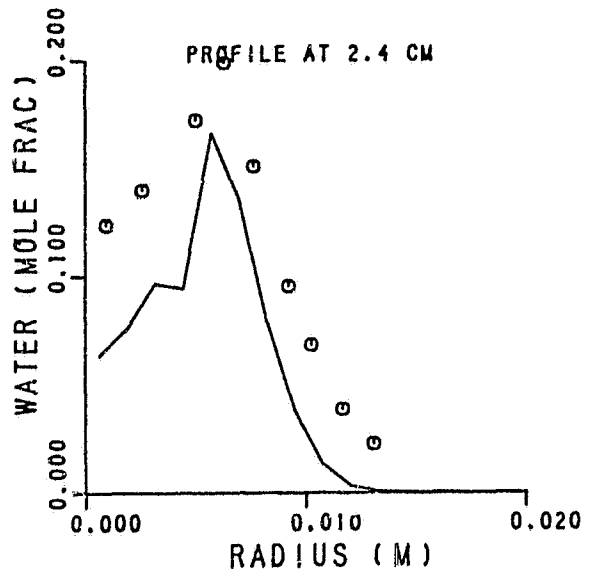
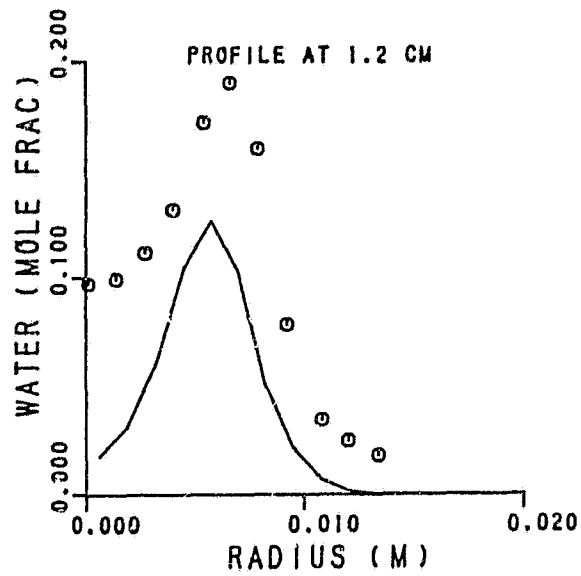


Figure 6.11-15. 4-Step Scheme, H₂O Profiles

6.12 Turbulent Premixed Flame in a Rectangular Duct

Another test case selected from the data base for evaluating kinetic schemes is the reacting flow of premixed propane/air in a rectangular duct with a flame stabilizer as shown in Figure 6.12-1. Measurements for this flow were made by Shipman,^{137, 138} et al.

Computations for this case were performed using the 2-D parabolic program and standard k-ε model, with the initial profiles obtained from measurements 0.0508 m downstream of the flame holder. The average inlet velocity was 18.288 m/s at a pressure of one atmosphere, having a turbulence intensity of 3 percent. Along the plane of symmetry, a zero radial gradient was specified for all the variables except V, which was set to zero. Along the outer radial boundary, wall function treatment was employed. Computations were performed with two-step and four-step kinetic schemes. On the two-step scheme, two different sets of rate constants were used. One of them corresponds with the constants established in the Army Combustor Design Criteria Program, and the other set is for the PM/PV combustion.¹² Table 14 provides the values of the Arrhenius pre-exponents and the activation temperatures for the reaction steps.

TABLE 14. TWO-STEP RATE CONSTANTS FOR GARRETT/AVLABS AND PREMIXED/PREVAPORIZING REACTION.

	REACTION STEP 1		REACTION STEP 2	
	Pre-Exponent	Activation Temperature	Pre-Exponent	Activation Temperature
Design Criteria	3.3×10^{14}	27,000	6.0×10^8	12,500
PM/PV	3.9×10^9	18,000	2.2×10^8	12,500

The predictions obtained using the Design Criteria constants are shown in Figures 6.12-2 through 6.12-8, and those using the PM/PV constants are presented in Figures 6.12-9 through 6.12-15.

The predicted mean axial velocity using the Design Criteria constant and the measurements are shown in Figure 6.12-2 at five

axial stations downstream of the flame holder. The predicted axial velocity profiles show slower mixing rates compared to the measurements. The velocities near the plane of symmetry are considerably smaller in the predictions than in the data.

Figure 6.12-3 illustrates the computed profiles of unburned fuel and data at five axial stations. The predicted unburned fuel mass fractions are higher than the measured values indicating slower fuel disappearance rate. Figure 6.12-4 illustrates the comparison between predicted and measured CO mass fraction. The predicted CO profiles are significantly lower than the data up to $x = 0.2032$, partly due to the slow reaction rates. Beyond this station, the CO mass fractions are in reasonable agreement with data. However, the radial spread of CO profiles are underpredicted by the model.

Since the reaction rates are underpredicted by the design criteria rate constants, the predicted temperatures (Figure 6.12-5) are also lower than the measurements. The radial spreading of temperature profile is also underpredicted by the model.

The other derived variables such as O_2 , CO_2 and H_2O are presented in Figures 6.12-6 through 6.12-8, respectively. Due to the lower fuel consumption rate, predicted O_2 profiles are higher than measurements. Similarly, the discrepancy between predictions and measured CO_2 can be explained. Apparent improvement in regard to H_2O profiles may be due to faster diffusion rates of this species compared to model assumptions of equal diffusivity for all species.

In conclusion, the Army Combustor Design Criteria rate constants appear to underpredict fuel consumption rate and temperature profiles. On occasions the design criteria constants have seemed to overpredict reaction rates. More extensive validation is needed to establish the two-step rate constants for both diffusion and premixed flames.

The predicted results for mean velocity, obtained by using the PM/PV rate constants, are presented in Figure 6.12-9. A substantial improvement can be observed in the agreement between data and predictions, when compared to the results using Design Criteria rate constants (Figure 6.12-2). This is due to faster fuel consumption. Figure 6.12-10 illustrates the comparison of data and predictions for unburned fuel. These profiles are in much better agreement than the results obtained from the first set of rate constants. However, the radial diffusion rates are still underpredicted by the model.

The comparison between predicted and measured CO_2 profiles are presented in Figure 6.12-11. Due to the improved convection rates, the reaction rates are expected to be higher, and hence the CO_2 values are higher than the values obtained from the design criteria rate constants. The CO_2 values predicted from the PM/PV rate constants are still smaller than the measured values.

The predicted and increased profiles for CO are illustrated in Figure 6.12-12. The predicted peak CO values are higher than the data and the predicted CO mass fraction profiles do not spread radially outwards as much as seen in the measurements.

The predicted temperature distributions using the PM/PV rate constants and the measurements are presented in Figure 6.12-13. Since the reaction rates are faster, it is expected that the predicted temperatures are also higher than those obtained using the design criteria rate constants. Overall these profiles are in good agreement with data.

Figures 6.12-14 and 6.12-15 show comparisons between measured and predicted profiles of O_2 and H_2O , respectively. Although there is improvement over the design criteria constants in regard to O_2

and CO_2 , the comparison is worse for H_2O . This may be due to a number of reasons, such as:

- o Incorrect approximation of fuel breakdown by simple two-step
- o Neglect of H_2 as one of the intermediate products
- o Assumption of equal diffusivities of all gaseous molecules
- o Turbulence/chemistry interaction represented by a simple eddy breakup model

Calculations were also performed using the four-step kinetic scheme outlined in Section 3.0. The rate constants used in this computation were obtained from the report of Hautman,¹⁹ et al. These rate constants have given good comparison with plug flow reaction as shown in Figure 6.10-1. The Arrhenius pre-exponents and the activation temperatures for each of the four steps are given in Table 15.

TABLE 15. RATE CONSTANTS FOR 4-STEP KINETIC SCHEME.

REACTION STEP	ARRHENIUS PRE-EXPONENT (K_0)	ACTIVATION TEMPERATURE	EDDY BREAKUP CONSTANT (C_R)
1	2.0893×10^{22}	24,800	3.0
2	5.0117×10^{19}	25,000	3.0
3	3.9811×10^{19}	20,000	3.0
4	3.3113×10^{18}	20,500	3.0

The predicted mean axial velocity profiles using the four-step kinetic scheme and the data are presented in Figure 6.12-16. The predicted velocities are significantly smaller than the measurements. Predicted unburned fuel profiles are shown in Figure 6.12-17 along with the data. Comparison with the two-step results (Figure 6.12-14) shows that there are no appreciable differences in the unburned fuel profiles between four-step and two-step.

The four-step predictions for CO are presented in Figure 6.12-18. Due to the slow reaction rates in the four-step scheme, the predicted CO values are smaller compared to both the data and the two-step scheme (Figures 6.12-4 and 6.12-12). Consequently, as shown in Figure 6.12-19 the four-step predicted temperature profiles are lower than the two-step (Figures 6.12-5 and 6.12-13) and the data. The other derived variables are similar including O₂, CO₂ and H₂O shown in Figures 6.12-20 through 6.12-22.

A number of reasons can be forwarded for delivering poor correlation with the four-step scheme. Numerical experimentation was made to demonstrate that the basic mechanism is valid and that future modifications to the approach will yield good comparison. Figures 6.12-23 through 6.12-29 present results with the first two reaction-step rate constants changed

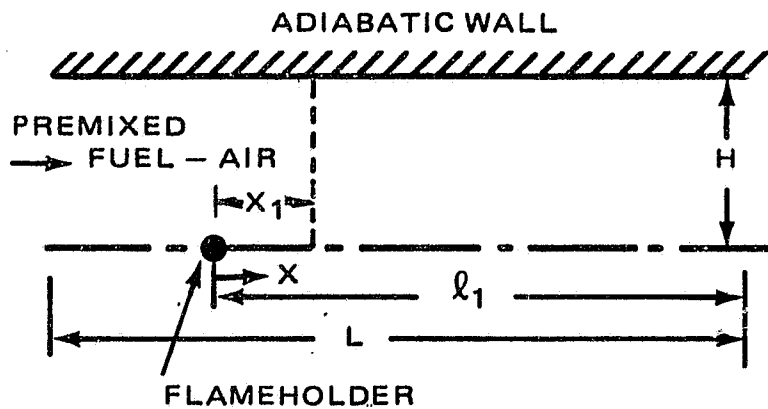
$$K_{O_1} = 2.0893 \times 10^{24} \quad C_{R_1} = 6.0$$

$$K_{O_2} = 5.0117 \times 10^{21} \quad C_{R_2} = 6.0$$

Significant improvement in predictions can be seen, and one can therefore conclude that the basic four-step hydrocarbon oxidation mechanism is valid.

SHIPMAN AND CO-WORKERS

CONFINED STOICHIOMETRIC FLAME STABILIZED ON A
CYLINDRICAL FLAMEHOLDER IN A RECTANGULAR DUCT



DUCT WIDTH = 0.0254 M
 $H = 0.0381$ M
 $X_1 = 0.0508$ M
 $l_1 = 0.3080$ M
 $L = 0.4286$ M

X_1 DENOTES FIRST MEASUREMENT LOCATION FROM WHICH
CALCULATIONS ARE STARTED.

AVERAGE $U = 18.288$ M/S
 $P = 1$ ATM

Figure 6.12-1. Geometry of Turbulent Premixed Flame
in a Rectangular Duct.

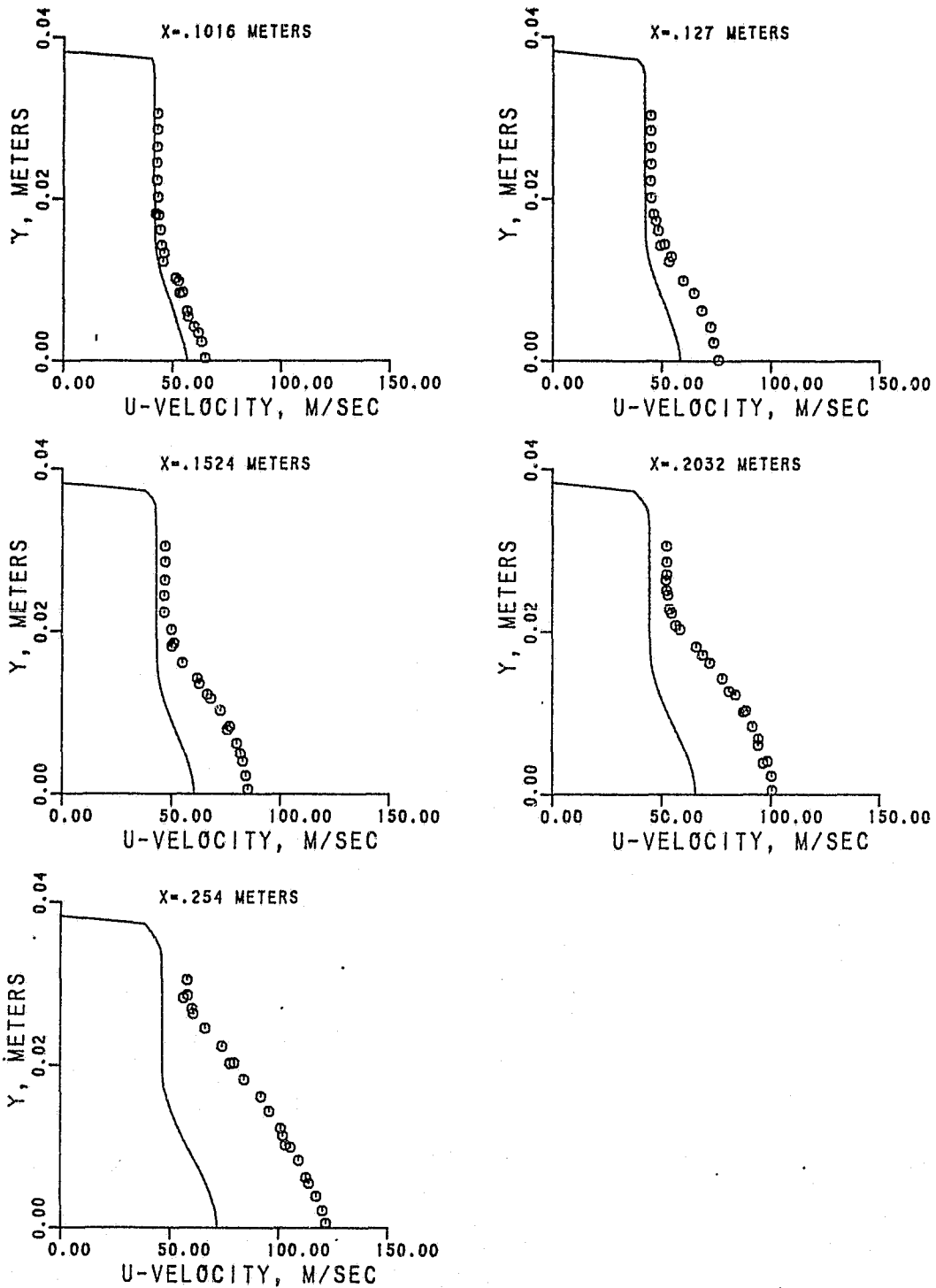


Figure 6.12-2. Predicted Velocity Profiles With Design Criteria Rate Constants.

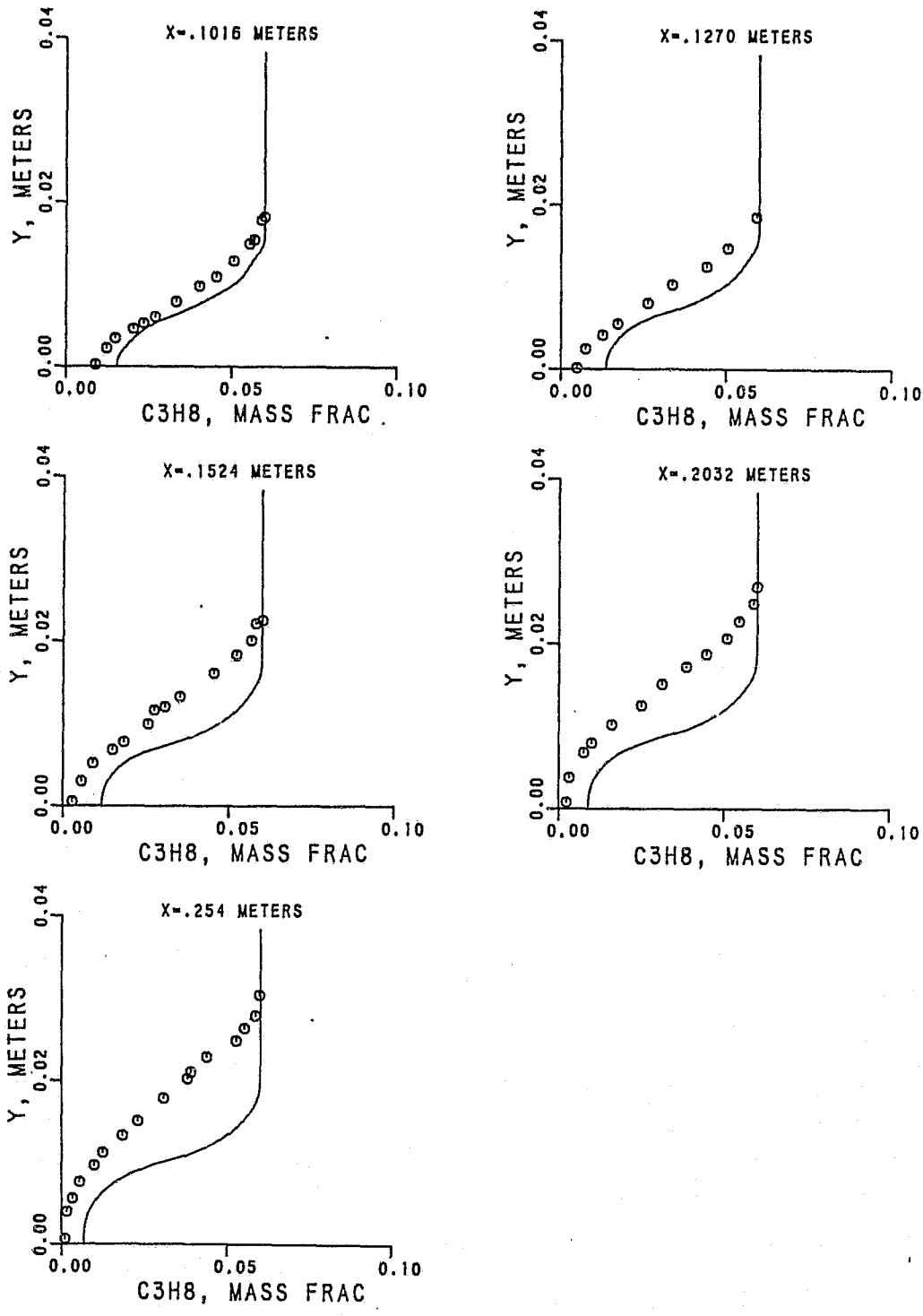


Figure 6.12-3. Predicted Unburned Fuel Profiles With Design Criteria Rate Constants.

ORIGINAL PAGE IS
OF POOR QUALITY

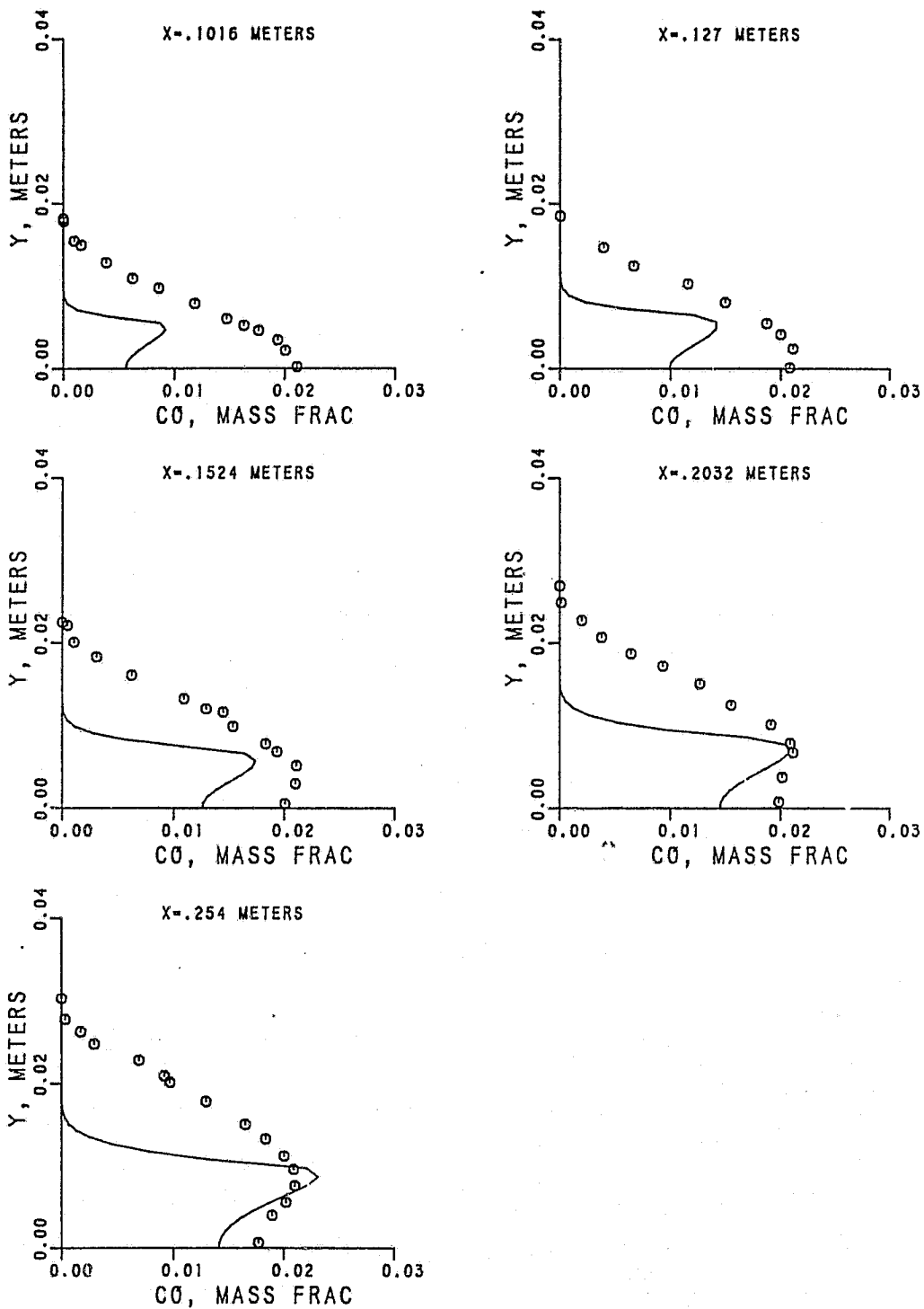


Figure 6.12-4. Predicted CO Profiles With Design Criteria Rate Constants.

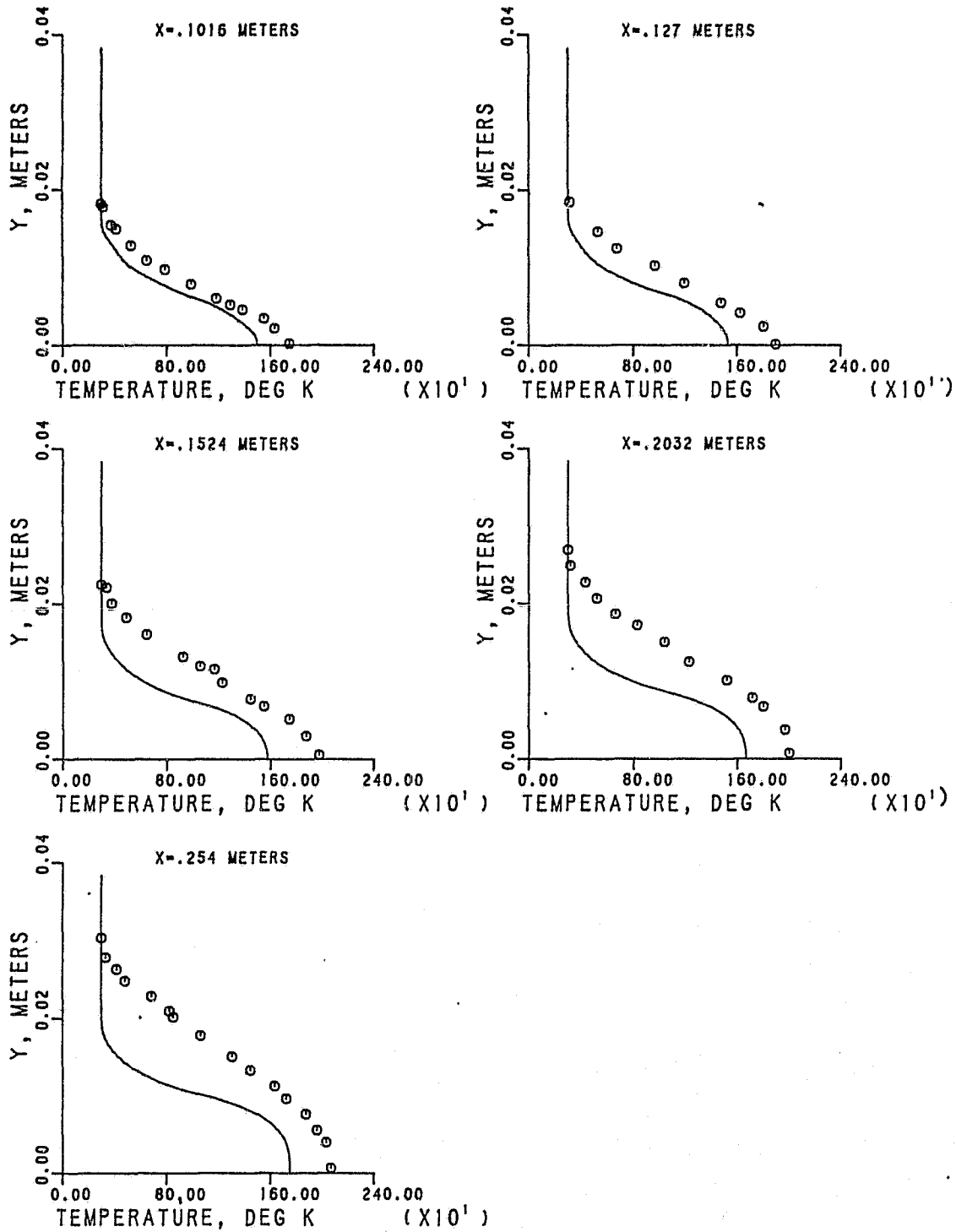


Figure 6.12-5. Predicted Temperature Profiles With Design Criteria Rate Constants.

ORIGINAL PAGE IS
OF POOR QUALITY

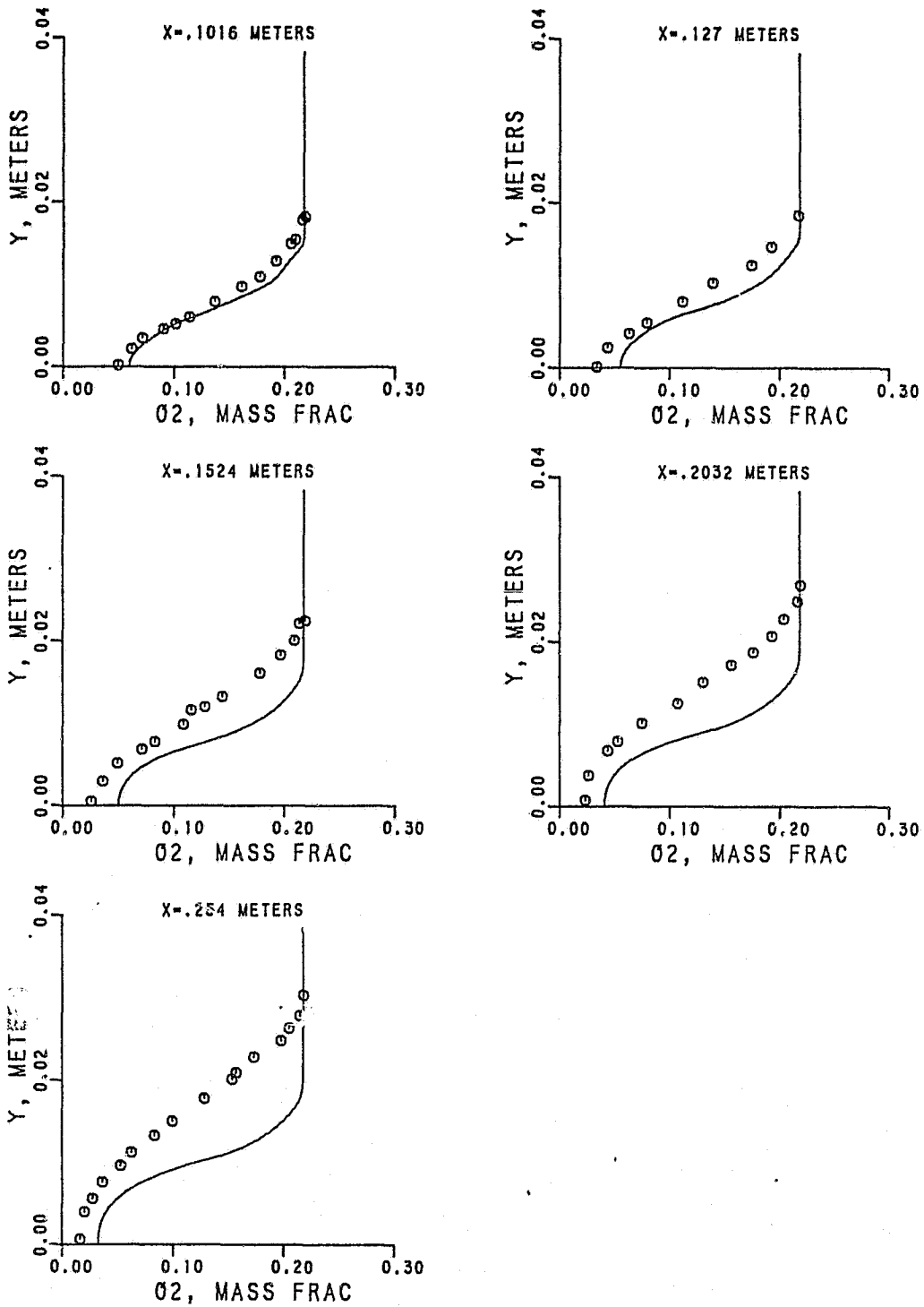


Figure 6.12-6. Predicted O₂ Mass Fraction With Design Criteria Rate Constants.

ORIGINAL PAGE IS
OF POOR QUALITY

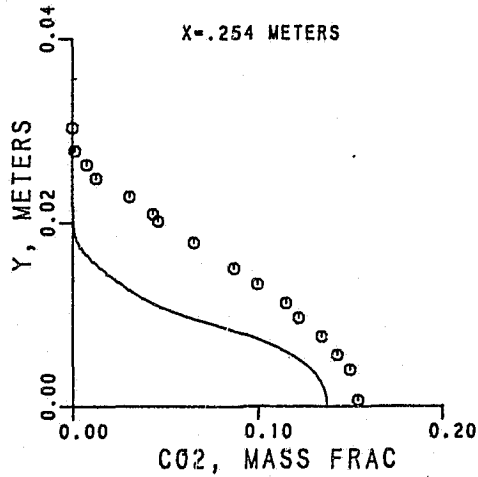
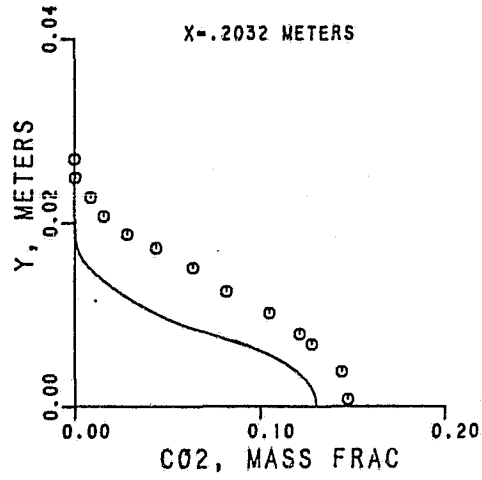
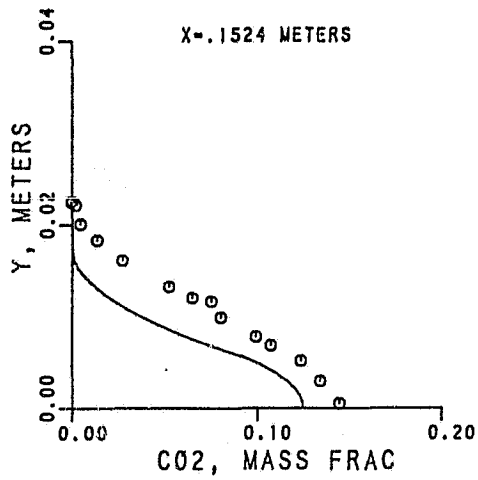
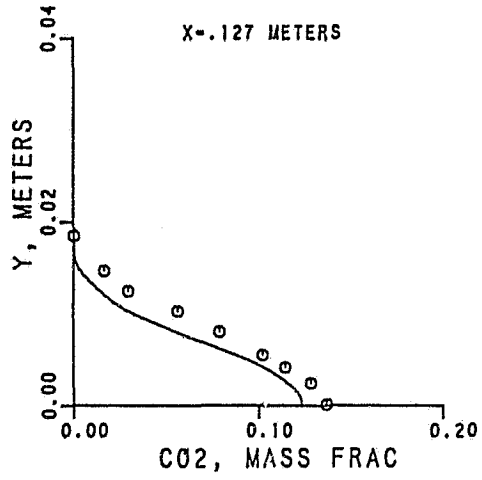
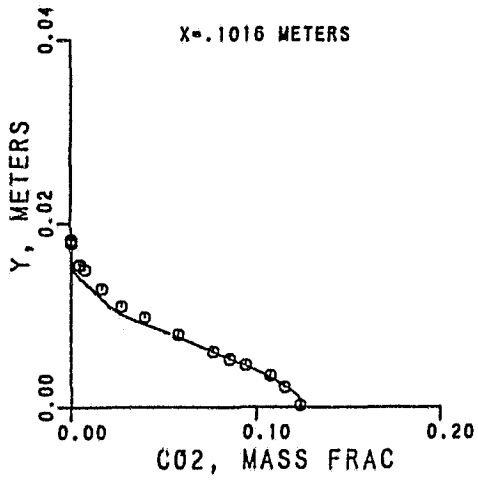


Figure 6.12-7. Predicted CO₂ Profiles With Design Criteria Rate Constants.

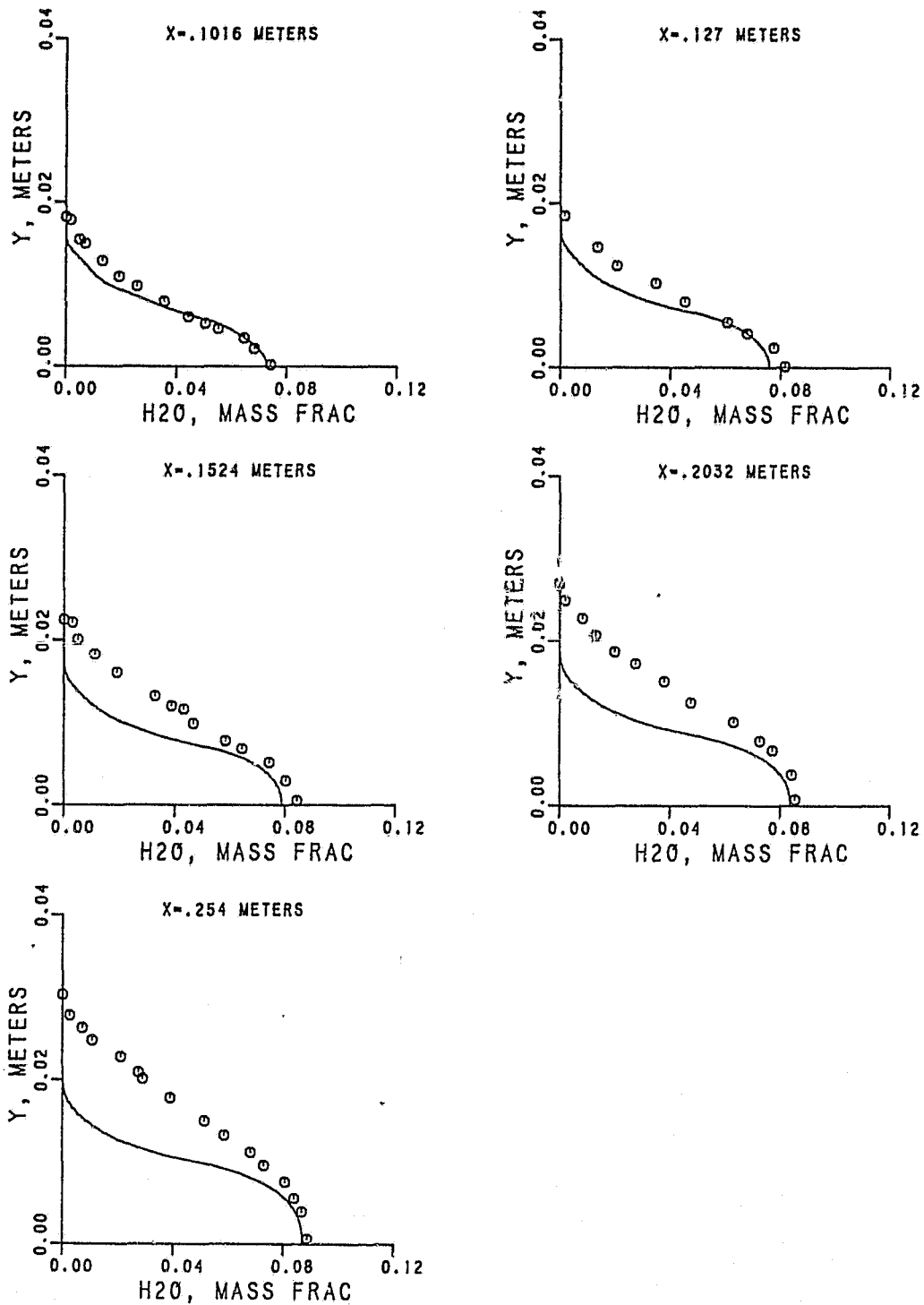


Figure 6.12-8. Predicted H_2O Profiles With Design Criteria Rate Constants.

ORIGINAL PAGE IS
OF POOR QUALITY

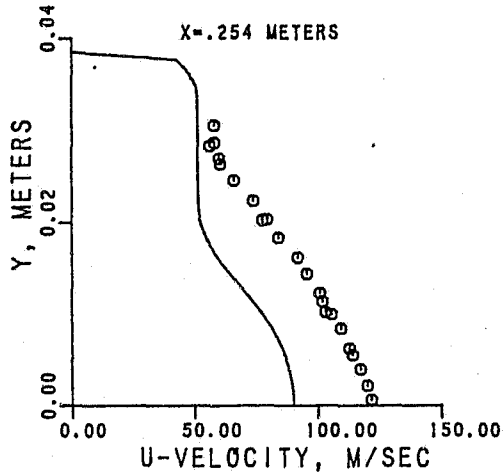
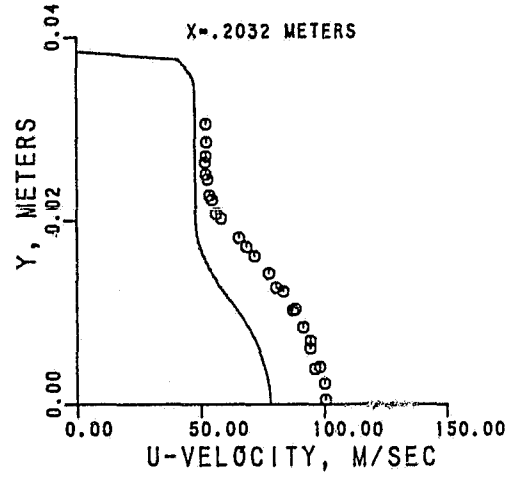
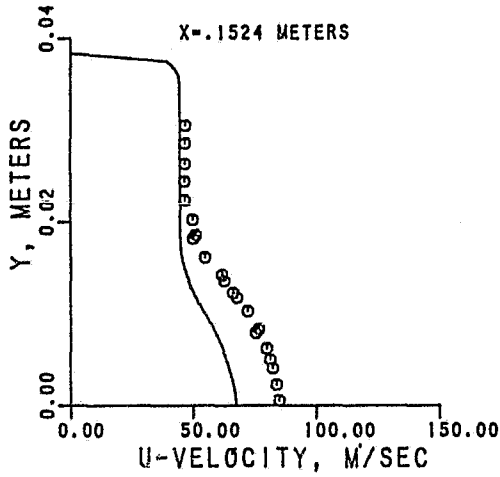
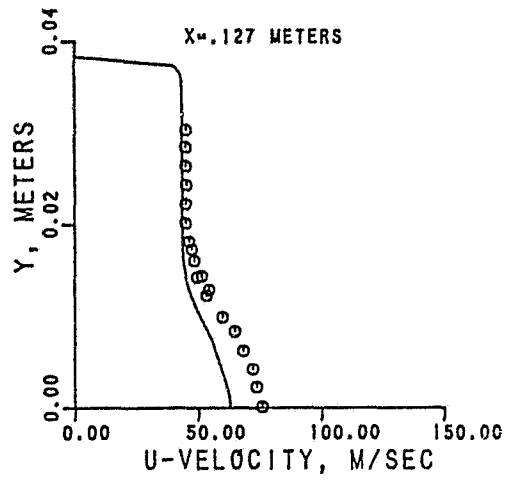
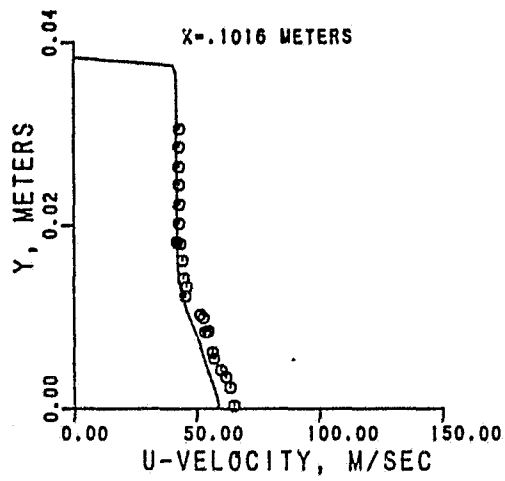


Figure 6.12-9. Predicted Velocity Profiles With PM/PV Rate Constants.

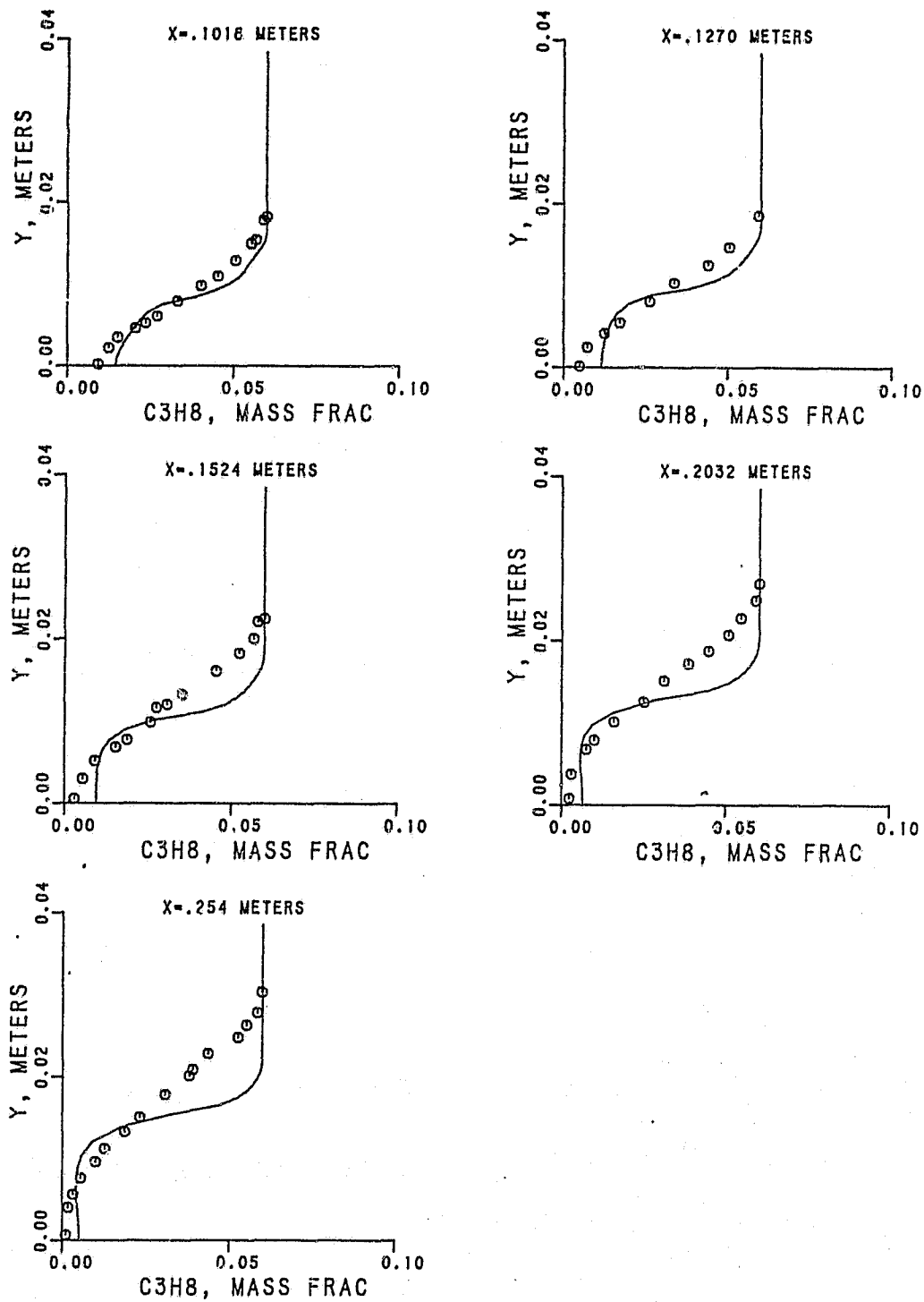


Figure 6.12-10. Predicted Unburned Fuel Profiles With PM/PV Rate Constants.

C-4

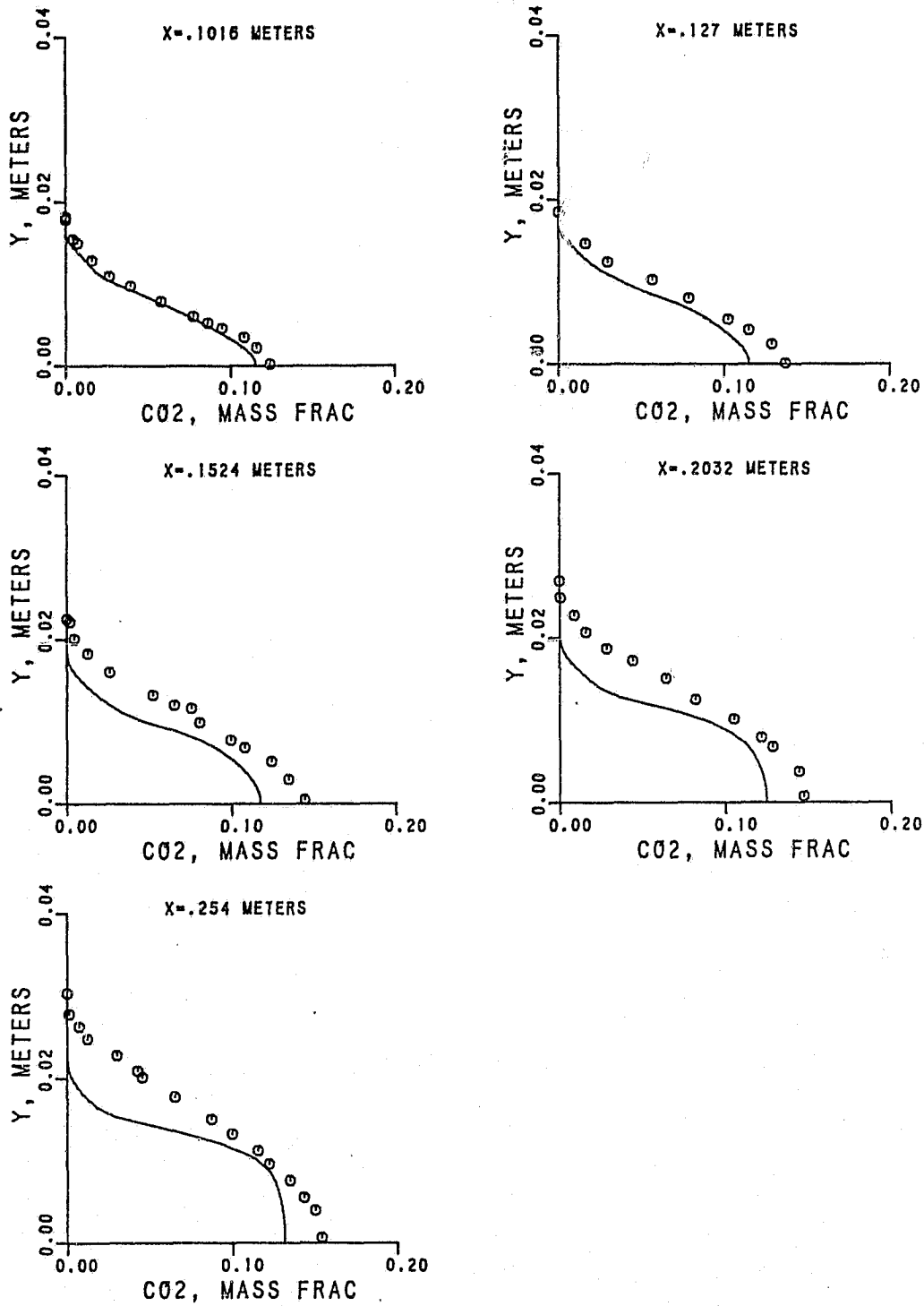


Figure 6.12-11. Predicted CO_2 Profiles With PM/PV Rate Constants.

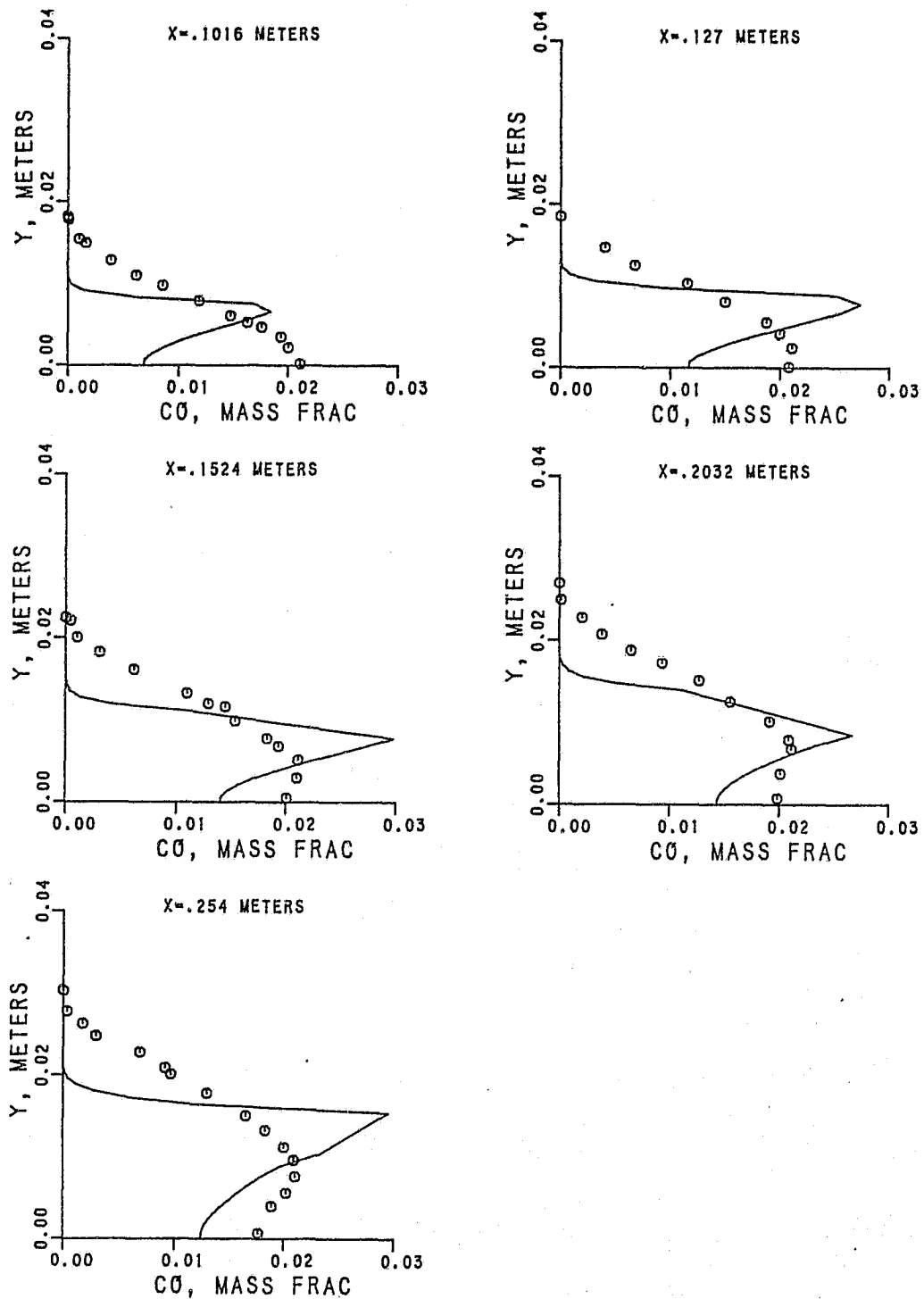


Figure 6.12-12. Predicted CO Profiles With PM/PV Rate Constants.

ORIGINAL PAGE IS
OF POOR QUALITY

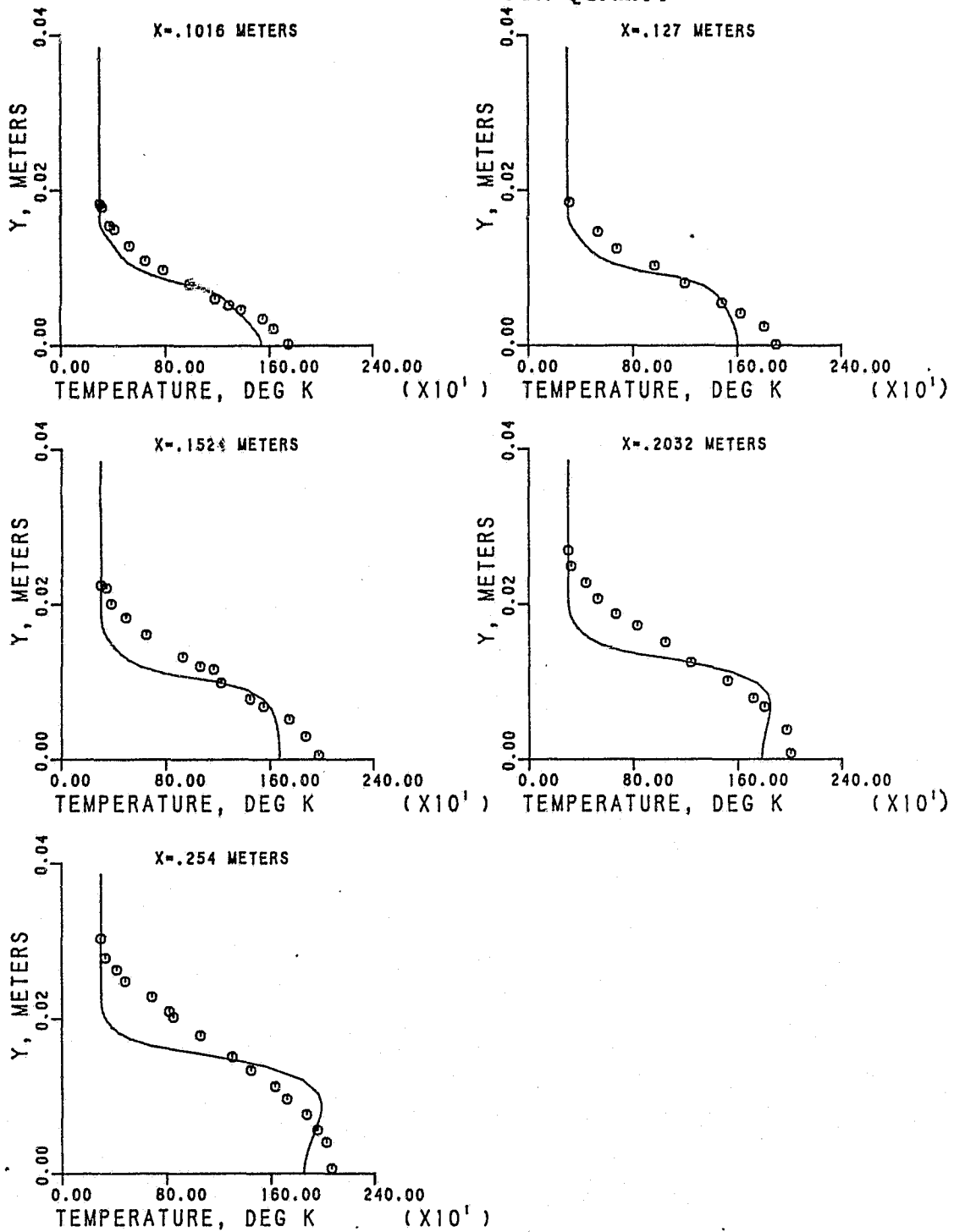


Figure 6.12-13. Predicted Temperature Profiles With PM/PV Rate Constants.

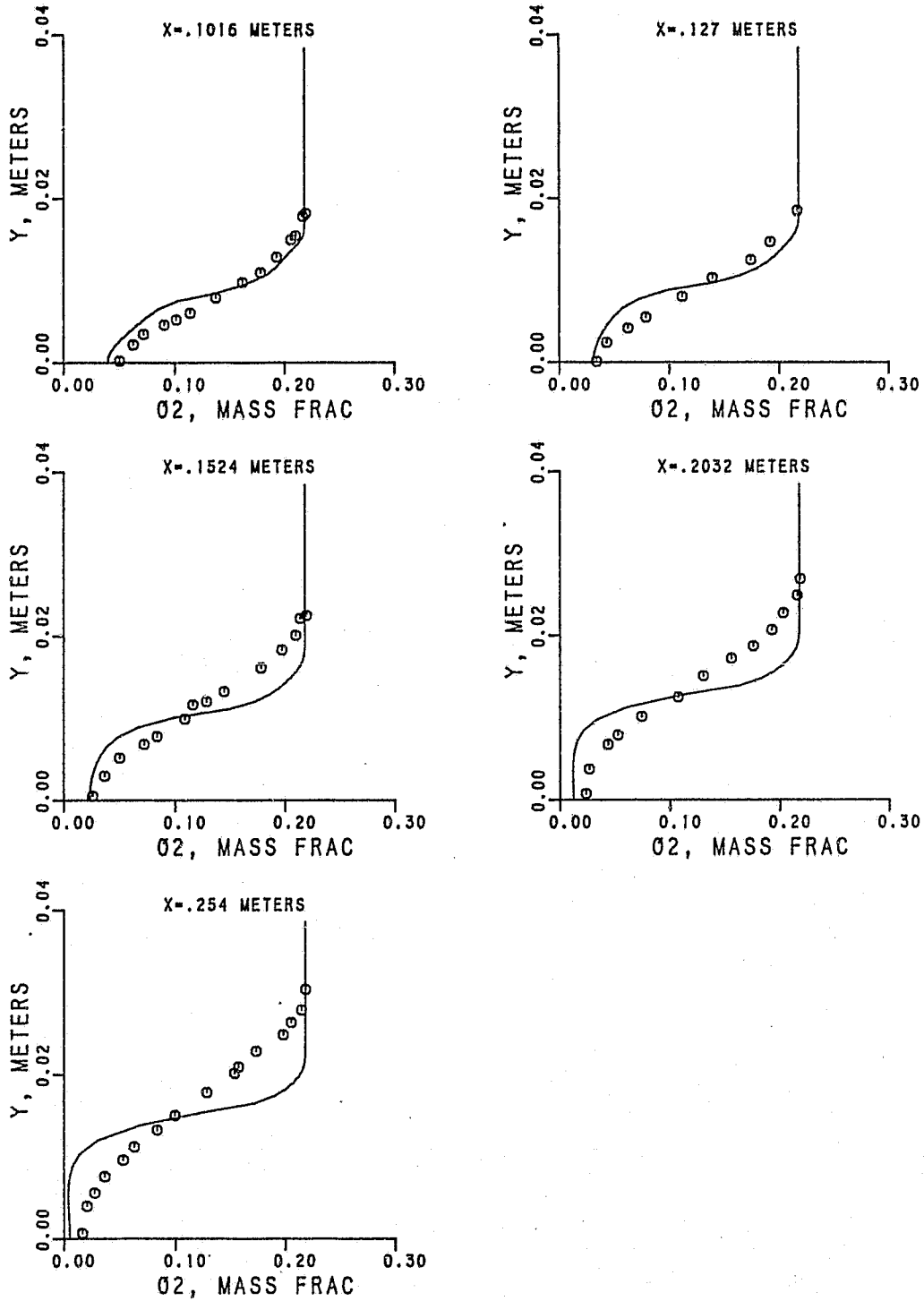


Figure 6.12-14. Predicted O_2 Profiles With PM/PV Rate Constants.

ORIGINAL PAGE IS
OF POOR QUALITY

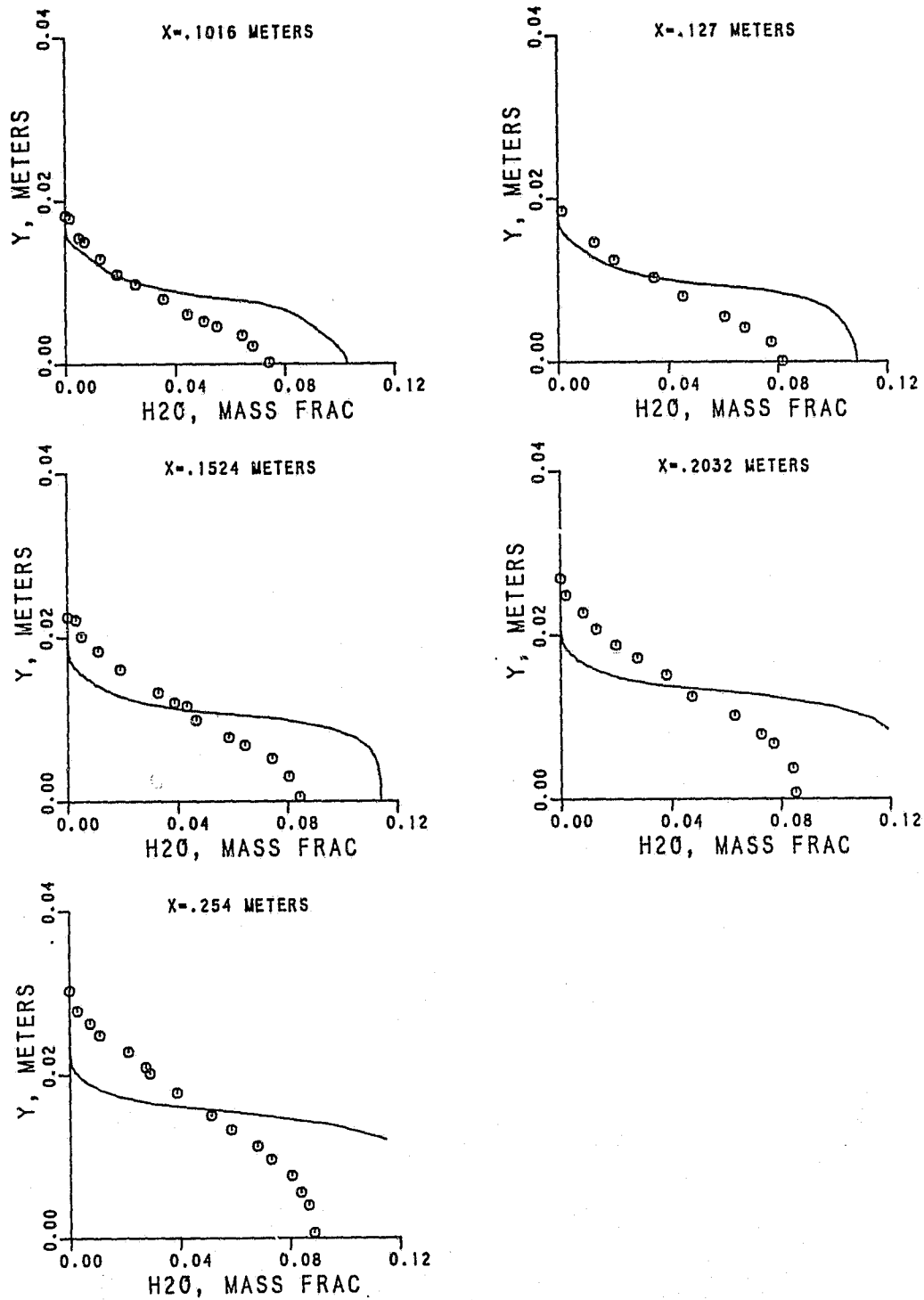


Figure 6.12-15. Predicted H₂O Profiles With PM/PV Rate Constants.

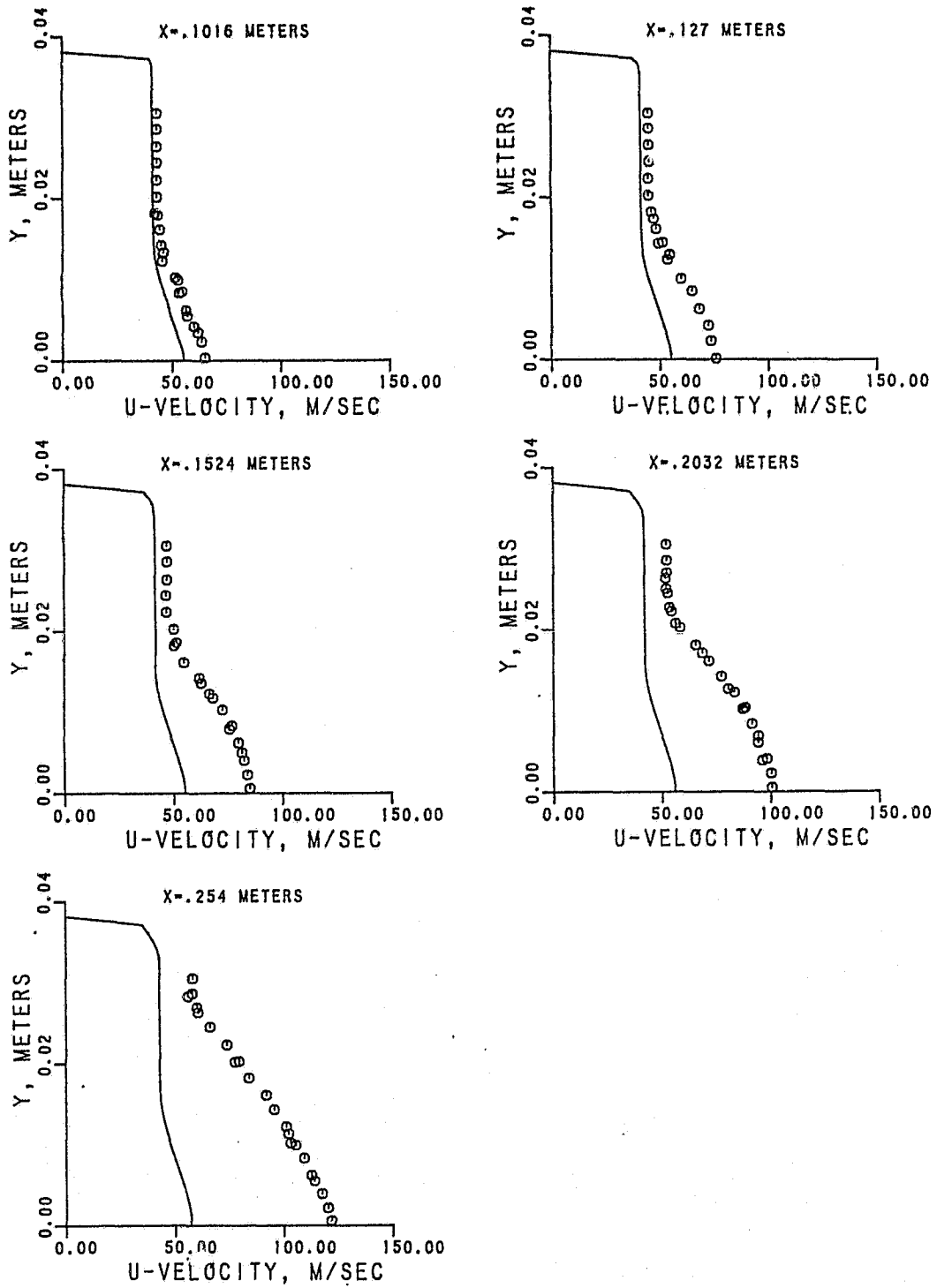


Figure 6.12-16. Predicted Velocity Profiles With The 4-Step Scheme.

ORIGINAL PAGE IS
OF POOR QUALITY

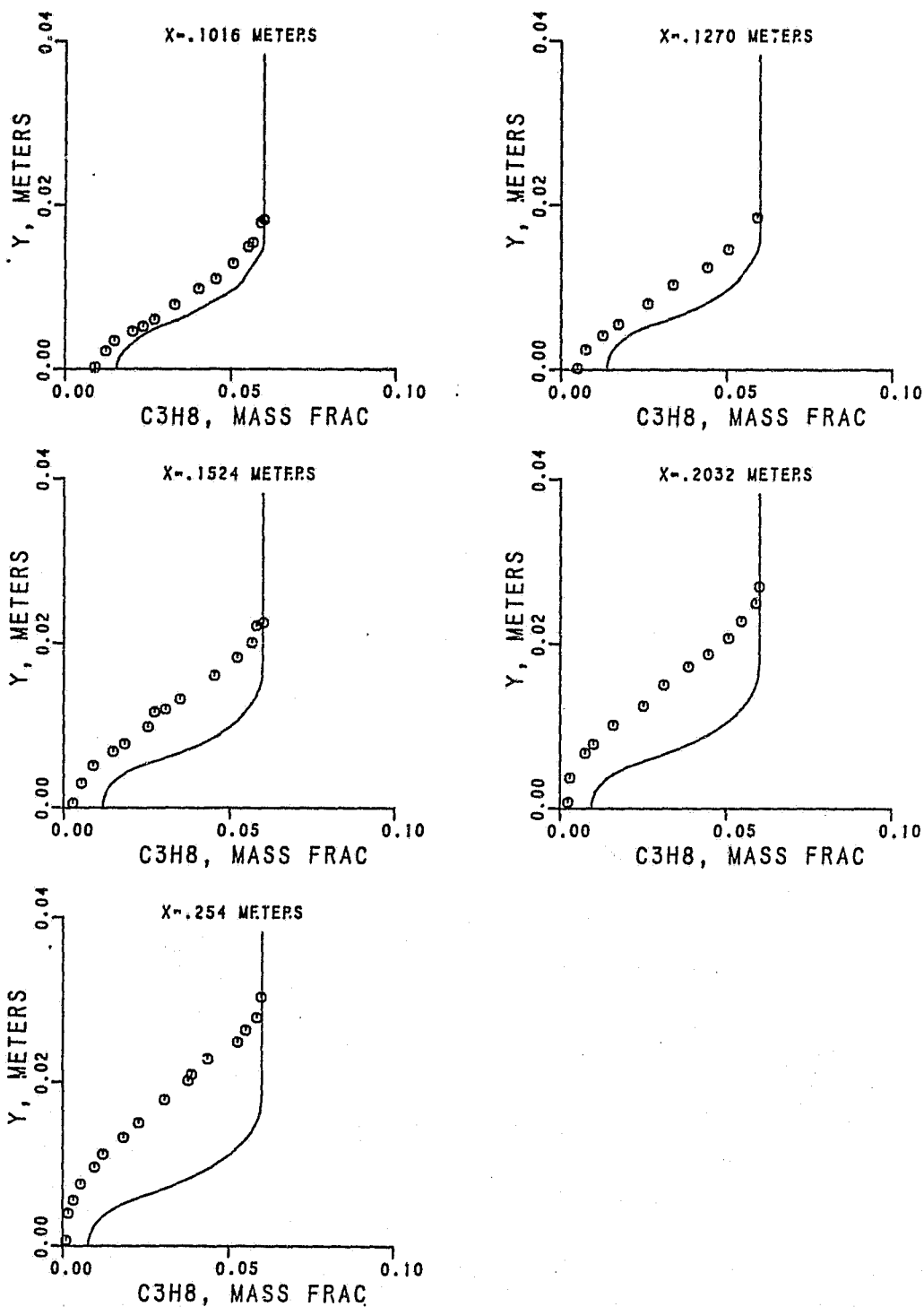


Figure 6.12-17. Predicted Unburned Fuel Profiles With The 4-Step Scheme.

ORIGINAL PAGE IS
OF POOR QUALITY

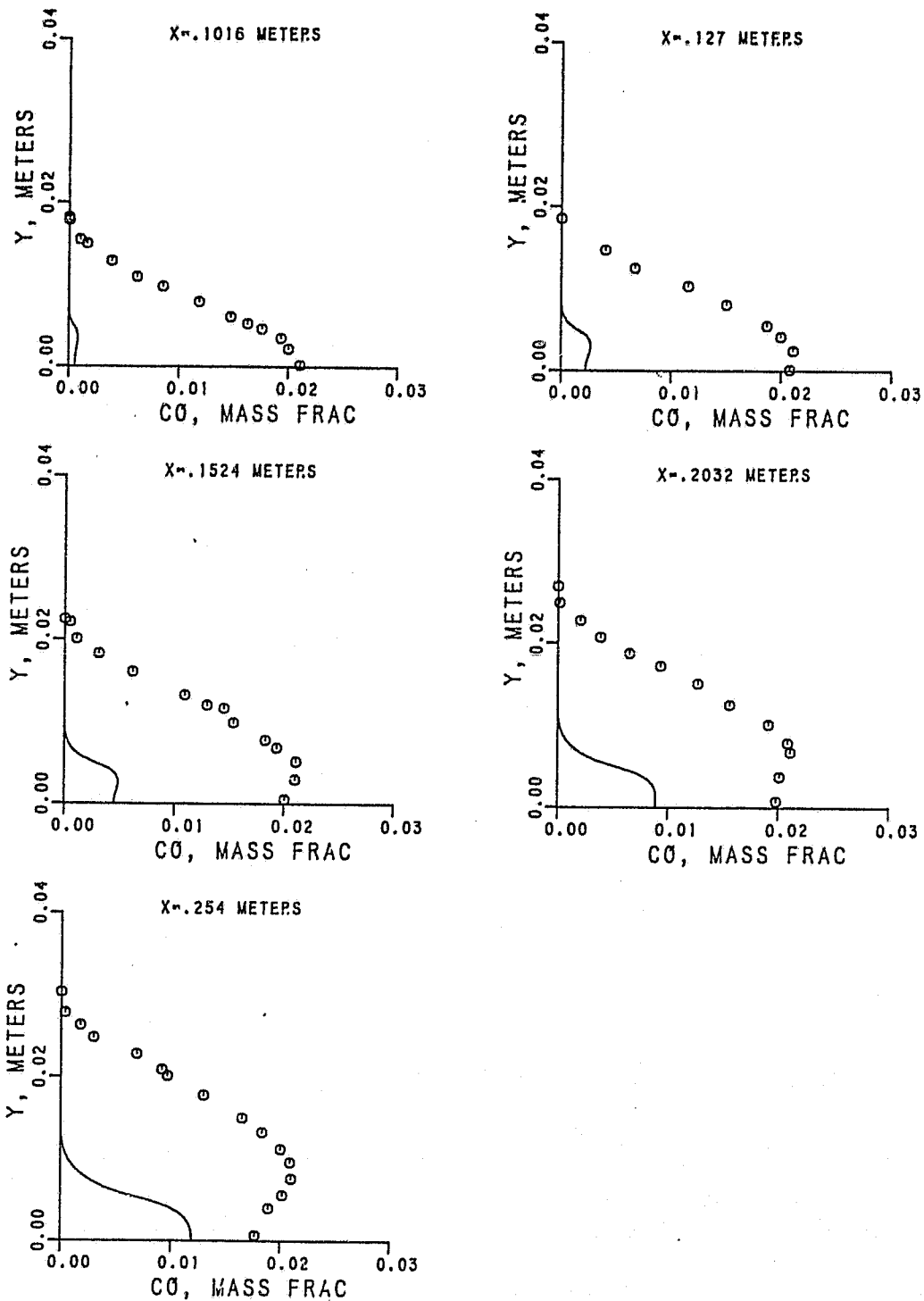


Figure 6.12-18. Predicted CO Profiles With The 4-Step Scheme.

ORIGINAL PAGE IS
OF POOR QUALITY

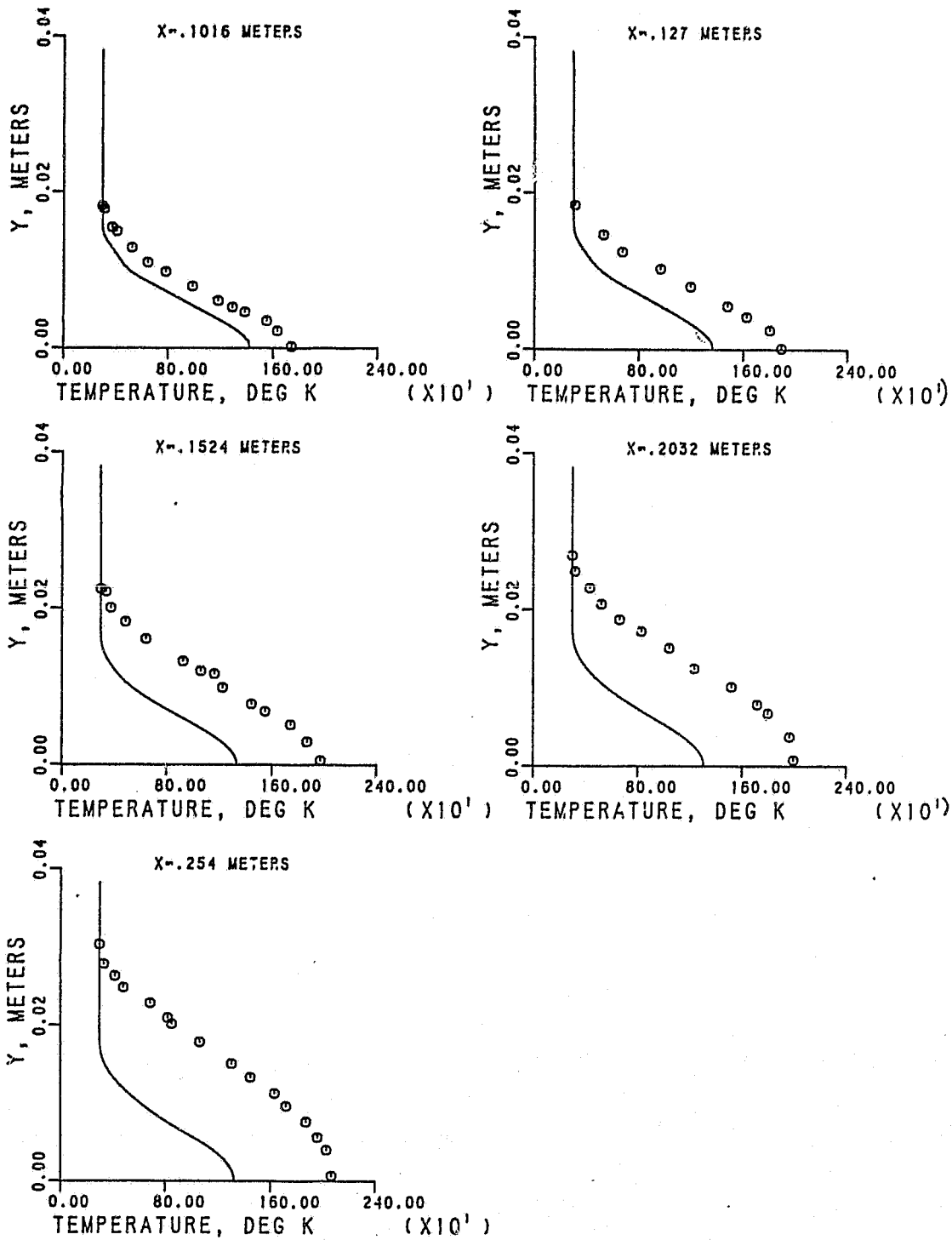


Figure 6.12-19. Predicted Temperature Profiles With The 4-Step Scheme.

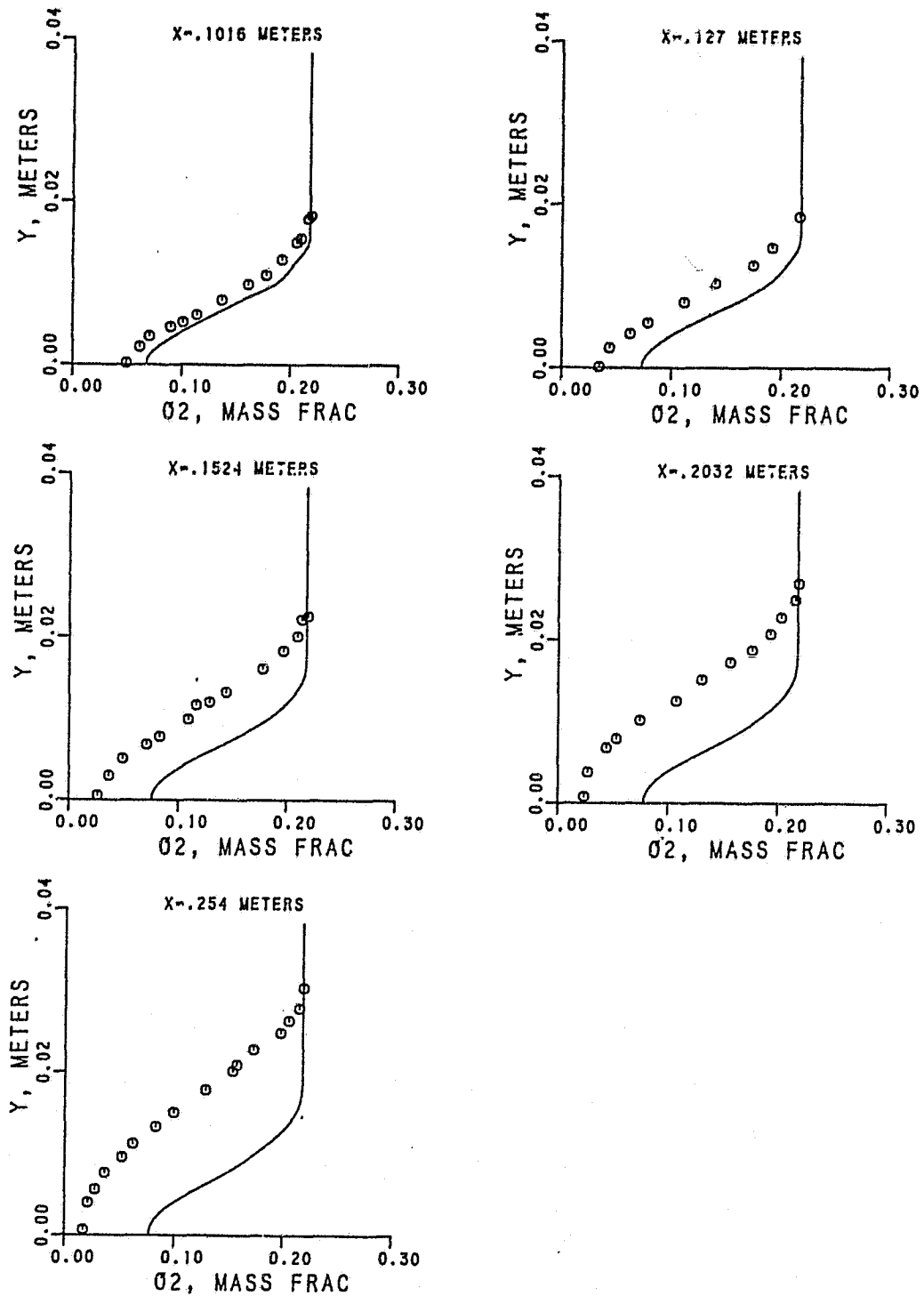


Figure 6.12-20. Predicted O₂ Profiles With The 4-Step Scheme.

ORIGINAL PAGE IS
OF POOR QUALITY

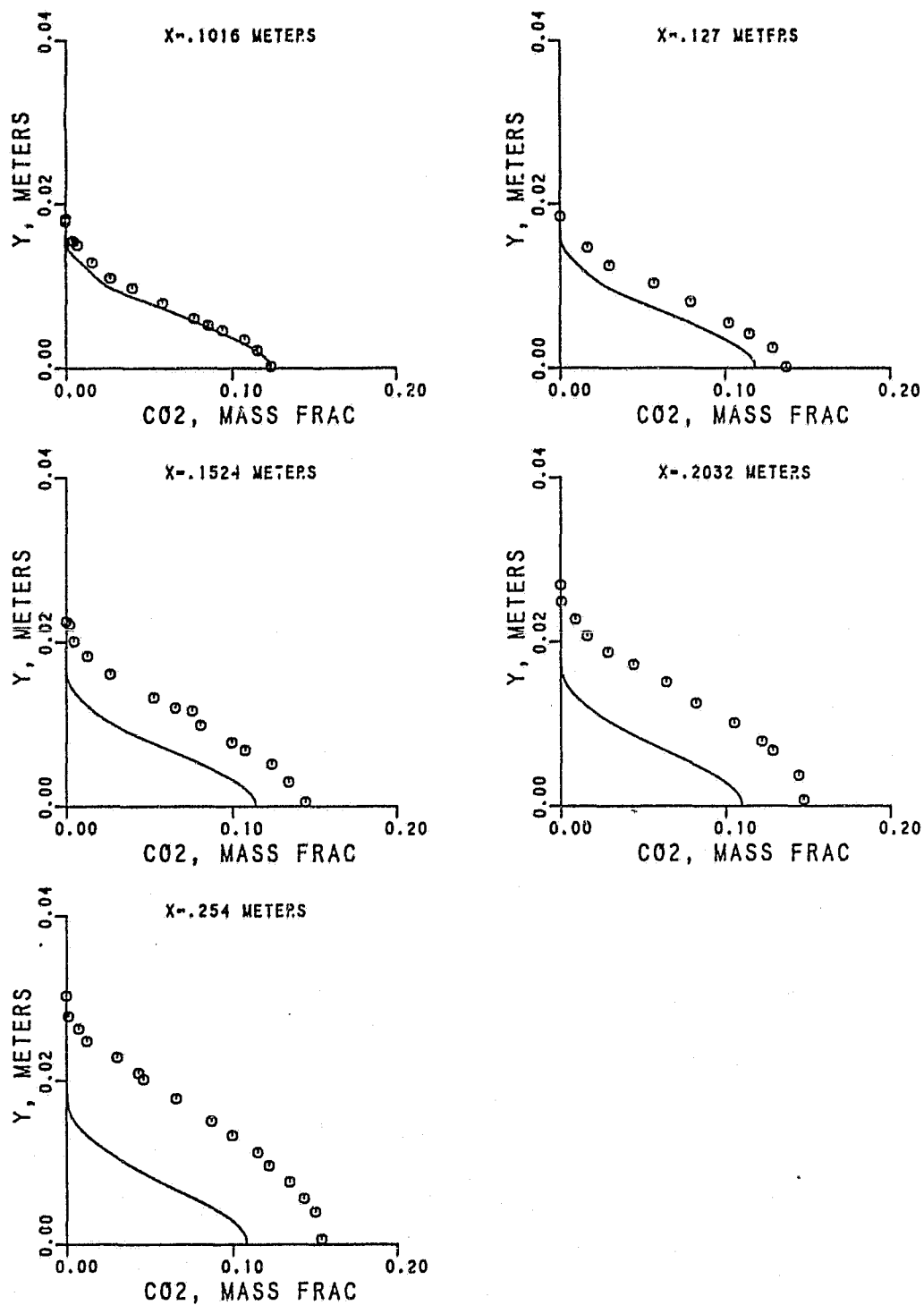


Figure 6.12-21. Predicted CO₂ Profiles With The 4-Step Scheme.

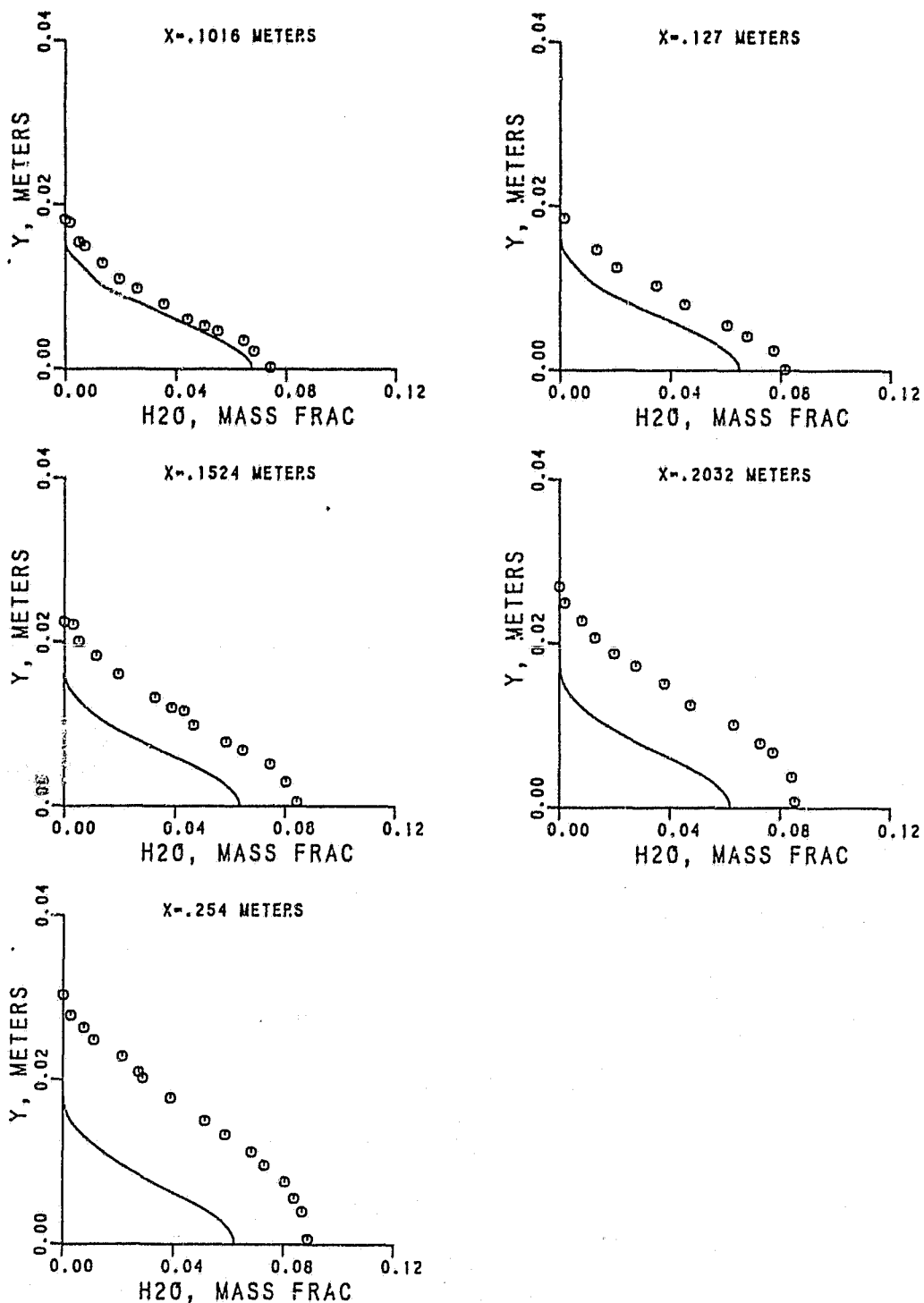


Figure 6.12-22. Predicted H₂O Profiles With The 4-Step Scheme.

ORIGINAL PAGE IS
OF POOR QUALITY

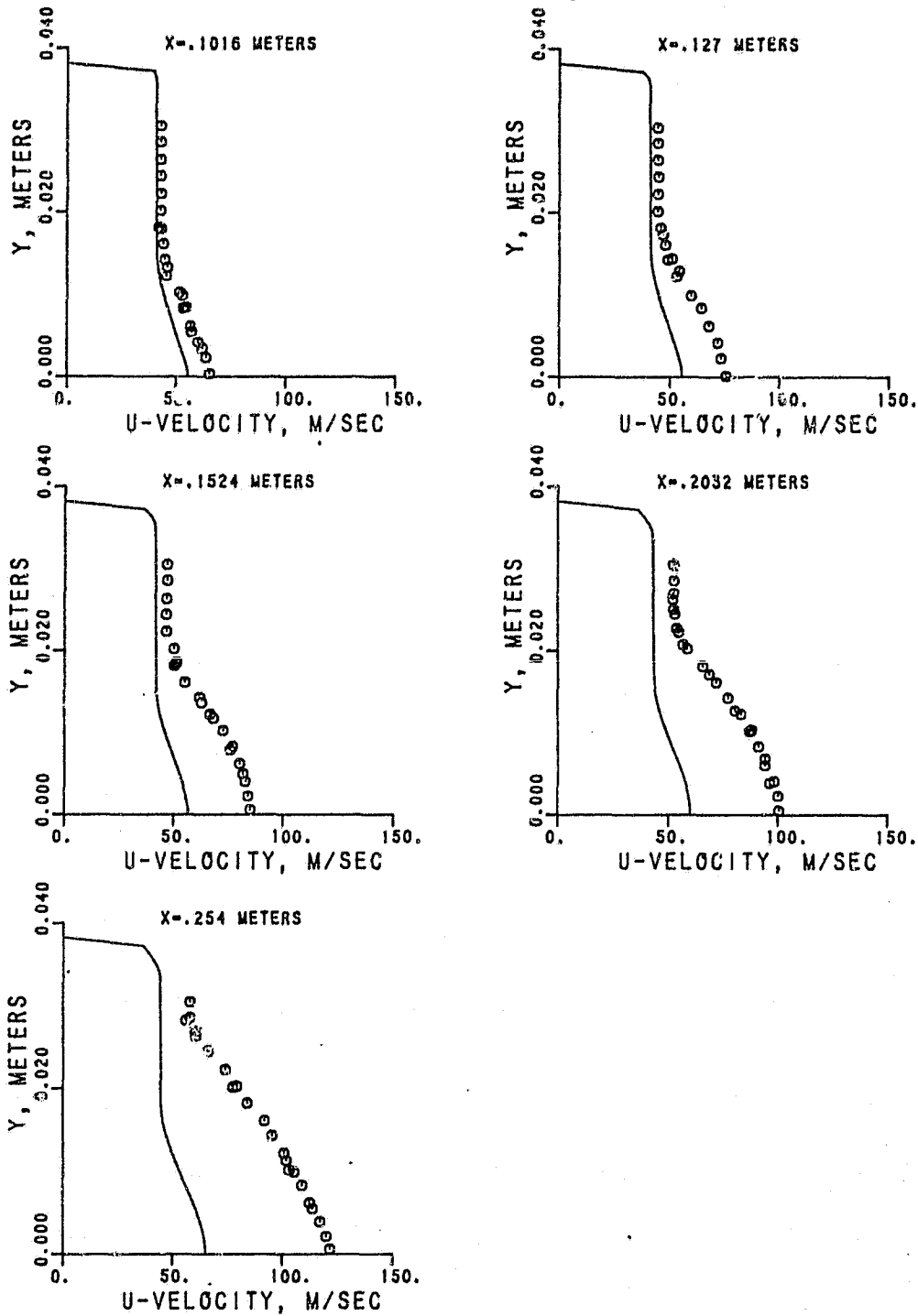


Figure 6.12-23. 4-Step Scheme With Modified Rate Constants For Fuel and Intermediate Fuel Reaction Steps (Modified 4-step) Axial Velocity Profile.

ORIGINAL PAGE IS
OF POOR QUALITY

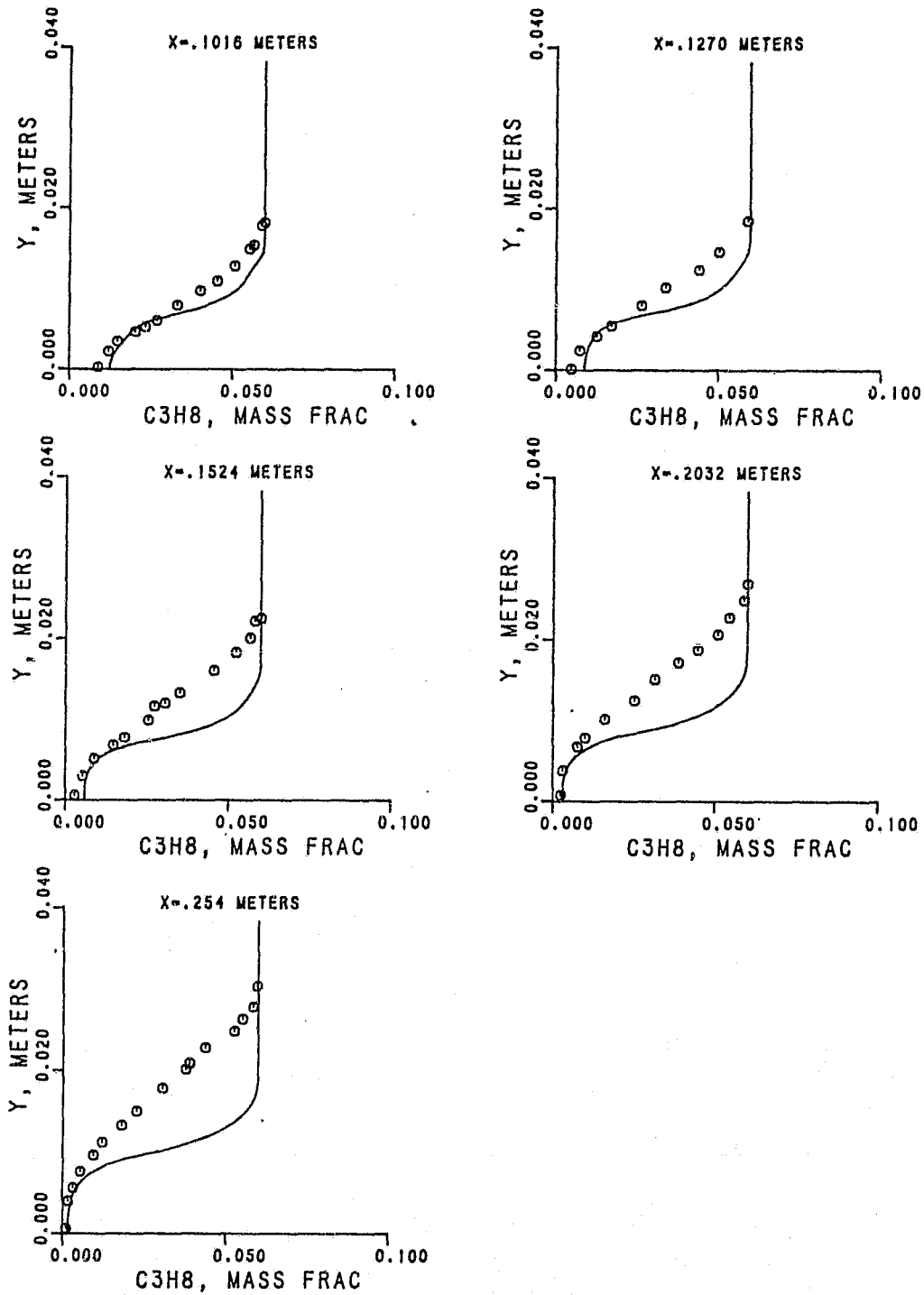


Figure 6.12-24. Modified 4-Step -- Unburned Fuel Profiles.

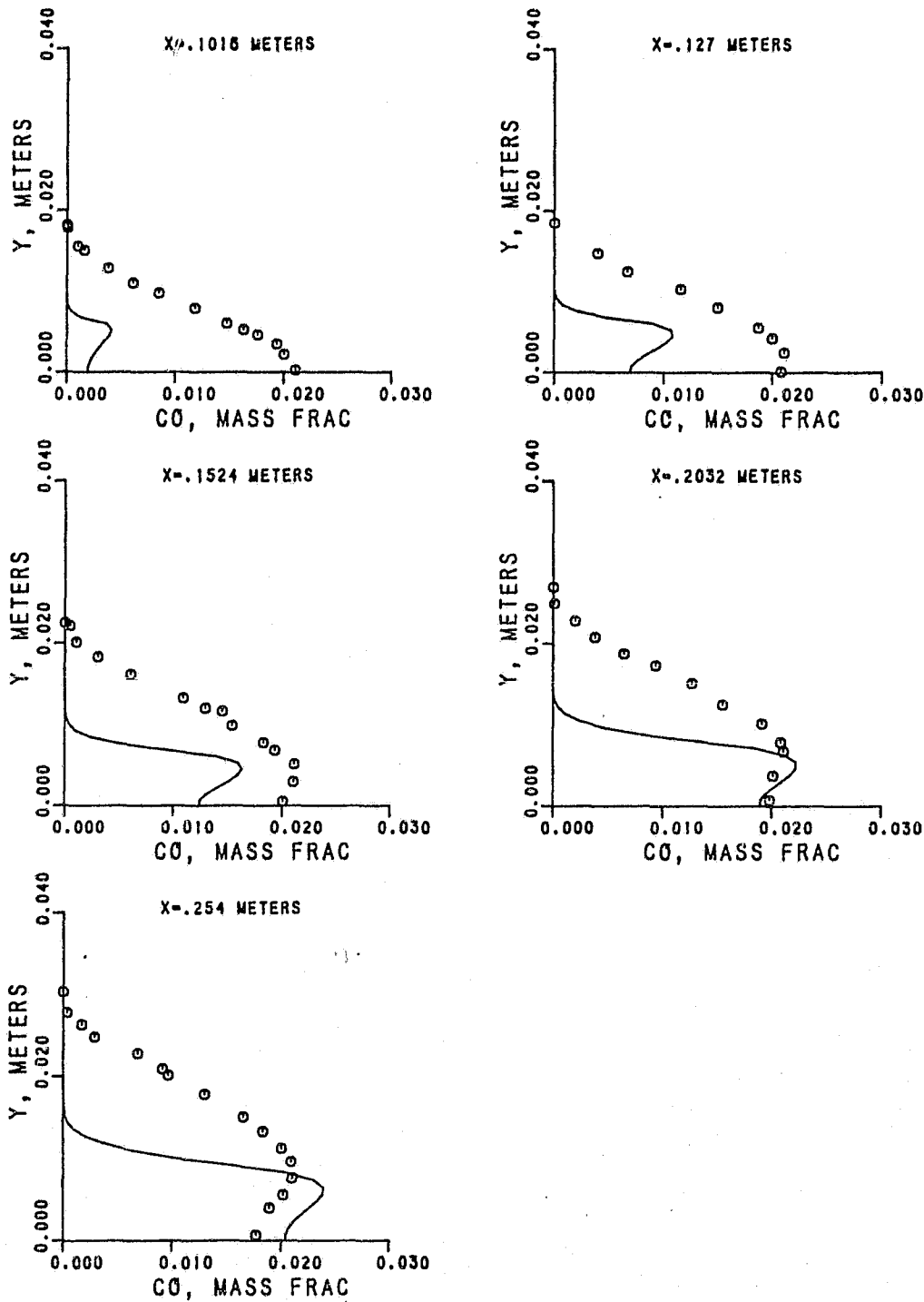


Figure 6.12-25. Modified 4-Step CO Profiles.

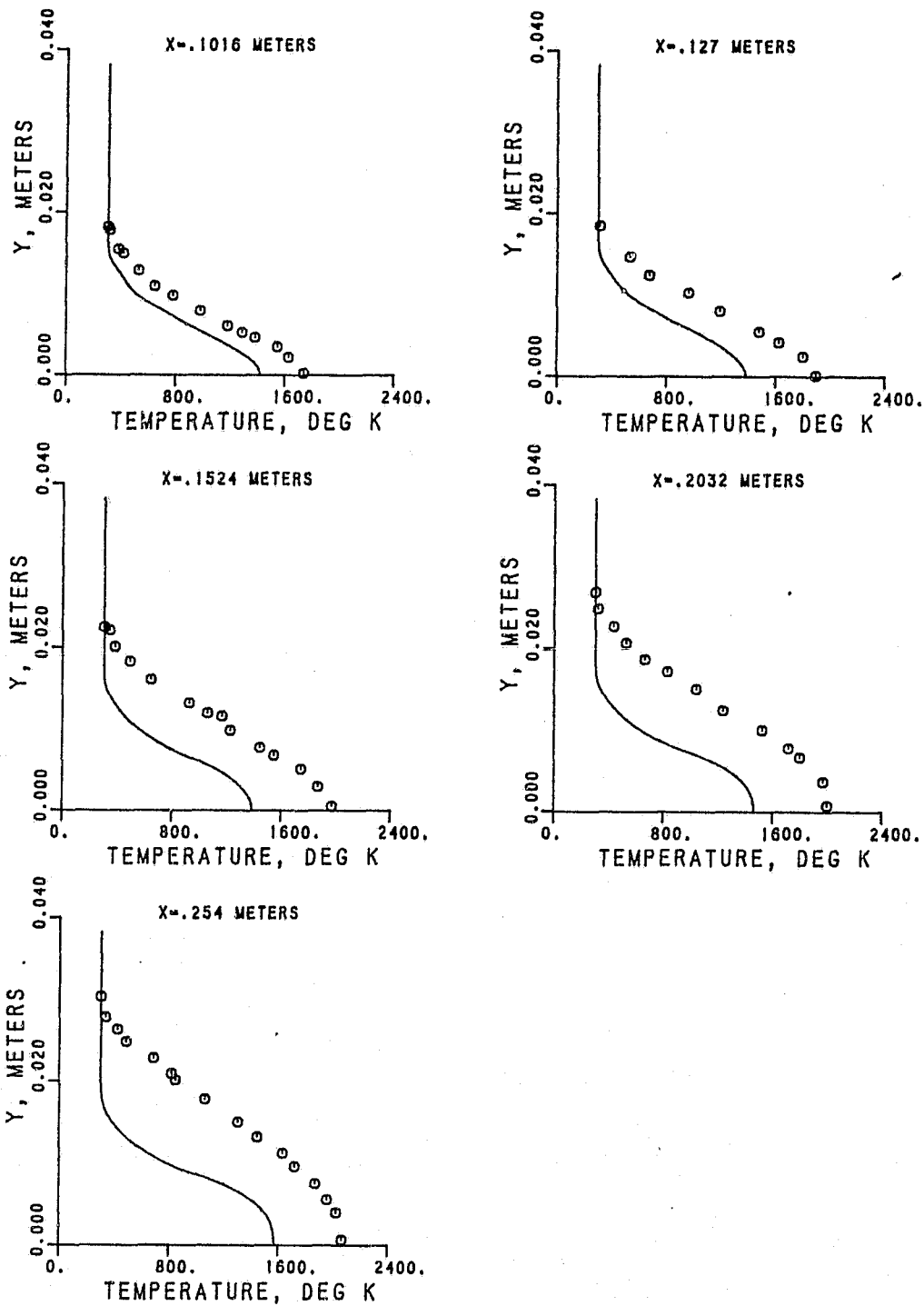


Figure 6.12-26. Modified 4-Step -- Temperature Profiles.

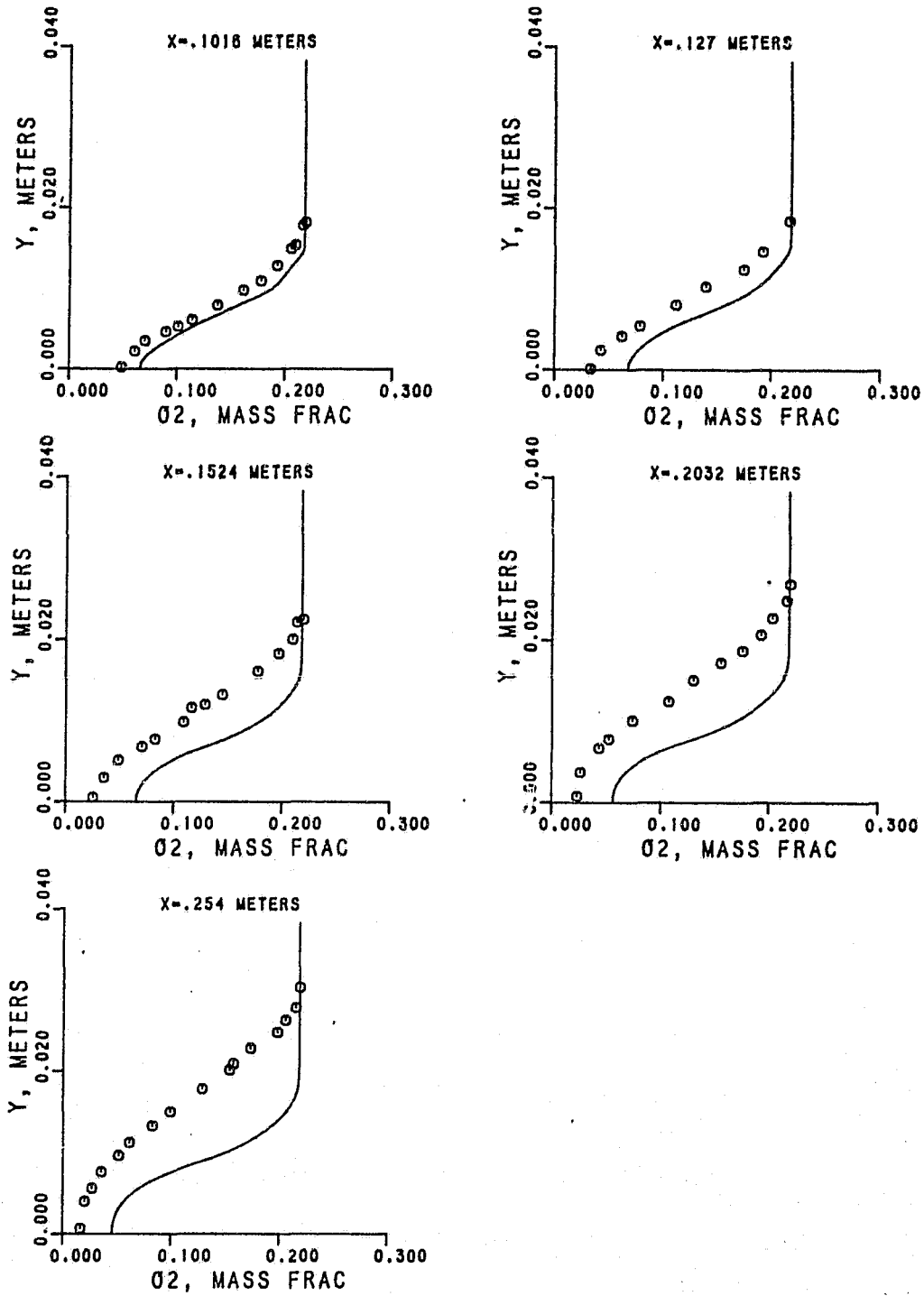


Figure 6.12-27. Modified 4-Step -- O_2 Profiles.

ORIGINAL PAGE IS
OF POOR QUALITY.

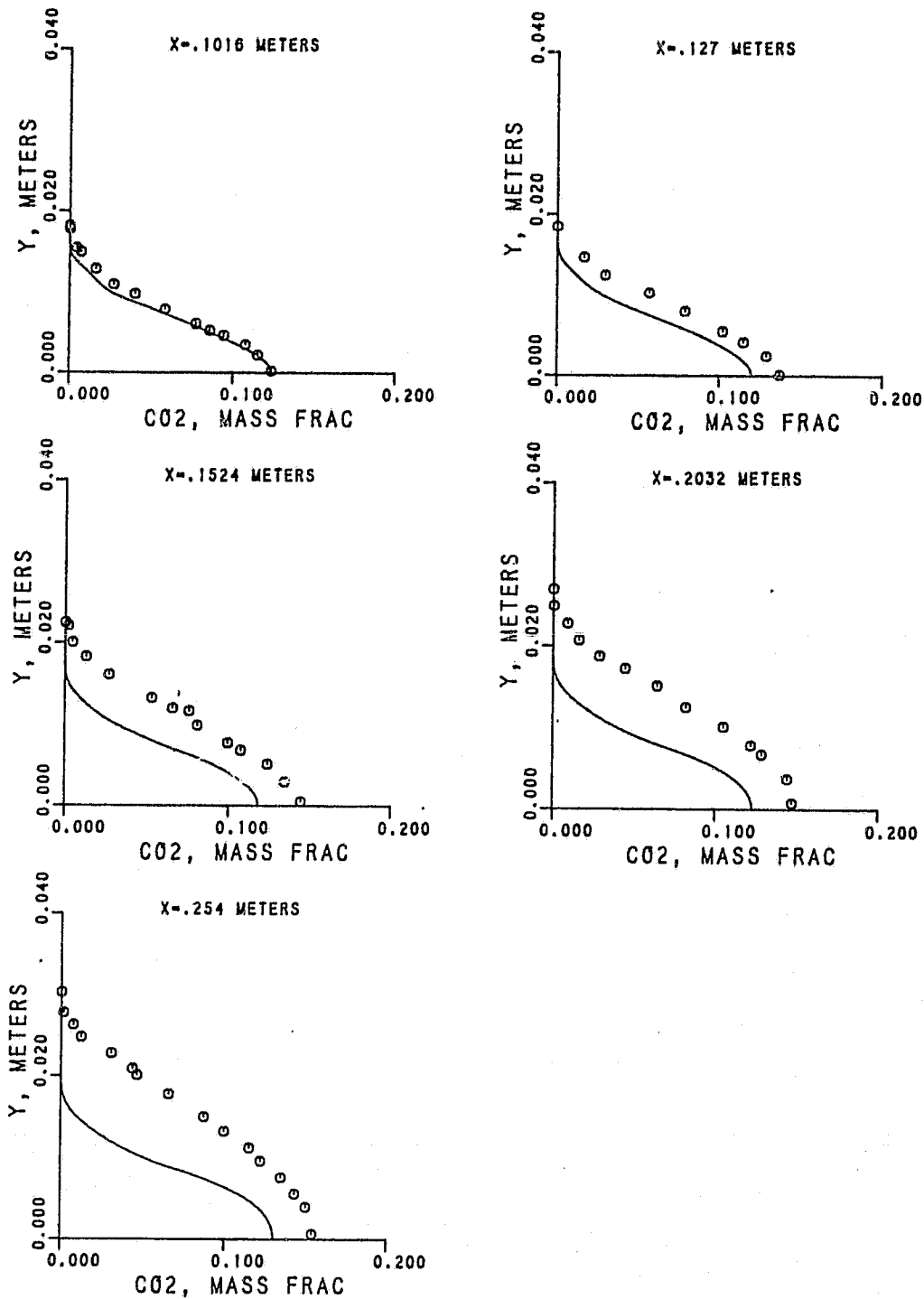


Figure 6.12-28. Modified 4-Step -- CO₂ Profiles.

ORIGINAL PAGE IS
OF POOR QUALITY

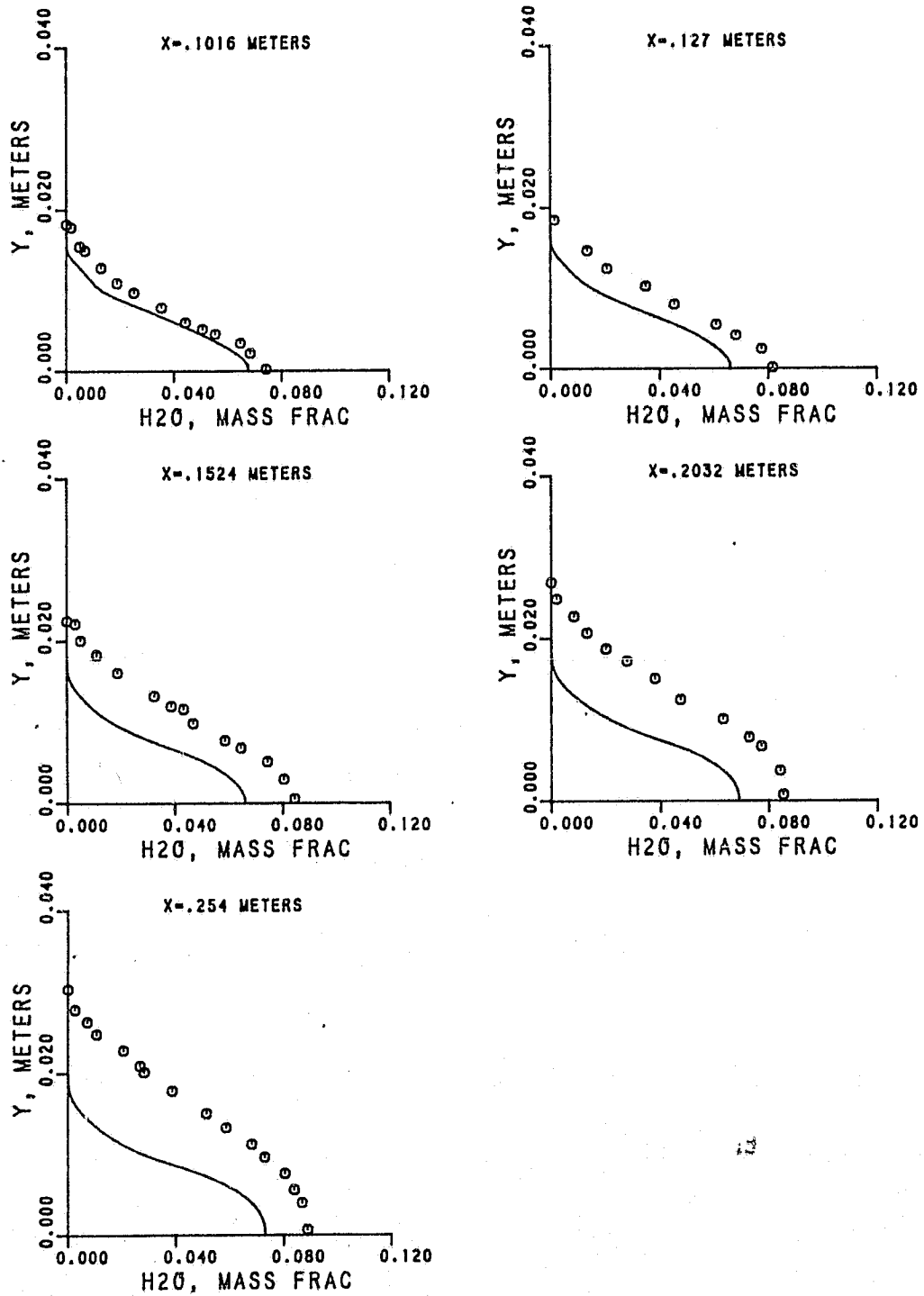


Figure 6.12-29. Modified 4-Step --- H₂O Profiles.

6.13 Free Methane Turbulent Jet Flame

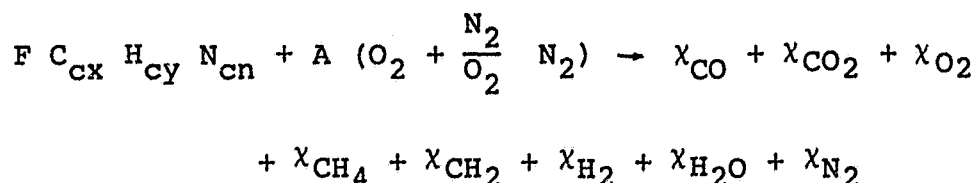
The free, turbulent, reacting methane jet investigated by Hassan, et al.,¹³³ was modeled here using the PDF-partial equilibrium approach of Bilger and Starner.²⁷ Although several configurations were studied by Hassan, the detailed data was available only on the flame that has been investigated here. The test setup was a vertical free turbulent methane jet issuing from a 7.74 mm diameter pipe as shown schematically in Figure 6.13-1. The jet Reynolds number was 15,000, with a bulk velocity of 39.9 m/s. The flame was stabilized by a co-annular flow of 1 percent (by mass) of hydrogen. A discussion of the data and the results of the numerical model are presented below.

From the initial (or tube exit) jet velocity, mass flow and assumed temperature of 59°F, mass and energy flux can be determined for comparison at downstream positions. The fuel was reported to be 94 percent methane. From the assumption of atmospheric pressure and the reported density, a molecular weight of 17.22 was determined. If the remaining 6 percent was composed of nitrogen and propane (typical dry natural gas composition), then 52.4 percent of that fraction being nitrogen would give the above molecular weight. From the reported mass flows of H₂ and fuel, the following mole fractions were determined,

$$X_{\text{fuel}} = 78.86\%, X_{\text{CH}_4} = 74.13, X_{\text{N}_2} = 2.48, X_{\text{C}_3\text{H}_8} = 2.25, X_{\text{H}_2} = 21.$$

The specific enthalpy at the jet exit is then $-4.154 \cdot 10^6 \frac{\text{J}}{\text{kg}}$ and energy flux is $-5858 \frac{\text{J}}{\text{sec}}$.

At four axial positions ($x/D = 36.2, 75, 113.7$ and 204) radial profiles of temperature, mole fractions of CO , CO_2 and O_2 were reported. Consider the reaction equation in mole fraction form,



Although dry measurements were made, the following analysis assumes that the reported results were based on the same reaction equation with the possible exception of CH_2 . Then, for the above reaction equation, there are four atom-balance equations and the sum of mole fractions identity for six unknowns (again exclude CH_2); therefore, an additional constraint is required. For this, the water/gas equilibrium²¹³ based on the measured local mean temperature and modified as described below, was chosen. Then at various radii in the cross section to give an adequate definition, the reported data were interpolated using cubic splines and the above unknowns computed. Also the asymptotic end of each measured profile was determined from cubic spline fitting (extrapolation). If the above system of equations gave a negative mole fraction of methane (occurring in the high temperature and lean boundary regions) or CO was nonexistent, then the water/gas equilibrium constraint was dropped and the reaction equation solved (excluding both CH_2 and CH_4). Lastly, the outermost regions would not have any free hydrogen (as evidenced by computing negative mole fractions of same). Then the carbon-balance constraint was dropped (taking the O_2 measurements as being more accurate), and the reaction equation solved for nitrogen, water, and stoichiometry.

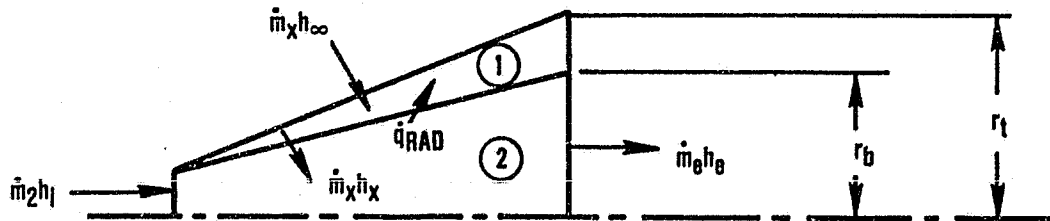
The water/gas equilibrium shift results of Mitchell, et al.,¹²⁹ were applied to the equilibrium constant (determined from measured temperature) in the rich regions of the flame. In the

lean regions at less than 1400°K, the reaction was assumed to be quenched (5) at 1400°K.

With an assumed jet profile of [19],

$$\frac{u}{u_b} = \left[1 - \left(\frac{r}{r_b} \right)^{3/2} \right]^2$$

where the jet radius (r_b) is minimum of the CO_2 or O_2 profile asymptote and the centerline velocity is determined by matching the energy flux. For this balance consider the following control volumes,



Continuity gives $\dot{m}_e = \dot{m}_i + \dot{m}_x$, where \dot{m}_x is the entrainment, and energy gives

$$\dot{m}_i \left[h_i + \frac{u_i^2}{2} \right] = \int_0^{r_b} \left[h + \frac{u^2}{2} \right] u \rho r dr - \left(\int_0^{r_b} u \rho r dr - \dot{m}_i \right) h_\infty$$

where,

r_t - radius of thermal boundary as determined from the temperature profile

\dot{q}_{rad} - radiation heat transfer outside jet boundary to mass entrained

ρ - local density

\dot{m}_i - initial jet mass flux

This procedure was attempted at all four measurement stations. For the first, $x/D = 36.2$, the energy flux matching gave $u_b = 26.85$ m/s. The other three stations have more enthalpy in the outer boundary region than matching will allow, indicating that temperature measurements there are high.

The partial equilibrium computations were made with the full stoichiometry adjusted (i.e. amount of CH_4 and N_2) to give the correct enthalpy flux. The 2-D turbulent jet calculations were based on a jet diameter 1 mm larger than that reported (i.e., the OD of the H_2 stabilizer). Then, an assumed fully developed pipe flow velocity profile at the exit was set to give the correct jet mass flux.²¹⁴ The turbulence intensity profile was taken from developed pipe flow results.²¹⁵ The partial equilibrium computations were based on the specific thermodynamic of the JANAF tables using the curve fits of Wakelyn and McLain,²¹⁶ the three body recombination kinetics of Jensen and Jones²⁸ and the global hydrocarbon breakdown of Duterque, et al.²⁹ Additionally, the flame sheet approximation had a pyrolysis mixture fraction of 0.073 and 0.2 mass fraction of organic fuel converted to intermediate at the pyrolysis flame sheet. In the 2-D turbulent jet calculations, the initial turbulent length scales were 0.1 inner (jet) and 0.2 outer, both based on the jet diameter. Also the free stream or ambient air was given a velocity of 0.25 m/s.

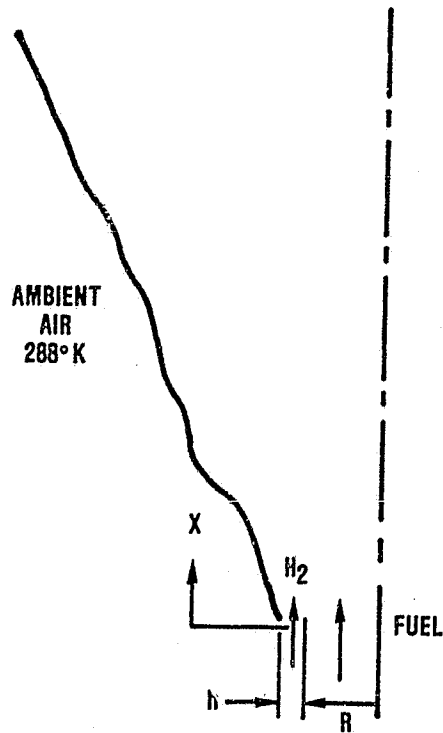
The axial plots of centerline temperature, CO, CO_2 , and O_2 are shown in Figure 6.13-2. The model-predicted centerline temperature profile agrees reasonably well in regard to temperature rise upstream and downstream of the flame tip at the center. The predicted peak temperature level and its axial location are slightly different from data. The initial CO buildup agrees well with data; but there is some discrepancy in the post-flame region. Similar conclusions can be made about the CO_2 profiles shown in Figure

6.13-2. For the initial portion of the flame ($x < 0.75$ m), measurements indicate finite concentration of O_2 at the centerline. Such a behavior cannot be predicted by diffusion flame models including Bilger's model which, for a high fuel-rich region, sets O_2 equal to zero.

Figure 6.13-3 shows a comparison between measured and predicted profiles of total fuel mass fraction, and unburned fuel profiles are presented in Figure 6.13-4. In the initial portion of the flame, the conclusions are good, but farther down stream the fuel oxidation rate is faster than what data would indicate. This also results in higher centerline temperature levels as shown in Figure 6.13-5. From the model predictions of total fuel mass fraction at $x/D = 113.7$, it is concluded that the Bilger model is predicting a faster jet spreading rate. This causes faster decay of the centerline temperature in the post-flame region as shown in Figure 6.13-5.

Comparison between measured and predicted CO profiles (Figure 6.13-6) show that, whereas the agreement is good up to $x/D = 75$, the post-flame region is not well correlated by the Bilger model. Similar conclusions can be made for the H_2 profiles as presented in Figure 6.13-7. For the O_2 profiles, (Figure 6.13-8) up to $x/D = 75$, the model predictions are reasonable. But further downstream the model is predicting higher spreading rate than measurements suggest. Similar levels of correlations are obtained for CO_2 profiles as shown in Figure 6.13-9.

ORIGINAL PAGE IS
OF POOR QUALITY



$R = 0.00387 \text{ M}$
 $h = 0.0005 \text{ M}$
 $U_{\text{FUEL}} = 39.9 \text{ M/S}$
 $T_{\text{FUEL}} = 288^\circ\text{K}$

Figure 6.13-1. Geometry of the Free Methane Turbulent Jet Flame Test Setup.

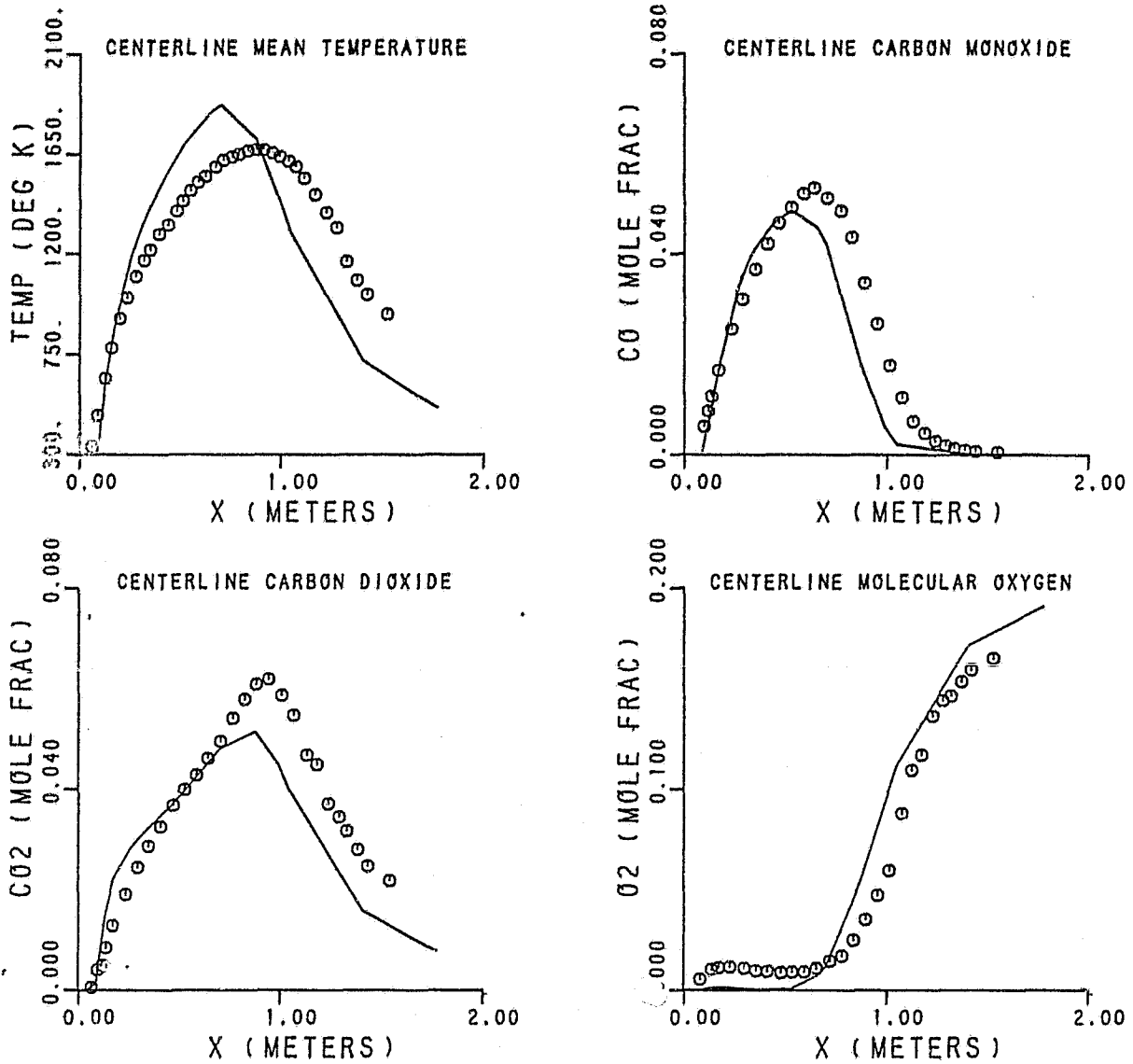


Figure 6.13-2. Comparison Between Bilger Model Predictions With Measured Centerline Profiles of Temperature, CO, CO₂ and O₂ for Hassan and Lockwood Methane Jet Flame.

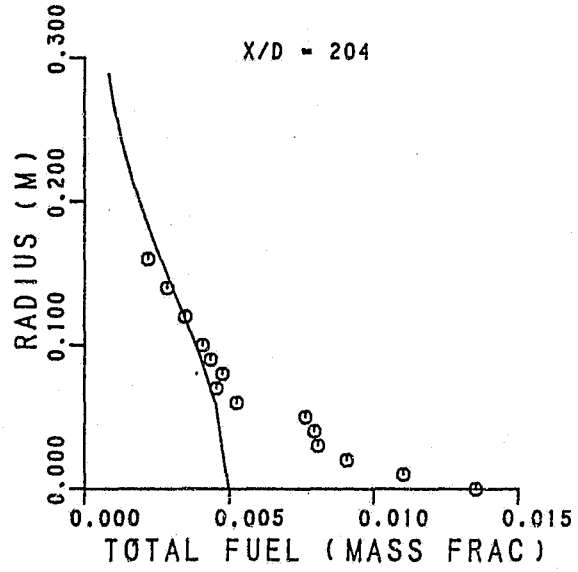
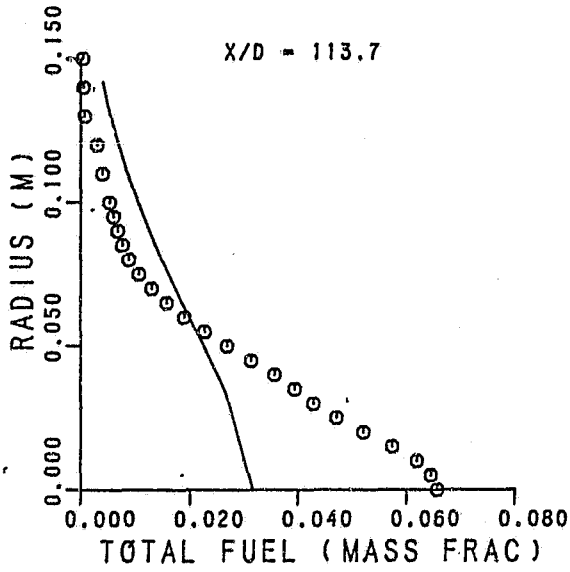
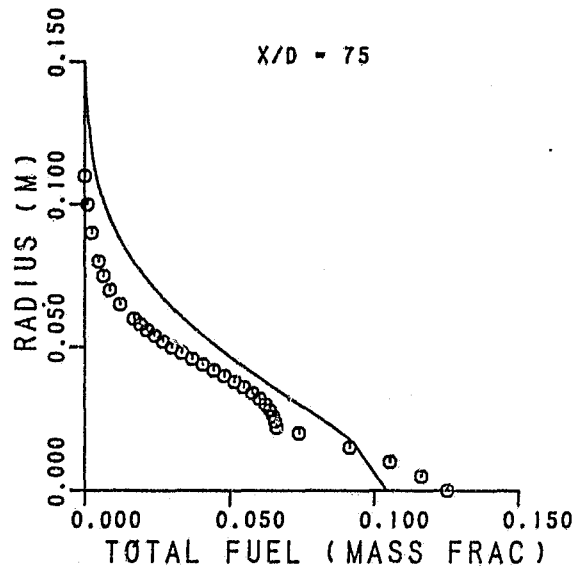
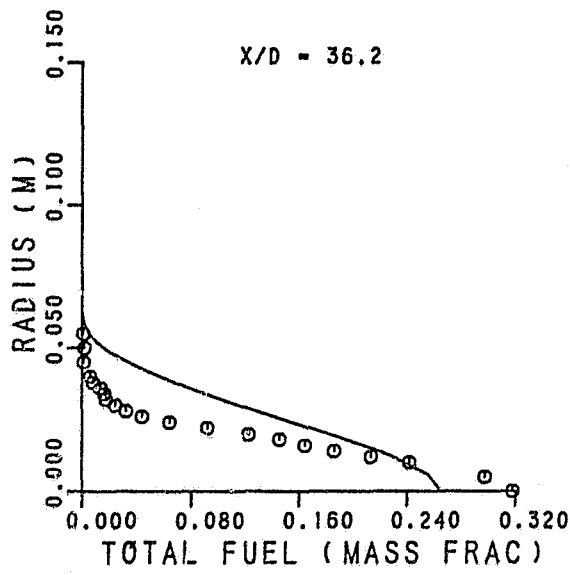


Figure 6.13-3. Radial Profiles of Total Fuel (Bilger's Model).

ORIGINAL PAGE IS
OF POOR QUALITY

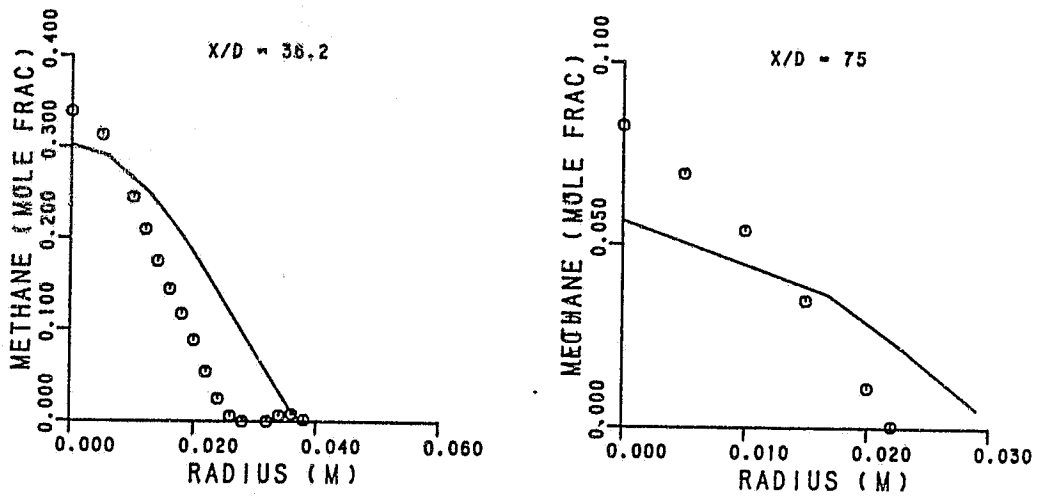


Figure 6.13-4. Radial Profiles of Unburned Fuel Mass Fraction.

ORIGINAL PAGE IS
OF POOR QUALITY

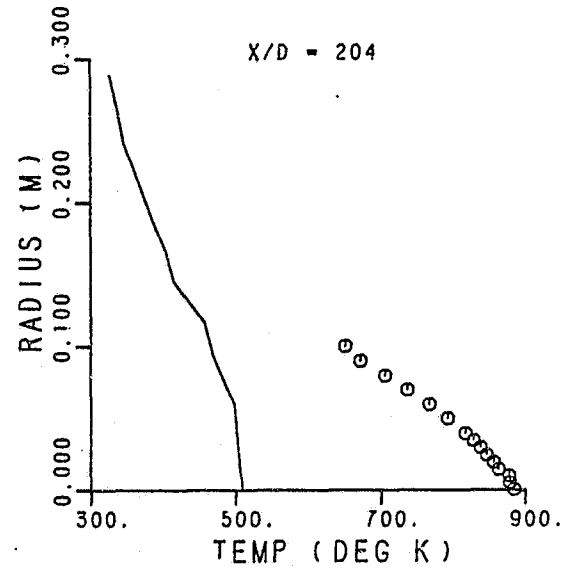
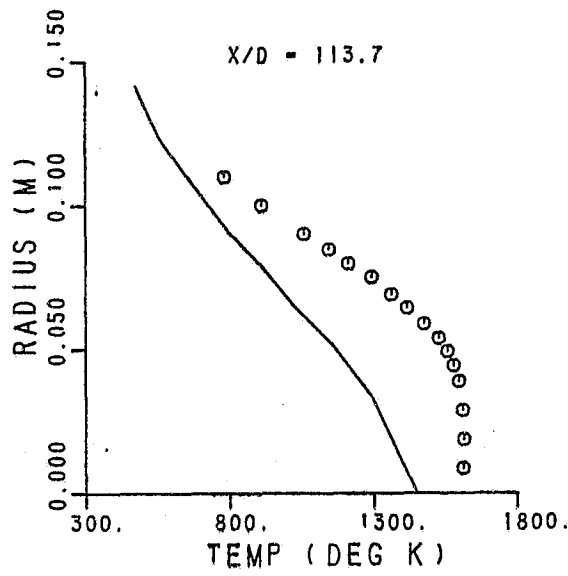
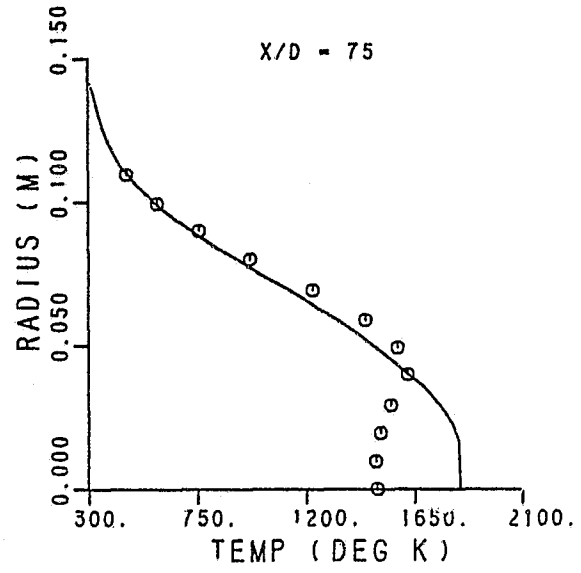
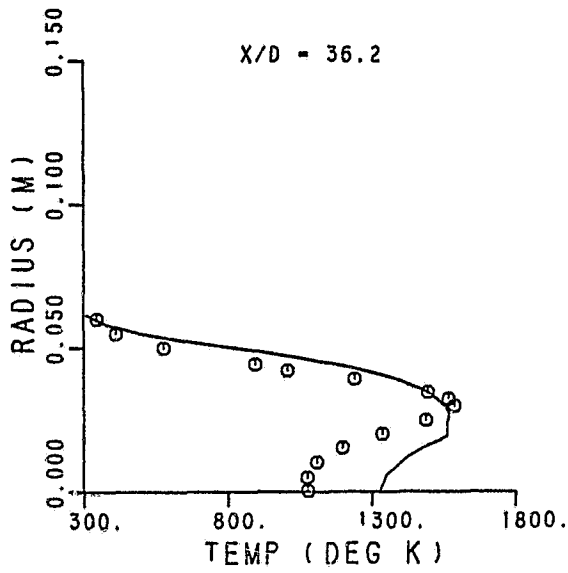


Figure 6.13-5. Radial Profiles of Temperature (Bilger's Model).

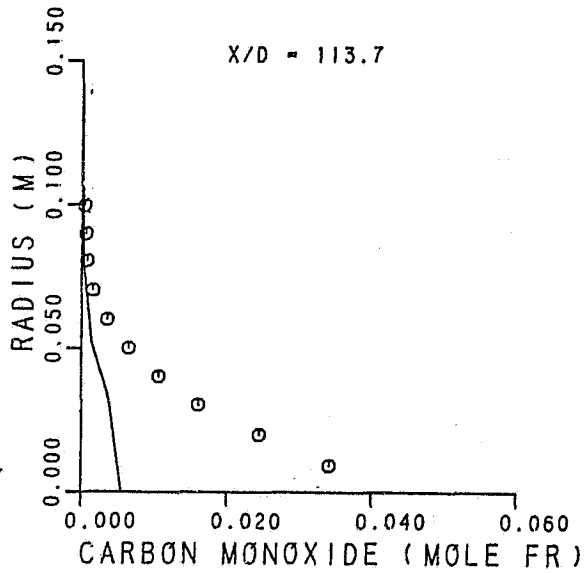
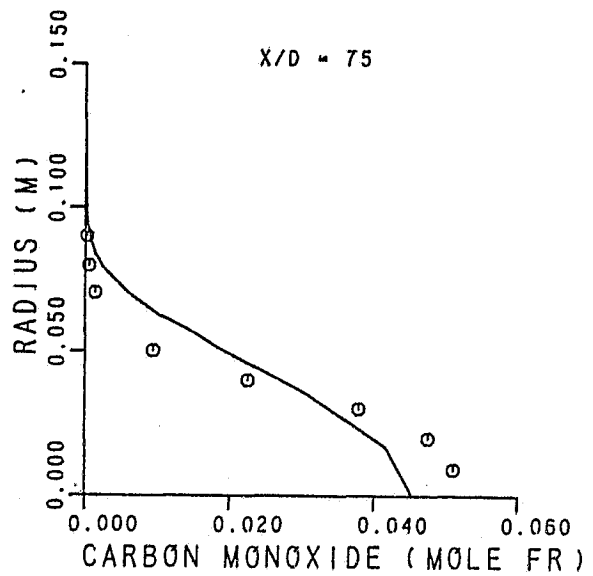
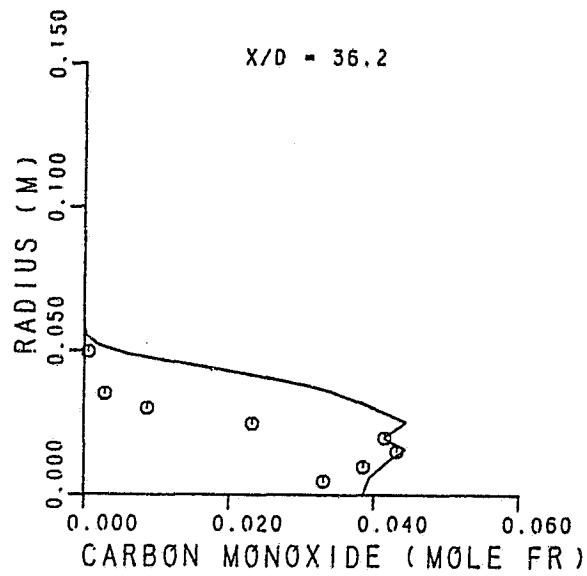


Figure 6.13-6. Radial Profiles of CO (Bilger's Model).

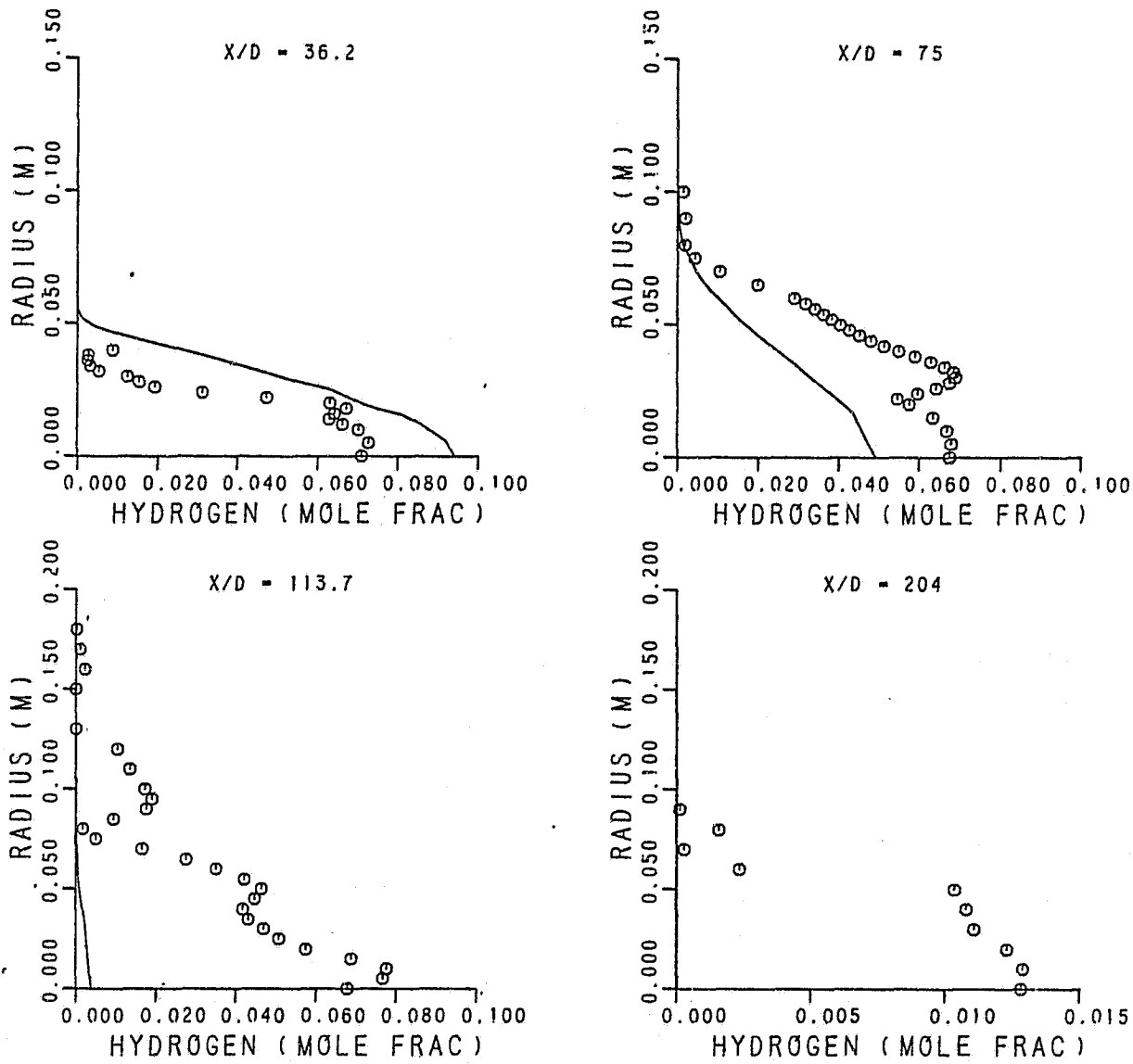


Figure 6.13-7. Radial Profiles of H₂ (Bilger's Model).

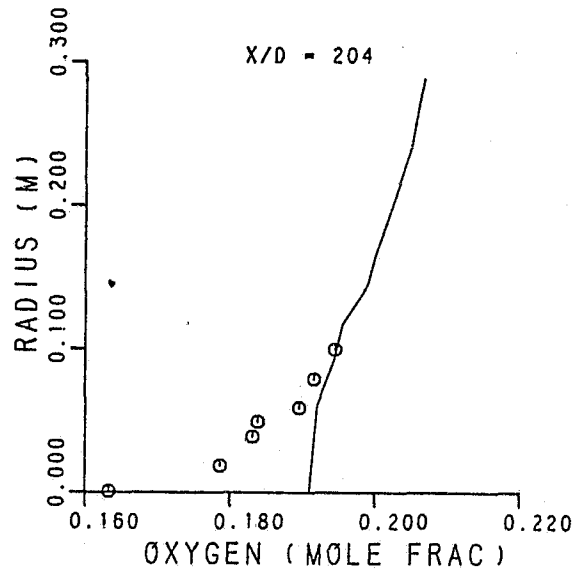
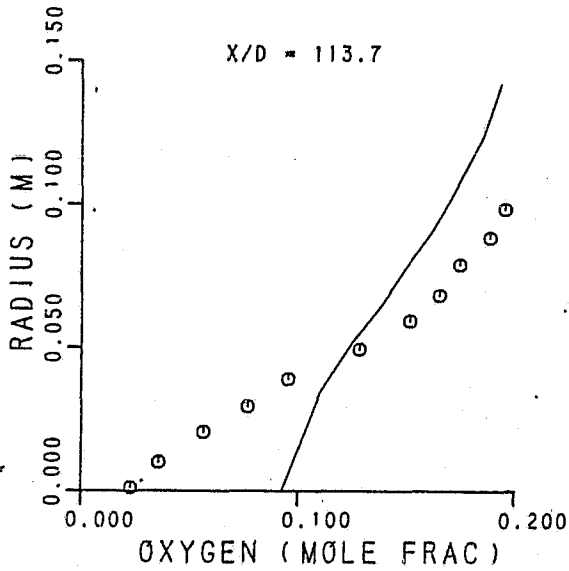
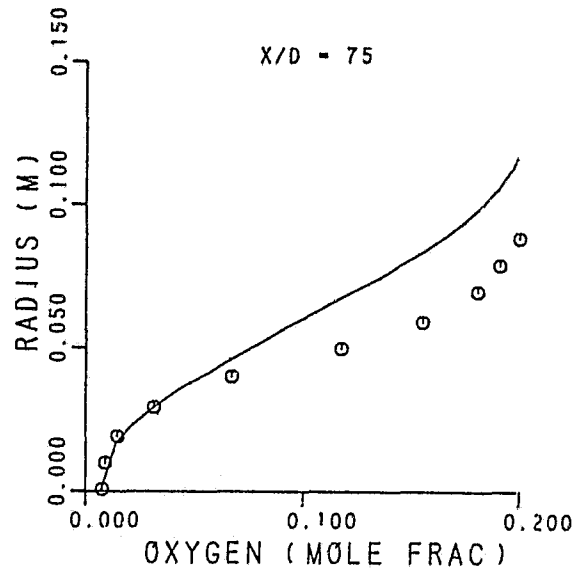
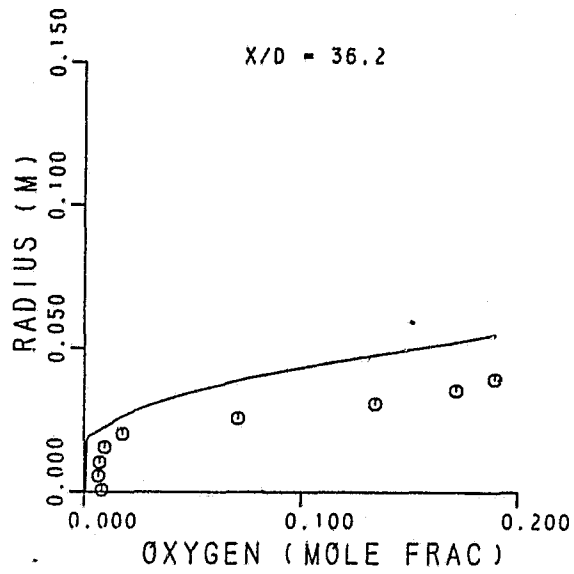


Figure 6.13-8. Radial Profiles of O_2 (Bilger's Model).

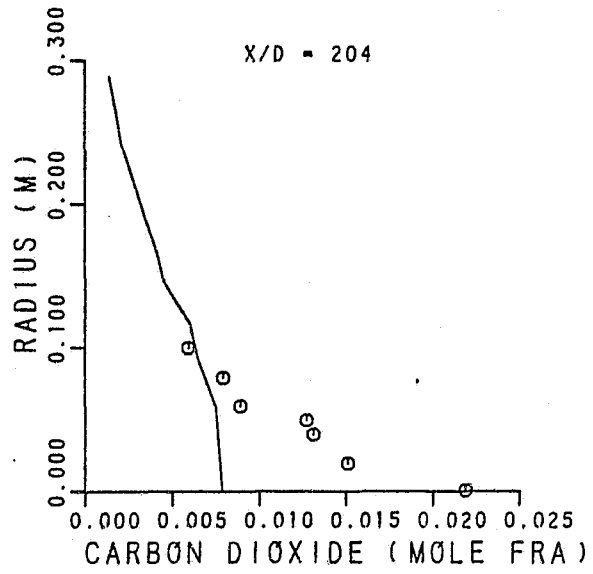
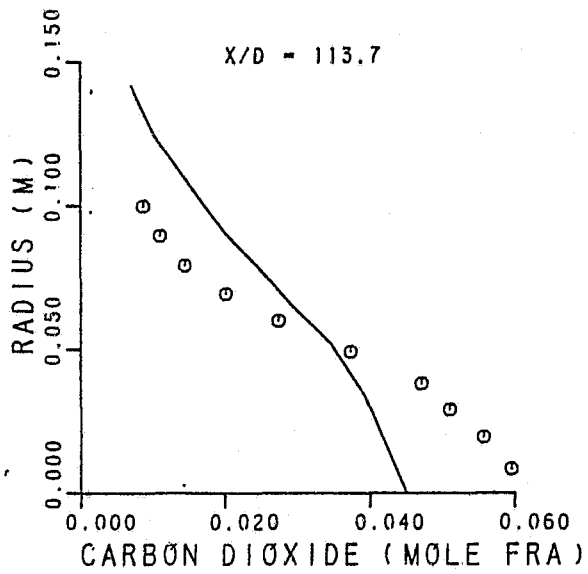
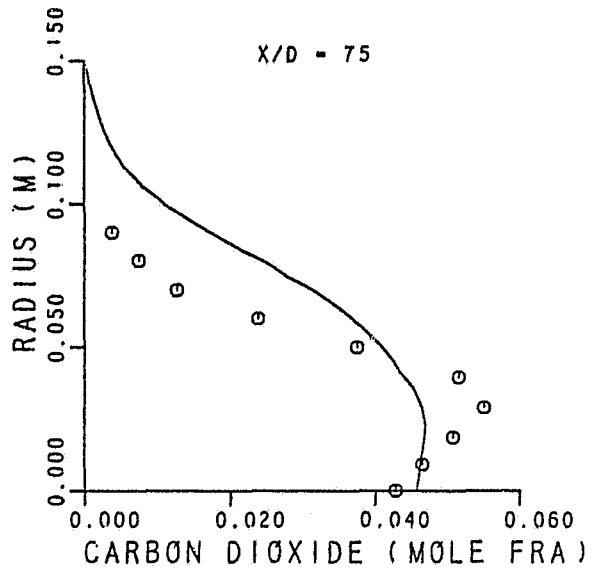
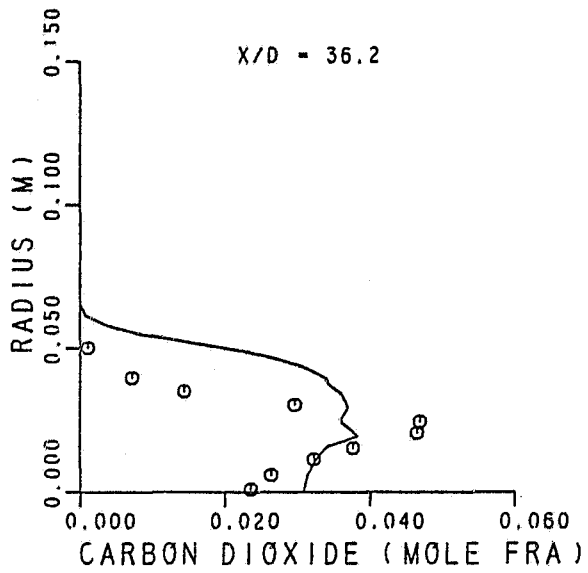


Figure 6.13-9. Radial Profiles of CO₂ (Bilger's Model).